The Small GTPase RAB18: Insights into cellular steatosis, lipophagy and the Non-alcoholic Fatty Liver Disease

Dissertation

Zur Erlangung des akademischen Grades des Doktors der Naturwissenschaften

(Dr. rer. nat.)

An der Fakultät für Chemie und Chemische Biologie der Technischen Universität

Dortmund

Vorgelegt von

Adrian Rieck M.Sc.

Dortmund 2021

First Examiner:

Prof. Dr. Jan Hengstler

Second Examiner:

Prof. Dr. Philippe Bastiaens

“I may not have gone where I intended to go, but I think I have ended up where I needed to be.”

- *Douglas Adams*

In memoriam Hermann Rieck

Für Dani

Table of content

Table of figures

List of tables

Zusammenfassung

Aufgrund steigender Fallzahlen gerät die Nicht-alkoholische Fettleberkrankheit zunehmend in den Fokus der Forschung. Das Hauptsymptom dieser Krankheit ist Steatose, welche als Ansammlung großer Fettablagerungen in den Hepatozyten in so genannten Lipidtröpfen (LT) beschrieben wird. Ein Oberflächenprotein dieser LT ist die GTPase RAB18. Rab-GTPasen sind bekannt für ihre Rolle in der zellularen Membranorganisation, weshalb angenommen wird, dass RAB18 in die Regulierung der LD-Biologie involviert ist. In der vorgelegten Arbeit werden neue Erkenntnisse zu dieser Regulierung und zur Lokalisierung RAB18s zur LD-Membran vorgestellt.

Die Lokalisierung RAB18s in die LT-Membran wurde mittels der Expression von RAB18-Mutanten in HepG2 Zellen untersucht. Dabei konnte die reversible zyklische Palmitoylierung des C-Terminus RAB18s als essenziell für die Lokalisierung festgestellt werden. In FRAP-Experimenten wurde gezeigt, dass die Inhibition der zyklischen Palmitoylierung durch niedermolekulare Inhibitoren die Lokalisation RAB18s veränderte, welche auch zu Veränderungen in der LT-Größe führte.

Die Reduktion der RAB18-Expression führte zu einer Vergrößerung der LT. Die kleinere LT Größe wurde durch Inhibition der Autophagie wiederhergestellt, jedoch war dieser Effekt war nur auf neu generierte LTs beschränkt.

Diese Experimente wiesen auf einen bisher unbekannten Mechanismus zur Kontrolle neu generierter LTs hin. In Folgeexperimenten wurden die Auswirkungen der Chloroquin-abhängigen Autophagieinhibition auf die LT-Größe *in vitro* in primären humanen Hepatozyten überprüft. Zellen, die mit Chloroquin behandelt wurden, entwickelten mehr, aber kleinere LTs, als unbehandelte Zellen. Dies war abhängig von der Chloroquin-Konzentration. Dieser Effekt konnte auch *in vivo* in Mäusen nachgewiesen werden. Mäuse auf einer fettreichen Diät, welchen täglich Chloroquin injiziert wurde, zeigten eine deutlich reduzierte LT-Größe. Die Blutwerte dieser Mäuse wiesen jedoch keine Veränderungen im Vergleich zur unbehandelten Kontrollgruppe auf.

Diese Arbeit kommt zu dem Schluss, dass die RAB18-Lokalisation zur LT-Membran über die cyclische Acylierung des C-Terminus kontrolliert wird. Die Funktion RAB18s besteht in der Reduzierung der LT-Größe durch die Regulierung der Autophagie neu gebildeter LTs. Dies ist ein wichtiger Mechanismus, welcher die LT-Anzahl sowie und Größe in Hepatozyten bestimmt.

Diese Ergebnisse identifizieren zwei wichtige Ziele für Entwicklung zukünftiger Steatosebehandlungen: Die zelluläre Palmitoylierungs-und die Autophagiemaschinerie.

Abstract

Non-alcoholic fatty liver disease is a rapidly growing concern for public health. Its most prevalent marker is steatosis, which is the accumulation of large lipid storage organelles called lipid droplets (LD) in the hepatocytes. RAB18, a member of the Rab family, localizes to the LD membrane. Rab family proteins are regulators of cellular membrane trafficking, therefore RAB18 is expected to play a role regulating LD biology. The presented work aims to elucidate this role as well as the mechanisms behind the localization of RAB18 to the LD membrane.

The localization of RAB18 was investigated by overexpressing mutant RAB18 variants in HepG2 cells. RAB18 localization was observed to depend on the reversible cyclical palmitoylation of its C-terminus. Using FRAP experiments, it could be shown that targeting the palmitoylation machinery with small molecule inhibitors modulated RAB18 localization. This coincided with changes in LD size in cells treated with de-palmitoylation inhibitors.

An overall increase in LD size was observed in HepG2 cells with RAB18 downregulation. The wild type LD size in these cells was restored by the inhibition of autophagy. This size reduction was due to newly created LDs. Inhibition of autophagy prior to LD accumulation was subsequently tested *in vitro* on primary human hepatocytes in sandwich culture. Inhibition of autophagy by chloroquine resulted in a dose dependent rise in LD number and a decrease in average LD size in these cells.

These effects could be translated to the *in vivo* situation in mice. Daily chloroquine injection of mice on a steatogenic diet resulted in a significant decrease of LD size *in vivo.* Conversely, no changes were detected in the blood-values of treated mice compared with the control.

This thesis demonstrates, that RAB18 localizes to the LD via a C-terminal acylation cycle. RAB18 reduces the size of LDs by modulating autophagy of newly formed LDs. This mechanism is important for LD number and size regulation in hepatocytes.

In conclusion, this study identifies two targets for future steatosis treatments: The regulation of the cellular palmitoylation and the autophagy machinery.

1. Introduction

1.1. Non-alcoholic fatty liver disease (NAFLD)

1.1.1. The creeping obesity "epidemic"

Caloric intake has been on the rise for the last decades, which corelates in a slow, but steady increase in obesity. This trend has been seen foremost in the wealthy western nations, but a rise in obesity has been also detected in the emerging nations in Asia, India and especially Oceania (Abarca-Gómez et al., 2017). The CDC and the WHO define obese individuals as having a BMI of larger than 30 kg/m^2 (CDC, 2020; Kim, 2016).Worldwide the mean percentage of men with a BMI larger than this threshold rose from 3.2% 1974 to 10.8% in 2014, whilst at the same time the rate of women rose from 6.4% to 14.9%. (Abarca-Gómez et al., 2017).

In the United States of America 39.8% of all adults were classified as obese in 2016 (Hales, 2017). The picture in Europe is similar, but less serious. In a study on weight conducted in 16 European countries excluding Germany, it was estimated that 12.8% of the adult population is to be classified as obese (Gallus et al., 2015). In Germany, the Robert Koch Institute estimated that 18.1% of German citizens were obese as of 2017. Even more troubling is the rising number of child obesity. After normalizing the BMI to age and gender, 6% of German children were obese as of 2018 (Schienkiewitz et al., 2017, 2018).

Besides the impact on the personal wellbeing, such as loss of mobility and endurance, obesity exhibits comorbidity for a variety of diseases such as cardiovascular diseases and type II diabetes. It has also been shown that obesity worsens the outcome of cancer as well as the recent corona pandemic (Schelbert, 2009; Schienkiewitz et al., 2012; Kwok et al., 2020).

1.1.2. Epidemiology of non-alcoholic fatty liver disease (NAFLD)

The liver is severely affected by obesity as well. The accumulation of fat in the liver, broadly termed non-alcoholic fatty liver disease (NAFLD), has been linked to obesity (Bence and Birnbaum, 2020). Though incidence numbers vary depending on the chosen detection method, it is assumed that the prevalence of NAFLD in the US, Europe and Japan was 10-30% in 2013.(Loomba and Sanyal, 2013). NAFLD is also connected to several severe liver related outcomes, such a cirrhosis and hepatocellular carcinoma. In the US diseases linked to end stage NAFLD were listed as the second leading cause of liver transplantation behind HCV infection in 2013 (Wong et al., 2015).

Due to the chronic gradual progression of NAFLD, it can be assumed that the worst is yet to come. Markov modeling of NAFLD progression in eight western countries predicted an increase of 68-156% in NAFLD derived cirrhosis by 2030. The prevalence of NAFLD related hepatocellular carcinoma (HCC) was estimated to rise 47%-130% by 2030. In line with these findings, the liver-related deaths were prognosed to rise by 182% by 2030 in France and 73% in Japan (Estes et al., 2018).

These prognoses reveal the urgency of the situation, and many studies have been conducted on NAFLD disease progression. But as much as we know about the spread of the disease, the underlying cellular and molecular mechanisms of NAFLD progression remain largely unknown.

1.1.3. NAFLD Progression

1.1.3.1. Defining NAFLD

NAFLD has been defined by the accumulation of fat in the hepatocytes of the liver, called steatosis, without evidence of alcohol consumption. In steatosis, although there is a heavy accumulation of fat, the liver is not damaged and there is no inflammation or fibrosis. From this simple steatosis NAFLD can progress into steatohepatitis (NASH) In NASH, the liver architecture is severely disrupted. Hepatocytes lose their typical shape and appear expanded to twice their size, which has been termed “ballooned”, and first signs of fibrosis might be detected (Chalasani et al., 2018; Wong et al., 2010).

In the next subsection, aspects of these stages shall be briefly discussed.

1.1.3.2. Steatosis: Abnormal lipid accumulation in the liver

Under physiological conditions, dietary lipids are emulsified in bile and taken up by the intestine as free-fatty acids (FFA). These FFA are gradually metabolized to triacylglycerides (TAGs). These freshly synthesized TAGs are then packaged with cholesterol esters in chylomicrons, which are released into the lymph bypassing the liver. From there they are delivered directly to muscle and adipose tissue, where fatty acids are stored or used for energy production. Under physiological conditions, the TAGs content in the liver does not exceed 5% of the liver weight. (Bechmann et al., 2012) (Figure *1*A).

The accumulation of fat in the liver is called steatosis. It is defined by the accumulation of TAGs in liver exceeding 5% of liver weight, without inflammation (Paradis and Bedossa, 2008). These TAGs are stored in cellular organs called lipid droplets (LD)

Many factors induce LD accumulation in the liver. In the current model, heavy obesity, diabetes type2 or insulin resistance is thought to induce fat overload in the adipocytes, which leads to lipolysis of TAGs within these cells. This releases FFA into the bloodstream. The FFAs are subsequently transported to the liver via the portal vein circulation. In the liver, the fatty acids are taken up by the hepatocytes. The hepatocytes metabolized the lipotoxic FFA to the non-toxic TAG. These newly formed TAGs are then stored in LDs until they can be degraded to FFA for energy consumption or release into the bloodstream (Lewis et al., 2002). Besides the adipocyte-derived lipids, TAGs synthesized from glucose via *de novo* lipogenesis were found to contribute up to 26% of the total lipid content in the liver during NAFLD (Donnelly et al., 2005) (Figure 1B).

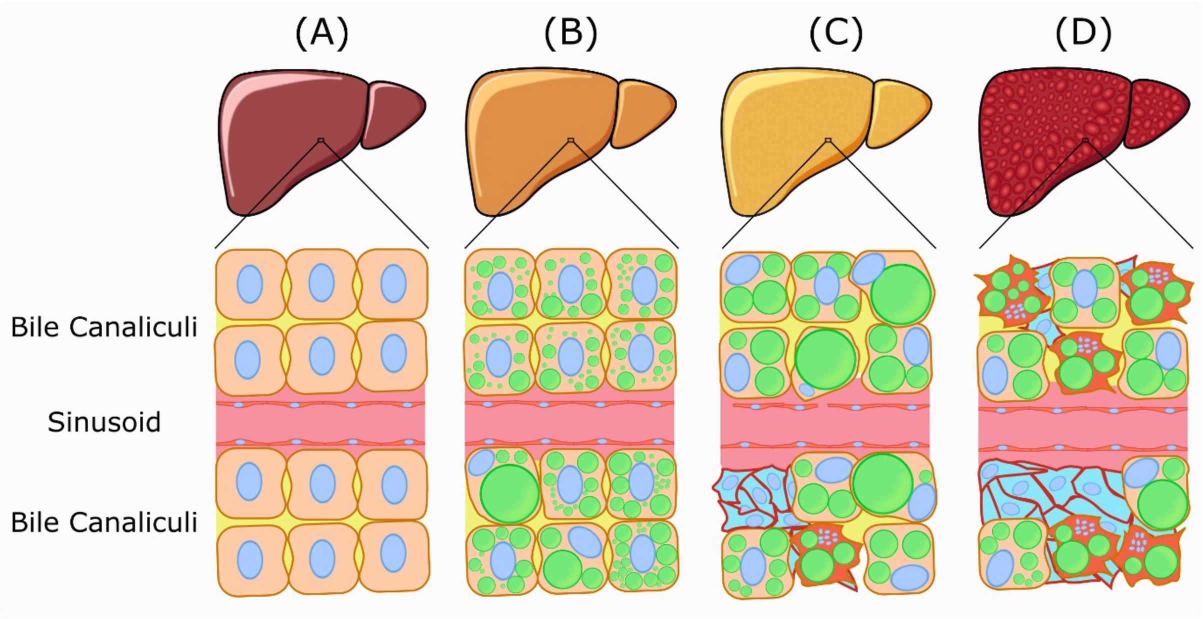

Figure 1 | NAFLD disease progression over time

The healthy liver **(A)** does not maintain large LDs under physiological conditions. The epithelial cells of the sinusoids form a permeable barrier. Hepatocytes form an interconnected luminal compartment through tight junctions called bile canalicular network (yellow). These canaliculi transport bile from the hepatocytes to the canal of Hering where it is further transported to the bile duct and ultimately to the gallbladder. In steatosis **(B),** liver cells fill up with large LDs (green). The liver structure is mainly intact, but over time LD growth and other factors disrupt the tissue architecture. If the disruption persists and inflammation ensues, the disease progresses to Non-alcoholic steatohepatitis (NASH) **(C)**. Hepatocytes start dying (brown) and inflammation of the tissue results in the activation of stellate cells. The activation of stellate cells results in scarring and fibrosis of the liver tissue (light blue). If the ongoing inflammation and fibrosis continue, the liver progresses into cirrhosis **(D)**. At this point numerous cells are either disrupted in their function or dying, fibrosis is rampant, and the liver architecture and function is impeded (adapted from Bessone et al., 2019).

Steatosis has been found to be a largely benign and highly reversible condition. Usually, the liver recovers back to normal LD number and size after diet and life-style changes have been applied (Martín et al., 2013). In a study following NAFLD patients over three years 15% of the patients recovered to a healthy liver, 62% remained steatotic and only 23% showed signs of fibrosis and inflammation progressing into NASH (Wong et al., 2010).

1.1.3.3. Non-alcoholic steatohepatitis (NASH)

Of all steatosis cases, 5-10% develop hepatic inflammation and NASH. The cause of this inflammation is heavily debated. Studies on NASH reveal a complex web of intra- and extra-hepatic influences forming the current "multiple parallel hit hypothesis". In this hypothesis FFA accumulation in liver is the consequence of multiple different "first hits" such as the previously described case for diabetes type 2. FFAs are lipotoxic, so to detoxify the liver, hepatocytes take up the FFA and metabolize them to TAGs for safe storage in LDs. This results in the accumulation of large LDs described in steatosis 1.1.3.2 (Bessone et al., 2019; Buzzetti et al., 2016).

After the hepatocytes reach their storage limits for TAG, the FFA concentration in the liver increases. Because of their lipotoxicity high concentrations of FFA are creating a pro-inflammatory environment. Under this condition the liver is rendered susceptible to further inflammatory promoting "hits", which include, LPS from the gut microbiome, intestine signaling, signaling of liver resident immune cells (Kupffer cells), oxidative stress and further dietary lipotoxic components (Bessone et al., 2019; Buzzetti et al., 2016).

One histological marker frequently found in NASH is the already mentioned "ballooned" hepatocytes. These hepatocytes double in size and lose their hexagonal shape. Staining shows that ballooned cells are filled with numerous medium to large sized LD. These LDs take up most space in the cell displacing the nuclei and any cellular organelles. The ballooned cells show how much the hepatocytes are capable to take up fatty acid to prevent the accumulation of FFAs (Brunt et al., 2004; Caldwell et al., 2010).

All these liver damaging factors increase the apoptosis as well as a special form of apoptosis called necroptosis of hepatocytes. The cell deaths further add onto the proinflammatory environment results in the progressively worse inflammation of the tissue (Kanda et al., 2018; Mohammed et al., 2021). In a follow-up study on NASH patients, 59% percent of all patients still had NASH at the end of the study. But also 35% returned to borderline NASH and one even regressed to steatosis. Showing that NASH is also reversible (Wong et al., 2010).

In cases that do not reverse to steatosis, the chronic inflammation of the liver in combination with the reoccurring injuries activate the specialized hepatic stellate cells. The activation of these cells results in fibrosis and scarring of the liver (Friedman, 2008) (Figure 1 C).

Only 30% of all NASH cases lead to fibrosis and the progression is very slow. In a meta-study including 11 cohort studies, it could be shown that annual fibrosis progression in NASH was 0.14, which translates to an average 7.1 years per stage progression (Singh et al., 2015). In another meta-study consisting of 13 cohort studies the progression of the fibrosis stage could be associated with liver mortality in NAFLD patients (Taylor et al., 2020).

Between 5 and 25% of NASH patients with fibrosis show signs of cirrhosis within a 7 year follow-up period (Hashimoto and Tokushige, 2011) (Figure 1 D). Though pharmacologic treatment of cirrhosis is possible and may elongate the patient's life, as of today liver transplantation remains the only cure. However, this is not without risk. The survival rates of liver organ transplantation lie at 68%-70% over 5 years. The mortality of liver cirrhosis without transplantation is 85% over 5 years (Schuppan and Afdhal, 2008; Kumari et al., 2018).

In addition to the cirrhosis coupled mortality risk, cirrhosis may also progress to hepatocellular carcinoma (HCC). In a study done on 168 individual the cumulative risk of HCC in patients with NASH linked cirrhosis was found to be 2.6% per year (Ascha et al., 2010). Once HCC has developed, only a small subset of HCC can be treated by hepatectomy or liver transplantation. The majority of HCC can only be treated palliatively (Kumari et al., 2018).

It can be clearly seen that the further NAFLD progresses, the more serious the condition becomes. Luckily, these stages progress slowly, but steadily and a patient with steatosis might be decades away from cirrhosis. During most of this time the most prevalent symptom of NAFLD is the amassing of large LDs in steatosis, so to treat it one has to understand the mechanics governing these small intracellular organelles.

1.2. The lipid droplet (LD), a neglected organelle

1.2.1. More than just fat droplets: The new role of LDs in cellular biology

For a long time, LDs were largely seen as inert fat accumulations or storage containers. It took nearly 100 years after their first description until LDs were finally recognized as a highly regulated organelle in the late 90s to early 2000s (Coleman, 2020).

The LD morphology is described as round spheres of varying size. In contrast to the other organelles, the LD envelope consists of only one phospholipid monolayer encapsulating a hydrophobic core of neutral LDs. The main contents of this core are TAGs and sterol esters, but

LDs have a very heterogenous composition otherwise (Onal et al., 2017; Tauchi-Sato et al., 2002; Horn et al., 2011). The primary role of LDs is presumed to be the storage of neutral fatty acids. From there they can be easily mobilized in times of nutrient deprivation and consumed for energy production by beta oxidation in the peroxisomes or the mitochondria. LDs have been shown to increase their mitochondria contact surface during starvation. It is thus thought that this way FFAs derived from autophagy can be funneled through the LDs into the mitochondria, which highlights the role of LDs as fatty acid transport hub (Rambold et al., 2015).

LDs have also been reported in the nucleus. The function of these new found nuclear LDs is debated, but it has been argued that these LDs are involved in the lipid homeostasis in the nucleus (Uzbekov and Roingeard, 2013; Lagrutta et al., 2017).

LDs have been shown to play various roles in transcription regulation. The Fat-specific protein 27 (FSP27) was detected to interact directly with the N-terminal region of nuclear factor of activated T cells 5 (NFAT5). It is hypothesized that this interaction regulates NFAT5 in adipocyte stress response (Ueno et al., 2013). In *Drosophila melanogaster* LDs act as storage for histones. During the earliest stages of embryogenesis, the protein Jabba acts as an anchor for histones fixating them to the LDs. This is hypothesized to ensure enough histones for further developmental stages afterwards (Z. Li et al., 2012; McMillan et al., 2018).

As it can be seen, LDs are full fledge multipurpose organelles and far away from inert accumulations of fat.

1.2.2. Detection of LDs

1.2.2.1. Staining of LDs

Following a growing interest in LD research, several detection methods have been developed over the years. LD detection can be achieved via staining with several LD specific dyes. Nile Red is a commonly used dye, whose unique fluorescent properties make it suitable for LD staining. Whilst the dye is non-fluorescence in hydrophilic environments, it becomes fluorescent in a hydrophobic environment. LDs, being the most hydrophobic compartment in the cell, are thus easily stained (Greenspan et al., 1985).

However, most dyes for LD are lipophilic. These dyes localize to hydrophobic compartments in living as well as fixed cells. The oldest, oil red, has been used for nearly 100 years (Proescher, 1927). The most common of the lipophilic LD dye today is BODIPY. In a direct comparison of Nile Red and BODIPY for LD staining in micro algae, BODIPY was detected faster and was more photostable than Nile Red (Govender et al., 2012).

Recently, fluorescent labelled lipid conjugated dyes have entered the market, which allow the tracking of fatty acids *in vivo*. The lipid conjugate BODIPY-C12, for example, was successfully used to track lipid distribution in cells (Rambold et al., 2015).

1.2.2.2. Coherent Anti-Stokes Raman Spectroscopy (CARS)

All dyes have one aspect in common: they are artificial labels that must be introduced into the system. A novel imaging method called Coherent Anti-Stokes Raman Spectroscopy (CARS) has recently been applied to detect LDs label free (Jüngst et al., 2011).

The principle behind CARS is based on Raman Scattering, also called the Raman-effect. The Raman-effect, first discovered by C. V. Raman, is a form of non-elastic light scattering (Raman and Krishnan, 1928). Light scattering occurs when a photon collides with a molecule. The energy of the collision elevates the molecule to a virtual energy state. Since the virtual state is not an eigenstate of the molecule, it reverts to either the ground state or the vibrational level emitting a photon. Spontaneous Raman Scattering occurs when this final state differs from the original state of the molecule. If the final state is higher than the original state, the wavelength of the emitted photon wavelength is longer (Stokes shift). If the final state is lower, the wavelength of the emitted photon is shorter (Anti-Stokes shift) (Jones et al., 2019) (Figure 2A).

The resulting signal linearly depends on the laser used to induce Spontaneous Raman Scattering. The signal, though comparatively weaker than fluorescence, can be used to image biological samples without photobleaching a typical problem of fluorescence microscopy (Uzunbajakava et al., 2003).

The weak signal of Spontaneous Raman scattering can be enhanced by CARS. By using two pulsed lasers, a tunable shorter wavelength pump laser and a longer wavelength stokes laser, specific molecular bonds can be transferred to the vibrational level in CARS. A third probe laser stimulates the resonant bond to a virtual level resulting in the emission of an anti-stokes shifted photon. In CARS microscopy the probe laser and the pump laser are identical, reducing the number of lasers needed to two (Rodriguez et al., 2006; Jones et al., 2019) (Figure 2B).

In contrast to the Spontaneous Raman signal, the CARS signal intensity is quadratically dependent to the laser power, resulting in higher signal strength. Additionally, the CARS signal is directional and both the forward-scattered and epi-scatter light can be detected (Jones et al., 2019; Moura et al., 2016; Rodriguez et al., 2006; Rostron et al., 2016). The CARS microscope used in thesis was equipped with two detectors for forward scattered FCARS and the epi-scattered ECARS (Figure 2C)

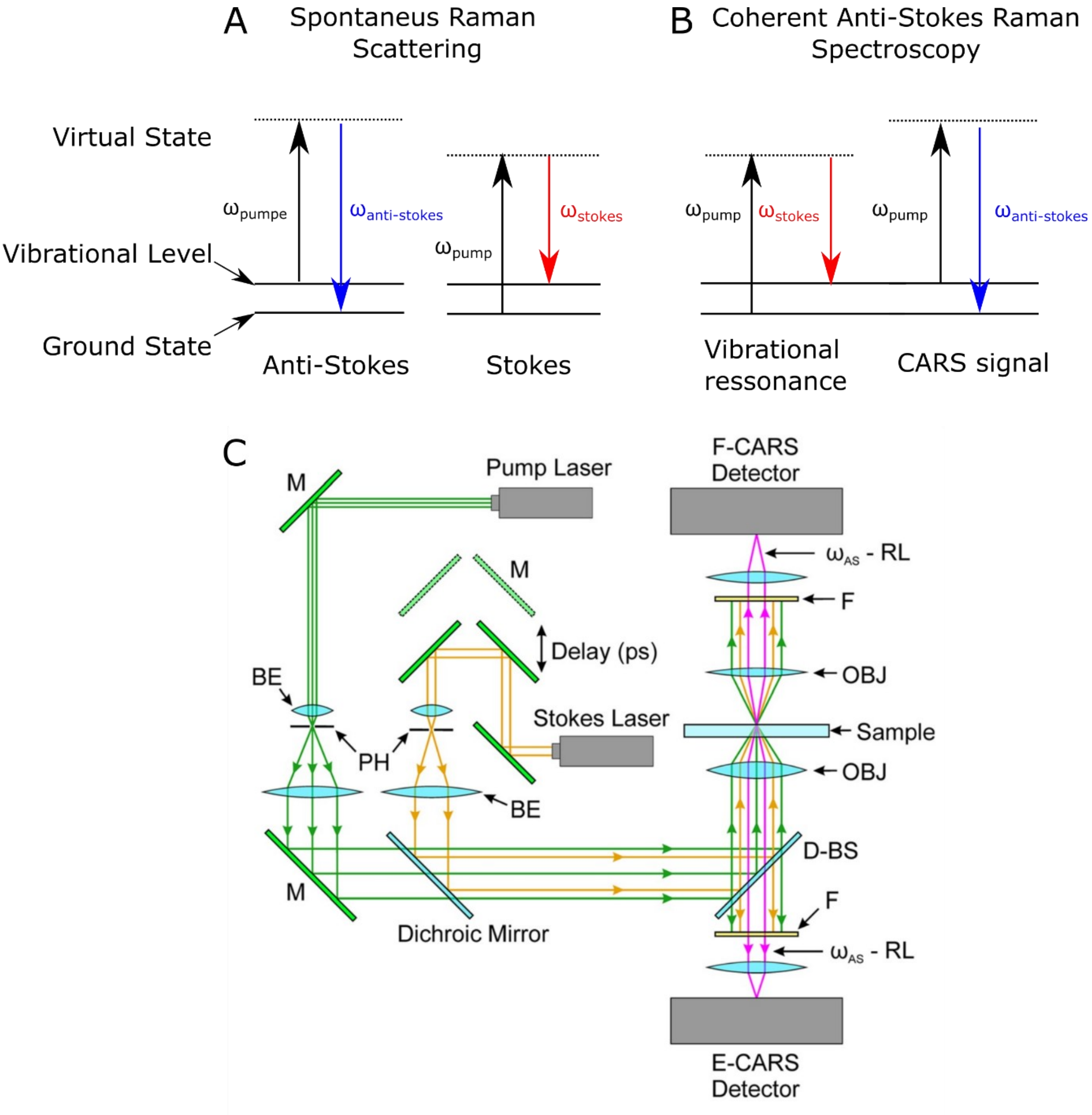

Figure 2 | Basic concept and schematic of a CARS microscope

When molecules are hit by a photon they are elevated to virtual state. In Spontaneous Raman Scattering **(A)** the molecule reverts to its ground state emitting either an anti-stokes or stokes shifted photon depending on the molecule's vibrational state. In Coherent Anti-Stokes Raman Spectroscopy **(B)** two photons (ω_{pump} and ω_{stokes}) are used to excite the resonance of a specific molecular bond. A second ω_{pump} stimulates the resonant molecular bond to a virtual state resulting in the emission of an anti-stokes shifted photon. This principle is used in CARS microscopy **(C)**. Two lasers are used for CARS detection: A tuneable Pump Laser and a Stokes Laser. Both are directed via dichroic beam splitter (D-BS) and objectives (OBJ) to the sample. Both forward (FCARS) and epi-scattered (ECARS) Raman light (RL) is filtered through bandpass filters (F) and detected by two PMT sensors. Images are obtained by raster scanning of the sample. M: mirror, PH: pinhole, BE: Beam expander (adapted from Rodriguez et al., 2006; Jones et al., 2019)

1.2.3. LD biogenesis

Although interest in LDs has risen sharply, little is known about how the organelle is formed. The current hypothesis is the budding of new LDs from the ER (Figure 3). The hydrophobic core of LDs consists mainly of TAGs, which are synthesized via enzymes called diglyceride acyltransferases (DGAT). DGATs catalyze the transformation of diacylglyceride (DAG) to TAG by covalently linking acyl-CoA to the glyceride backbone of DAGs (Cases et al., 1998).

Humans have two DGAT enzymes named DGAT1 and DGAT2. Whilst DGAT2 localizes to the mitochondria, ER and LDs, DGAT1 is only detected on the ER (Stone et al., 2009; Xu et al., 2012). The crystal structure of DGAT1 reveals an opening from the catalytic core into the hydrophobic space between the ER leaflets. This suggests that the resulting TAG is subsequently released into the ER bilayer (Wang et al., 2020) (Figure 3A). Biophysical modelling calculated that hydrophobic TAGs coagulate as a lens between the two sheets of the ER lipid bilayers. This lens formation can be further enhanced by the ER morphology (Thiam and Forêt, 2016; Choudhary et al., 2018).

The transition from the lipid lens to nascent LD has been extensively studied in yeast and mammalian cells. In *S. cerevisiae*, the FLD1 protein is essential for LD development. Its mammalian homologue SEIPIN has been linked to Berardinelli–Seip congenital lipodystrophy, which is a disease marked by the inability to create LDs (Magré et al., 2001). *In vitro* studies show that cells mutant for SEIPIN form a multitude of extremely small LDs. These smaller LDs were less bound to the ER, highlighting the importance of SEIPIN for LD-ER contact (Salo et al., 2016).

Studies on its structure have shown that SEIPIN forms a heterogenic oligomer with a novel protein called the lipid droplet assembly factor 1 (LDAF1). This oligomer is thought to provide a platform for LD growth and budding, which allows other lipid synthesizing proteins like the long-chain-fatty-acid-CoA ligase 3 (ACSL3) to localize to the forming LDs (Chung et al., 2019; Salo et al., 2016).

The localization of these proteins to the forming LD catalyzes the further concentration of neutral lipids between the bilayer, leading to an increased bump between the two sheets of the membrane forming a nascent LD. At a certain size this nascent LD matures to bud from the membrane (Chung et al., 2019; Wang et al., 2016) (Figure 3B)

The steps between formation of a nascent LD (Figure 3C) and a fully budded cytosolic LD (Figure 3D) are still largely unknown. Calculations based on biophysical modeling concluded that after reaching a certain size the matured LD favors its own encapsulation, but so far, no protein has been determined to be essential for catalyzing the encapsulation process. After encapsulation the outer lipid layer of the ER-membrane forms the single LD membrane (Thiam and Forêt, 2016).

Once budded, LDs remain far from being inert organelles. Depending on size, LDs have been shown to have different proteins associated with them. LD associated proteins have been divided into two distinct classes. Class I proteins target the LD membrane through ER membrane transfer. Class II proteins localize to the LD via the cytosol. These proteins are thought to regulate LD growth, motility and number. In the following known processes for LD growth regulation shall be further discussed (Kory et al., 2016).

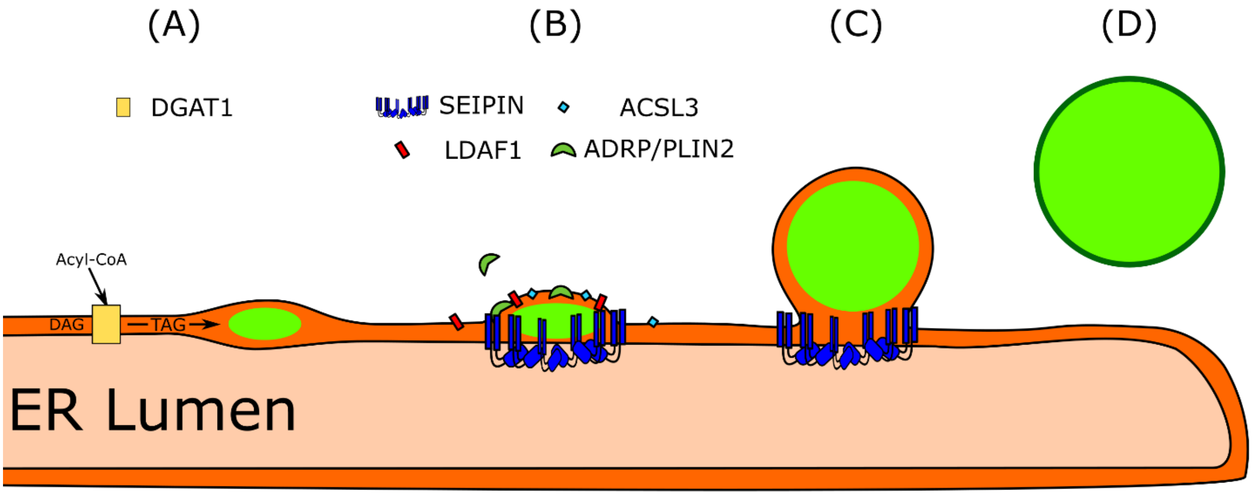

Figure 3 | Budding model of LD *de novo* synthesis

DGAT binds Acyl-CoA to DAG releasing TAG into the ER membrane **(A)**. There the TAG accumulates, forming a hydrophobic lens between the sheets. SEIPIN and LDAF1 stabilize this lens allowing for further proteins to localize **(B)**. Among them are ACSL3 and ADRP, which further the LD growth. The nascent LD forms an outgrow of the ER membrane **(C)** after which it buds with the outer sheet of the ER membrane bilayer forming the outer LD membrane **(D)** Adapted from Chung et al., 2019; Thiam and Forêt, 2016.

1.2.4. LD growth

Depending on cell type and metabolic state, LDs largely differ in size and number. LD usually remain around their budding size of 100-200 nm diameter. Yet in cells like white adipocytes these LDs can reach up to 100 µm in diameter (Walther and Farese, 2012). With recent progress being made in LD research more mechanisms governing the LD size increase were discovered.

1.2.4.1. *ER-tethering*

Application of electron microscopy has revealed that freshly budded LDs maintain contacts to the ER, peroxisomes, and mitochondria. In *S. cerevisiae*, all LD have been shown to stay in contact or at least proximity with the ER. The protein SEIPIN, described in section 1.2.3, appears to play a role at these post-budding ER-LD contact sites, too. Thus, it has been argued that these sites are necessary to transfer lipids from the ER membrane to the LD (Novikoff et al., 1980).

Further studies into ER-LD contact sites show a central role of the COPI complex in LD-ER tethering. The ARF1/COPI complex removes parts of the LD membrane by excising tiny 60 nm LDs. This process is thought to increase the surface tension of LD, which in terms allows it to form membrane bridges with the cytoplasm facing ER membrane leaflet (Thiam et al., 2013).

The resulting bridges allow for the exchange of lipids and membrane proteins such as adipose triglyceride lipase (ATGL) and glycerol-3-phosphate acyltransferase 2 (GPAT2) (Wilfling et al., 2014). The ER membrane protein fatty acid transport protein 1 (FATP1) also has been reported to translocate onto the LD via LD-ER contact sites. On the LD FATP1 acts as a binding site for DGAT2 (Xu et al., 2012).

1.2.4.2. *On-site lipid synthesis*

Upon oleic acid loading DGAT2 localizes to the LD membrane via the FATP1 protein in adipocytes (Xu et al., 2012). This localization to the LD membrane allows the local synthesis of TAG which increases the LD size (Kuerschner et al., 2008). However, DGAT2 is not the only protein localizing to the LD. ACSL1 and ACSL3 which supply the acyl-CoA needed for TG synthesis were also detected on the LD membrane. GPAT and AGPAT, both enzymes which synthesize TAG precursors lysophosphatidic acid and phosphatidic acids were detected to localize to the LD in *Drosophila* S2 cells, indicating that LD growth can occur by TAG synthesis directly on the LD (Wilfling et al., 2013).

1.2.4.3. *Fusion of cytosolic LD*

LD size increase has also been reported as a result of an atypical LD fusion event. During fusion events, two LDs coalesce into one increasing LD size whilst simultaneously decreasing LD number. A fusion event starts with the contact of two different sized cytosolic LDs.

The contact site formation is mainly governed by the two DFF45-like effector (CIDE) proteins CIDEA and B. First associated with cell death, CIDEA and B were also detected on LDs. There they specifically localize to the LD-LD contact sites. Because the N-termini of CIDEA and B interact with each other, a complex is formed stabilizing the contact site. The interaction between CIDEA and CIDEB also stabilizes the localization of the third protein CIDEC, also known as FSP27 (Inohara et al., 1998; Xu et al., 2016). The CIDEC-N-termini are theorized to form a helical structure with a diameter of 8nm, which could support the creation of a LD-LD pore at the contact site (Choi et al., 2017).

Through this pore fatty acids transfer from the smaller LD to the bigger LD, which is presumably powered by the hydrophobic forces and the pressure differences inside the two LDs. However, the exact mechanism remains uncertain (Jüngst et al., 2013). After completion of the transfer, the two LDs coalesce into one (Gong et al., 2011).

1.2.5. LD size reduction

LDs not only need to expand and take up fatty acids, but also release them in times of nutrient deprivation. This happens in a process called lipolysis. During lipolysis, the TAGs in the LD core are stepwise hydrolyzed to the glycerol backbone and FFA. However, this has been proven to be only one of two possible degradation mechanisms. LDs can also be removed via the cellular autophagy machinery in a process called lipophagy. A quick review over both mechanisms shall be given in the following sections.

1.2.5.1. Lipolysis

The most studied mechanism to reduce LD content is the lipolysis pathway. Via this pathway, the TAG content of LDs is degraded in a stepwise process catalyzed by three hydrolases: ATGL, the hormon sensitive lipase (HSL) and the monoacylglycerol lipase (MGL) (Schweiger et al., 2006). The FFAs released from the LD by lipolysis are subsequently further degraded for energy consumption via beta-oxidation in either the peroxisomes or in the mitochondria (Bartlett and Eaton, 2004; Lazarow and De Duve, 1976).

The first step in lipolysis is catalyzed by ATGL. It has a high affinity for TAG catalyzing the hydrolysis of one of the three fatty acid chains. The product diacylglycerol (DAG) is the substrate for further downstream hydrolysis, making ATGL activity a rate-limiting step of lipolysis (Zimmermann et al., 2004). ATGL levels are regulated by PPARγ signaling and mTOR activity (Roy et al., 2017; Chakrabarti et al., 2010).

In the liver ATGL activity is inhibited by Perilipin 5, which binds ATGL and protects LD content from lipolysis. Upon phosphorylation Perilipin5 is inhibited, which activates ATGL activity on the LD hydrolyzing the TAG content to DAG (Langhi et al., 2014; Wang et al., 2011).

DAG is the main substrate of HSL, which is the next enzyme in the lipolysis chain. HSL can bind both TAG and DAG but shows 10x higher affinity towards DAG. Its activity depends on phosphorylation via AMP or PKA pathway. When phosphorylated, it catalyzes the hydrolysis of DAG to monoacylglycerol (MAG) releasing one fatty acid chain (Strålfors et al., 1987).

Finally, MAG is further hydrolyzed via the monoacylglycerol lipase (MGL). It catalyzes the last hydrolysis of MAG, removing the last fatty acid from the glycerol backbone (Tornqvist and Belfrage, 1976).

In summary, the lipolysis chain releases three fatty acids and one glycerol molecule for each TAG slowly catabolizing the content of the LD which reduces its size.

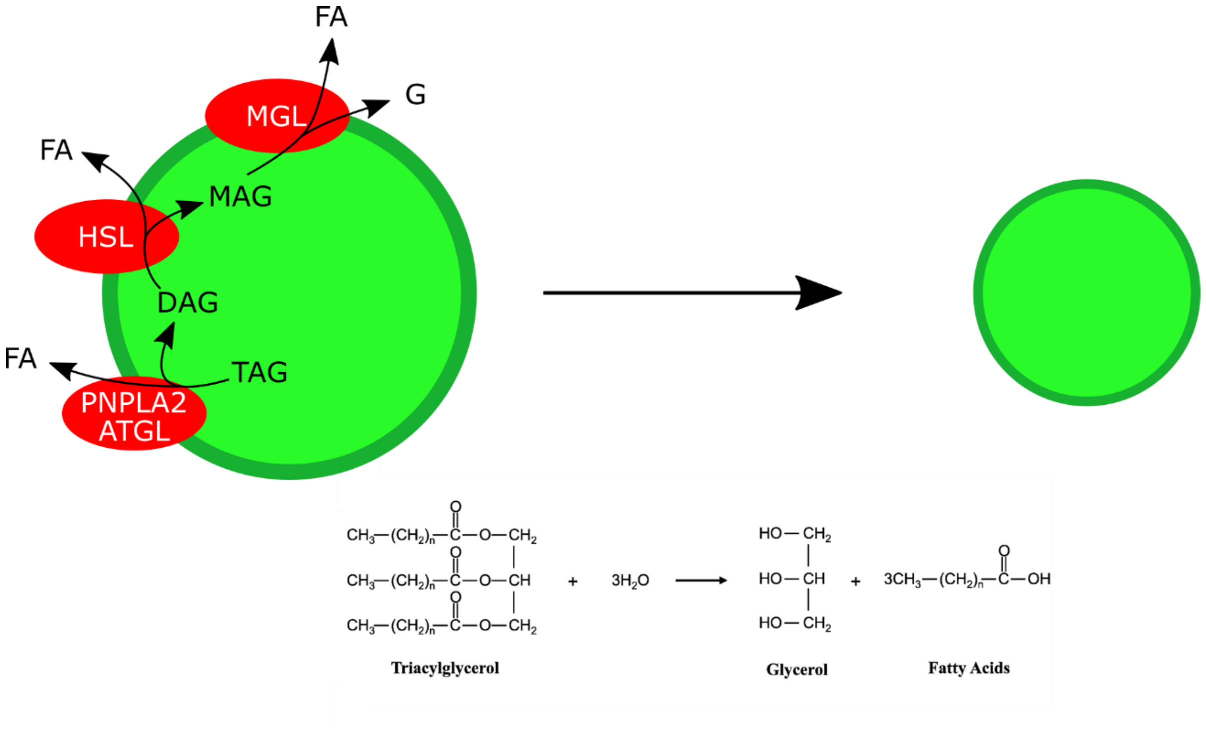

Figure 4 | The lipolytic hydrolysis chain

In lipolysis TAGs are degraded in a stepwise process. ATGL hydrolyses TAG to DAG under the release of one fatty acid chain (FA). HSL hydrolyses DAG to MAG under the release of another FA chain. Finally MGL metabolizes MAG to glycerol (G) and one fatty acid (adapted from Lampidonis et al., 2011; Zechner et al., 2012).

1.2.5.2. Lipophagy

Recent findings suggest that LDs can be removed via the cellular autophagy machinery. In a landmark study conducted in hepatocytes it was shown that LDs co-localize with LC3B and LAMP1 both markers for autophagy (Singh et al., 2009).

Autophagy is an essential cellular process, which recycles cellular components for homeostasis or in times of stress and nutrient deprivation. It is broadly divided into three main mechanisms: macro-, micro- and chaperon mediated autophagy, which are to be discussed in the following (Dossou and Basu, 2019).

1.2.5.2.1. Macroautophagy

Macroautophagy is the best understood of the three autophagy mechanisms. In a nutrient rich environment, the mTOR1 protein phosphorylates the kinase ULK1/2, as well as ATG13. The phosphorylation inhibits the function of these proteins. Inhibition of mTOR1 with rapamycin or starvation signals activates ULK1/2 which in terms phosphorylates itself, ATG13, and FIP200. Independent from the mTOR1 pathway, AMPK signaling has also been reported to activate ULK1 (Jung et al., 2010; Kim et al., 2011) (Figure 5A).

Upon activation ULK1, it localizes together with its complex to the ER, where they create a membrane fold called the omegasome. Another complex comprising the phospho-inositol-triphosphate (PI3P) kinase VPS34, BECLIN1 and either ATG14 or UVRAG localizes to this omegasome in proximity to the ULK1 complex. The activity of the VPS34 kinase subsequently increases the local concentration of PI3P, recruiting further downstream effectors to the omegasome. These effectors then initialize the nucleation of the phagophore, which is the precursor of the autophagosome (Folkerts et al., 2019; Mercer et al., 2018) (Figure 5B).

The phagophore is a cup-shaped double membrane structure which elongates upon target recognition to encapsulate its substrate in a double membrane structure called the autophagosome. The elongation has been found to be catalyzed by two ATG ubiquitin-like conjugation systems. In the first system ATG12's C-terminus is first conjugated to ATG7, which acts as an E1 ligase. This leads to ATG12's conjugation to ATG10, an E2 ligase, which subsequently conjugates ATG12 to its last partner ATG5. This ATG12-ATG5 dimer interacts with ATG16L1 forming a complex which binds to the elongating phagophore (Romanov et al., 2012; Folkerts et al., 2019; Mizushima, 2020).

In the second system LC3 is C-terminal truncated by ATG4 to form LC3I. The E1 enzyme ATG7 then conjugates LC3I to Atg3. Subsequently, the LC3I-ATG3 conjugate interacts with the ATG12-5-16-complex of the first system, which acts as an E3 ligase for LC3I. The E3 ligase activity of ATG12-5-16 lipidates LC3I with phosphatidylethanolamine creating the final product called LC3II. LC3II localizes to nucleated phagophore causing its elongation. The mechanism by which LC3II elongates the phagophore and forms the autophagosome is yet to be unraveled. (Rubinsztein et al., 2012; Folkerts et al., 2019; Mizushima, 2020).

Upon achieving the engulfment of its target, the phagophore encapsulates itself from the cytoplasm, which results in a double membrane autophagosome. LC3-II on the outside disassociates from the autophagosome, while LC3-II in the inside remains membrane bound, which is used as an autophagosome marker (Figure 5C). The autophagosome then fuses with lysosomes, creating an autophagolysosome. The lysosomal lipases and proteases in combination with the acidic environment break down the inner membrane sheet, followed by its content (Li Fang and Zhang Hanrui, 2019; Folkerts et al., 2019)(Figure 5D).

Autophagosomes have been shown to engulf LDs in hepatocytes, which is thought to remove the entire LD by macro autophagy (Singh et al., 2009). After fusion with the lysosome, these LDs are degraded by the lysosomal lipases. Especially the protein lysosomal acid lipase (LAL) has been shown to be important for lipophagy (Pearson et al., 2014).

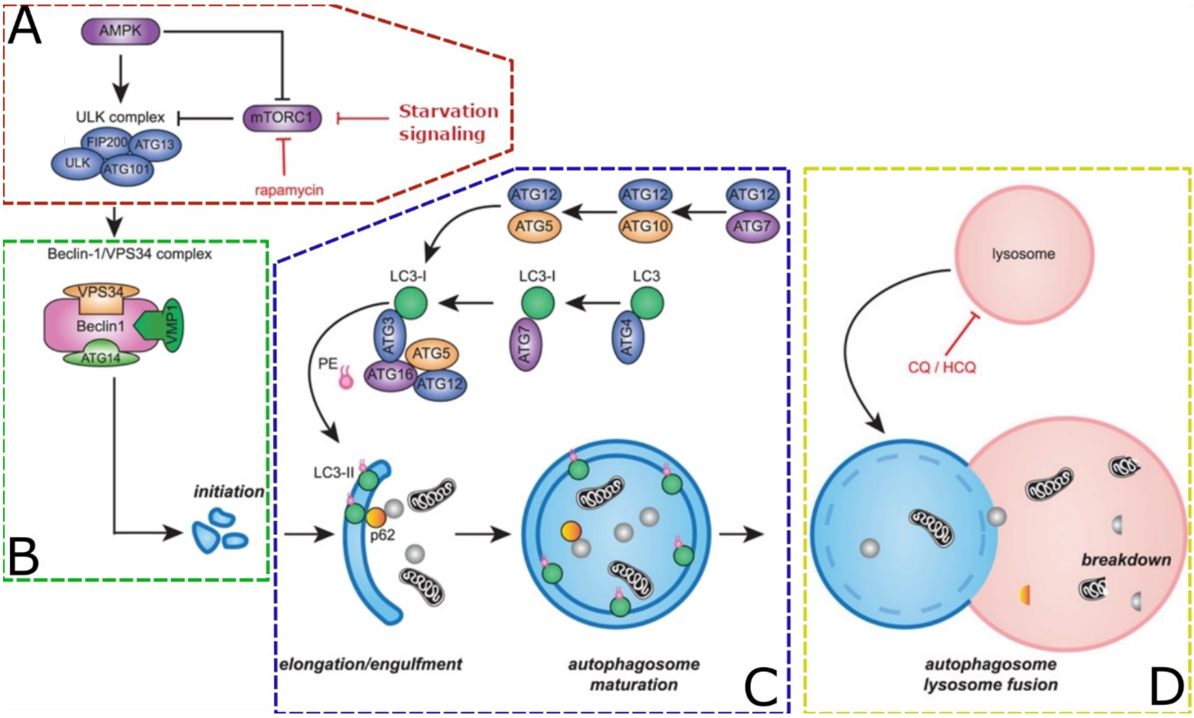

Figure 5 | Macroautophagy signal pathway

Under fed conditions mTOR1 inhibits the ULK kinase complex. Starvation signalling, AMPK signalling or Rapamycin inhibition inhibits mTOR1. The ULK kinase phosphorylates the complex resulting in its localization to the ER (**A**). Soon after ULK, Beclin-1/VSP34 complex localizes to the ER membrane, it initializes the formation of the phagophore (**B**). The two ubiquitination systems covalently link LC3 with phosphatidylethanolamine which elongates the phagophore until an enclosed autophagosome is formed (**C**). The autophagosome fuses with a lysosome to the autophagolysosome and the proteases and lipases in the lysosome break down the content of the autophagosome. This fusion can be inhibited by (Hydroxy-) Chloroquine (HCQ/CQ) (**D**). (Adapted from Folkerts et al., 2019)

1.2.5.2.2. Chaperon mediated autophagy (CMA)

Whilst macroautophagy engulfs large parts of the cytoplasm and whole organelles, chaperon mediated autophagy (CMA) is a highly specific form of autophagy. It depends on HSC70, a cytosolic chaperon, which binds the pentapeptide motif KFERQ. Substrate displaying this pentapeptide are targeted by HSC70 for autophagic removal (Kaushik and Cuervo, 2018).

After binding its substrate, HSC70 is transported to the lysosome. The interaction partner of HSC70 on the lysosome is the lysosome associated membrane protein type 2A (LAMP2A). Its cytosolic tail binds HSC70 resulting in transfer and unfolding of the substrate. LAMP2A forms the multimeric protein complex essential for substrate translocation into the lysosomal lumen, where the substrate is degraded by proteases and lipases (Kaushik and Cuervo, 2018).

CMA has been observed to catalyze autophagy of LD surface protein, enhancing LD size degradation via macroautophagy and lipolysis (Kaushik and Cuervo, 2015). In hepatocytes LAMP2A knock out has been shown to lead to dysregulation of lipid metabolism and steatosis, which underlines the importance of CMA in LD size regulation although the exact mechanism is not yet fully understood (Schneider et al., 2014).

1.2.5.2.3. Microautophagy

Microautophagy is the least understood of all three autophagy mechanisms. During microautophagy, the lysosome directly engulfs cellular compounds without intermediary autophagosome enclosure or CMA involvement. At the beginning of microautophagy an inward facing cup-shaped invagination is formed in the lysosome membrane. The target is taken up into this cup and incorporated into the lysosome. After taking up the target, the invagination is subsequently sealed. This results in the target's encapsulation as a slowly degrading vesicle into the lysosomal lumen. Endosomal sorting complex (ESCRT) proteins are assumed to create the alterations of the lysosome membrane, but most of the mechanism remains undiscovered (W. Li et al., 2012; Schuck, 2020).

Recently, microautophagy of LD via direct lysosome interaction could be observed in AML12 hepatocyte cell line. 15% of all LDs were reported to interact directly with lysosomes during starvation. Electron microscopy of this interaction revealed that lipids are directly transported into the lysosomal lumen via cup shaped membrane invaginations. This transport was independent of both macro autophagy and CMA, hinting at a role of microautophagy in hepatic LD metabolism (Schulze et al., 2020).

1.2.6. The mechanisms of autophagy in hepatic LD size regulation

Comparing lipophagy with lipolysis in hepatocytes, it was discovered that large LDs were not targeted by autophagy (Schott et al., 2019). Instead, large LDs were subject to lipolysis, whilst small LDs were found to be removed by autophagy. This gave rise to the current model, that lipolysis and lipophagy are not isolated processes in hepatocytes. Instead, they work in sequence to remove large LD. First large LDs are shrunk to be subsequently removed via autophagy (Schott et al., 2019). RAB18, a RAB GTPase linked to LD size regulation, has been recently connected with autophagic processes, which makes it a promising candidate for regulating this process (Feldmann et al., 2017; Bekbulat et al., 2020).

1.3. RAB18 involvement in LD size regulation

1.3.1. Ras-superfamily of small GTPases

RAB18 is part of the Ras superfamily of small GTPases, which is a group of small monomeric GTPases. GTPases can be seen as small molecular switches, which regulate cellular processes. The Ras superfamily is sub-divided into several families, each regulating separate processes (Macara et al., 1996; Wennerberg et al., 2005). Members of the Ras family of GTPases are involved in cellular growth signaling processes. They have been studied the most in cancer biology because their mutation are widely associated with tumor development (Bos, 1989). The members of the Rac/Rho family of GTPases have been associated with changes in the cyto-skeleton additionally to signaling (Mackay and Hall, 1998). Finally, the members of the largest family of Arf and Rab GTPases, are involved in intracellular membrane trafficking. Proteins belonging to this group of GTPases have been associated with vesicle, endosome, ER, Golgi and LDs (Chavrier and Goud, 1999; Zerial and McBride, 2001).

All Ras/Rab proteins have two common features unique to the superfamily. They share a highly conserved GTPase domain consisting of G box GDP/GTP-binding motifs as well as a hypervariable C-terminus (Wennerberg et al., 2005). The GTPase domain boxes form two conserved structures named Switch I and Switch II. Both can switch between two conformational states depending on the GTPase's loading state. The 'active' GTP bound state and the 'inactive' GDP bound state. Upon signaling, Guanosine exchange factors (GEF) exchange the bound GDP with GTP, changing the GTPases conformation from the 'inactive' conformation to the 'active'. Once activated, the GTPases recruit and bind downstream effectors, which results in changes to downstream processes depending on the GTPase (Vetter and Wittinghofer, 2001).

With a half-life of 30 minutes, the GTPase activity of small GTPases is very ineffective at hydrolyzing GTP to GDP on their own. To catalyze the hydrolysis a second regulator protein, the GTPase activating protein (GAP) is essential. As a result, the overall activity of Ras/Rab small GTPases is determined by the ratio of GEF to GAP activity (Hennig et al., 2015).

1.3.2. Ras/Rab protein localization

The hypervariable C-terminus of Ras/Rab superfamily proteins serves as a site for posttranslational acylation in form of the reversible S-palmitoylation and irreversible prenylation. In the C-terminus of all RAS and some RAB proteins a special CAAX-box motif was detected, which is essential for the post-translational prenylation of these proteins. Without this post-translational prenylation, RAS and RAB proteins were found to lose their membrane affinity and distinct cellular localization pattern (Kato et al., 1992; Leung et al., 2007).

This reveals another form of GTPase regulation, which is the control of localization. Transport of the GTPases to and from its target membrane is in part dependent on the GDP dissociation inhibitor (GDI). Binding of the GDI on a GDP bound small GTPase results in the translocation of the GDI-GTPase complex from intracellular membrane structures to the cytoplasm. This removes the GTPase from its activity sites, thus inhibiting activation. A special GDI displacement factor (GDF) on the target membrane is able to remove the GDI resulting in target membrane localization of the GTPase (Pfeffer et al., 1995; Pfeffer and Aivazian, 2004)

In addition to C-terminal prenylation, RAS proteins are reversibly palmitoylated which increases their membrane affinity (Hancock et al., 1989). Specifically, HRAS was detected to circulate between the Golgi and the plasma membrane depending on its palmitoylation state. Inhibition of HRAS palmitoylation resulted in the loss of plasma membrane localization. Instead, an increase of HRAS localization to the Golgi proving that reversible palmitoylation is mandatory for HRAS plasma-membrane localization (Rocks et al., 2005).

De-palmitoylation of HRAS depends on the cytoplasmic thioesterase APT1 (Duncan and Gilman, 1998). Inhibition of HRAS de-palmitoylation via APT1 inhibition resulted in the opposite outcome of palmitoylation inhibition. HRAS cellular localization increased, while the localization to the Golgi decreased (Dekker et al., 2010).

Together these results demonstrate, that HRAS localization depends on a reversible acylation cycle. Palmitoylation followed by directional transport increases local membrane affinity of the protein at the destination. Cytoplasmic de-palmitoylation results in less membrane affinity of mis-localized protein (Dekker et al., 2010). The low membrane affinity of the non-palmitoylated, but prenylated protein has been shown to lead to aspecific membrane targeting of the protein. Many Ras and Rab proteins share similar palmitoylation sites in the hypervariable C-terminus, which implies that localization based on acylation cycle is another conserved regulatory mechanism among small GTPases (Rocks et al., 2010; Fukata et al., 2016).

1.3.3. The small GTPase RAB18

Since its detection in 1993, RAB18 has been found ubiquitously expressed and associated with a range of functions depending which organelle and cell type were studied. A few of these results are to be discussed in the following (Helen et al., 1993; Dejgaard and Presley, 2019).

Investigating the Golgi apparatus, RAB18 overexpression or RAB18 knock down resulted in the disruption of the Golgi architecture and reduced vesicle trafficking (Dejgaard et al., 2008). Aside from the Golgi architecture, RAB18 is also deemed essential for maintaining ER-architecture. In Hela cells RAB18 is recruited to the ER by its GEF RAB3A. Failure of ER localization resulted in an enlargement of the ER-sheets (Gerondopoulos et al., 2014). Besides intracellular membrane systems, RAB18 has also been found on vesicles. Studies done in somatotropes could detect RAB18 on the secretory granules. RAB18 overexpression inhibited the secretion in these cells (Vazquez-Martinez et al., 2007; Vazquez-Martinez et al., 2008).

Mutations resulting in dysfunctional RAB18 regulation and activity were determined as the cause of a genetic disorder called Warburg-micro syndrome. It causes, among other symptoms, infertility, blindness and mental retardation in humans and mice (Bem et al., 2011; Carpanini et al., 2014; Liegel et al., 2013). Investigation of the Warburg micro syndrome by downregulation of RAB18 during brain development revealed a failure in neuron migration. This coincided with the reduction of N-Cadherin levels in neurons. It is thus theorized that RAB18 prevents the lysosomal removal of N-cadherin, which is essential for neuron migration. Supporting this theory, recent results show colocalization of RAB18 with RAB7, which is a marker for late-endosomes and lysosomes (Wu et al., 2016; Nian et al., 2019).

However, the organelle RAB18 is associated the most with is the LD. RAB18 presence on the LD has been reported to cause their close localization to the ER in HepG2 (Ozeki et al., 2005). In fibroblast, the subset of LDs which were positive for RAB18 were found to be more motile. The number of these LDs positive for RAB18 localization increased after the induction of lipolysis. This could be confirmed and expanded upon in a study done in adipocytes.

Conversely, RAB18 has also been found to induce lipogenesis during adipocytes differentiation (Martin et al., 2005, p. 18; Pulido et al., 2011).

In the liver carcinoma cell line, Huh-7 RAB18 was found co-localized with the Apolipoprotein B on the LD. Functional RAB18 was deemed necessary for Apolipoprotein B recruiting to these LDs. Treatment with an acyl-CoA-cholesterol acyltransferase (ACAT) inhibitor resulted in an increase of cholesterol in the cytoplasm, which caused RAB18 re-localization to the ER. This led to an increase in LD size and LD fusing with the ER in cells with high free cholesterol (Makino et al., 2016).

RAB18 knock out mutants were first described in adipocytes. The RAB18KO in these cells resulted in larger and fewer LDs than in WT cells. Small LDs were found in the proximity to the larger LDs, which are could be in the process of fusing with the large LD. In the case of RAB18 overexpression the LD area was decreased. This knockout phenotype could be confirmed in studies done in fibroblasts (Xu et al., 2018; Bekbulat et al., 2020).

Interestingly, RAB18 function seems to be not essential for LD regulation in all cell types as RAB18 deficiency was not influencing LD biogenesis or turnover in mammary carcinoma cells (Jayson et al., 2018).

1.3.4. RAB18 regulation

The enigmatic phenotypes of RAB18 have sparked great interest in RAB18 regulation. So far, two GEFs were associated with RAB18. The first GEF, Rab3GAP, was identified to play a role in maintaining the ER structure, as well as preventing Warburg micro syndrome in humans (Gerondopoulos et al., 2014; Bem et al., 2011). Additionally, the RAB3A knockout replicated the enlarged LD phenotype of RAB18 knock out (Xu et al., 2018). A second GEF was found in the TRAPPII complex. Knockout of TRAPPII components resulted in increased LD sizes and lack of RAB18 localization to the LD (Li et al., 2016).

With TBC1D20 only one RAB18 GAP has been identified (Liegel et al., 2013). Only little GAP activity could be detected *in vitro*, but loss of TBC1D20 caused Warburg-Micro syndrome in mice. Mutation of TBC1D20 was observed to induce autophagy defects, with autophagosomes rendered unable to mature (Sidjanin et al., 2016).

Two activity mutants have been described in the literature. RAB18-Q67L is a reported constitutive active mutant of RAB18. The mutation of glutamine 67 results in the loss of the GTPase activity thus RAB18 remains in its ‘active’ conformation after binding GTP. Overexpression of Q67L resulted in increased lipolysis and lipogenesis in adipocytes (Martin and Parton, 2008; Pulido et al., 2011)

S22N has been proposed as a dominant negative mutant of RAB18. The mutation of serin 22 renders the GEFs of RAB18 unable to exchange GDP with GTP, thus it competitively inhibits GEF activity. RAB18-S22N does not localize to LD and led to an increase in LD size in myoblasts (Ozeki et al., 2005; Deng et al., 2021). Expression of this mutant also disrupts the Golgi apparatus architecture and inhibits neuron migration (Dejgaard et al., 2008; Martin and Parton, 2008; Tang et al., 2014; Wu et al., 2016).

RAB18 belongs to the small group of RAB proteins carrying a C-terminal CAAX-box motif. Upon translation this box is proteolytically cut at the cysteine following an irreversible geranylgeranylation. After the deletion of this domain resulted RAB18 failed to localize to the LD-membrane (Leung et al., 2007; Bem et al., 2011). Upstream of the CAAX box is another cysteine, which is hypothesized to be S-palmitoylated due to sequence similarities to other RAB proteins (UniProt Consortium, 2021).

1.3.5. Effectors of RAB18

The effectors of RAB18 are largely unknown, but in pulldown assays it could be shown that RAB18 recruits the NRZ complex. This complex consisting of NAG, RINT and ZW10, which are known interactors with SNARE proteins, is found on the ER membranes. Thus, it has been hypothesized that RAB18 may play a role in LD-ER tethering (Xu et al., 2018).

Following up on these findings, the RAB18-ZW10 complex was found to interact with the FYVE Domain protein DFCP1 in COS7 cells. Both RAB18 and DFCP1 were essential to form stable ER-contacts for nascent LDs. RAB18's function in COS7 could therefore is the stabilization of the ER contact, whereas DFCP1 was shown to increase the LD size (D. Li et al., 2019).

In *Drosophila melanogaster* it could be shown that RAB18 interacts with the PIP3 kinase VPS34, whose deletion phenotype resulted in a LD phenotype similar to RAB18 deficiency (Takáts et al., 2021).

1.3.6. RAB18 lipolysis and lipophagy

The most common phenotype of RAB18 downregulation is the increased LD size. As discussed in chapter (1.2.5) there are mainly two ways of LD size regulation, lipolysis and lipophagy. The role of RAB18 in either LD size regulation mechanism is heavily debated.

Most of RAB18 research done in adipocytes indicated that RAB18 is involved in lipogenesis, but also lipolysis. In two studies RAB18 localization was found to be increased after lipolytic signaling (Martin et al., 2005; Pulido et al., 2011). It could also be shown that glycerol release is increased in adipocytes with RAB18 overexpression (Pulido et al., 2011). The link to lipolysis was further strengthened by identifying TRAPPII as a RAB18 GEF. The TRAPPII complex is associated with lipolysis via the COPI-Arf complex (Li et al., 2016). Specifically, ARF4 is recruited to the LD by RAB18. ARF4 localization in turn is recruiting ATGL to the LD, which is the first protein in lipolysis (Dejgaard and Presley, 2019b). Conversely, fibroblasts with a RAB18 knock out were found to have increased ATGL localization to the LD (Bekbulat et al., 2020).

Most recent studies linked RAB18 function to autophagy. In studies conducted in fibroblasts it could be shown that RAB18 knock down resulted in the decrease of autophagic flux whereas overexpression increased autophagic flux. Contradicting this study, experiments conducted in fibroblasts with RAB18 knock out reported no decrease in autophagic flux. However, the RAB18 knock out cells were rendered unable to respond to starvation with increased autophagy. Expression of autophagic pathway components such as ATG5, UVRAG and ATG12 were increased in RAB18KO cells. Investigations of the phosphorylation status of ATG9A protein to estimate activation revealed that fed RAB18KO cells showed ATG9A activation similar to starved WT cells. (Bekbulat et al., 2020). This indicates that RAB18 is increasing autophagy (Feldmann et al., 2017). However, in stellate cells the opposite effect was reported, with RAB18 deficiency resulting in an increase in autophagy (BasuRay, 2019)

In the model system of larval fat cells of *Drosophila melanogaster*, RAB18 knock out created chains of autophagolysosomes. This indicated that autophagy was halted and autophagosome maturation was stopped. The analysis of the phenotype showed similarities to a VPS34 knockout, which was observed to interact with RAB18 (Takáts et al., 2021).

Together these finding suggests that RAB18 indeed is involved in the regulation autophagy, but its role might be more complex than activation or deactivation of the autophagosomal pathway. Although RAB18 has been intensively studied over the past years, the function of RAB18 on the LD remains enigmatic.

2. Scope and aims of this work

Steatosis is the most common liver pathology observed in the western world. Left untreated, it progresses to diseases such as steatohepatitis, cirrhosis which compromise liver function and eventually to HCC, which has fatality rates exceeding 97%. The hallmark of steatosis is the accumulation and enlargement of small cellular organelles called **lipid droplets** in the hepatocytes. Understanding this process is therefore a fundamental requirement to develop a treatment for steatosis and consequent diseases. The lipid droplet is a specialized cellular vesicle and as with all vesicles, its dynamics are influenced by Rab GTPases. RAB18 is localized to lipid droplets in mammalian cells. However, the mechanism by RAB18 modules lipid droplet dynamics, especially in the context of steatotic disease in hepatocytes, remains largely undiscovered.

The primary objective of the presented work is to elucidate the influence of RAB18 on lipid droplet dynamics in a hepatocyte-derived cell line HepG2, primary cells and live mice; its resultant contribution to steatotic disease; and to identify ameliorating interventions that can prevent or reverse steatosis.

These objectives lead to the following salient questions that were addressed in this work:

1. Does RAB18 activity influence the LD size in hepatocytes?
2. Is it possible to modulate RAB18 activity to affect LD size in hepatocytes?
3. Is localization of RAB18 to the LD essential for its function?
4. What is the mechanism by which RAB18 localizes to the LD?
5. Is it possible to influence LD dynamics by modulating the localization of RAB18 to the LD?
6. Having known the functions of RAB18, is it possible to influence the surrounding context – other cellular pathways such as autophagy to compensate, reverse or ameliorate steatosis caused by lipid load?
7. Can these interventions be performed using cell-permeable small-molecule pharmacological agents which are expected to be more suitable for clinical translation?
8. Are our findings in the cell line HepG2 applicable to primary hepatocytes subjected to a similar steatogenic load, or in live mice that are placed on a steatogenic diet?

3. Material & Methods

3.1. Material

3.1.1. Key Resource Table

REAGENT or RESOURCE	SOURCE	IDENTIFIER
Antibodies		
Donkey αrabbit Alexa 647	Thermo Fisher Scientific	A31573
Donkey αmouse 800 nm	LICOR	925-2212
Goat αrabbit 680nm	LICOR	925-68071
Mouse αRAB18	Invitrogen	MA5-24744
Rabbit LC3B	Cell signaling	2775
Rabbit αGAPDH	Sigma	69545
Rabbit αLC3B	Abcam	Ab 51520
Bacterial and Virus Strains		
MAX Efficiency™ DH5α Competent Cells	Invitrogen	18258012
XL10 Gold competent cells	Agilent	200315
Chemicals, Peptides, and Recombinant Proteins		
10x PBS	GIBCO	70011-044
1kb Plus DNA ladder	NEB	N3200S
2-Bromohexadecanoic acid (2-bromopalmitate)	Sigma-Aldrich	21604-1G
Agarose	Roth	3810.4
Ampicillin sodium salt	Sigma-Aldrich	A0166-5G
Antioxidant	Invitrogen	BT0005
APT1 inhibitor palmostatin B	Sigma-Aldrich	178501-5mg
atglistatin	Sigma-Aldrich	SML1075-25MG
BamHI-HF	NEB	R3136S
BODIPY™ 493/503 (4,4-Difluoro-1,3,5,7,8-Pentamethyl-4-Bora-3a,4a-Diaza-s-Indacene)	Invitrogen	D3922

Bovine Serum Albumin fatty acid free, low endotoxin, lyophilized powder	Sigma	A8806-5G
Oleic Acid-Albumin from bovine serum	Sigma Sigma-Aldrich	O3008-5ml
Chameleon Duo Pre-stained Protein Ladder	Licor	928-60000
Chloroquine diphosphate salt powder	Sigma-Aldrich	C6628-50G
cOmplete™, Mini Protease Inhibitor Cocktail	Roche	4693124001
Cutsmart Buffer	NEB	B7204S
DAPI	Thermo Scientific	62248
Dexamethasone	PAN Biotech	D4902
DMEM, w: 4.5 g/L Glucose, w: stable Glutamine, w/o: Sodium pyruvate, w: 3.7 g/L $NaHCO_3$	PAN Biotech	P04-04500
DMSO (Dimethyl sulfoxide Hybri-Max™)	Sigma-Aldrich	2650-100ML
EcoRI-HF	NEB	R3101S
EDTA	Roth	8043.2
Ethidium Bromide	Invitrogen	15585-011
Fetal Bovine Serum, heat inactivated, qualified, One Shot™, Brazil	Gibco	A3840402
Gel Loading Dye (6x)	NEB	B7024S
Gentamicin, 50 mg/ml	PAN Biotech	P06-03001
Glacial acid	Roth	3738.5
Hoechst 33342 Trihydrochloride, Trihydrate, 100mg	Invitrogen	H1399
Insulin/ ITS liquid media	Sigma-Aldrich	I3146-5ML
Kanamycinsulfat	Sigma Aldrich	60615
LAlistat2	Sigma-Aldrich	SML2053-25MG
LB Broth (Lennox)	Sigma-Aldrich	L3002-1KG

MES SDS Running Buffer (20x)	Invitrogen	B0002
Methanol	Roth	4627.5
MfeI-HF	NEB	R3589S
NH4Cl	Roth	K-2981
Penicillin-Streptomycin, 10,000 U/ml Penicillin, 10 mg/ml Streptomycin	PAN Biotech	P06-07100
PstI-HF	NEB	R3140S
Rapamycin	LKT Labs	R0161
Rat tail Collagen I	Roche	11179179001
RIPA Lysis and Extraction Buffer	Thermo Scientific	89900
RNAimax lipofectamine Lipofectamine™	Sigma-Aldrich	13778075
Roth-Histofix (Paraformaldehyde-PFA)	Roth	6640
S.O.C. Medium	Invitrogen	15544034
Smart Cut Buffer	NEB	B7204S
Stable L-glutamine Stable Glutamine 200 mM (100 x)	PAN Biotech	P04-82100
T4 DNA Ligase	NEB	M0202S
TBS blocking buffer Intercept® (TBS)	LICOR	927-60001
Torin2	Sigma-Aldrich	SML1224
Transfer Buffer (20x)	Invitrogen	NP00061
Tris-base	Roth	4855.2
Triton 100	Sigma-Aldrich	T8787-250ML
Trypan blue (0.4%)	Sigma-Aldrich	T8154
William's Medium E, w/o: L-Glutamine, w/o: Phenol red, w: 2.24 g/L NaHCO3	PAN Biotech	P04-29510

Critical Commercial Assays		
Effectene Transfection Reagent	Qiagen	301425
MinElute Gel Extraction Kit	Qiagen	28604
Pierce™ BCA Protein Assay Kit	Thermo Scientific	23250
Q5® High-Fidelity PCR Kit	NEB	E0555S
QIAGEN Plasmid Maxi Kit	Qiagen	12163
QIAGEN Plasmid Mini Kit	Qiagen	27106
QIAquick PCR Purification Kit	Qiagen	28104
QuikChange II	Agilent	200524
Deposited Data		
RAB18 Protein sequence	Uniprot	https://www.uniprot.org/uniprot/Q9NP72
Raw and analyzed Data	This Thesis	
Experimental Models: Cell Lines		
HepG2	ATCC	HB 8065
Primary Human Hepatocytes	BIOVIT	F00995
Experimental Models: Organisms/Strains		
Mice	C57BL/6NRj	Janvier Labs, France
Oligonucleotides		
Primers for RAB18 mutation see 3.1.3	This thesis	
RAB18 siRNA A UGGAUGGAAAUAAGGCUAAACUUGC	OriGene	SR307888A
RAB18 siRNA B ACCAACUUGUACAGACUAAUAAATC	OriGene	SR307888B
RAB18 siRNA C ACCUGUGAUGGUGUACAAUGUGCCT	OriGene	SR307888C
Scrambled non-targeting siRNA: Sense 5’ CGUUAAUCGCGUAUAAUACGCGUAT Antisense 5’ AUACGCGUAUUAUACGCGAUUAACGAC	OriGene	S3004

Recombinant DNA		
HCMV-RAB18-turboGFP	OriGene	RG205505
mCherryBFP-SEC61b	Zurek N, Sparks L, Voeltz G, 2011	Addgene plasmid # 49154
pEX-PK-hLC3	Isei Tanida, Takashi Ueno, Yasuo Uchiyama,2014	Addgene plasmid # 61458
pFusionRed-C vector	Evrogen	FP411
pTagGFP2-C vector	Evrogen	FP191
Software and Algorithms		
Anaconda	Anaconda Inc.	https://www.anaconda.com/
FIJI (FIJI is just ImageJ)	Schindelin, J.; Arganda-Carreras, I. & Frise, E. et al. (2012),	https://imagej.net/Fiji
GNU Image Manipulation Program (GIMP 2.10.2)	Copyright © 1995-2018 Spencer Kimball, Peter Mattis and the GIMP Development Team	www.gimp.org
Inkscape: Open-Source Scalable Vector Graphics Editor 1.0	Harrington, B. et al (2004-2005)	https://inkscape.org/release/inkscape-1.0/
Jupyter Notebook	Project Jupyter	https://jupyter.org/about
Origin 2021 (64-bit) 9.8.0.200	OriginLab Corporation	www.originlab.com
Serial Cloner 2.6	SerialBasics	http://serialbasics.free.fr/Serial_Cloner.html
StarDist - Object Detection with Star-convex Shapes	Uwe Schmidt, Martin Weiger, Coleman Broaddus and Gene Myers., 2018	https://github.com/mpicbg-csbd/*StarDist*
Other		
Cell Scraper	Sarstedt	83.18
Mouse control diet	Ssniff R/M-H, 10 mm standard diet	Ssniff, Soest, Germany
Mouse steatogenic diet	D16022301	BROGAARDEN Smedevangen 5 350 Lynge, Denmark
8-Well Ibitreat µ-slide	Ibidi	80826

8-Well glass bottom slide	Ibidi	80827
8-Well removable chamber slide	Ibidi	80841
4-Well glass bottom slide	Ibidi	80427
Pre-cast 4-12% Bis-Tris gels Bolt™ 4 to 12%, Bis-Tris, 1.0 mm, Mini Protein Gel, 15-well	Invitrogen	NW04125BOX
Immobilon-P Blotting Sandwich (PVDF membrane 0.45µm pore size)	Millipore	IPSN07852
X-GAL, Carbenicillin ready-made Agar plates	Teknova	L906

3.1.2. Media and Buffers

Solution	**Product**	**Amount added**
Media		
HepG2 cell medium	DMEM, w: 4.5 g/L Glucose, w: stable Glutamine, w/o: Sodium pyruvate, w: 3.7 g/L $NaHCO_3$	450 ml
	Fetal Bovine Serum, heat inactivated, qualified, One Shot™, Brazil	50ml
Primary human hepatocyte culturing medium	William's Medium E, w/o: L-Glutamine, w/o: Phenol red, w: 2.24 g/L $NaHCO_3$	489 ml
	Gentamicin, 50 mg/ml	500 µl
	Dexamethasone (1µM)	500 µl
	Stable glutamine (200mM)	5 ml
	Insulin/ ITS liquid media (100x)	5 µl
	Penicillin-Streptomycin, 10,000 U/ml Penicillin, 10 mg/ml Streptomycin	5 ml

Buffer		
PBS (1x)	10x PBS	50 ml
	ddH_2O	450 ml
TAE Buffer (50x)	Tris-base	242 g
	0.5M EDTA	100 ml
	Glacial Acid 100%	57.1 ml
	ddH_2O	842.9 ml
MES SDS transfer buffer (1x)	MES-SDS transfer buffer (20x)	100ml
	ddH_2O	1900 ml
Transfer Buffer (1x)	Transfer Buffer 20x	50 ml
	Antioxidant	1 ml
	Methanol	100ml
	Deionized water	849ml

3.1.3. Primer Table

Name	Sequence (5'-3')	Legend
Amplification-RAB18-forward	TAACGAATTCGATGGACGAGGACGTGCTAAC	EcoRI, RAB18
Amplification-RAB18-reverse	AGATGGATCC**TTA**TAACACAGAGCAATAACCACCAC	BamHI, **STOP Codon**, RAB18
Amplification-SEC61B-forward	CGATCTGCAGGCAGCACAAGCTTAATTCCGGAC	PstI, SEC61B
Amplification-SEC61B-reverse	CGGACAATTGGAATTCCTACGAACGAGTGTAC	MfeI, SEC61
Mutagenesis-C199S-forward	CAAGGAGGAGGAGCCAGTGGTGGTTATTGCT	Mutation, RAB18
Mutagenesis-C199S-reverse	AGCAATAACCACCACTGGCTCCTCCTCCTTG	Mutation, RAB18
Mutagenesis-C203S forward	GAGGAGCCTGTGGTGGTTATAGCTCTGTGTTTATAA	Mutation, RAB18
Mutagenesis-C203S-reverse	TTATAACACAGAGCTATAACCACCACAGGCTCCTC	Mutation, RAB18
Mutagenesis-PolyC-forward	TCAAACTGTCACACAGGTGCGAAGGCCAATGCGGAGGAGCCTGTGGTGG	Mutation, RAB18
Mutagenesis-PolyC-reverse	CCACCACAGGCTCCTCCGCATTGGCCTTCGCACCTGTGTGACAGTTTGA	Mutation, RAB18
Mutagenesis-PstI-site-forward	GGAGGAGGAGCCTGTGGTGGTTA **CTGCAG** TGTGTTATAAGGAT	Mutation, RAB18 **PstI**
Mutagenesis-PstI-site-reverse	ATCCTTATAACACA **CTGCAG** TAACCACCACAGGCTCCTCCTCC	Mutation, RAB18 **PstI**
Mutagenesis-Q67L-forward	CAATATGGGATACTGCTGGTCTAGAGAGGTTTAGAACATTAAC	Mutation, RAB18
Mutagenesis-Q67L-reverse	GTTAATGTTCTAAACCTCTCTAGACCAGCAGTATCCCATATTG	Mutation, RAB18
Mutagenesis-S22N-forward	CTCAAGAGCAGGCTGTTCTTGCCCACCCCACT	Mutation, RAB18
Mutagenesis-S22N-reverse	AGTGGGGTGGGCAAGAACAGCCTGCTCTTGAG	Mutation, RAB18
FusionRed-RAB18 Sequencing-forward	CCACCTGATCTGCAACC	
RAB18 Sequencing-reverse	GAGTTTGGACAAACCACAA	
Seq-61B Sequencing reverse	TCTGCAACCTTGAGACCACA	

3.1.4. Technical equipment

Instrument	**Manufacturer**
Lab equipment	
Analytical balance	Toledo
Analytical balance BL150S	Sartorius AG, Goettingen-Germany
Casy cell counter	Roche
Centrifuge (Avanti JXN-26)	BECKMAN COULTER, USA
Centrifuge, minispin	Eppendorf
Centrifuge, table centrifuge 5424R	Eppendorf
Centrifuge, High Speed	Beckman Coulter
CO_2 cell culture incubator	Binder GmbH, Tuttlingen-Germany
Microwave Oven	Sharpe Electronics, Germany
Mini-Gel tank	Invitrogen
Mini-blot module	Invitrogen
Nanodrop ND-100	Thermo Fisher Scientific
Rocking Platform	VWR
Sterile hood	Heraeus, Thermo Fisher Scientific
T3000 Thermocycler	Biometra GmbH, Goettingen, Germany
Vacusafe vacuum pump	Integra Bioscience AG, Zizers, Switzerland
Water bath	Fisher scientific GmbH, Schwerte, Germany
Microscopes & Imaging systems	
Bright field microscope Ax10	Carl Zeiss GmbH, Jena, Germany
Bright field microscope BX41	Olympus GmbH, Hamburg, Germany
Bright field microscope Eclipse TS100	Nikon Instruments Europe BV, Amsterdam, Netherlands
Bright field microscope Primo Vert	Carl Zeiss GmbH, Jena, Germany
CARS laser system Pico Emerald S	APE Angewandte Physik & Elektronik GmbH, Berlin, Germany
Confocal laser scanning microscope for live cell imaging LSM 880	Carl Zeiss GmbH, Jena-Germany
Confocal laser scanning microscope for live cell imaging SP8	Leica Microsystems GmbH, Wetzlar, Germany

EVOS FLoid	Thermo Fisher Scientific, Waltham, USA
Microplate reader (Infinite 200Pro)	Tecan Trading AG, Männedorf, Switzerland
Odyssey CLx	LI-COR Biotechnology GmbH, Bad Homburg Germany
The Brick, CO2 gas mixing system	Life Imaging Services, Basel, Switzerland

3.2. Methods

3.2.1. Molecular Biology

3.2.1.1. Origin of sequences and primers

The molecular biology experiments detailed in the following were conducted on plasmids obtained from OriGene, evrogene and Addgene. Primers for sequencing and mutagenesis were custom designed and ordered to be synthesized by ThermoFisher.

3.2.1.2. Amplification of the RAB18 cDNA-sequence

A RAB18-TurboGFP plasmid was acquired from the company OriGene to amplify the RAB18 cDNA sequence via PCR. The primers were designed with the restriction enzyme target sequences for EcoRI and BamHI. The RAB18-TurboGFP (OriGene) template was diluted in ddH_2O to a concentration of 1 ng/µl. This dilution was added to the Q5 Polymerase-primer mix according to ***Table 1***. It was gently mixed using a pipette and quickly centrifuged, before running following PCR program given in ***Table 2.***

Table 1 | PCR-mix for RAB18 amplification

	Water Control	**RAB18 PCR Product**
Forward Primer (10µM)	2.5 µl	2.5 µl
Reverse Primer (10µM)	2.5 µl	2.5 µl
Template DNA (1ng/µl)	-	1 µl
Master mix (2x)	25 µl	25 µl
Nuclease Free Water	20 µl	19 µl
Σ	50 µl	50 µl

Table 2 | RAB18 PCR-amplification program

Step	**Temperature (°C)**	**Time**
Initial Denaturation	98	30 seconds
PCR Repeated for 35 Cycles	98	10 seconds
	70	10 seconds
	72	18 seconds
Final Extension	72	2 minutes
Hold	4	∞

The obtained PCR products were purified using the PCR-Purification kit (Qiagen™) following its protocol. The purified product's concentration was measured with a Nanodrop spectrometer and its quality was controlled with a gel-electrophoresis using a 1.5% agarose gel.

3.2.1.3. Agarose gel-electrophoresis

DNA quality control was conducted via gel-electrophoresis. An 1 % or 1.5 % agarose gel was created by melting 1 or 1.5 g agarose respectively in 100 ml 1x TAE buffer. DNA was stained with the intercalating dye EtBr. After pouring the gel into the mold, 10µl EtBr added directly into the gel before polymerization to avoid contamination of glassware. The gel was left to polymerize at room temperature, after which samples were supplemented with 6x Loading dye and loaded onto the gel. 5µl of a 1-kB DNA ladder (NEB) was run parallel to the samples to estimate fragment size and concentration. Gels were run at 120 V in TAE for 30 min and analyzed using an E-box illuminator. Photographs of the gel were taken, saved digitally and printed out.

3.2.1.4. Ligation of pHCMV-Fluorescent-Protein-RAB18 constructs

Before ligating the DNA constructs, both RAB18 sequence amplified in 3.2.1.2 and fusion protein vectors obtained from evrogene (pFusionRed-C and pGFP2-C) were cut with the restriction enzymes EcoRI and BamHI using the digestion mixes detailed in ***Table 3*** and ***Table 4***, respectively.

Table 3 | PCR-Product digestion mix

Reagent	Volume
PCR Product (Insert)	1 µg
EcoRI	1 µl
BamHI	1 µl
Buffer CutSmart	5 µl
ddH₂O	Add to 50µl
Σ	50 µl

The digestion was conducted for 2 hours at constant 37° C. The resulting digested DNA strands were purified using the PCR Purification kit (Qiagen™) to remove the restriction enzymes, before their final concentrations were determined using the Nanodrop spectrometer.

Table 4 | Vector digestion mix

Reagent	Volume
Vector	500 ng
EcoRI	0.5 µl
BamHI	0.5 µl
Buffer CutSmart	2 µl
ddH₂O	Add to 20 µl
Σ	20 µl

With the concentrations established, a reaction mixes for the ligation of RAB18 and the vector was calculated using the equation (1).

$$m_{Insert} = 50\,ng \times \frac{Basepairs_{Insert}}{Basepairs_{Vector}} \times F \qquad (1)$$

A fivefold molar excess (F) of insert to vector was deemed suitable. With an insert size of 650 bp and a vector size of 47000 bp, the insert mass needed for ligation with 50 ng vector was calculated to be 35 ng. An additional ligation was created for each vector to control for re-ligation, as detailed in the ligation mix in ***Table 5***.

Table 5 | Ligation mix

Reagent	Ligation	Re-ligation control
Insert (digested 17 ng/µl)	35 ng	-
Vector (digested 9 ng/µl)	50 ng	50 ng
T4 Ligase	1 µl	1 µl
T4 Ligase Buffer (10x)	2 µl	2 µl
ddH₂O	Add to 20 µl	Add to 20 µl
Σ	20 µl	20 µl

Controlling for cut efficiency, 50 µg of the digested vectors without reaction mix were set aside. The ligation and its controls were preferably incubated at RT for 2 hours. Alternatively, ligation was incubated in an ice bucket left at RT to create a temperature gradient o.n. before ligations were transformed into competent DH5α *E. coli.*

3.2.1.5. *Transformation of competent E. coli via heat shock with ligation mix*

Transformation was done in two different competent *E. coli* strains. XL10 Gold and DH5α cells were thawed on ice and aliquoted in 1.5 ml reaction tubes. For each transformation, 45 µl bacteria were prepared. XL10 Gold cells were treated with 4 µl β-Mercapto-ethanol supplied with the kit. Both competent bacteria suspensions were supplemented with either 2 µl of the ligation mix to be transfected, its re-ligation or digestion controls, and quickly stirred using the pipette.

Bacteria and DNA mixes were incubated on ice for 15 min before the bacteria suspension was heat shocked at 42 °C for exactly 45 sec. Following the heat shock bacteria were kept on ice for 2 minutes. At the end of the incubation, 500 µl of S.O.C. medium pre-warmed to 37 °C was added. The bacteria were incubated for 45 min at 37 °C to express antibiotics resistance against Kanamycin encoded on the plasmid.

After this incubation bacteria were centrifuged at 8.000 rpms for 1 minute in an Eppendorf table centrifuge. 250 µl of the supernatant was removed, and the pellet suspended in the remaining medium. Of the obtained suspension 100 µl and 200 µl were plated onto two Kanamycin containing agar plates. The plated bacteria were incubated o.n. at 37° C.

On the following day, colonies were counted on each plate. Using the number of colonies formed after transformation of the ligation and the colonies formed after transformation of the controls, the probability of picking a correctly transfected clone was calculated in equation (2).

$$P_{correctly\ ligated\ plasmid} = 1 - \frac{cfu_{Re-LigationControl}}{cfu_{Ligation}} \qquad (2)$$

Several medium size colonies were picked from the transfection according to this calculated probability and added to 4 ml LB medium containing 50 µg/ml Kanamycin. The suspension was then incubated o.n. at 37°C. Bacteria stock solutions were created for each plasmid by adding 500 µl of the overnight suspension to 500 µl of 50% Glycerine. The created stocks were stored at -80 °C.

The rest of the suspension was used for DNA extraction following the instruction of Qiagen™ Miniprep kit and eluted in 50 µl ddH$_2$O. After extraction plasmids were controlled by control digestion and sequencing.

3.2.1.6. *Control digest of plasmid solutions*

For quality control, plasmids carrying various fluorescentprotein-RAB18 fusion proteins were regularly subjected to control digests. Extracted DNA solution was added to the digestion mix given in ***Table 6*** and incubated for 2 hours at 37 °C.

The digested samples were mixed with 4 µl 6x Gel Loading dye and analyzed on a 1% agarose gel electrophoresis discussed in 3.2.1.3. After insert verification, samples of the plasmid solution were sent for sequencing with Microsynth-Seqlab. The obtained sequencing data was aligned with the predicted *in silico* plasmid created in the software "Serial Cloner" to detect unwanted changes to the ORF the sequence alignment can be found in Appendix 7.1.

Table 6 | Control digestion mix

Reagent	Volume
DNA Preparation	1 µl
EcoRI	1 µl
BamHI	1 µl
Buffer, CutSmart	2 µl
ddH$_2$O	15 µl
Σ	20 µl

3.2.1.7. *Mutation of wildtype RAB18 sequence*

The RAB18 sequence of the plasmids created in 3.2.1.4 was subjected to a mutagenesis kit (Ampligen) to induce point mutation in the ORF. Plasmids were subjected to a PCR amplification with mismatching primers at the desired positions. To control for mutagenesis efficiency, a control pWhitescript plasmid was mutated according to instructions. A Mutagenesis-mix was created in PCR reaction tubes, as detailed in ***Table 7***. After mix preparation 1µl of PfuUltra DNA-polymerase was added. Tubes were mixed gently and quickly centrifuged. The mutagenesis was run on these samples, as detailed in ***Table 8***.

Table 7 | Mutagenesis mix

Reagent	Volume
Reaction buffer 10x	5 µl
pWhitescript (4.5 kb)/ Plasmid	10 ng
Oligonucleotide primer 1	125 ng
Oligonucleotide primer 2	125 ng
dNTP mix	1 µl
QuickSolution reagent	3µl
Add ddH$_2$O to 49µl	
Σ	49 µl

Table 8 | Mutagenesis PCR-program

Step	Temperature (°C)	Time
Primary denaturation	95	1 min
PCR Repeated for 18 Cycles	95 60 68	50 sec 50 sec 5 min 20 sec (1 min/kbp for 5.3 kbp)
Final elongation	68	7 min
Hold	4	∞

Afterwards, the template DNA plasmid was digested by adding 2 µl DpnI directly on the reaction mix. The DNA was digested for 2 hours at 37 °C, before successful PCR amplification was checked using a 1% agarose gel-electrophoresis as detailed in 3.2.1.3. If amplification was detected, the plasmids were transformed in XL10 Gold cells analogous to 3.2.1.5.

According to the protocol given in 3.2.1.5, 45 µl XL10 Gold bacteria suspension were thawed on ice and incubated with 2 µl β-Mercapto-ethanol for 15 min on ice. 2 µl of the DpnI digested DNA was added and bacteria were incubated for another 15 minutes on ice. XL10 Gold bacteria were then heat shocked and incubated with S.O.C. medium.

Bacteria transformed with mutated RAB18 constructs were plated on Kanamycin plates, whereas bacteria transformed with the control pBWhitescript were plated on Carbenicillin plates coated with XGAL and IPTG. The next day, bacteria forming blue colonies were counted on the mutation control plate. The probability of correct mutagenesis was calculated using a variation of equation (3).

$$P_{correctly\ mutated\ plasmid} = \frac{cfu_{blue}}{cfu_{Control}} \qquad (3)$$

Medium size colonies were picked according to the calculated probability, grown o.n. and DNA was extracted as detailed in 3.2.1.5. To evaluate success of mutagenesis obtained plasmids were sent for sequencing and aligned with the sequences of an in silico calculated mutation using the software "Serial Cloner". For complete sequence alignment see Appendix 7.1.

3.2.1.8. Generation of RAB18-SEC61b fusion protein

Suitable digestion sites were needed for creating a SEC61b C-terminal fusion protein. Therefore, a mutation introducing a PstI digestion site was conducted in the RAB18 C-terminus of the RAB18-FusionRed plasmid using the approach detailed in 3.2.1.7.

The donor plasmid carrying an BFP-SEC61B ORF was obtained from Addgene. From this plasmid, a SEC61b insert carrying the suiting digestions sites PstI and MfeI were amplified analogous to 3.2.1.2. The obtained insert was digested as depicted in ***Table 9***, whereas the vectors' digestion is shown in ***Table 10***.

Table 9 | SEC61b insert digestion mix

Reagent	Volume
DNA	2µg
PstI	1 µl
MfeI	1 µl
Buffer CutSmart	5 µl
Add ddH$_2$O to 50µl	
Σ	50 µl

Table 10 | SEC61b vector digestion

Reagent	Volume
DNA	2 µg
PstI	0.5 µl
MfeI	0.5 µl
Buffer CutSmart	2 µl
Add ddH$_2$O to 20µl	
Σ	20 µl

The digest was incubated for 2 hours at 37°C, after which they were purified using the Qiagen™ PCR-Purification kit. The concentration was measured for both insert and plasmid using a nanodrop spectrophotometer. For Ligation, five times the molar ratio of insert to plasmid was calculated for fivefold molar excess as given in equation (1) and a ligation mix was created given in ***Table 11***.

Table 11 | SEC61b ligation mix

Reagent	Volume SEC61b
Vector	16 ng
Insert	50 ng
T4 Ligase	1 µl
T4 Ligase Buffer (10x)	2 µl
Add ddH$_2$O to 20µl	
Σ	20 µl

Ligation was performed o.n. in an ice bucket at RT. Letting the ice melt at RT created a temperature gradient which enabled ligation. The ligation was transformed into DH5α and DNA was extracted according to 3.2.1.5.

Integrity of the DNA code was verified as analogous to 3.2.1.6 using PstI and MfeI instead EcoRI and BamHI as restriction enzymes.

3.2.1.9. *Plasmid amplification*

The plasmids created in this thesis were kept as bacterial glycerol stock. To gain high concentrated plasmid solution, these stocks were amplified to extract DNA. A sample of the frozen glycerol stock was taken with a pipette and added to 4 ml of LB containing 50 µg/ml Kanamycin. This suspension was incubated o.n. at 37 °C under shaking. The following day, this suspension was added to 250 ml of LB containing 50 µg/ml Kanamycin. The upscaled bacterial suspension was incubated o.n. at 37 °C under shaking. After this incubation, the suspension was centrifuged at 6,000xg and 4 °C. The bacterial pellet was lysed, and DNA extracted using the Qiagen Maxiprep kit following the kit's instruction.

3.2.1.10. *Protein extraction*

For protein extraction cells were lysed using a RIPA based lysis buffer. The lysis buffer was freshly created for each experiment by adding one complete protease inhibitor tablet into 10ml RIPA buffer. Cells to be lysed were washed three times in 1xPBS, after which the 1xPBS was completely aspirated and replaced with 50 µl lysis buffer. Subsequently, the cells were lysed using cell scrapers and collected in 1.5 ml reaction tubes. The cell lysate was subsequently centrifuged at 4 °C and 6000xg for 10 min to separate lysate from cell debris. The pelletized cell debris was removed with a pipette. If not used on the same day, lysates were stored at -20°C for further use.

3.2.1.11. *Protein analysis via western blot*

Lysates generated in 3.2.1.10 were analyzed via western blot. Stored samples were thawed on ice and protein concentration were established in a BCA assay. To establish the protein concentration, a BSA dilution row was prepared according to ***Table 12***.

The dilution row was transferred in triplicates of 25 µl to a 96-well plate. The protein lysates to be measured were diluted 1:5 in 25 µl water in duplicates onto the same plate. As a solvent control the RIPA buffer used in the lysis was diluted 1:5 analogous to the samples.

The BCA mix was produced by diluting the assay reagent B 1:50 in the reagent A for each well. 200µl of this mix were added onto each well of the plate, which was subsequently incubated at 37 °C for 30 minutes. The plate was measured with a Tecan Reader set to detect at 562 nm with 25 flashes.

Table 12 | Dilution row for BSA

Concentration	Standard stock 2 mg/ml	Double distilled H_2O
0µg/ml	0 µl	80 µl
125µg/ml	5 µl	75 µl
250µg/ml	10 µl	70 µl
500µg/ml	20 µl	60 µl
750µg/ml	30 µl	50 µl
1000µg/ml	40 µl	40 µl
1500µg/ml	60 µl	20 µl
2000µg/ml	80 µl	0 µl

Using the known concentration of the dilution row, a calibration curve was calculated with which the protein concentration of the samples was determined. With the established concentration the sample reduction mix given in ***Table 13*** was prepared for each sample.

Table 13 | Sample reduction mix

Reagent	Volume
Lysate	20-40 µg
Reducing agent	2 µl
LICOR sample mix	5 µl
Add ddH_2O to 20µl	
Σ	20 µl

The gel tank was assembled with commercially available 4-12% BisTris Gels and filled with MES-SDS running buffer Before loading the gel pockets were washed in MES-SDS buffer using a 200 µl pipette. The protein samples were denatured at 95 °C for 5 minutes and consequently added to. To identify protein size 3 µl Chameleon duo pre-stained protein ladder was mixed in equal parts and loaded onto the gel. After sample loading, the gel was run at 200 V for approximately 30 min.

A 0.45 nm PVDF membrane was used for blotting which was activated in 100% MetOH for 15 seconds before equilibration. The membrane, sponges and filter paper were equilibrated separately in transfer buffer for 15 minutes.

After finishing the gel run, the gel cassettes were rinsed in ddH_2O. The plastic casing was broken up, and the gels were transferred to an equilibrated filter paper. Then, the membrane was placed on top of the gel followed by another equilibrated filter paper. The blotting sandwich was pressed together multiple times before assembling the blot between the two parts of the mini-blot module. Lastly, the assembled module was then filled with transfer buffer, whilst the surrounding tank was filled with ddH_2O. The module was connected to a power source to be run at 20 V for 35 min.

The blotted membrane was transferred to a light-proof box, in which it was incubated in 100% methanol for 15 sec. The methanol was subsequently removed from the membrane and it was equilibrated in ddH_2O for 5 min under gentle shaking at room temperature.

The membrane was blocked in the TBS blocking buffer (Odyssey) for one hour. A primary antibody mix was prepared in TBS blocking buffer (Odyssey) as given in ***Table 14***.

Table 14 | Primary antibody mix

Antibody	Dilution
Mouse α RAB18	1:250
Rabbit α GAPDH	1:20,000
Rabbit α LC3B	1:500

The membrane was incubated in the primary antibody solution under gentle shaking at 4 °C o.n. After the incubation, the western blot was washed three times in TBST under gentle rocking at room temperature for 15 min. The blot was then incubated with the secondary antibodies mix prepared in TBS blocking buffer given in ***Table 15*** under gentle rocking at RT for two hours.

Table 15 | Secondary antibody mix

Reagent	Dilution
Goat α rb 680	1:20,000
Donkey α m 800	1:20,000

Finally, the blot washed three times in TBST under gentle rocking at RT for 15 min each. Then the blot was imaged at the highest quality using the Odyssey system (Licor) using automatic setting. The images were quantified in FIJI and the blots were dried and stored at 4°C for future reference.

3.2.2. HepG2 in vitro experiments

3.2.2.1. HepG2 maintenance

For experiments with human hepatocellular carcinoma cells, a HepG2 cell line from ATCC was maintained. Cell stocks were kept in 90% FCS and 10% DMSO at -165°C. Stock vials were thawed for 120 sec. at 37°C, before adding them to 10ml pre-warmed HepG2 culturing medium with 10% FCS in a 25ccm flask. Cells were left to attach to this flask at 37°C and 4% CO_2 o.n. The medium was exchanged the next day to remove the residual DMSO as well as dead cell debris. The cultured cells were kept at 37°C and 4% CO_2 from thereon.

Upon reaching confluency cells were split twice per week. Remaining medium was removed before the cells were washed in 10 ml pre-warmed 1xPBS. After aspirating the remaining 1xPBS, the attached cells were trypsinated with 2.5 ml Trypsin for 3 min at 37 °C and 4% CO_2. To quench the trypsination, 7.5ml of pre-warmed FCS containing HepG2 culturing medium was added resuspending the cells. The cells were singularized by repeated pipetting and the suspension was split into new flasks in ratios 1:4 and 1:6. The remaining suspension was used for the experiments.

3.2.2.2. Transfection of HepG2

The transfection of plasmids into HepG2 was conducted using the Effectene transfection kit (Qiagen™). HepG2 trypsinated in 3.2.2.1 were diluted 1:6 in HepG2 culturing medium. 300 µl of the diluted cell suspension was seeded in each well of an 8-Well chambered slide (Ibidi). The cells were incubated at 37 °C and 4% CO_2 for a minimum of 6 hours and at maximum o.n..

Before the end of the incubation, a transfection mix was created according to ***Table 16***. Per well 0.5-2 µg plasmid DNA was diluted in 100 µl buffer EC. Then, 8µl Effectene enhancer solution was added for each µg DNA added. This mix was incubated for 2 min on RT, before being quickly vortexed. To this mix 1.25 µl of Effectene reagent per well to be transfected was added. The transfection mix was quickly vortexed and incubated for a maximum of 10 minutes. Of the final transfection mix 105 µl were added to each well of the HepG2 seeded 8-Well chambered slide. Expression of the transfected construct could be detected after o.n. incubation.

Table 16 | Plasmid transfection mix

Reagent	Volume per well to transfect
Plasmid	0.5-2 µg
EC-Buffer	100µl
Enhancer	8 µl/ µg Plasmid
Effectene reagent	1.25 µl

3.2.2.3. *Localization of RAB18 mutants*

HepG2 were seeded and transfected with plasmids encoding RAB18 variants as described at 3.2.2.2. The transfected HepG2 cells were incubated o.n. before LD development was induced. The medium was therefore replaced with HepG2 culturing medium containing 400µM BSA complexed OA. As a vehicle control, cells were also treated with 200 µM BSA alone. The HepG2 cells were incubated for 24h, before the medium was exchanged for fresh HepG2 culturing medium containing 1 µM BODIPY staining the cells' LDs for 45 min at 37 °C and 4% CO_2. To identify cell nuclei, 1 µg/ml Hoechst was added and cells were incubated for another 15 minutes. The remaining dye was carefully washed off the cells using pre-warmed HepG2 culture medium.

The washed cells were transferred to a confocal microscope with an environmental chamber equilibrated at 37 °C and 5% CO_2. Cells were imaged taking single images scans. Hoechst, BODIPY and FusionRed tagged RAB18 variants were detected in sequence imaging each frame separately. The localization of RAB18 was compared to the LD staining in single-cell imaging.

3.2.2.4. *Fluorescence recovery after photobleaching (FRAP)*

3.2.2.4.1. FRAP of different RAB18 variants

Circulation of RAB18 and variants to the LD was investigated using a fluorescence recovery after photobleaching (FRAP) approach. Cells were transfected with all available RAB18 variants fused with FusionRed as given in 3.2.2.2. The HepG2 cells were subsequentially treated with 200 µM BSA and 400 µM BSA complexed OA or left untreated for 24h.

FRAP experiments were conducted on 5-10 transfected cells of each condition and RAB18 variant. In one iteration of the experiment, cells with sufficient fluorescently tagged RAB18 expression were selected. For the experiment, an ROI around a suitable LD was chosen and the fluorescent protein bleached for 5 sec using the white light laser at 586 nm wavelength. When localized protein was not available as LD marker, LDs were stained with BODIPY and suitable LDs were bleached. The recovery of the fluorescence was subsequently imaged each second for 180 seconds. The obtained image sequence was consequently exported and evaluated using the image analysis pipeline described in 3.2.2.4.3.

3.2.2.4.2. Effect of (de-)palmitoylation inhibitors on RAB18 localization

Investigating the effect of palmitoylation on RAB18 localization, inhibitors against palmitoylation and de-palmitoylation were tested for effects on RAB18's fluorescent recovery. 2-bromopalmitate, a palmitate analogue, competitively inhibits the cells palmitoylation machinery. palmostatin B inhibits APT1, which de-palmitoylates Ras/Rab family proteins.

HepG2 were seeded and transfected with GFP-WT-RAB18 analogous to 3.2.2.4.1. After effective transfection, cells were incubated for 20 h with DMEM, OA or BSA as vehicle control for OA incubation. At the end of the incubation 50 µM 2-bromopalmitate or DMSO as solvent control was added to the cells for additional 4 hours at 37 °C and 4% CO_2. For palmostatin B testing cells were treated with 10 µM palmostatin B and incubated for 10 minutes. Five transfected cells were picked for FRAP experiments as described in 3.2.2.4.1. LDs were bleached for 5 seconds using an Argon laser at 20%. Post bleach imaging was conducted each second for 150 seconds. The obtained image sequence was analyzed using the image analysis.

3.2.2.4.3. Automatic FRAP evaluation

The FRAP time series were loaded into FIJI and automatically read out using a custom algorithm. To determine the bleached area, the last pre-bleach series image intensity values were divided by the first postbleach series image intensity values. The area was thresholded and masked to measure the recovery. This areas' mean intensity was read out frame by frame to gain the fluorescent recovery curve. To correct for imaging dependent photobleaching the change of fluorescence intensity of the whole transfected cell was also measured as a reference.

The FRAP experiments was corrected for imaging dependent photobleaching and double normalized as proposed by Phair et al given in equation (Phair et al., 2003) (4).

$$I_{frap-norm} = \frac{I_{reference-pre}}{I_{reference}(t) - I_{background}(t)} \cdot \frac{I_{bleach}(t) - I_{background}(t)}{I_{bleach-pre}} \qquad (4)$$

The generated bleach corrected data was then further normalized to maximum according to following equation (5):

$$I_{normalized} = \frac{I_{frap-norm}(t) - \min(I_{frap-norm})}{\max(I_{frap-norm}) - \min(I_{frap-norm})} \qquad (5)$$

The calculations were done automatically and exported as csv to OriginLab for plotting. A mono-exponential fit was applied to extract kinetics (τ) and mobile fraction (A) according to equation (6).

$$y = Yb + A \times [1 - e^{-\frac{(x-TD)}{\tau}}] \quad (6)$$

RAB18 half-life was calculated using the following dependency described in (de Jong, 2015) given in equation (7).

$$t_{1/2} = \frac{\ln(2)}{\lambda} = \tau \ln(2) \quad (7)$$

Outliers, which showed large volatility or sharp drops in signal were removed from the dataset. The remaining mobile fraction and half-life of each curve were plotted in boxplots.

3.2.2.5. *Effect of (de-)palmitoylation inhibitors on LD development*

HepG2 cells were split 1:6 and seeded in 8-Well following the protocol detailed 3.2.2.1. After letting them attach for 20 h, cells were treated with 50 µM 2-bromopalmitate for 4h and 100 µM palmostatin B for 10 minutes. After the incubation, cells were treated with 400 µM OA for 24 h without media exchange. After 24 h of simultaneous (de-)palmitoylation inhibition and LD growth induction. LDs were stained using BODIPY and Hoechst analogous to 3.2.2.3. 5x5 tile scans were taken of stained LD and nuclei. LD were counted using the *StarDist* algorithm detailed in 3.2.6.2.2.

3.2.2.6. *siRNA transfection*

3.2.2.6.1. Transfection of 8-Well chambered slides (Ibidi)

For transfection in an 8-Well chambered slides (Ibidi) 4.8 pmol RAB18 siRNA or randomized scrambled RNA control were added to 40µl of DMEM medium in each well of a slide. To complex the siRNA 0.4 µl RNAimax lipofectamine was added, and the solution was incubated for 30 minutes. After this incubation, HepG2s were split 1:6, as given in 3.2.2.1 and 260 µl seeded in each 8-Well.

3.2.2.6.2. Transfection in 6-Well plates

Transfection in the 6-well format was conducted analogous to the 8-well transfection detailed in 3.2.2.6.1. In each well of the 6-Well 500µl of DMEM was added. In this medium, 30 pmol of siRNA and 5 µl RNAimax were diluted for complexation. After the 30 minutes incubation period, HepG2 cells were split 1:6 and 2 ml were seeded in each well for a total volume of 2.5 ml.

The knockdown was verified via western blotting. Cells were lysed 24 h, 48 h and 72 h post transfection and protein collected according to 3.2.1.10. The collected lysates were frozen to be analyzed via western blot as discussed in 3.2.1.11.

Single channel images taken with the LICOR system were exported as .tiff files and evaluated using FIJI. The obtained RGB images were transformed to 8-bit. Using the gel analyzer plugin in FIJI intensity density was plotted and read out.

The RAB18 intensity density was normalized to GAPDH's intensity density in OriginLab. The normalized RAB18 levels were divided by the levels detected in mock transfected cells to calculate the effective downregulation, which was plotted in a barplot.

3.2.2.7. *Analysis of LD phenotype after RAB18 Knockdown*

RAB18 knockdown was confirmed 72h post transfection, with RAB18 targeting siRNA A (OriGene), in the following called siRNA. Transfection of the 8-Well chambered slide (Ibidi) was done as described in 3.2.2.6.1. After transfection HepG2 cells were incubated at 37 °C and 4% CO_2 for 72 h. At this point cells were prepared for o.n. imaging. Cells were stained for 1h with 0.1 µM BODIPY. The dye was subsequently washed off 3 times in pre-warmed cell culture medium.

Before the imaging process, the incubation chamber of a confocal LSM880 microscope was equilibrate with 37 °C and 5% CO_2 for 30 minutes. For o.n. imaging the dish was fixated with adhesive tape on the objective table in the equilibrated incubation chamber. The chamber was left to incubate for another 30 minutes with the dish inside. In each well 3 positions and the corresponding focus level were saved, before a pre-incubation image was taken of all positions.

Next, 20 µl of the cell culture medium was removed and replaced with pre-warmed 20 µl 3 mM OA with 1 µM BODIPY amounting to 200µM OA per well. 20 µl 1.5 mM BSA with 1 µM BODIPY were added as a vehicle control. Imaging settings, positions and focus were readjusted according to focus drift. For the next 20 h, LD growth in cells was imaged every 15 minutes o.n..

3.2.2.8. *Rescue of RAB18 knockdown LD phenotype*

HepG2 were transfected with siRNA analogous to 3.2.2.6.1. After 8 h to o.n. incubation at 37 °C and CO_2, cells were transfected with different FusionRed-RAB18 variants. Transfection mixes were created using the Effectene transfection kit as described in 3.2.2.2. Upon transfection cells were incubated for 48 h at 37 °C and 4% CO_2.

72 h post siRNA transfection, the medium was exchanged with medium containing 400 µM OA and HepG2 were incubated for 20 h at 37 °C and 4% CO_2. After fatty acid incubation, the medium

was replaced with 300 µl DMEM containing 10% FBS as well as 1 µM BODIPY. The cells were stained in this solution for 45 minutes before adding 0.4 Hoechst 10 mg/ml to each well. The cells were incubated for another 15 minutes at 37 °C and 4% CO_2. After 1 h of staining the cells were washed three times in pre-warmed DMEM. Cells were then imaged in 5x5 tile scans under the same settings as 3.2.2.3. The resulting images were analyzed by manual counting as described in 3.2.6.2.1.

3.2.2.9. Inhibition of lipolysis during RAB18 knockdown

The role of RAB18 in lipolysis was investigated via the inhibition of lipolysis with the small molecular inhibitor atglistatin. Endogenous RAB18 was downregulated with siRNA as described in 3.2.2.6.1. Cells were seeded in an 8-Well glass bottom chambered slide (Ibidi) and incubated at 37 °C and 4% CO_2. After 48h of incubation cells were then incubated with 50 µM atglistatin for 24 h before treating cells with 400 µM OA for 24 h. Finally, the cells were imaged using CARS imaging at wavelength 2847 cm^{-1}. 5x5 Tile scans were analyzed with the *StarDist* algorithm as given 3.2.6.2.2.

3.2.2.10. Inhibition and activation of autophagy during RAB18 downregulation

Inhibition of autophagy was conducted using 50 µM lalistat2 and 30 µM Chloroquine. Activation was tested with 1 µM Rapamycin for mTOR1 inhibition and 1 µM Torin2 for mTOR2 inhibition. The protocol described in 3.2.2.6.1 was followed and cells were seeded into an 8-Well glass bottom chambered slide (Ibidi). 48 h post siRNA transfection cells were treated with the corresponding small molecular inhibitors for 24 h. After this modulation of autophagy, 400 µM OA was added to the medium to induce LD formation. HepG2 cells were subsequently imaged using CARS at a wave-number of 2847 cm^{-1}. 5x5 tile scans were taken and analyzed given in 3.2.6.2.2.

The role of autophagy was also investigated after formation of LDs. A siRNA mediated knockdown of RAB18 was conducted as given in 3.2.2.6.1. LD growth was induced by addition 400 µM OA 72 h post transfection. After 24 h of LD growth, the medium was exchanged with medium carrying 60 µM Chloroquine. Autophagy was blocked for 24 h before cells were imaged using CARS at 2847 cm^{-1}. LDs were segmented using the *StarDist* algorithm as described in 3.2.6.2.2. and analyzed as detailed in 3.2.6.2.3.

3.2.2.11. Measuring autophagy in cells with RAB18 knockdown

3.2.2.11.1. Immunostainings of LC3B

HepG2 were seeded in an 8-well removable chamber slide (Ibidi) and treated as given in 3.2.2.10. After the experiment, the cells were washed three times in pre-warmed 1xPBS. The washed cells were fixed in 4% paraformaldehyde for 20 minutes. The fixed cells were washed again three times in 1x PBS, before they were treated with 50 mM NH_4CL for 10 minutes. After this the NH_4CL was washed off with PBS for 5 min.

The fixed cells were permeabilized with 0.5% Tx100 triton in PBS for 10min. The triton was washed off in three consecutive wash steps for 5 min each. Epitopes were blocked with 5% BSA in PBS for 90 minutes. After washing, the fixed cells were incubated in a primary antibody diluted in 2% BSA in PBS o.n. at 4°C (***Table 17*)**.

The next day, cells were washed in 2% BSA solution in PBS, which was followed by 2 hours of incubation with the secondary antibody dilution containing 0.1mg/ml DAPI for nuclear staining. The stained cells were imaged in 5x5 tilescans using a LSM880 confocal microscope (***Table 17***).

Table 17 | Immunostaining antibody solutions

	Primary antibody	**Secondary Antibody**
Antibody	Rabbit α LC3B	Donkey α rabbit Alexa fluor 647
Dilution	1:100	1:100

3.2.2.11.2. Evaluation of LC3B staining

The LC3B *punctae* in the images obtained in 3.2.2.11.1 were analyzed using a segmentation pipeline custom made in FIJI. Images of LC3B punctae were duplicated and blurred. The blurred duplicate was thresholded using the auto-threshold algorithm developed by Li et al (Li and Tam, 1998). The thresholded duplicate was converted to a mask, which was used to segment the LC3B *punctae* from background noise. To separate the individual punctae the segmented image was thresholded using the imageJ version of the IsoData algorithm("Picture Thresholding Using an Iterative Selection Method," 1978). The binary thresholded image was subsequently watershed using the binary watershed method supplied by FIJI. The singular LC3B punctae were then analyzed using the "Analyze particles…" function inf FIJI and a list of measurements was exported.

The stained nuclei were counted manually. To gain the LC3B *punctae* per cell the number of LC3B punctae were normalized to the nuclei count. The results were plotted in a boxplot.

3.2.2.11.3. Overexpression of the pHluorin-mKate2-LC3B construct

To test the pHluorin-mKate2-LC3B construct, cells were seeded in 8-Well glass bottom chambered slides (Ibidi) and transfected with the plasmid according to 3.2.2.2. After 24 h incubation 10 representative transfected cells were imaged on an SP8 confocal microscope, before half of the wells were treated with 20 µM chloroquine for LC3B accumulation. The other half was treated with PBS as solvent control. After 4h chloroquine treatment, 10 representative transfected cells of each condition were imaged. This was repeated after 24h of chloroquine treatment, before the cells were supplemented with 400 µM OA. Following 24h of OA supplementation, again 10 representative transfected cells of each condition were imaged.

To investigate the effect of RAB18 siRNA HepG2 cells were fist seeded and transfected with RAB18 and scrambled siRNA in 8-Well glass bottom chambered slides (Ibidi) as described in 3.2.2.6.1.. After 24h of incubation these cells were then transfected with the pHluorin-mKate2-LC3B plasmid according to 3.2.2.2. The cells were incubated for 24h, before half of the wells were treated with 20µM chloroquine for LC3B accumulation, whereas the other half was treated with PBS as solvent control. After 24h of incubation, the cells were supplemented with 400µM OA to induce the formation of LD. At the end of this incubation period 10 representative transfected cells of each condition were imaged.

The autophagosomes positive for mKate2-LC3B were manually segmented analogous to 3.2.6.2.1. and the number of autophagosomes per cell was calculated and plotted in a boxplot. To establish the fraction of autophagolysosomes, the intensity of the pHluorin-GFP was automatically measured for each manually annotated autophagosome. Additionally, the mean intensity of pHluorin-GFP of the cell was measured. Using the mean intensity of the cell as a threshold, autophagosomes which had a pHluorin-GFP intensity below the mean intensity of the cell were counted as autophagolysosome. The number of autophagolysosomes was then divided by the number of autophagosomes to obtain the fraction of autophagolysosomes, which was plotted in a boxplot.

3.2.2.11.4. Western Blot detection of LC3B2

HepG2 cells were seeded, and siRNA was transfected in two 6-Well plates according to 3.2.2.6.2. All cells were consecutively incubated for 48 h at 37 °C and 4% CO_2. Next, half of the wells of each plate were treated with 20 µM Chloroquine as positive control. After 24 h incubation at 37 °C and 4% CO_2, cells of the first plate lysed for protein extraction as discussed in 3.2.1.10. 400 µM OA was added to the remaining plate and the cells were incubated for an additional 24 h, before they were lysed according to 3.2.1.10.

The extracted protein was run on a blot and LC3B, GAPDH and RAB18 were detected as explained in 3.2.1.11.

Single channel images taken with the LICOR system were exported as .tiff files and evaluated using FIJI. The obtained RGB images were transformed to 32-bit and manually thresholded to remove any background from the blot. Using the gel analyzer plugin in FIJI intensity density was plotted and read out.

The intensity density of LC3B and RAB18 was normalized to the GAPDH values in OriginLab. LC3B values of cells transfected with siRNA in which compared to the control more than 10% RAB18 was detected were excluded from the quantification. To calculate the ratio of LC3B1 to LC3B2 the unnormalized intensity density values of LC3B2 were divided by the sum of the intensity density values of LC3B1 and LC3B2. The autophagic flux was calculated by subtracting the normalized LC3B2 value of Chloroquine treated cells by the one detected in vehicle treated cells. The LC3B2 levels normalized to GAPDH, the ratio of LC3B2 to total LC3B and the autophagic flux were plotted as boxplot.

3.2.3. Primary human hepatocytes

3.2.3.1. Collagen coating of dishes (Ibidi)

One day prior to the seeding, a 1 mg/ml rat tail Collagen I solution was prepared in 10 ml 0.2% glacial acid and stored o.n. at 4 °C. The day of seeding 3 ml of this collagen solution was added to 350 µl 10x DMEM medium. The pH of the collagen I solution was adjusted by titrating with approximately 150 µl 1 M NaOH. Once the indicator reflected a basal pH titration was stopped and 150 µl collagen solution was added into each well of a 4-Well glass bottom chambered slide (Ibidi). To evenly coat the slide, it was hit carefully on the side. The coated dishes were then set aside to polymerize at RT for approximately 30 minutes. The remaining collagen solution was used as a reference for the polymerization state of the dish.

3.2.3.2. Seeding of primary human hepatocytes

Primary human hepatocytes were taken from liquid nitrogen and were thawed at 37 °C for 2 minutes. The stock was transferred completely to 10 ml of primary human hepatocyte culturing medium supplemented with 10% FBS. 50 µl of this suspension were removed and mixed with trypan blue for cell counting with a Neubauer counting chamber to establish cell concentration.

To each well of a collagen coated chambered slide (see 3.2.3.2) 200,000 cells were added. The volume of each well was adjusted to 300µl by addition of primary hepatocyte culturing medium supplemented with 10% FBS. The cells were then incubated at 37 °C and 5% CO_2. Seeded cells were shaken gently every 15 minutes for three times. After this, the hepatocytes were left to attach at 37 °C and 5% CO_2.

Three hours post seeding, the seeding medium was removed and cells were washed in hepatocyte growth medium. Then the medium was thoroughly aspirated before another layer of 200 µl collagen was added analogous to 3.2.3.1. The collagen layer was left to polymerize at 37 °C and 5% CO_2. Remaining collagen solution was kept in a 37 °C water bath as reference for the polymerization status of the dish. When the collagen reference fully polymerized fresh pre-warmed primary human hepatocyte culturing medium was added, and cells were incubated at 37 °C and 5% CO_2 o. N.

3.2.3.3. *Chloroquine treatment of Human hepatocytes*

On the first day post plating the medium was exchanged for fresh hepatocyte culturing medium containing 10 µM, 25 µM, 50 µM and 100 µM Chloroquine. The cells were incubated at 37 °C and 5% CO_2 for 24 h. After the incubation, 400 µM BSA complexed OA or 200 µM BSA was added to each well. Cells were incubated for an additional 24 h, before being subjected to CARS imaging at 2847 cm^{-1}. LDs were segmented using the *StarDist* algorithm as described in 3.2.6.2.2. and analyzed as detailed in 3.2.6.2.3.

3.2.4. Mouse experiments

3.2.4.1. *Study approval and mouse treatment*

All experiments were approved by the official state animal care and use committee (LANUV, Recklinghausen, Germany AZ 84_02.04.2016.A473) The mice were housed under specific-pathogen-free conditions according to the guidelines of the Federation for Laboratory Animal Science Associations (FELASA). All experiments were conducted in accordance with the German federal law regarding the protection of animals and 'Guide for the Care and Use of Laboratory Animals' (National Institutes of Health publication 8th Edition, 2011).

3.2.4.2. *Study design*

Twenty-eight mice were divided in two groups. Group one was subjected to daily intraperitoneal injection with 60 mg/kg body weight Chloroquine phosphate solved in PBS. The control group two was injected with a corresponding volume of PBS. The mice were treated this way for one week before the liver of one mouse of each group was imaged as given described in 3.2.4.3.

After one week of Chloroquine treatment 7 mice of each group were set either on the fat heavy research diet or a control diet. Mice were fed for four weeks. One representative mouse of each group fed with the research diet was imaged each week to observe the gradual development of steatosis *in vivo.* After 4 weeks, all mice were imaged and subsequently euthanized. Blood was taken for further analysis with the German mouse clinic, Munich.

3.2.4.3. *In vivo CARS imaging of mice*

Mice were anaesthetised with a combination of ketamine (64 mg/kg), xylazine (7,2 mg/kg) and acepromazine (1.7 mg/kg) given intraperitoneally. The abdomen of the animal was shaved, and a ~1.5 cm midline incision made to expose the xiphoid process which was retracted to allow dissection of the falciform ligament. The left lobe of the liver was then gently exteriorised, and the animal inverted onto a glass coverslip mounted within a custom-made imaging platform. To prevent dehydration, the liver was covered with sterile PBS-soaked gauze. Images were taken on a Leica SP8 confocal laser scanning microscope in a light proof environmental chamber, which was maintained at 37 °C and constant humidity.

The usage of the CARS system made injection of dyes unnecessary whilst allowing for both CARS and second harmonics imaging. A still region of the mouse liver was selected and 5x5 tile scans were taken.

3.2.5. Imaging

3.2.5.1. *Fluorescent imaging*

Imaging was done on a Leica SP8 and Zeiss LSM880 confocal laser scanning microscope. Fluorescent imaging of stained and transfected cells on the LSM 880 was done using a UV diode (405nm), an Argon (488 nm) and a He/Ne (561 nm) laser. The objective used was a 40x oil immersion objective;

Fluorescent imaging on the SP8 was conducted using an argon and a white light laser. Cells were imaged with a 63x motorized correction collar water immersion objective.

3.2.5.2. *Label free CARS imaging*

Label free CARS and second harmonic imaging were done using an APE picoEmerald IR laser system. The system consisted out of a picosecond pulsed tunable pump laser and a stokes laser set at 1031nm. Imaging was done using an IR optimized 40x objective with a NA of 1.1. In CARS the stimulated sub-molecular pattern is specific to the pump/stokes laser settings. Since the settings for every CARS microscope are different, CARS settings in this thesis are given in wavenumber (ṽ) calculated as given in equation (8).

$$\tilde{v} = \frac{1}{\lambda_{pump}} - \frac{1}{\lambda_{stokes}} \qquad (8)$$

With λ_{stokes}= 1031nm for this system.

The IR laser was set for 0.2 W laser power on both stokes and pump laser at 45% output power for *in vitro* imaging of cells. For *in vivo* imaging in mice, CARS laser power was increased to 0.5 W with 70% output for both lasers. Second Harmonics imaging was conducted *in vivo* using only the 1031nm stokes laser with 95% output and 0.5 W laser power. LDs were imaged at 2847 cm^{-1}.

3.2.6. Image analysis

3.2.6.1. Source code location

All source code is publicly available in the author's GitHub repository (amrieck/AR PhD-Thesis Coding). For instructions on how to apply the provided code please refer to the respective readme.txt file found within the repository.

3.2.6.2. LD segmentation

3.2.6.2.1. Manual LD segmentation

For gaining certain insight into the exact LD composition of cells with RAB18 downregulation, LDs of these experiments were counted manually in FIJI.

Transfected cells were singled out and duplicated. In the duplicated images' LDs were segmented by using circular selection tools marking them in the ROI-manager tool. Selected ROIs were saved separately alongside the duplicated images and measured for area and mean intensity. These measurements were transferred into OriginLab for further analysis as given in 3.2.6.2.3.

3.2.6.2.2. Training and LD segmentation with the *StarDist* machine learning algorithm

Though more accurate manual segmentation was slow. However, based on this manual data, a machine learning model was trained. The shape based *StarDist* algorithm developed my Schmidt et al (Schmidt et al., 2018) was selected for the proposed problem and at least ten images already annotated in 3.2.6.2.1 were used to train different models for LD segmentation.

After achieving a precision over 80% at an Intersection over Union of 50%, which was obtained through the provided code, the models were tested against manually annotated data not used for the training was used to test the trained models' accuracy. After establishing a well-trained model, 5x5 tile scans of BODIPY stained LDs derived from 3.2.2.5 were stitched and segmented. 5x5 tile scans of CARS images obtained in 3.2.2.9, 3.2.3 and 3.2.4 were stitched and also analyzed using this form of segmentation. ROIs provided by the algorithm were automatically measured providing a list of size and signal intensity of each detected LD. The dataset was transferred to OriginLab to be analyzed as detailed in 3.2.6.2.3.

3.2.6.2.3. LD Data analysis

In vitro experiments LDs smaller than 1 µm² were excluded from the data. In *in vivo* experiments this cutoff was raised to 3 µm² due to tissue background. For comparison of LD size, mean LD area per experiment or mouse were plotted in a boxplot using OriginLab. For comparison of LD size distributions, frequency counts of every replicate of each single experimental condition were made by binning single LD measurements in 0. 2µm² bins between 1 and 8 µm². The cumulative counts of these frequency distributions were normalized according to equation (9).

$$Fraction\ of\ total\ LDs\ in\ bin_x = \frac{n_{LD\ bin_x} - n_{LD\ 1\mu m\ bin}}{n_{LD\ total} - n_{LD\ 1\mu m\ bin}} \quad (9)$$

A mean frequency distribution of all replicates of an experiment was calculated and plotted for comparison in a cumulative histogram with the inter-experimental standard deviation depicted by the error bars.

To compare LD CARS signal, images were background subtracted in FIJI using the rolling ball algorithm with a pixel width of 10. The LD Intensity Density was analyzed with FIJI and averaged for each tile scan. These mean intensity values were plotted as boxplot using OriginLab.

LD number per cell was calculated by manually counting each nuclei of every tile scan. The number of segmented LD was then divided by the nuclei count of the corresponding tile scan to calculate the number of LD per nuclei.

3.2.7. Statistics and outlier treatment

Statistics were tested using the two-sample t-test in OriginLab and p-value are depicted above the boxplots. Whether data fulfilled the t-test criteria of normal distribution was tested with the Shapiro-Wilk test at an alpha level of 0.05, If this criterium was not met, hypothesis testing was done using the Kolmogorov-Smirnov test. The test used to obtain p=values is given in each figure legend. Equal variance was also tested for using the two-sample variance test provided by the OriginLab software to ensure applicability of the t-test. The number of experimental replicates is described as N, whereas the number of singular values per experiment are described as n in the figure legend. If not given N/n=1. Values larger than twice the standard deviation were labeled as outliers and disregarded in the evaluation of the experiments.

4. Results

4.1. RAB18's localization to the LD depends on its C-terminal palmitoylation

4.1.1. Creation of RAB18 mutants

To investigate the mechanism regulating RAB18's localization to the LD, fluorescently tagged WT and mutant RAB18 were created. First, RAB18 cDNA was inserted in an overexpression vector which was expressing either GFP2 or FusionRed fluorescent proteins under the control of an HCMV promoter. The resulting fusion protein comprised a fluorescent protein fused to the RAB18 N-terminus, which left the RAB18 C-terminus, deemed crucial for localization, free of any obstruction A plasmid map of the FusionRed-RAB18 plasmid is given in the appendix section 7.1.1.. Using this fluorescent protein tagged WT-RAB18 as a template, changes were introduced to the RAB18 sequence by site directed point mutation to cause amino acid exchanges. By this approach, the two activity mutants, Q67L and S22N described in chapter 1.3.4, were created to investigate the effect RAB18's activity had on its localization.

Based on RAB18 sequence homology to other Ras/Rab superfamily proteins, it was surmised that removing the palmitoylation site in RAB18's C-terminus, which was predicted to be located at cysteine 199, would inhibit its localization to the LD-membrane. Thus, to prevent S-palmitoylation, the sequence was mutated to encode a serin instead of the cysteine (C199S). Serin lacks the residue necessary for S-palmitoylation, which results in the loss of the palmitoylation site. Analogous to this, the prenylation site at C203, deemed essential for general membrane localization, was also mutated, exchanging the cysteine for serin (C203S). For further insights into the relation between activity and palmitoylation, two RAB18 double mutants were created. Q67L and S22N were mutated at C199 to remove the palmitoylation site, creating the double mutants Q67L-C199S and S22N-C199S.

Besides the loss of palmitoylation, the effect of multiple palmitoylations was also studied. Therefore, RAB18 C-terminus sequence was mutated to encode two additional cysteines at positions 191 (E191C),195 (G195C). Assuming that S-palmitoylation is not context sensitive, this mutant should be theoretically triple palmitoylated post translation. For the sake of readability, this mutant is referred to as PolyC in the following.

Each of the described point mutations were conducted and the resulting plasmids were sequenced. Alignment of these sequences with the RAB18 wildtype sequence confirmed that all mutants were successfully created without off target alterations to the RAB18 sequence (***Table 18***). For the full alignment please see appendix section 7.1.2-8.

Besides the mutation of the RAB18 ORF, RAB18's C-terminus was fused to the cytoplasmic N-terminus of the ER transmembrane protein SEC61b. The resulting fusion protein is tethered to the ER by the SEC61b transmembrane, so it was treated as a positive control for RAB18 ER localization. The plasmid map of this fusion protein is located in the appendix section 7.1.1.

Table 18 | RAB18 point mutations and resulting amino acid exchange

Juxtaposition of wildtype and mutated cDNA sequence. The changes are highlighted in red.

	WT sequence	**Point Mutation**
Constitutively active (Q67L)	GCT GGT CAA GAG AGG TTT AGA A65 G66 Q67 E68 R69 F70 R71	GCT GGT CTA GAG AGG TTT AGA A65 G66 L67 E68 R69 F70 R71
Dominant negative (S22N)	GTG GGC AAG TCC AGC CTG CTC V19 G20 K21 S22 S23 L24 L25	GTG GGC AAG AAC AGC CTG CTC V19 G20 K21 N22 S23 L24 L25
Palmitoylation site (C199S)	GGA GGA GCC TGT GGT GGT TAT G196 G197 A198 C199 G200 G201 Y202	GGA GGA GCC AGT GGT GGT TAT G196 G197 A198 S199 G200 G201 Y202
Prenylation site (C203S)	GGT GGT TAT TGC TCT GTG TTA G200 G201 Y202 C203 S204 V205 L206	GGT GGT TAT AGC TCT GTG TTA G200 G201 Y202 S203 S204 V205 L206
Multiple Palmitoylation sites (E191C & G195C) abbreviated as PolyC	AGG GAA GAA GGC CAA GGA GGA GGA GCC TGT GGT GGT TAT TGC TCT GTG TTA R190 E191 E192 G193 Q194 G195 G196 G197 A198 C199 G200 G201 Y202 C203 S204 V205 L206	AGG TGC GAA GGC CAA TGC GGA GGA GCC TGT GGT GGT TAT TGC TCT GTG TTA R190 C191 E192 G193 Q194 C195 G196 G197 A198 C199 G200 G201 Y202 C203 S204 V205 L206

4.1.1. Localization of different RAB18 variants in HepG2

After creating the FusionRed-RAB18 mutant plasmids and the FusionRed-RAB18-SEC61b plasmid, each of these plasmids were transfected into HepG2 cells to analyze the cellular localization of the expressed fusion proteins. As a negative control, the empty vector backbone, only expressing FusionRed, was also transfected. Following the successful transfection, the onset of steatosis was simulated in the transfected cells by supplementing the HepG2 cells with 400µM BSA complexed oleic acid (OA) for 24h. The LDs were subsequently stained with BODIPY and representative transfected cells were imaged.

FusionRed-RAB18 was detected as ring-like structures around LDs, indicating LD membrane localization, which replicated the reported localization of RAB18 described in 1.3.3. Analogous to the WT, the constitutively active Q67L mutant also showed LD membrane localization. However, the dominant negative S22N mutant was not detected on the LD membrane. Instead, S22N mis-localized to the cytoplasm outside the nucleus, which suggests that only active RAB18 localizes to LD. OA supplementation did not cause changes in the localization of the WT RAB18 or its mutants (Figure 6).

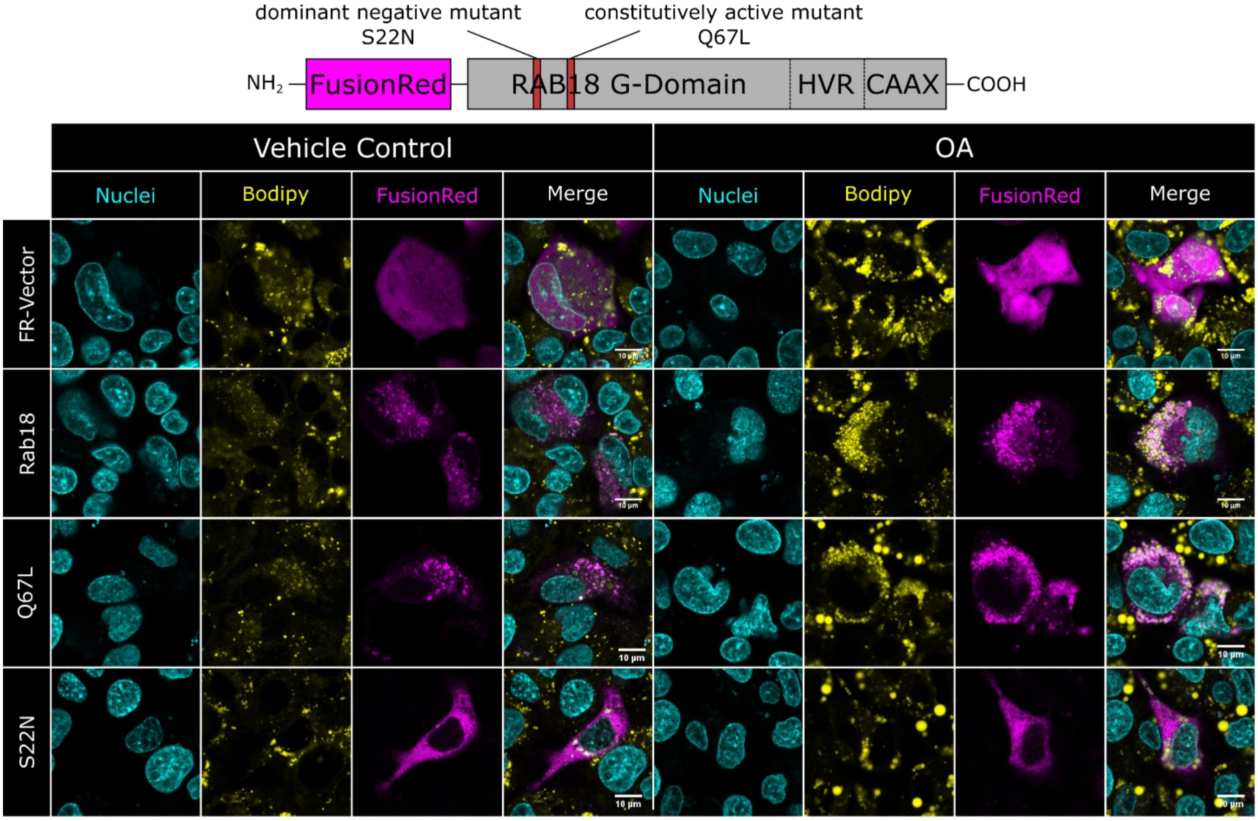

Figure 6 | Active RAB18 localizes to the LD membrane

Schematics indicate the mutations on fluorescent tagged RAB18 **HVR**: highly variable region. Panels of confocal images indicate localization of the respective mutants in HepG2 post-LD induction (Magenta). BODIPY staining marks LDs (Yellow). Image contrast was maximized for display. Fusion-Red tagged constitutionally active and wild type RAB18 localize to LDs. Inactive RAB18 localizes to the cytoplasm.

After establishing the localization of known RAB18 activity mutants, the influence of the C-terminal modification was investigated. Like the WT, the PolyC mutant, which carried additional palmitoylation sites, was detected on the LD membrane. However, the C199S mutant, which had no palmitoylation site, mis-localized to the cytoplasm outside of the nucleus. Thus, it was shown that without palmitoylation RAB18 does not localize to the LD membrane (Figure 7).

The dominant active RAB18 double mutant Q67L-C199S did not display any LD membrane localization, proving that the loss of palmitoylation cannot be compensated for by increased activity. The dominant negative S22N-C199S double mutant also localized to the cytoplasm. (Figure 7).

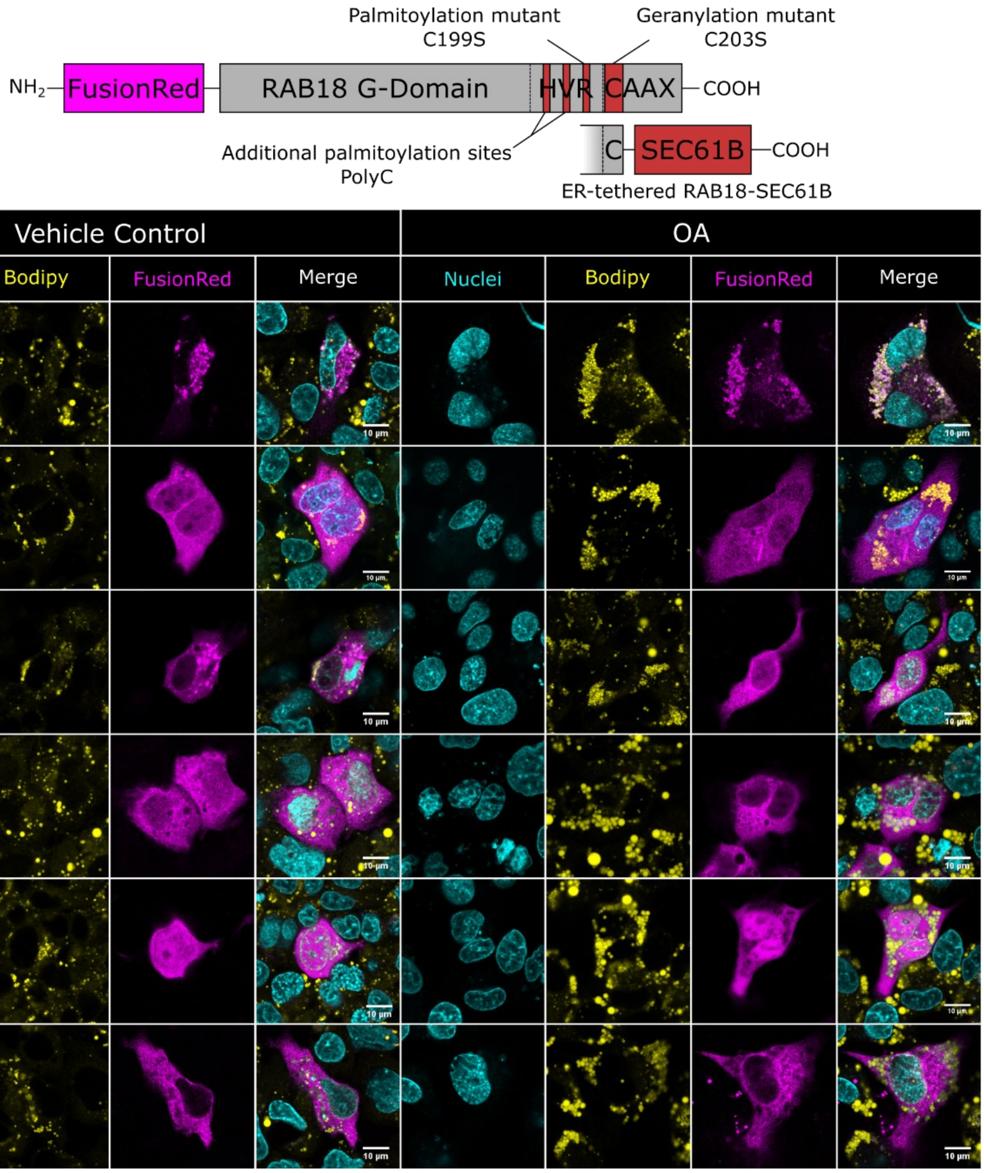

Figure 7 | The localization of RAB18 depends on C-terminal S-palmitoylation and prenylation

Schematics indicate the mutations on fluorescent tagged RAB18 **HVR**: highly variable region. Hyper-palmitoylated, prenylated PolyC with high membrane stability localizes to LDs upon OA-stimulation, while un-palmitoylated C199S or unprenylated C203S do not. ER membrane-tethered RAB18-SEC61B does not localize to LDs, indicating membrane affinity is not sufficient for specific LD localization. The mis-localization of the constitutive active -palmitoylation double mutant (Q67L) indicates that activity is necessary but not sufficient for specific LD localization. Taken together, palmitoylation at C199S through the acylation cycle and GTP-loading are essential prerequisites for RAB18 localization to LDs.

Mutation of the geranylgeranylation site C203S resulted in a cytosolic localization of RAB18 marked by an even distribution throughout the cell and the nucleus. Since this localization was similar to the localization of FusionRed encoded on the vector backbone, it is assumed that C203S lost its membrane affinity. RAB18, which was tethered to the ER by its C-terminally fused SEC61b, mis localized to the cytoplasm in a pattern similar to C199S and S22N. This implies that C199S, S22N, Q67L-C199S and S22N-C199S are localized to the ER instead of the LD membrane, which is most likely conferred by the C-terminal geranylation at C203. Analogous to the WT and the activity mutants, supplementation of OA did not affect the localization pattern of ER tethered RAB18 and the RAB18 variants carrying mutations in their C-terminus (Figure 7).

In summary, only active RAB18 localizes to the LD, but its localization is dependent on its C-terminal modification. Whilst the post-translational geranylgeranylation confers its membrane affinity, the palmitoylation is essential for the LD localization.

4.1.2. Localization of RAB18 is dynamical

In the analysis of RAB18 mutants, C-terminal palmitoylation was established to be essential for RAB18's localization to the LD mem. However, it remained uncertain whether this localization was static or dynamic. To quantify the dynamics of RAB18 localization to the LD, fluorescence recovery after photobleaching (FRAP) experiments were conducted. HepG2 cells transfected with each RAB18 mutant. They were then supplemented with either vehicle control or OA or kept under basal condition (DMEM medium) for 24h before being subjected to FRAP experiments. For one FRAP experiment one LD was selected in a transfected cells and the fluorescent protein around it was bleached. The recovery of fluorescence intensity following the bleach was subsequently measured over time (Figure 8A &B).

In the experiments RAB18 was found to dynamically localized to the LD with and without supplementation of OA and different recovery curves were detected for the different mutants. To compare the differences in recovery, the recovery curves were fitted with a mono exponential curve fit to calculate two parameters of RAB18 LD localization. The mobile fraction (A) describes the fraction of exchanged protein on the LD-membrane. The time constant of the recovery (τ) was used to calculate the half-life of RAB18 recovery (Figure 8B).

Under basal condition it could be observed that all variants of RAB18, but PolyC and Q67L had a mobile fraction of around 80%. Both the hyper-palmitoylated PolyC mutant as well as the constitutively active mutant Q67L had a decreased mobile fraction of about 57%, which indicates that there is a lower turnover of theses mutants on the LD membrane (Figure 8C).

Interestingly, no significant differences were detected in HepG2 cells after supplementation with the vehicle indicating an effect of the vehicle (BSA) on RAB18 localization. After OA supplementation, the constitutively active Q67L's mobile fraction dropped significantly to 49%, which implies that activity is the deciding factor in RAB18's LD retention after OA supplementation, but not the palmitoylation (Figure 8C)

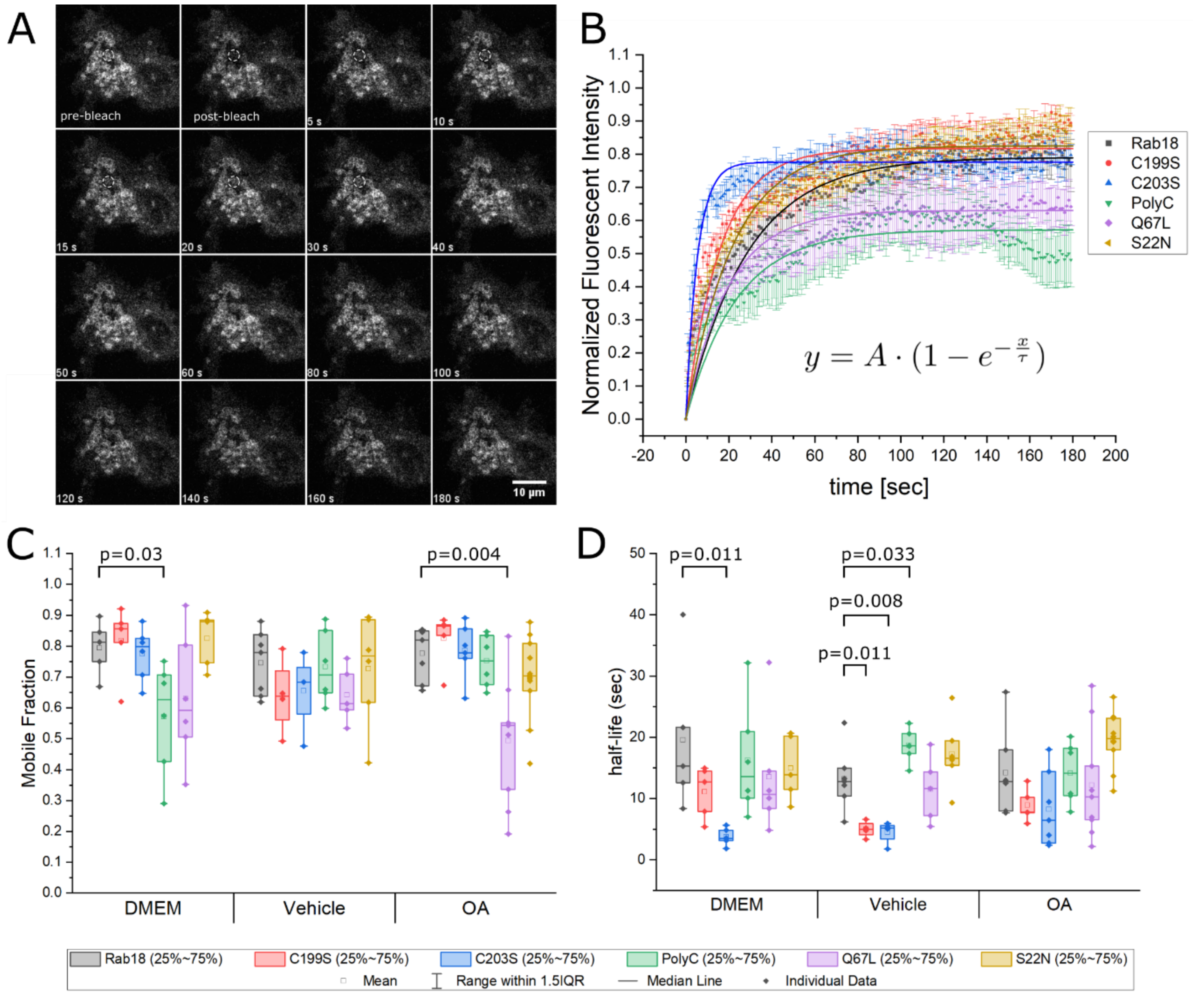

Figure 8 | RAB18 recovers dynamically

Fluorescence recovery after photobleaching (FRAP) was measured after bleaching FusionRed-RAB18 localized to the LD membrane (dotted line indicating bleach area) **(A)**. Exemplary mean fluorescent recovery curve after normalization and bleach correction is overlayed with a mono-exponential curve fit as indicated by the formula given below the graph. The error bars represent standard error. **(B)** Boxplots display the mobile fractions **(C)** and half-life **(D)** of different RAB18-variants calculated based on the curve fitting. Statistical testing was done with students t-test and p-values given on top of the boxplot. n≥4

The half-life of RAB18 recovery could be determined at around 19 seconds under basal conditions. Compared to the half-life of WT RAB18, mutation of the geranylgeranylation and palmitoylation site significantly reduced the half-life. Although, only for the half-life of C203S a statistically significant difference could be established. No changes of PolyC, Q67L and S22N half-lives were unchanged to RAB18. In cells supplemented with vehicle control, the half-life C199S recovery comparable to the half-life of C203S. Both half-lives were significantly faster than WT-RAB18. PolyC however, recovered significantly slower, indicating that increased palmitoylation slowed RAB18 localization to the LD membrane. Q67L and S22N recovered at the same rate as WT-RAB18. No significant changes were observed post-LD-accumulation with OA. Noticeably, the biggest alterations were detected in the palmitoylation and geranylation mutants, highlighting the importance of these post-translational modifications (Figure 8D).

In summary, the localization of RAB18 is dynamical. Whilst the tun-over of RAB18 on the membrane is decided by the activity, the localization half-life is determined by the palmitoylation state.

4.1.3. RAB18 localization can be pharmacologically altered

After demonstrating the dynamic localization of RAB18 to the LD, it was investigated whether modulating the cell's palmitoylation machinery via small molecule inhibitors would affect RAB18 localization. The inhibitor 2-bromopalmitate (2-BP) was used to inhibit the cellular palmitoylation machinery. Since the de-palmitoylation of RAB18 was hypothesized depend on APT1, the APT1 inhibitor palmostatin B was used to inhibit de-palmitoylation. For both substances DMSO served as a solvent control. The effect of these inhibitors on GFP-RAB18 LD localization was measured analogous to 4.1.2 using FRAP under basal conditions (DMEM medium) and after vehicle (BSA) as well as OA supplementation for 24h (Figure 9).

Under basal conditions RAB18 was demonstrated to have a mean mobile fraction of 80% replicating the results shown in 4.1.2. This mobile fraction did not change after supplementation with the vehicle or OA. After incubating the HepG2 cells with the solvent for 4h, the mean mobile fraction significantly decreased to 67% under basal conditions. However, after treatment with the vehicle for OA supplementation (BSA), no difference could be detected between solvent treated and untreated cells. After supplementation with OA solvent treatment significantly increased the mobile fraction (Figure 9C).

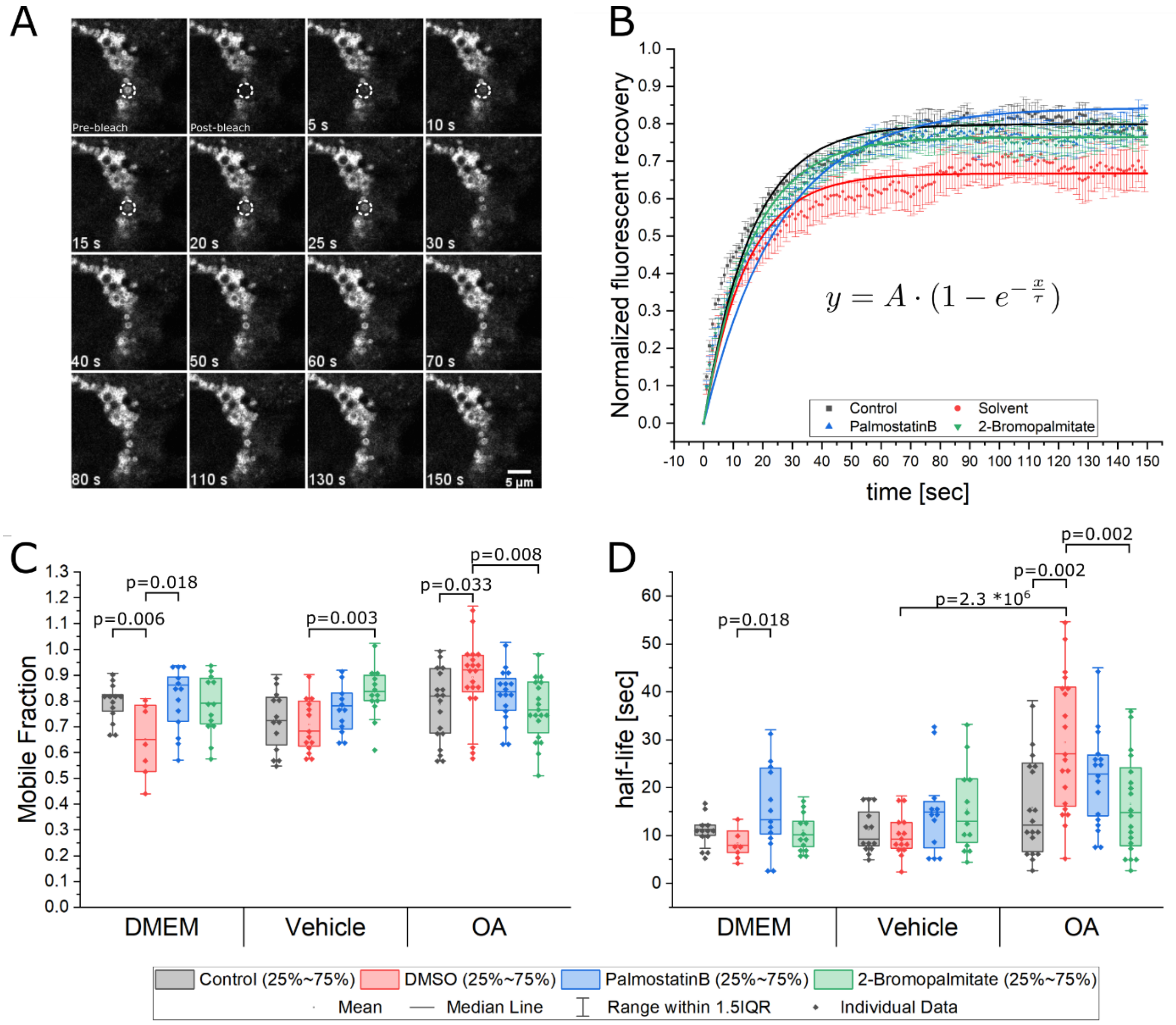

Figure 9 | Inhibition of (de-)palmitoylation changes RAB18 LD localization

RAB18 palmitoylation was inhibited with 2-bromopalmitate. De-palmitoylation was inhibited by palmostatin B. DMSO served as vehicle control. The representative time series shows the fluorescent recovery after photo bleach (FRAP) of GFP-RAB18 indicated with the dotted line **(A)**. Exemplary mean fluorescent recovery curve after normalization and bleach correction (scatterplot) is overlayed with a mono-exponential curve fit (lines). The error bars represent standard error **(B)**. Inhibition of de-palmitoylation increased both half-life and mobile fraction of RAB18 without OA induction. Inhibition of palmitoylation decreased both after OA induction, indicating RAB18 palmitoylation is induced upon LD growth **(C)**. Statistical significance was tested with the two sample ttest. n≥8

Compared to solvent treated HepG2 cells, inhibition of de-palmitoylation with palmostatin B significantly increased the mean mobile fraction to 84%. This difference was no longer detected after supplementation with the vehicle control. No difference was also detected in the mobile fraction between solvent control and palmostatin B treatment after supplementation of OA (Figure 9C).

In contrast, the inhibition of the cellular palmitoylation with 2-BP showed no significant changes in the mobile fraction under basal conditions. In cells supplemented with only the vehicle, a significantly higher mobile fraction was observed after inhibition of palmitoylation. After OA supplementation, 2-BP treatment was found to result in a significantly reduced RAB18 mobile fraction, indicating that turnover of RAB18 on the LD has been reduced by inhibiting palmitoylation (Figure 9C).

The half-life of RAB18 localization under basal conditions was determined to be 11 seconds. No significant differences in half-life could be detected after supplementation with the vehicle control. After supplementation with OA the RAB18 localization half-life was found to be increased, but no statistical significance could be detected. Treatment with the solvent did not change RAB18 half-live under basal conditions and incubation with the vehicle. However, after supplementation of OA, treatment with the solvent significantly increased RAB18 half-life compared to untreated cells. Inhibition of de-palmitoylation with palmostatin B treatment was found to increase the average half-life to approximately 18 seconds under basal condition. This was not observed after vehicle or OA supplementation. Instead RAB18 half-life was detected at approximately the same level as the solvent. Inhibition of palmitoylation with 2-BP was detected to not alter the half-life of RAB18 under basal condition or after vehicle supplementation. However, after OA supplementation, the mean half-life of RAB18 was detected significantly reduced in HepG2 cells treated with 2-BP, when compared to solvent treated cells (Figure 9D).

In summary, under basal conditions, inhibition of de-palmitoylation increased both mobile fraction and localization half-life, yet no changes were observed after OA supplementation. In contrast, inhibition of palmitoylation did not cause changes under basal conditions, but increased the mobile fraction and decreased half-life after OA supplementation.

4.2. RAB18's role in LD size regulation

4.2.1. Validation of the *StarDist* algorithm for LD segmentation

Before investigating the effects of RAB18 on LD size, a precise method to measure LD size had to be established. Manual segmentation, although considered the gold standard, was slow, therefore, an accurate automatic approach was needed for high throughput analysis.

Two key problems arose concerning automatic LD segmentation: the variability of signal within large droplets and the tendency of LDs to form large clusters. When using an intensity-based thresholding approach, these LD properties resulted in the detection of a large number of either false negatives or false positives, depending on the chosen threshold. This problem is similar to the segmentation of the much larger nuclei. Nuclei staining also display large internal intensity variance as well as a tendency to cluster and overlay. Recently the machine learning algorithm *StarDist* was published to solve this issue for nuclei (Schmidt et al., 2018). The proposed solution to the challenges, which arise for nuclei segmentation, is to map star-shaped polygons onto foreground objects to detect their borders. In a second step, overlapping polygons are removed by Non-Maximum-Suppression. Since the difference between LD and nuclei segmentation appeared to be merely in size, the application of *StarDist* algorithm to LD segmentation was therefore evaluated (Figure 10A).

The parameters for *StarDist* segmentation are established by machine learning as so-called models. Following the pipeline provided by the developers, two different models were trained for the two different LD detection methods used in this thesis. One model was trained with 34 images containing a total of 2635 manually annotated LDs detected with BODIPY 493/503 staining. The other was trained with 10 images containing 8051 manual annotated LDs detected with CARS imaging. Both models were first evaluated using the diagnostics given within the supplied pipeline until a precision of over 80% was achieved. They were then tested against a manually annotated test set not used in the machine learning (Figure 10B).

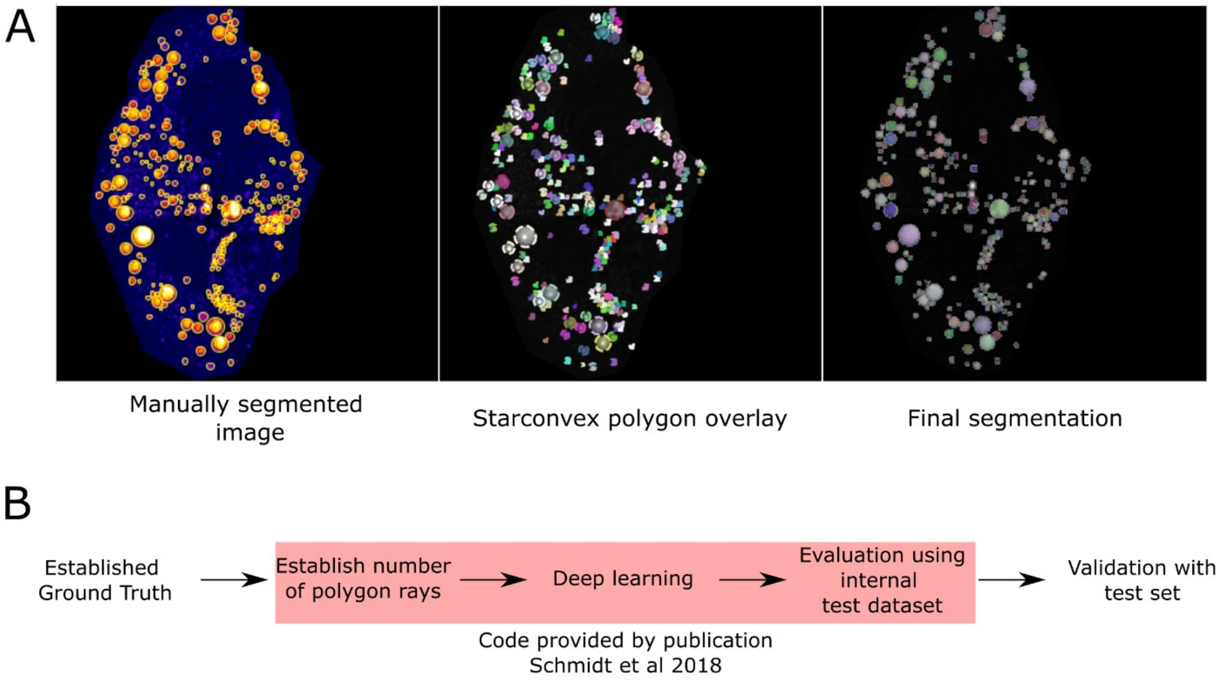

Figure 10 | StarDist algorithm

Comparison of a manually segmented image with the same image overlayed with star-convex polygons predicted by the *StarDist* machine learning algorithm and the resulting automatic segmentation (**A**). The parameters were established by training with manually annotated images of LDs stained with BODIPY 493/503 or imaged directly with CARS. During training the images were run through the code supplied by precision Schmidt et al. (red box) following the developer's instruction (**B**).

The resulting BODIPY model was tested against six data sets not used for training the model. Three sets contained images of cells without LD accumulation, the other three contained images after OA supplementation. Each test-set contained of three manually annotated experiments of LDs larger than 1 µm^2 that were treated as Ground Truth. LDs were segmented using *StarDist* to measure LD areas and compared to the manual annotation. The BODIPY model failed to detect the same amount of LD as manual annotation. In cells without LD accumulation, the *StarDist* model detected on average only 1/3 of the LDs. Post LD accumulation 78% of manually detected LDs were also detected by the algorithm. The large number of false negatives did not influence the estimated mean LD area, which was on average only 5% smaller than the mean of manual annotation in cells without LD accumulation. Comparing automatically and manually segmented images of HepG2 cells after OA supplementation showed that the mean area obtained by the algorithm was on average 4% larger than the one gained by manual annotation. (Figure 11A).

For investigating the size distribution, a cumulative histogram of all LDs between the sizes 1 µm^2 and 8 µm^2 was created. Both the hand annotated and automatically segmented LDs detected in cells post LD accumulation were compared with each other. Differences were only detected in the frequency of small LDs below an area of 3 µm^2. The fraction of these LD was slightly overestimated in comparison to the manual annotated ground truth, which indicates that the automatic segmentation underestimated the number or the size of the larger LDs (Figure 11A).

The model for segmenting LD imaged with CARS was tested against eight test sets, which comprised CARS images of HepG2 cells after OA supplementation for 24h and were manually annotated without an area threshold. The *StarDist* model correctly predicted the LD number, overestimating the LD number and mean area by an average 6%. The calculation of a cumulative histogram of the LD size distribution revealed next to no changes in the mean size distribution. Thus, both models were within an error range of approximately 5% which was deemed sufficient for further use in the detection of LDs (Figure 11B).

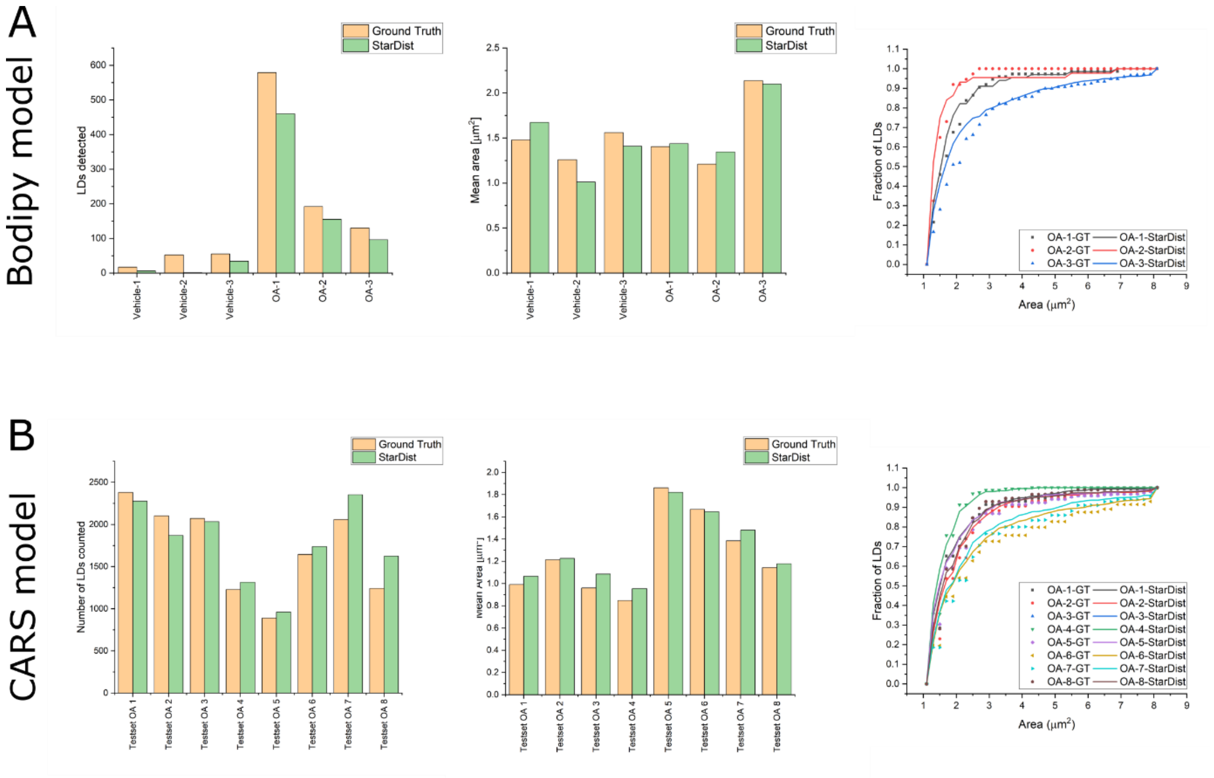

Figure 11 | Validation of models trained with the *StarDist* algorithm

The model for BODIPY 493/503 stained LD was tested against 6 Ground Truth test sets consisted of images in which LDs above 1µm² were manually segmented. Three test sets contained images with cells after OA induced LD accumulation and the other three contained images of cells without LD accumulation. LD number and mean area were quantified with *StarDist* and compared to the Ground Truth. A cumulative frequency count was calculated for LDs detected in the range between 1µm² and 8µm² with a bin-size of 0.2µm² and normalized to maximum LD count. The Ground truth (scatterplot) was overlayed with the *StarDist* derived cumulative histogram (lines) **(A)**. The CARS model was tested against 8 Ground Truth test sets of manually annotated LDs without an area threshold. LD number, area and size distribution were compared analogous to A **(B).**

4.2.2. Inhibition of RAB18's palmitoylation cycle changes LD size

With a consistent method for automatic LD size evaluation established, the effect of inhibiting the (de-) palmitoylation of RAB18 on LD size was investigated next. Analogous to 4.1.3, palmitoylation was inhibited with 2-BP, whereas de-palmitoylation was inhibited using palmostatin B. HepG2 cells were treated with either of these inhibitors or DMSO as solvent control and subsequently supplemented with OA for 24h to induce the formation of LDs. After the incubation, the LDs were stained with BODIPY and their size was automatically quantified using *StarDist* (Figure 12).

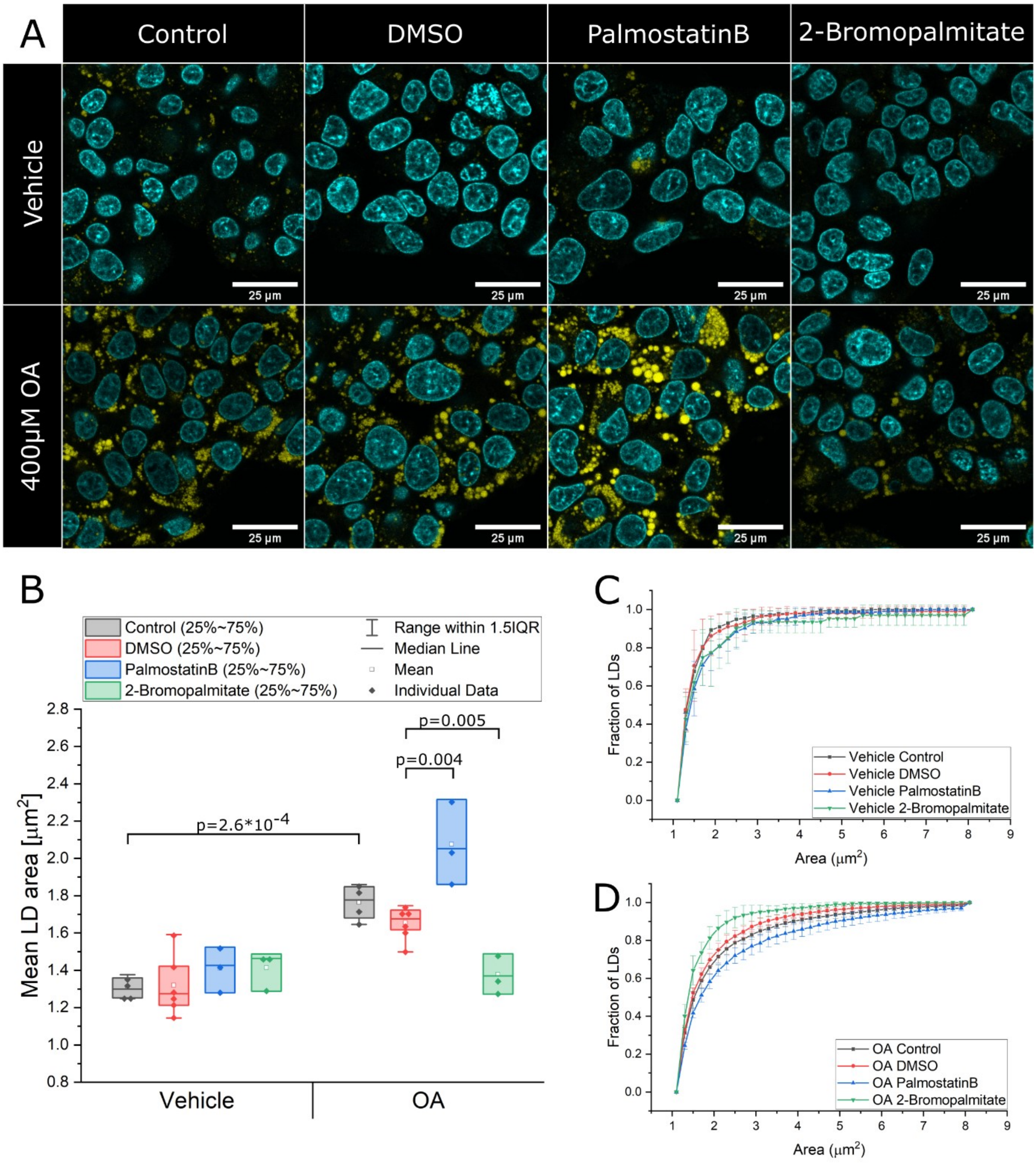

Figure 12 | Effect of (de-)palmitoylation inhibition on LD size

Representative confocal images of HepG2 cells after simultaneous treatment with either 50 µM 2-bromopalmitate or 100 µM palmostatin B and OA for 24h. BSA serves as vehicle control for OA and DMSO as solvent control for the inhibitors. LDs were stained with BODIPY 493/503 (yellow) and Nuclei with Hoechst (cyan) **(A)**. LDs were segmented with *StarDist* algorithm and LD area of LD larger than 1 μm^2 was quantified. Mean area was calculated per experiment and depicted as boxplot (**B**). A cumulative frequency count of LDs between 1 μm^2 and 8 μm^2 with a bin size of 0.2 μm^2 was calculated and normalized to maximum count. The mean of 3 experiments' histograms treated with vehicle control (**C**) and OA (**D**) were plotted. The error bars represent the standard deviation. Statistical significance was calculated with a two-sample t-test. P-values if found below 0.05 are depicted over the boxplot. N=3

The mean LD area in HepG2 cells was found to be significantly larger with OA supplementation than without OA supplementation. Despite having shown an effect on RAB18 localization (4.1.3) the solvent did not significantly change the mean LD area in HepG2 cells with and without OA supplementation. Without OA supplementation, the mean LD area was not observed to be altered by inhibiting palmitoylation or de-palmitoylation. However, after OA supplementation, inhibition of de-palmitoylation resulted in a significant increase of mean LD area compared to the solvent control. In contrast to this, the inhibition of palmitoylation reverted the effect of OA supplementation, causing the mean LD area to significantly decrease to the area detected in HepG2 cells without OA supplementation (Figure 12B).

The LD size distribution was determined to analyze the cellular LD population. In HepG2 cells without OA supplementation, over 80% of all LD above 1 μm^2 were between 1 and 2 μm^2. The inhibition of (de-)palmitoylation did not affect this distribution (Figure 12C). In HepG2 cells with OA supplementation, a strong shift towards larger LDs was detected, mirroring the increase in mean LD area. In untreated and solvent treated cells only 65-70% of detected LDs were in the 1-2 μm^2 range and 10% of the LD were found between 2-4 μm^2. Inhibition of de-palmitoylation further shifted the distribution towards larger LDs, with 60% of all LDs having an area of 1-2 μm^2 and 20% an area between 2-4 μm^2. In contrast to this 2-BP treated cells only developed smaller LDs. About 80% of the LDs detected were found in the 1-2μm^2 range, which was comparable to the vehicle treated cells (Figure 12D).

In summary, inhibition of de-palmitoylation increased the mean LD area after OA supplementation, whilst inhibition of palmitoylation decreased the mean LD area.

4.2.1. RAB18 downregulation leads to increased LD size

In the previous section, the palmitoylation state of RAB18 was shown to affect the LD area, which indicates that RAB18 regulates LD size in HepG2 cells. Based on this and published data for RAB18, it was therefore hypothesized that the depletion of RAB18 resulted in the increase of LD size in HepG2. To test this hypothesis, endogenous RAB18 was depleted via a siRNA mediated knockdown in HepG2 cells. First, an effective knockdown needed to be established, so HepG2 cells were transfected with three RAB18 targeting siRNA sequences and their effect on the RAB18 protein levels was evaluated using western blotting (Figure 13A). One siRNA reduced the RAB18 protein level by over 90% compared with vehicle control after 72h (Figure 13B).

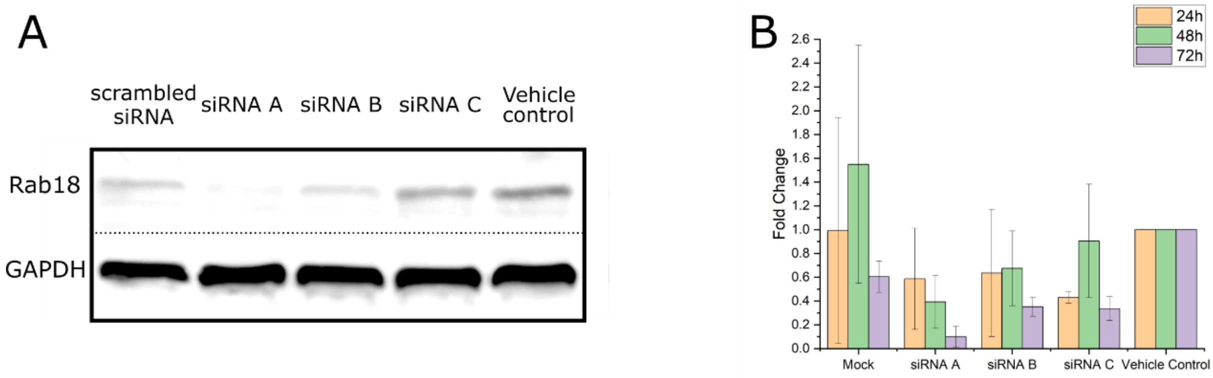

Figure 13 | Establishing RAB18 knock down

Scramble RNA and three RAB18 siRNA were transfected into HepG2. RAB18 protein levels were detected by western blotting 72h post transfection with GAPDH serving as loading control (**A**). Protein lysates were taken at 24h-72h and RAB18 level was determined by western blot. Blots were analysed with FIJI and normalized to GAPDH loading control. Normalized RAB18 levels were divided by RAB18 levels of un-transfected vehicle control (**B**). N=3

After establishing the RAB18 knockdown (RAB18 KD) at 72h post siRNA transfection, an experimental template was devised to investigate the function of RAB18 on LD development. HepG2 cells were transfected with scrambled siRNA and RAB18 targeting siRNA and incubated until maximum RAB18 downregulation was reached after 72h. The long incubation time between siRNA transfection and downregulation allowed for the co-transfection of plasmids as well as small molecule inhibitor pre-treatment. At 72h the HepG2 cells were supplemented with OA to induce the formation of LD, which subsequentially could be identified and quantified via imaging (Figure 14).

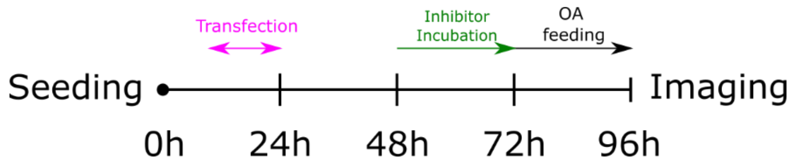

Figure 14 | Experimental template for RAB18 downregulation

The late time point of RAB18 downregulation opens widows to enhance the basic siRNA mediated RAB18 downregulation experiment (black). Transfection (magenta) conducted from 8h to 24h post transfection could be used to transfect reporter proteins. Cells could also be pre-treated with small molecule inhibitors right up to the feeding with OA at 72h (green).

Following this experimental template, the effect of OA supplementation on the LD size after RAB18 downregulation was investigated first. At the 72h timepoint, the HepG2 cells were supplemented with OA and BODIPY. After supplementation, the HepG2 cells were imaged for over 20h, following the formation of LD stained with BODIPY. In cells without RAB18 KD, OA induction resulted in a rapid increase of LD number during the first few hours of the experiment. This was followed up by a slow consolidation of smaller LDs into larger LDs as the experiments progressed (Figure 15).

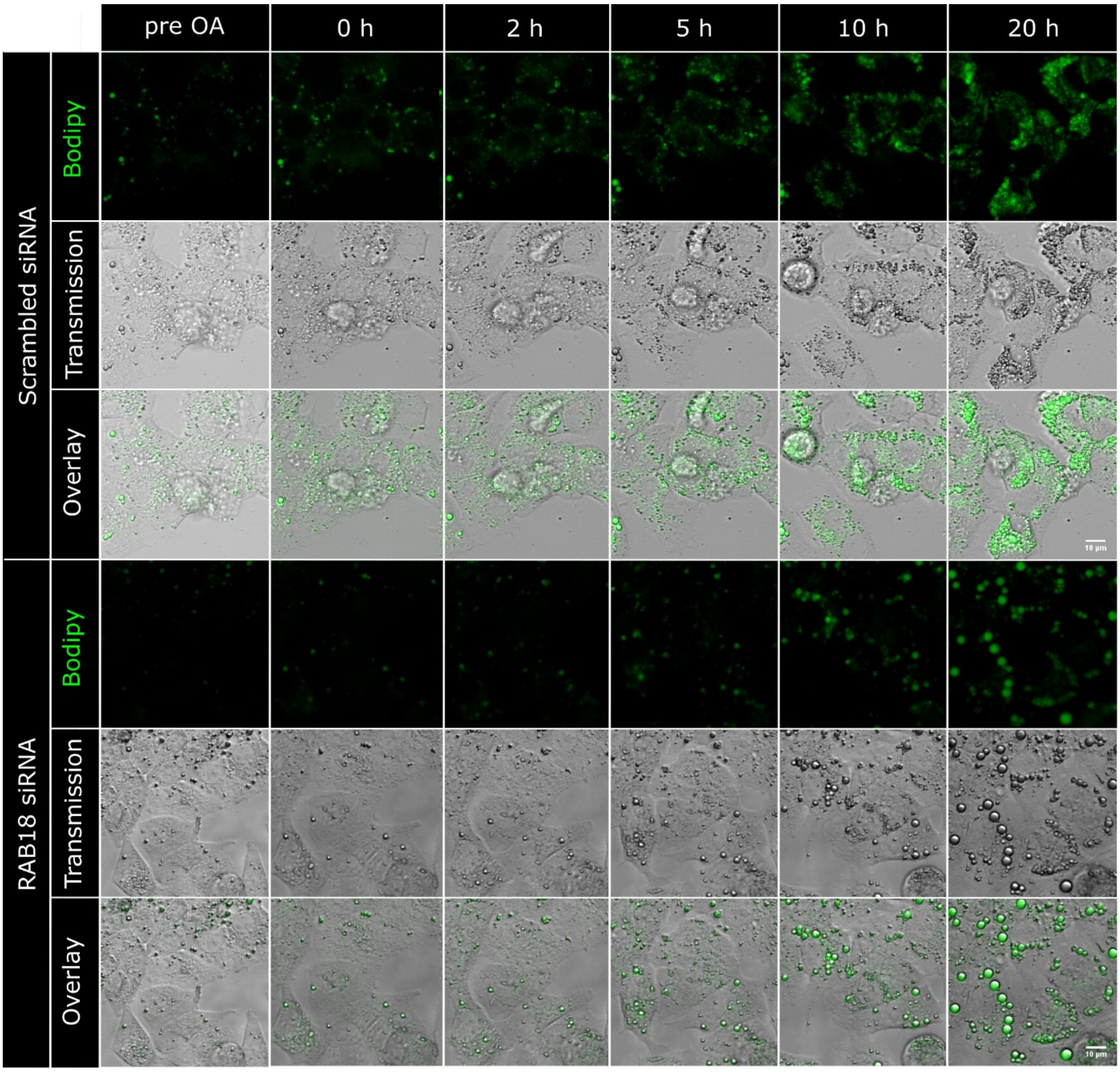

Figure 15 | RAB18 downregulation causes increased LD area

Time series of HepG2 cells transfected with scrambled and RAB18 targeting siRNA. To induce LD growth, cells were supplemented with OA. The LDs were identified by BODIPY (green) staining. After OA supplementation, an increase in LD size and a simultaneous decrease of LD number in cells with RAB18 downregulation compared to cells without RAB18 downregulation.

Upon OA supplementation less LDs were formed in HepG2 cells with RAB18 KD than in cells without RAB18 KD. Instead, the few remaining LDs in the cells increased their size over the course of the experiment. If small LDs were detected in HepG2 cells with RAB18 KD, they were observed to fuse with the larger LDs. Consequently, LDs in HepG2 cells with RAB18 KD had comparable fewer, but larger LDs than cells without downregulation after 20h (Figure 15).

In summary, whilst HepG2 cells without RAB18 KD form numerous small LDs upon OA supplementation, HepG2 cells with RAB18 KD form fewer larger LDs displaying a distinct RAB18 KD phenotype. It is thus concluded that the function of RAB18 is to prevent the LD size increase and increase the LD number.

4.2.2. WT LD-distribution is only rescued by localizing RAB18 mutants

After establishing the RAB18 KD phenotype, it was investigated whether the RAB18 mutants created in section 4.1.1 could influence LD size in HepG2 cells with and without RAB18 KD. Following the experimental template (Figure 14), HepG2 cells were transfected with siRNA before being co-transfected with different RAB18 reporter plasmids. and the FusionRed vector backbone as a negative control. At the 72h time point, the HepG2 cells were supplemented with OA to induce LD formation for 20h. After OA supplementation, the LDs were stained with BODIPY and transfected cells were imaged. The LDs in transfected cells were then manually quantified to ensure optimal precision (Figure 16 & 17).

In HepG2 cells without RAB18 KD, which were transfected with the vector backbone, 70-80% of the LDs had an area below 2µm^2. Compared to cells transfected with the vector, transfection with the RAB18, PolyC or Q67L did not change this size distribution. Therefore, it was concluded, that without RAB18 downregulation the overexpression of RAB18 did not affect LD size in HepG2 cells (Figure 16B). The downregulation of RAB18 in HepG2 cells resulted in enlarged LDs after OA supplementation, replicating the phenotype described in 4.2.1. In HepG2 cells with RAB18 KD, which were transfected with the vector backbone, only about 50% of the LDs had an area smaller than 2 µm^2 in cells. However, in HepG2 cells with RAB18 KD, which overexpressed RAB18, PolyC or Q67L, 70%-80% of the LDs had an area below 2 µm^2. Since all of these mutants localize to the LD it was concluded that WT RAB18 and RAB18 mutants which localize to the LD prevented the increase in LDs size, which rescued the RAB18 KD (Figure 16C).

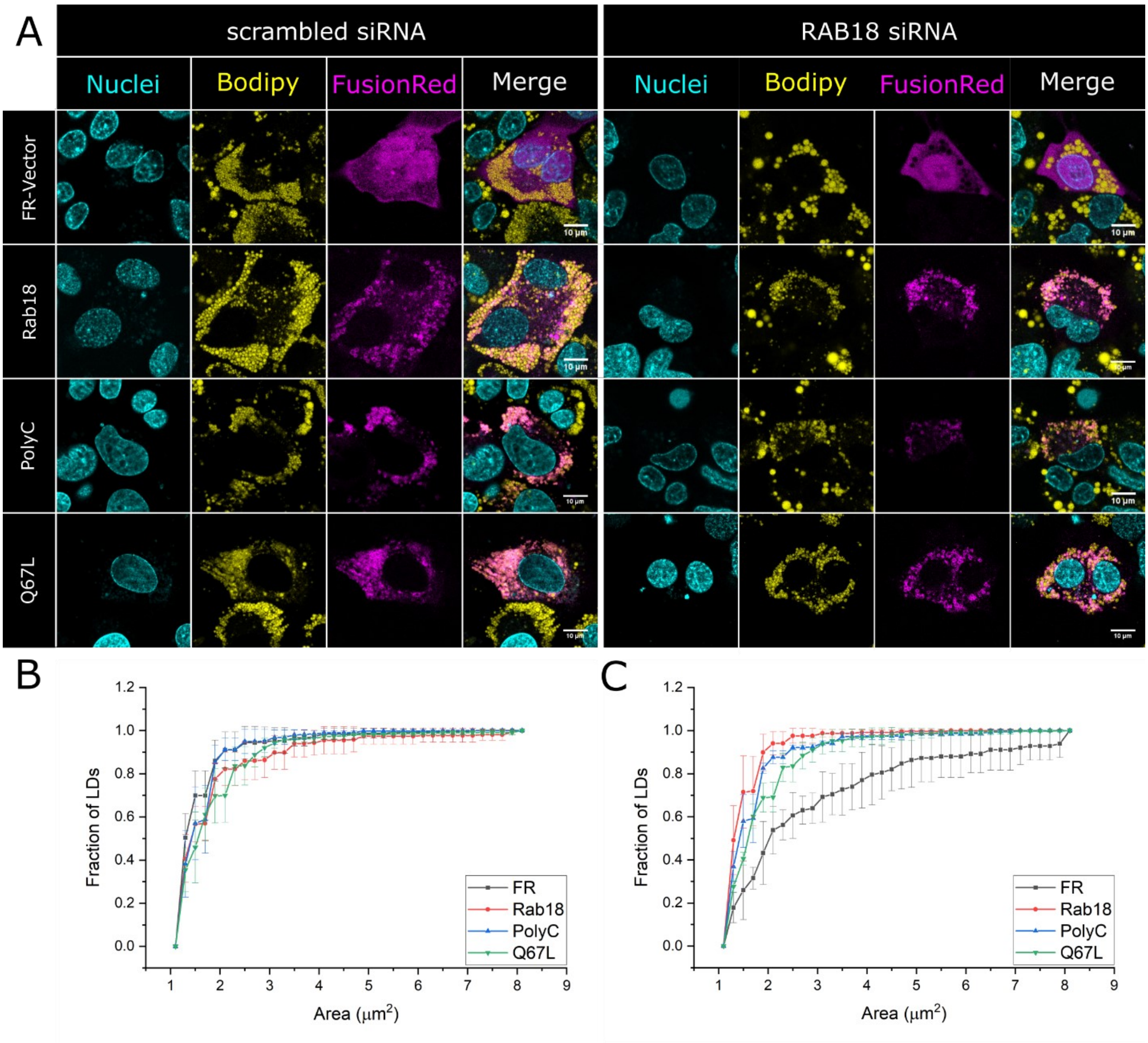

Figure 16 | Localizing RAB18 variants rescue LD size distribution in RAB18 KD cells

Representative images of HepG2 cells transfected with localizing FusionRed-RAB18 variants (Magenta) after transfection of random scrambled RNA or RAB18 siRNA. LD growth was induced 72 h post siRNA transfection for 20 h. LDs were stained with BODIPY493/503 (Yellow) nuclei with Hoechst (Cyan) (**A**). LDs were manually segmented in FIJI for five cells per experiment. Only LDs above a 1 µm² threshold were quantified and a cumulative frequency count of the LD area in HepG2 cells without (**B**) and with RAB18 KD (**C**) was calculated. Curves represent the mean of 3 experiments bars represent the standard deviation. N=3, n≥5

The overexpression of mis-localizing RAB18 mutants, even the dominant negative mutant S22N, did not affect LD size in HepG2 cells without RAB18 KD. After the transfection with any mis-localizing mutant, the small LD population between 1 and 2 μm^2 remained the dominant population. About 60-70% of total LDs were detected in that size range, which indicates, that the assumed dominant negative mutant is only an inactive mutant in HepG2 cells (Figure 17B).

In HepG2s with RAB18 KD overexpression of the inactive S22N and its double mutant S22N-C199S did not rescue the RAB18 KD. Instead, HepG2 cells with RAB18 KD transfected with S22N or S22N-C199S showed a LD size distribution similar to cells transfected with only the vector backbone. Transfection of the mis-localizing C199S, Q67l-C199S and the ER bound RAB18-SEC61b also failed to prevent the increase in LD size and thus did not rescue the LD size distribution in cells with RAB18 KD. The same result could be observed after overexpressing C203S, which mis-localized to the cytoplasm. Therefore, it was concluded that mis-localizing RAB18 mutants are unable to rescue the RAB18 KD in HepG2 cells (Figure 17C).

In summary, only transfection with RAB18 or active RAB18 mutants, which localize to the LD, prevented the formation of enlarged LDs in HepG2 cells with RAB18 KD and thus rescues the RAB18 KD. The transfection of mis-localizing RAB18 mutants did not affect the formation of enlarged LDs in HepG2 cells with RAB18 KD. Therefore, it is the activity of RAB18 on the droplet which is preventing the LD size increase.

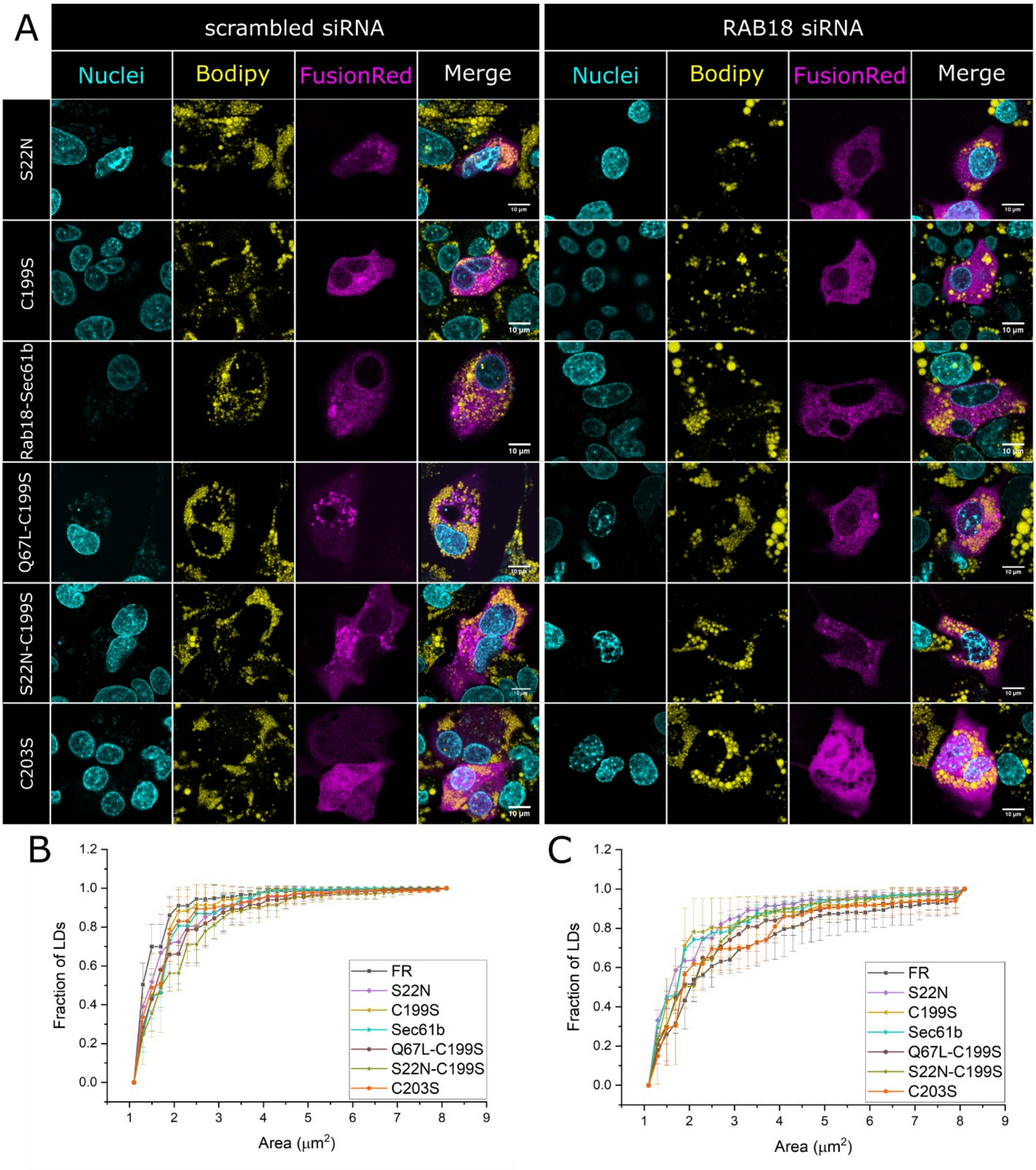

Figure 17 | Mis-localizing RAB18 variants cannot rescue LD size distribution in cells with RAB18 KD

Representative images of HepG2 cells transfected with mis-localizing FusionRed-RAB18 variants (Magenta) after transfection of random scrambled RNA or siRNA. LD growth was induced 72h post siRNA transfection for 20h. LDs were stained with BODIPY493/503 (Yellow) nuclei with Hoechst (Cyan) (**A**). LDs of five cells per experiment were manually segmented in FIJI. Only LDs above a 1 μm^2 threshold were quantified and a cumulative frequency count of the LD area in HepG2 cells without (**B**) and with RAB18 KD (**C**) was calculated. Curves represent the mean of 3 experiments bars represent the standard deviation. N=3, n≥5

4.3. RAB18 downregulation phenotype is linked to autophagy

4.3.1. Inhibition of lipophagy reverts the LD size increase in HepG2 with RAB18 downregulation

In the previous chapter, it could be shown that RAB18 localization to the LD membrane reduces the LD size preventing the increase of LD size. This size reducing function of RAB18 has been previously ascribed to two fundamental cellular mechanisms: on the one hand lipolysis which gradually digest the LDs' TAG content; on the other, the removal of LDs via lipophagy, which is a special form of autophagy. To test which of these mechanisms was linked to the function of RAB18 in HepG2 cells, small molecule inhibitors were used to inhibit both processes. atglistatin, which inhibits ATGL, was used to inhibit lipolysis, whilst lalistat2, which inhibits the lysosomal acid lipase (LAL), was used to inhibit lipophagy. Following the basic experimental template for RAB18 KD (Figure 14), HepG2 cells were transfected with scrambled and RAB18 siRNA. After 48h lipolysis or lipophagy were inhibited for 24h, before the medium was supplemented with OA to induce the formation of LDs. After 24h incubation with OA, the effect of the inhibition on the LD size was subsequently measured using Coherent Anti-Stokes Raman Spectroscopy (CARS).

CARS is a novel imaging method which uses the specific vibrational properties of sub-molecular structure to create contrast. This native imaging comes with a row of advantages such as the independence from the lipid dyes and avoidance of photobleaching. In the following experiments the specific vibration of C-H bond stretches at 2847 cm^{-1}, which are mainly prevalent in lipids, were used to detect LDs. By detecting lipids instead of hydrophobic compartments stained by BODIPY, a higher specificity towards LDs was achieved. This was deemed important for the correct evaluation of LD formation after the inhibition of lipophagy, which may cause the accumulation of hydrophobic autophagosomes.

The inhibition of lipolysis with atglistatin prior to OA supplementation did not show any effect on the LD size in HepG2s transfected with scrambled siRNA after OA supplementation. In cells transfected with RAB18 siRNA the LD size distribution showed an increase fraction of enlarge LDs post OA supplementation replicating the RAB18 KD phenotype. Inhibition of autophagy with atglistatin prior to OA supplementation did not alter the LD size distribution in cells with RAB18 KD. Since the inhibition of lipolysis did not affect the LD size in cells with and without RAB18, it is concluded that lipolysis does not play a role in the function of RAB18 (Figure 18 A&B).

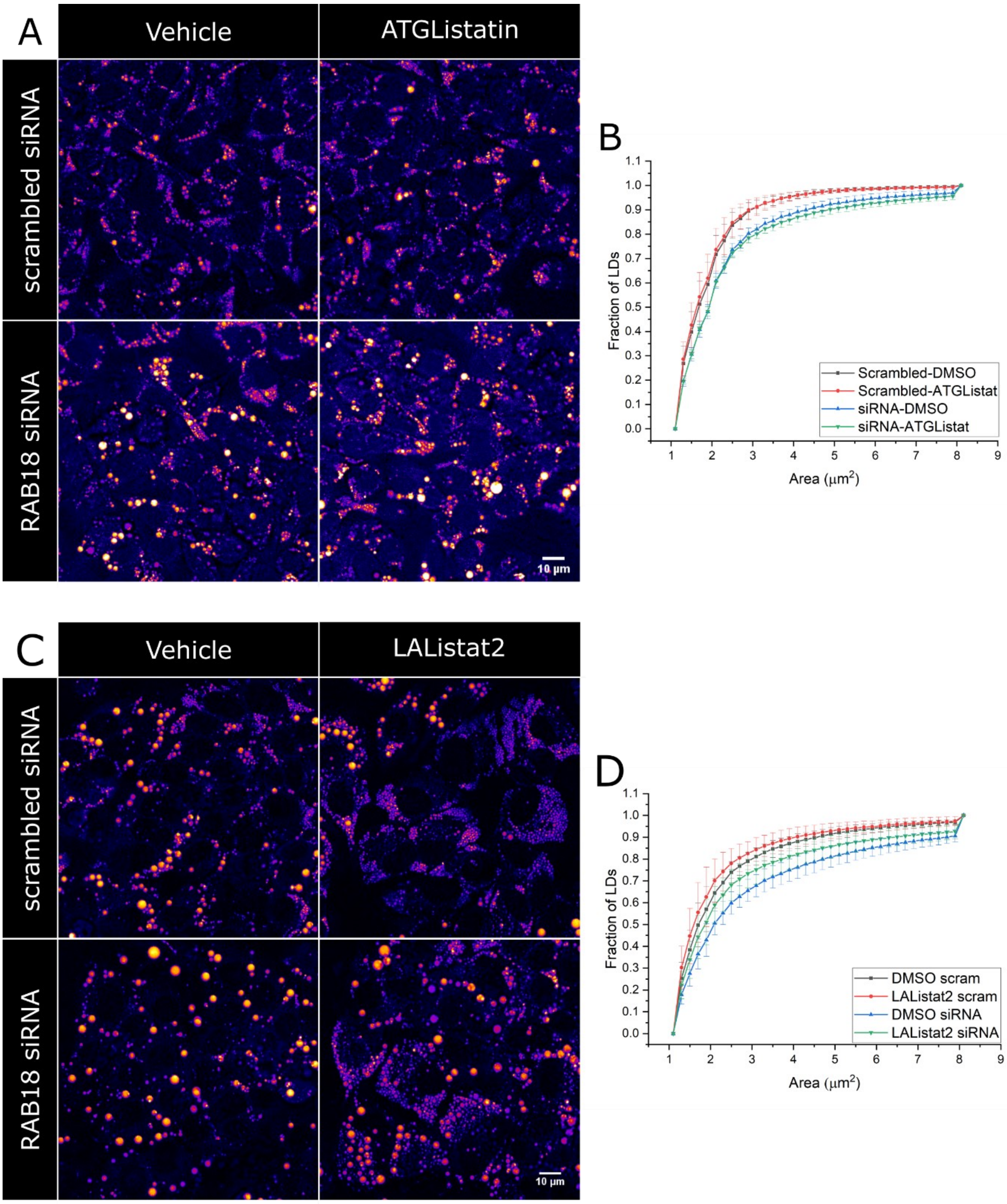

Figure 18 | Inhibition of lipophagy and not lipolysis rescues the LD size in HepG2 with RAB18 downregulation

Exemplary confocal CARS images of cells were treated with 50 µM atglistatin (**A**) or 50 µM lalistat2(**C**) 48 h post siRNA transfection. After 24 h incubation with either inhibitor, LD formation was induced for 24h. Lipids in the cells were consecutively imaged using CARS at 2847 cm^{-1} by enhancing C-H-bond stretches. LDs were automatically segmented using a trained model and the *StarDist* algorithm. LDs below a 1 μm^2 threshold were not considered. LD area was quantified and a cumulative frequency count with a bin size of 0.2μm^2 calculated. Curve displays mean cumulative histogram of atglistatin (**B**) and lalistat2 (**D**) pre-treated cells. Error bars represent standard deviation. N≥3.

The inhibition of lipophagy with lalistat2 resulted in an increase of small LDs in HepG2 cells transfected with scrambled siRNA after OA supplementation. The Inhibition of lipophagy also resulted in the formation of LDs smaller than 3µm^2 in cells transfected with RAB18 siRNA and hifted the LD size distribution towards smaller LDs in cells with RAB18 KD. Although only a partial reversion of the RAB18 KD phenotype was achieved by lalistat2 inhibition, it was thus concluded that the LD size increased observed after RAB18 KD was linked to lipophagy and not lipolysis (Figure 18C&D).

4.3.2. Immunofluorescence staining shows an increased autophagosome formation in RAB18 KD HepG2

Since the inhibition of lipophagy was demonstrated to reduce the LD area in HepG2 cells with RAB18 KD, it was surmised that autophagy would be elevated in these cells. Autophagy is marked by the local accumulation of the protein LC3B which catalyses the formation of autophagosomes. Therefore, highly localized LC3B concentrations, called *punctae,* are deemed to be a marker of autophagosome formation. Thus, LC3B was detected via immunostaining to detect LC3B *punctae* to investigate the state of autophagy in HepG2 cells with RAB18 KD.

HepG2 cells were transfected with scrambled and RAB18 targeting siRNA and supplemented with OA after 72h incubation according to the experiment template (Figure 14). To further elucidate the connection between autophagy and RAB18 KD, HepG2 cells with and without RAB18 KD were additionally pre-treated with either of the two activators of autophagy rapamycin and torin2 or the autophagy inhibitor chloroquine for 24h before OA supplementation. After the OA supplementation, the HepG2 cells were fixed and permeabilized, before LC3B was detected by immunostaining (Figure 19A).

The number of LC3B punctae per cell was quantified and significantly more LC3B *punctae* were formed in HepG2 cells with RAB18 KD than in HepG2 cells without RAB18 KD. This indicates that in cells with RAB18 KD autophagy is increased. Oddly, the treatment with the autophagy activator rapamycin did not result in an increase in LC3B *punctae* compared to untreated cells. This indicates that rapamycin treatment might not have activated autophagy. Treatment with torin2 lead to a slight, but not statistically significant increase in LC3B *punctae* in cells with and without RAB18 KD, implying a weak activation of autophagy. Chloroquine has been reported to block autophagy by inhibiting the fusion of autophagosomes with the lysosome (Mauthe et al., 2018). Treatment with it resulted in a significant increase in LC3B *punctae* mirroring the accumulation of autophagosomes. However, no difference could be detected between cells with and without RAB18 KD after Chloroquine treatment (Figure 19B).

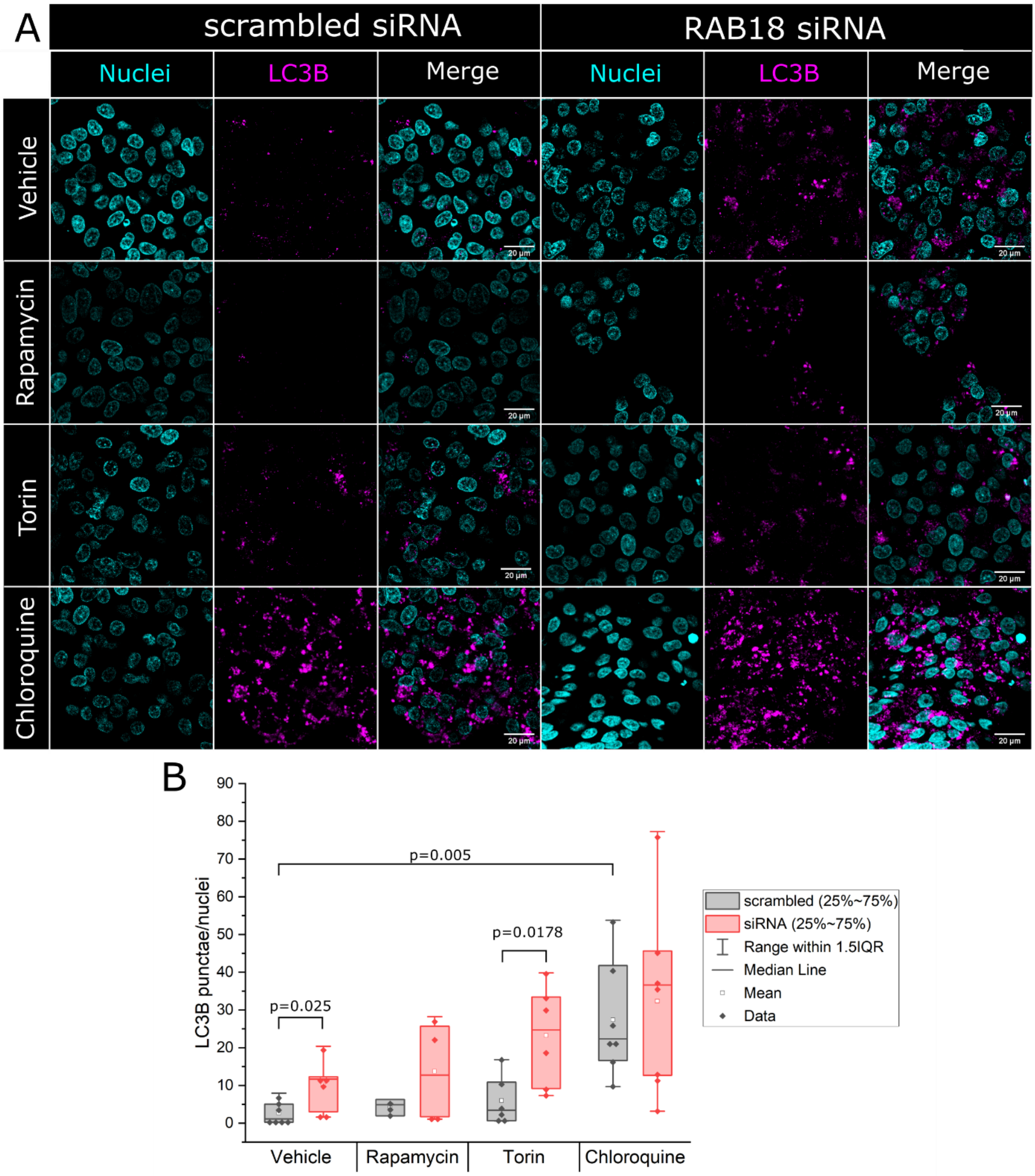

Figure 19 | RAB18 KD results in LC3B *punctae* increase

Representative confocal images of cells stained for LC3B (magenta). Cells were fixed 96h after transfection with siRNA and 24h post LD accumulation. Nuclei were stained with DAPI (Cyan). LC3B *punctae* were detected via immunostaining. Cells treated with Chloroquine 20µM for 24h before the 72h timepoint were used as positive control. DMSO served as solvent control (**A**). LC3B punctae were quantified and normalized to nuclei count (**B**). N≥3. Statistics were calculated using two-sample t-test. P-values below 0.05 are indicated above the boxplots.

In summary, RAB18 KD results in the accumulation of LC3B *punctae* and thus the number of autophagosomes in HepG2 cells. However, this accumulation can be offset by blocking autophagy.

4.3.1. Western blot analysis reveals no changes in LC3B2 protein level and autophagic flux

After establishing the accumulation of LC3B *punctae* via immunostaining, the LC3B protein levels in RAB18 KD were determined by western blot. LC3B1 is lipidated after autophagy induction to form LC3B2, which is why the LC3B2 levels can be used as an autophagy marker. To evaluate the effect of RAB18 KD on LC3B2 protein level cells were transfected with siRNA or were mock transfected following the established experimental template (Figure 14). As a positive control cells were treated with chloroquine for 24h, before LD formation was induced with OA supplementation 72h post siRNA transfection. Cells were lysed pre-and post OA supplementation and their LC3B2 protein levels were detected via western blot (Figure 20A).

Before OA supplementation, only low levels of LC3B2 were detected in scrambled, RAB18 siRNA or mock transfected cells. Inhibition of autophagy with chloroquine resulted in the significant accumulation of LC3B2. After OA supplementation, LC3B2 levels did not differ from the LC3B2 levels before OA supplementation. The inhibition of autophagy also resulted in a significant increase in LC3B2 after OA supplementation, mirroring the accumulation of autophagosomes detected in 4.3.2. In all of these conditions, no significant differences in the LC3B2 levels were detected between scrambled, RAB18 siRNA and mock transfected cells. (Figure 20B).

The amount of LC3B2 protein in cells depends not only on the conversion of LC3B1 but also on the expression of LC3B. To gain insight into the conversion rate of LC3B1 to LC3B2, the ratio of LC3B2 to total LC3B was calculated. Without the supplementation of OA, the fraction of LC3B2 in HepG2 cells transfected with scramble and RAB18 siRNA was found slightly, but not statistically significantly, increased compared to mock transfected cells. Inhibition of autophagy with Chloroquine resulted in a strong increase in LC3B2 conversion, yet no difference between scrambled, RAB18 siRNA or mock transfected cells were detected. After supplementation of OA there was a slight increase of the fraction of LC3B2 levels in cells transfected with RAB18 siRNA when compared to cells transfected with scrambled siRNA or mock transfection. However, this shift was also not statistically significant. Inhibition of autophagy with chloroquine resulted in a significant accumulation of LC3B2 with nearly all LC3B detected being LC3B2. No differences between the ratios in scrambled, RAB18 siRNA and mock transfected cells was detected after inhibition with chloroquine and OA supplementation (Figure 20C).

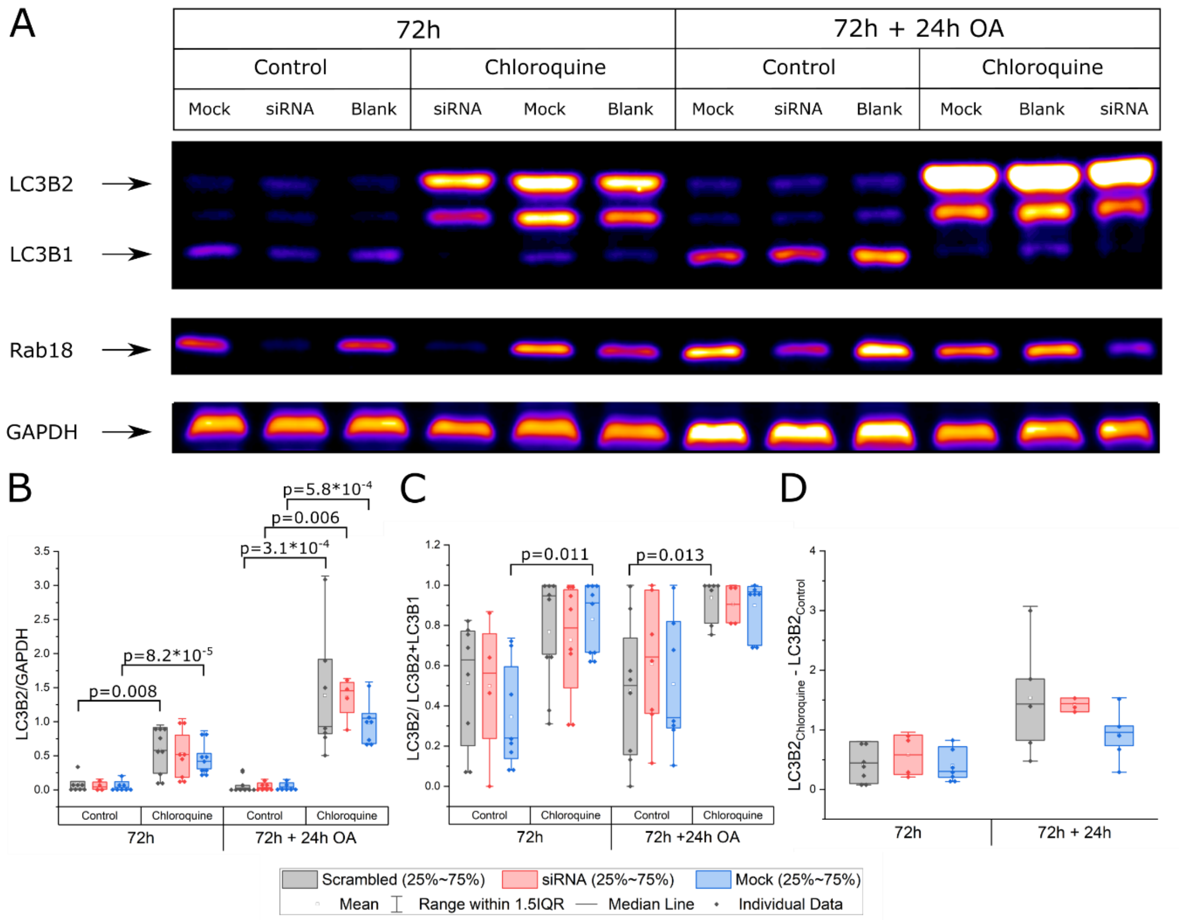

Figure 20 | LC3B2 detection by western blot

RAB18 KD (siRNA) and WT (scram) cells were lysed pre and post LD accumulation with OA. LC3B and RAB18 protein levels were detected via western blot (**A**). The LC3B2 level were evaluated in FIJI and normalized to the GAPDH loading control (**B**). The conversion rate of LC3B1 to LC3B2 was calculated by dividing the amount of LC3B2 by total amount of LC3B protein Autophagic flux was calculated by subtracting LC3B protein levels without autophagy inhibition from autophagy inhibition with chloroquine. (**C**). Statistical testing was done using the Kolmogorov-Smirnov test. N≥3

Finally, the autophagic flux was calculated by subtracting the LC3B2 level of HepG2 cells without autophagy inhibition from the LC3B2 levels detected in HepG2 cells with inhibition of autophagy by chloroquine. Before OA supplementation, the autophagic flux was found elevated in HepG2 in cells transfected with RAB18 siRNA cells, but no statistically significant differences could be established compared to mock and scrambled transfected cells. After OA supplementation, the autophagic flux of cells transfected with either scrambled or RAB18 siRNA was found to be higher than in mock transfected cells. However, again no statistically significant difference was detected (Figure 20 D).

In summary, LC3B2 levels and autophagic flux in cells with RAB18 KD were not significantly different from the levels of cells without RAB18 KD. This indicates that RAB18 does not directly influence autophagy in HepG2 cells.

4.3.2. Autophagy sensor plasmid shows increased autophagosomes formation, but no changes in autophagic flux in cells with RAB18 KD

Since the LC3B immunostainings revealed an increased number of autophagosomes, but the western blots showed no increase in autophagic flux the link between RAB18 and autophagy remained ambiguous. Thus, to gain further insight into the connection between RAB18 and autophagy, both autophagosome number and autophagy rate were investigated in live cells using an LC3B reporter plasmid, created and gifted by Isei Tanida (Tanida et al., 2014).

This reporter plasmid expresses a fusion protein, which consists of a super-ecliptic pHluorin, mKate2 and LC3B (Figure 21A). When expressed, the LC3B localizes to early autophagosome, where it can be detected by the fluorescent signal of the fused pHluorin GFP's and the far-red mKate2. However, super-ecliptic pHluorin is an acid sensitive GFP mutant. Thus, when the pH decreases after the fusion of the autophagosome with the lysosomes the super-ecliptic pHluorin bleaches. As a consequence, late stage autophagolysosomes, in the following referred to as lysosomes, can only be detected by their mKate2 signal, but not by their pHluorin signal. Thus, the fraction of lysosomes to autophagosomes can be used as a relative measure of autophagic flux (Figure 21B).

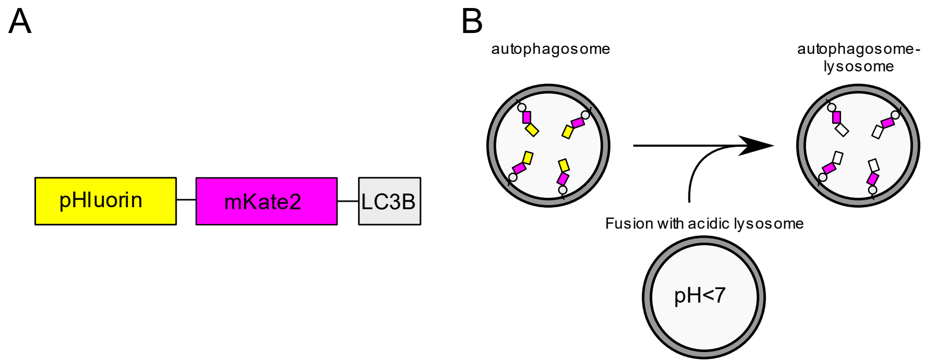

Figure 21 | Mechanism of the pHluorin based autophagy sensor

Scheme represents the LC3B fusion protein used to detect autophagy (**A**). This fusion protein localizes to autophagosome and can be detected by the pHluorin signal as well as mKate2. Fusion of the autophagosome with the acidic lysosome bleaches the pHluorin, thus autophago-lysosomes can only be detected by the mKate2 signal (**B**).

First, the pHluorin sensor's response to the established experimental template (Figure 14) was tested without transfection of siRNA. HepG2 cells were transfected with the sensor and autophagy was inhibited with chloroquine for 24h. After 24h inhibition, the cells were additionally supplemented with OA to induce the formation of LDs. To evaluate the sensor's response during the experiment transfected cells were imaged at 0h, 4h, 24h and 48h (Figure 22).

Using the mKate2 signal to identify LC3B *punctae,* autophagosomes were detected and quantified for each transfected cell. Without inhibition of chloroquine, HepG2 cells formed about 30 autophagosomes per cell, which did not change significantly over 48h and after OA supplementation. In contrast, inhibition of autophagy with chloroquine resulted in a significant increase of mean autophagosome number over the first 4h hours. The mean number of autophagosome per cell continued to increase, reaching its maximum number after 24h of treatment. After 48h of Chloroquine treatment and 24h of OA supplementation, the mean number of autophagosomes was reduced, but it was still significantly higher than the mean number of autophagosomes in untreated cells (Figure 22B).

The number of lysosomes was established by measuring the pHluorin signal of each detected autophagosome. Autophagosomes whose pHluorin signal intensity was below the mean pHluorin intensity of the cellular background were counted as lysosome. The number of lysosomes was then normalized to calculate the fraction of lysosomes to autophagosomes. When comparing the fraction of lysosomes to autophagosomes the mean of the fractions was highly susceptible to single cells with higher autophagic flux. Therefore, the median value was compared instead.

In cells without chloroquine treatment, the median fraction of lysosome was low and did not change significantly over 24h. After OA supplementation the fraction of lysosomes slightly increased, but no statistically significant difference could be detected. Although chloroquine significantly increased the number of autophagosomes after 4h the median fraction of lysosomes remained on the same level, which indicates a block of autophagosome acidification and maturation. After 24h of chloroquine inhibition the median fraction of lysosomes slightly increased, but no statistically significant difference was detected. After OA supplementation the median fraction of lysosomes significantly increased, which in combination with the reduced number of autophagosome implies that the effect of autophagy inhibition was subsiding at this timepoint Taken together these results suggest that the inhibition of chloroquine peaked at 24h (Figure 22C).

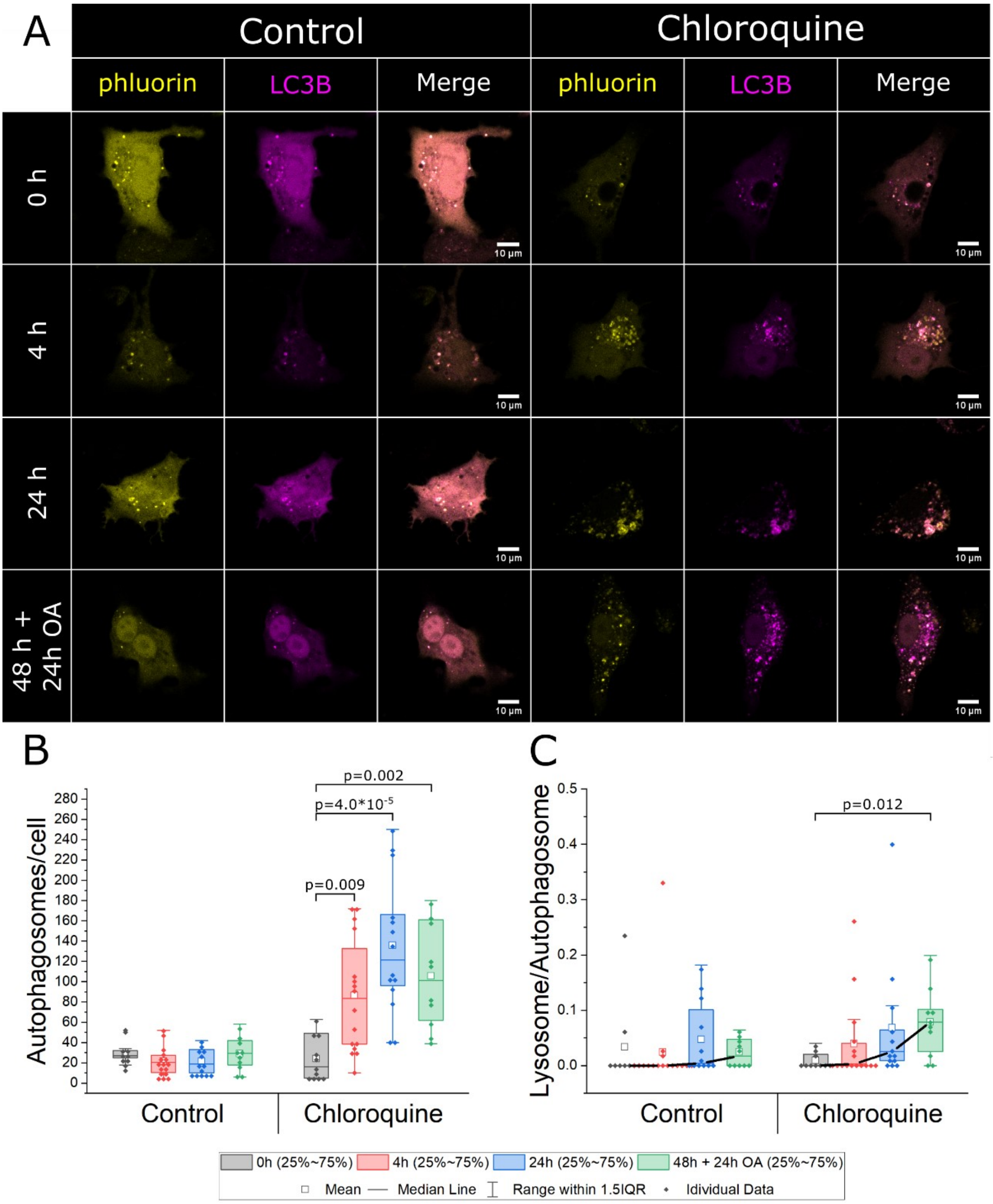

Figure 22 | Test of the pHluorin sensor

Confocal images of cells transfected with a pHluorin-LC3B-mKate2 sensor plasmid. HepG2 cells were treated with solvent control or 20 µM Chloroquine for 48h. After 24h of Chloroquine treatment, cells were supplemented with OA for 24h (**A**). The number of autophagosomes per cell were manually quantified and displayed in a boxplot (**B**). Lysosomes were identified as autophagosomes, which had a pHLuorin signal below the mean intensity of the cellular background. Based on this, the fraction of lysosomes per autophagosome was calculated and given as boxplot. A connecting line was drawn between the median to highlight the changes over time (**C**). n≥10. Statistical significance was calculated with the Kolmogorov-Smirnov test. P levels below 0.05 are given on top of the boxplot.

After establishing the pHluorin sensor, it was used to investigate the effect of RAB18 KD. Following the basic experimental template (Figure 14) HepG2 transfected with scrambled siRNA and RAB18 KD cells were transfected with the pHluorin sensor plasmid 24h post siRNA transfection. 48h post siRNA transfection these cells were treated with vehicle control or chloroquine for 24h, before inducing LD accumulation with OA for 24h. After OA supplementation cells were imaged detecting the pHluorin and mKate2 signal in transfected cells (Figure 23A).

Compared to the scram transfected cells, a significant increase of autophagosomes per cell was detected in HepG2 cells transfected with RAB18 siRNA, confirming the findings of the immunostaining (4.3.2). Inhibition of autophagy with chloroquine significantly increased the number of autophagosomes, but no significant difference between scram and RAB18 siRNA transfected HepG2 cells was detected. This indicates that inhibition of autophagy overrides the effect of RAB18 KD on autophagosome formation (Figure 23B).

The fraction of lysosomes per autophagosome was determined for each cell to estimate the autophagic flux. Without chloroquine treatment, the median fraction of lysosomes HepG2 cells with and without RAB18 KD did not differ, showing that the additional autophagosomes did not increase autophagic flux. After 48h inhibition of autophagy with chloroquine and 24h of OA supplementation, the median fraction of lysosomes was found significantly increased, which replicating previous results without siRNA transfection. Again, the median fraction of lysosomes did not differ between cells with and without RAB18 KD. Taken together these findings corroborate the results of the western blot, that RAB18 KD does not affect autophagic flux (Figure 23C).

In conclusion, using the LC3B sensor plasmid the results of the LC3B immunostainings and western blots could be confirmed. The downregulation of RAB18 resulted in the increased formation of autophagosomes, however the autophagic flux remained unchanged. To consolidate these findings, it is thus hypothesized that, rather than influencing autophagy itself, RAB18 regulates the susceptibility of LDs to autophagy. In the absence of RAB18, autophagy of LDs is no longer prevented, which causes the increased incorporation of LDs in autophagosomes. This increases the number of autophagosomes, but does not change the autophagic rate.

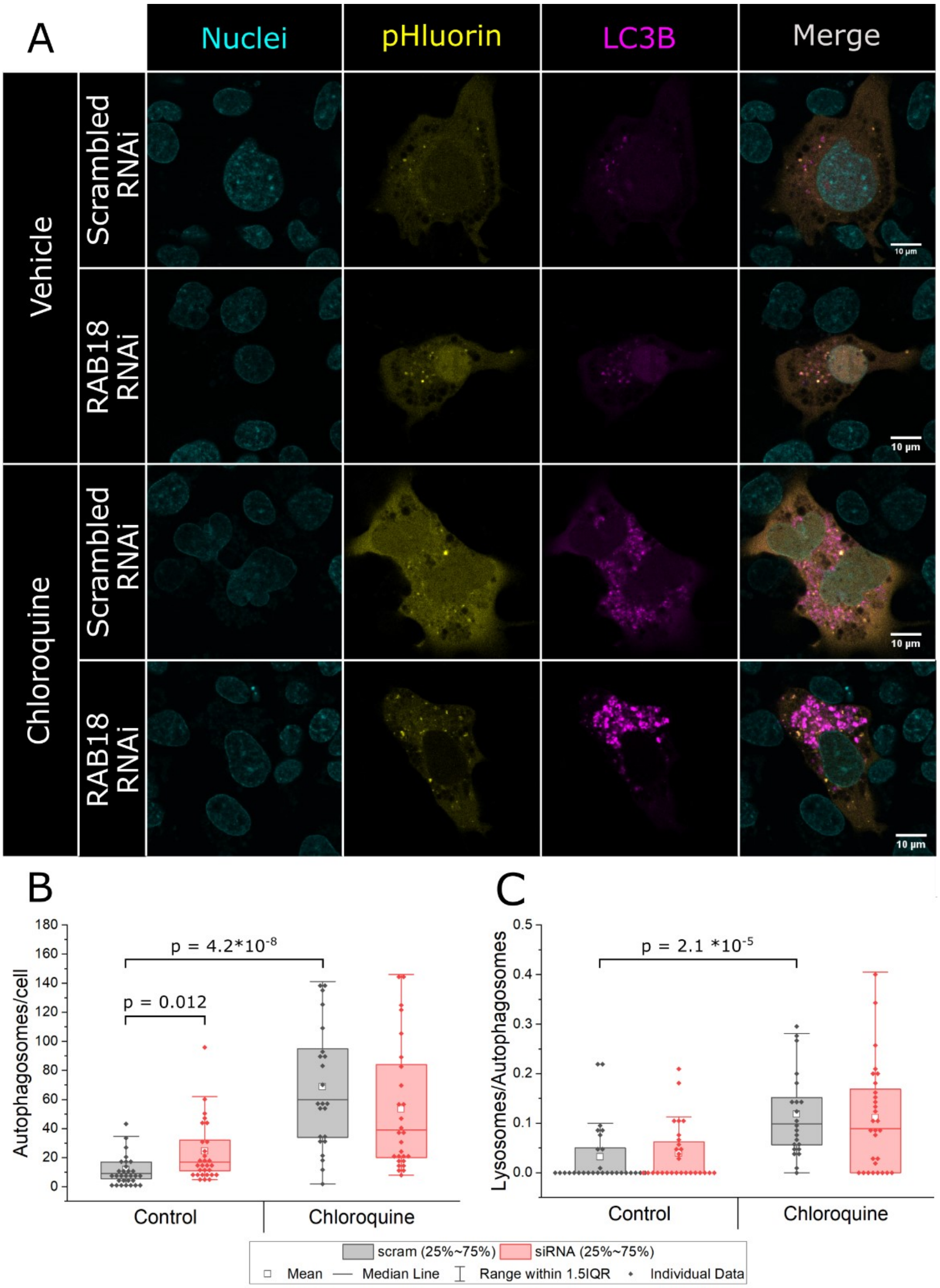

Figure 23 | pHluorin-mKate2 sensor reveals an increase in LC3B *punctae*

Confocal images of cells transfected with a pHluorin-LC3B-mKate2 -reporter plasmid. HepG2 cells were transfected with RAB18 targeting and scrambled RNAi, before transfection with the reporter plasmid. 48h after siRNA transfection cells treated with solvent or 20 µM Chloroquine as positive control. After 24 h of inhibition LD formation was induced by OA supplementation. The cells were imaged after 24h of OA supplementation (**A**). LC3B mKate2 *punctae* were segmented manually for each condition. Total count per cell is depicted in a boxplot (**B**). (**C**). N=3 n=10. Statistical significance was calculated with the Kolmogorov-Smirnov test. P levels below 0.05 are given on top of the boxplot.

4.4. Modulation of autophagy affects LD growth

4.4.1. Autophagy modulation prior to LD growth induction affects LD size

After detecting an accumulation of autophagosomes in HepG2 cells with RAB18 KD without changes to the autophagic rate, it was postulated that the presence of RAB18 on the LD prevents the autophagy of the LD. This hypothesis was tested by modulating the autophagy through the application of small molecular inhibitors prior to OA supplementation. Following the established experimental template for RAB18 KD cells were transfected with RAB18 targeting siRNA to induce RAB18 KD at 72h post transfection. After 48h of incubation, these cells were treated with either rapamycin or torin2 to activate autophagy. To inhibit autophagy, they were treated with either chloroquine or lalistat2. The cells were incubated with each of these compounds for 24h, before being supplemented with OA for an additional 24h to induce the formation of LDs. LDs were detected with CARS imaging at 2847 cm^{-1} and their area, CARS signal intensity and number quantified (Figure 24).

In these experiments, the mean LD size of HepG2 cells with RAB18 KD was higher than those of scram-treated cells, replicating the previously described effect of RAB18 KD. No change in mean LD area was detected between the vehicle and rapamycin treatment in cells both with and without RAB18 KD. However, mean LD area was significantly increased in cells treated with torin2. The inefficacy of rapamycin is likely due to its low cytosolic concentrations in HepG2 cells, as indicated by the lower occurrence of autophagosomes in rapamycin treated cells, compared to torin2 treated cells. These data indicate that the effect on LDs mean area is a result of autophagy-induction by torin2 rather than an unknown pleiotropic effect (Figure 24B).

The inhibition of autophagy with both lalistat2 and chloroquine in scram-treated cells (no RAB18 KD-induced LD enlargement) showed a minor reduction in mean LD-area that was not statistically significant. This indicates that LDs in HepG2 cells are at their minimum detectable size under standard conditions. However, in cells with RAB18 KD and correspondingly enlarged LDs, both chloroquine and lalistat2 showed a significant reduction of LD mean area, confirming that autophagy inhibition leads to a reduction in LD size that counters and even completely ameliorates the LD enlargement effect induced by RAB18 KD. (Figure 24B).

The CARS signal intensity correlates directly with the concentration of the excited molecular bonds, and therefore can be used as a relative measure of lipid concentration. As with LD mean area, the relative concentration of lipids per LD is higher in RAB18 KD cells, compared to scram-treated cells. As before, rapamycin was ineffective in increasing mean lipid concentration in droplets, corroborating the results seen on LD size. Enhancement of autophagy with torin2 led to an increase in mean lipid concentration per droplet, similar to its effect on LD size (Figure 24C).

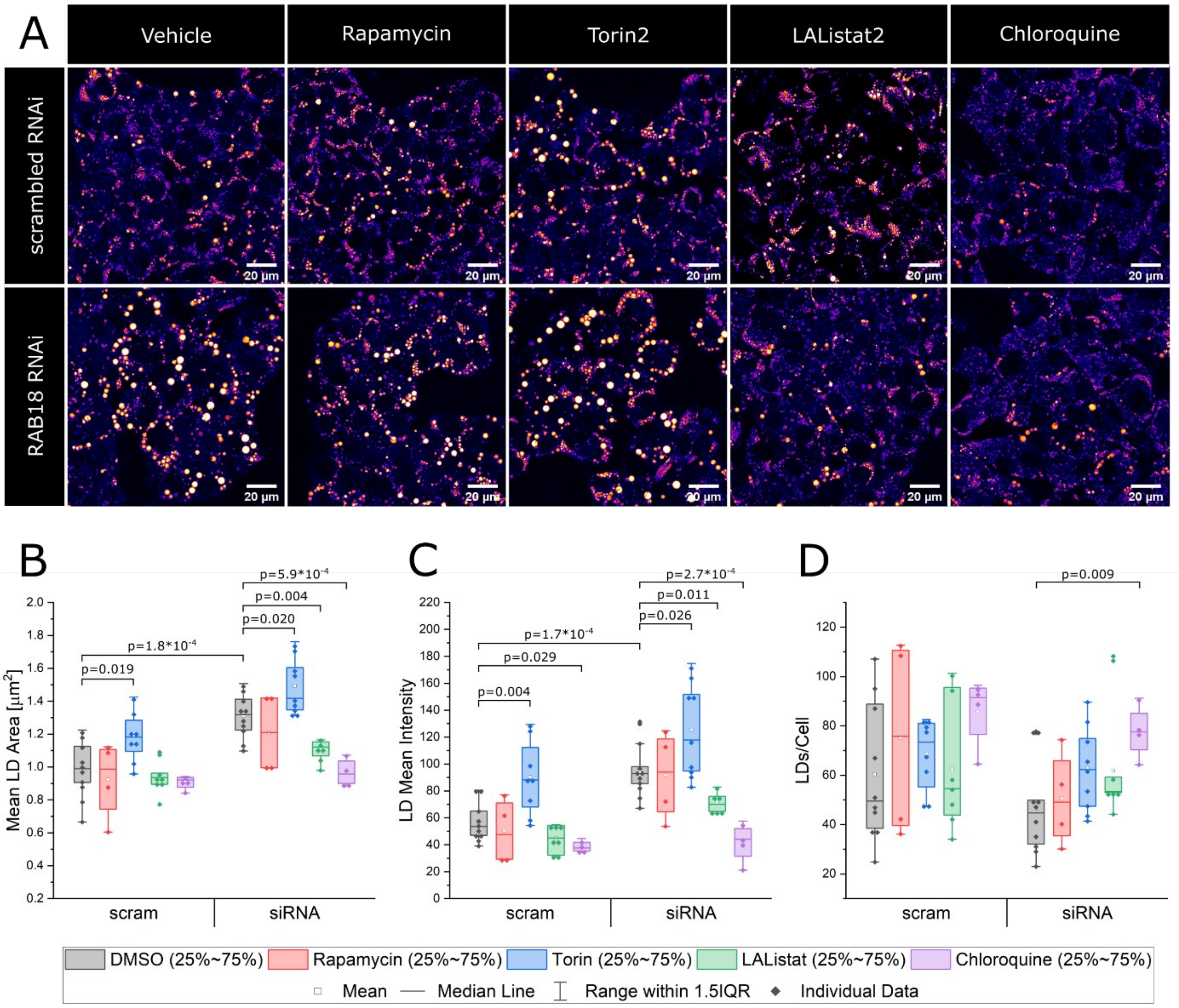

Figure 24 | RAB18 downregulation phenotype is rescued by autophagy inhibition

Representative confocal FCARS images taken at 2847 cm^{-1} of cells with (siRNA) and without (scrambled) RAB18 KD downregulation which were treated with autophagy enhancers (rapamycin &torin2) or autophagy inhibitors (lalistat2 & chloroquine) for 24 h, before being fed with OA **(A)** LDs were segmented with the *StarDist* algorithm and mean LD area **(B)**, mean intensity**(C)** and number per cell **(D)** was quantified. $N \geq 4$. Statistics were calculated using two-sample t-test. P-values below 0.05 are indicated above the boxplots.

Inhibition of autophagy with chloroquine and lalistat2 corroborated this reciprocal relationship between LD size/concentration and LD numerosity. Previous results show that these treatments led to a reduction in LD size and mean lipid concentration. Simultaneously, both treatments also led to an increase in lipid droplet number per cell in scram-treated as well as RAB18 KD cells, with the effect being more pronounced in the latter. On the other hand, enhancement of autophagy did not change the LD number significantly in both scram-treated and RAB18 KD cells (Figure 24C).

Together, these results suggest that autophagic flux is *per se* not the primary influencer of LD enlargement and numerosity, but rather that RAB18 KD increases the susceptibility of LDs to autophagic destruction. The relatively mild effects of autophagy enhancement in general indicate that nascent LDs are likely destroyed by autophagy at a high (maximal) rate in HepG2 cells. However, as would be expected in this case, inhibition of autophagy strongly counters the increased susceptibility of LDs under RAB18 KD conditions, spares nascent LDs from autophagic destruction and thus allows them to be available for LD storage. The lipid load the cell faces can then be distributed into more numerous, small and less concentrated LDs. Thus, autophagy inhibition completely overrides the LD enlargement caused by increased susceptibility of LDs to autophagic destruction in the absence of RAB18.

4.4.2. Autophagy inhibition after OA LD growth does not decrease LD area

In later stages of NAFLD, steatotic tissue is already characterized by the presence of large LDs. In this clinical scenario, reduction in LD size and reversal to normal physiological LD sizes is desirable. Since inhibition of autophagy with chloroquine prior to OA supplementation was shown to prevent the increase in LD size in cells with RAB18 KD, it was investigated whether inhibition of autophagy after the formation of LD would also reduce the size of already enlarged LDs.

Following the established experimental template for RAB18 KD, HepG2 cells were transfected with siRNA and LD formation was induced by OA supplementation 72h post siRNA transfection. Cells were treated with the vehicle substance and not supplemented with OA, as a control. Next, the HepG2 cells were treated with chloroquine for an additional 24h. LDs were detected 120h post siRNA transfection using CARS at 2847cm^{-1} and the LD area was quantified (Figure 25).

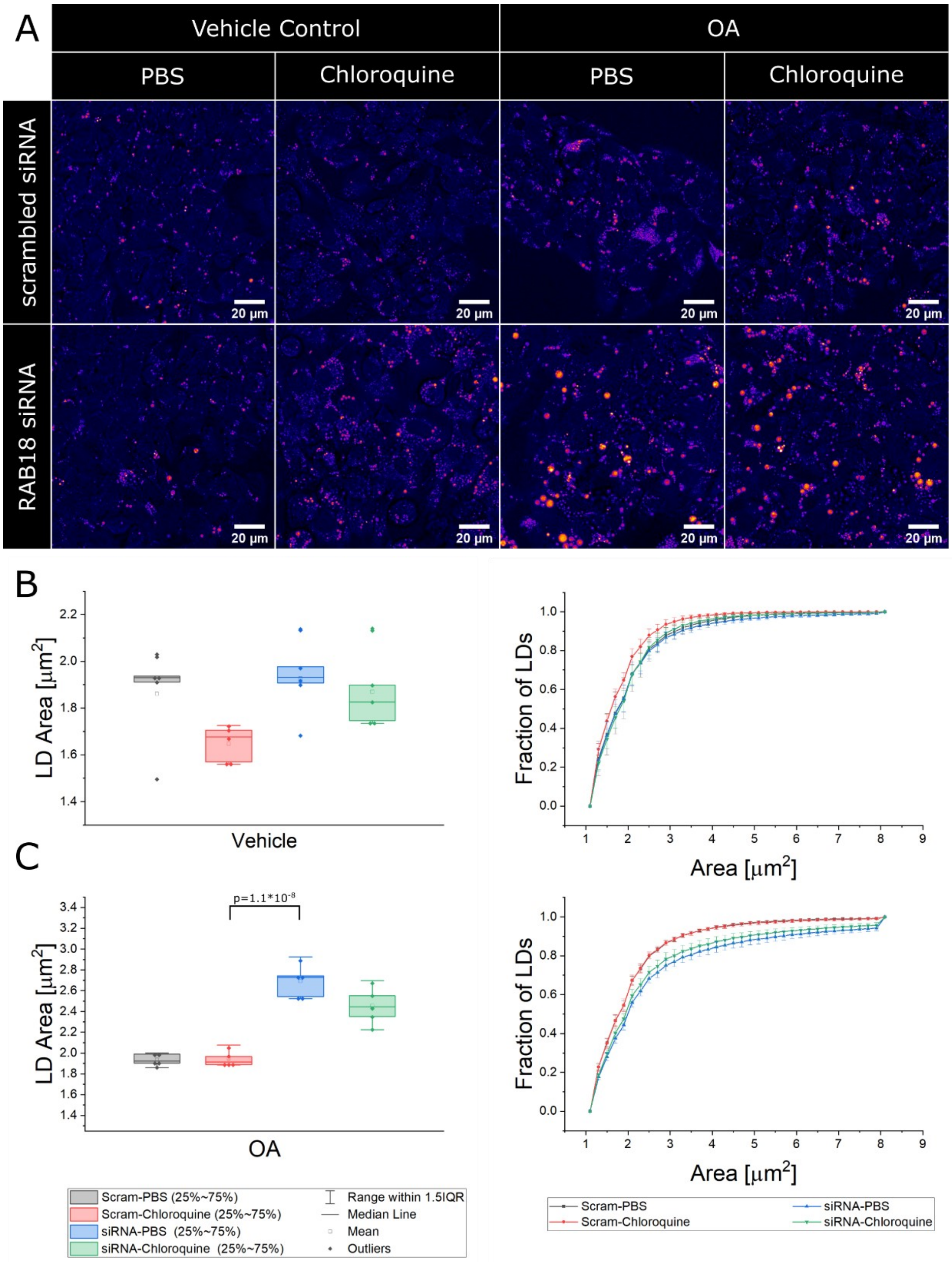

Figure 25 | Inhibition of autophagy after OA induced LD growth does not reduce LD size

Representative confocal FCARS images at 2847 cm^{-1} of cells with (siRNA) and without (scrambled) RAB18 KD. Cells were incubated with OA for 24 h, before being treated with Chloroquine or the solvent control (PBS) for 24 h(**A**). LDs larger than 1µmwere segmented using the *StarDist* algorithm and LD area was quantified. A cumulative frequency count with a bin size of 0.2 μm^2 was calculated and normalized to the maximum number of LDs. Depicted are boxplots as well as the mean cumulative histograms of cells treated with vehicle control (**B**) or OA (**C**). The histograms error bars represent standard deviation. N=5 Statistics were calculated using two-sample t-test. P-values below 0.05 were indicated above the boxplots.

Without OA supplementation, the mean LD area did not differ significantly between HepG2 cells with and without RAB18 KD (Figure 25B). Only after supplementation with OA, the mean LD area of HepG2 cells with RAB18 KD were found to be significantly larger than cells without RAB18 KD, which replicates the previously reported results. This indicates that RAB18 KD affects mostly the distribution of lipids (Figure 25C).

Compared to solvent treatment (PBS) chloroquine treatment resulted in a reduction of the mean LD area in HepG2 cells without supplementation and without RAB18 KD. This was also reflected by a shift in the LD size distribution towards smaller LDs. However, no statistically significant difference could be determined. In HepG2 cells with RAB18 KD, Chloroquine treatment did not impact the mean LD area either, which was mirrored by a largely identical LD size distribution (Figure 25B).

In HepG2 cells with OA supplementation, chloroquine treatment after the formation of LD did not significantly reduce the LD area in HepG2 cells with and without RAB18 KD. This is also mirrored by the LD size distribution. HepG2 cells with and without RAB18 KD display clearly different LD size distributions. However, the LD size distribution after chloroquine treatment matched the distribution detected after solvent treatment. Thus, in contrast to chloroquine treatment prior to LD formation (shown in 4.4.1), chloroquine treatment post LD formation failed to ameliorate or reverse the LD size increasing effect of RAB18 KD (Figure 25C).

In summary, chloroquine treatment does not affect the size of already present LDs, which implies that LD size reduction observed after chloroquine treatment is dependent on the formation of new LDs.

4.4.3. Autophagy inhibition with chloroquine reduces LD size in primary hepatocytes

Since in HepG2 cells with RAB18 KD only inhibition of autophagy prior to OA supplementation was shown to decrease LD area post OA supplementation, it was hypothesized that overal LD size in primary human hepatocyts (PHH) could be reduced by blocking autophagy and increasing the number of newly formed LDs. To test this theory, PHHs were treated with increasing dosages from 10-100 µM of chloroquine for 24h. Next, LD formation was induced by supplementing with OA for 24h. To control for OA independent formation of new LDs, cells were only vehicle treated without OA supplementation. After 24h supplementation, LDs were detected using CARS at 2847 cm^{-1} and LD area, CARS signal intensity and LD number per cell were quantified (Figure 26).

The experiments showed that PHHs maintained few LDs smaller than 1µm² even without OA supplementation. After supplementation with OA, PHHs developed significantly larger LDs. In PHHs without supplementation chloroquine treatment with up to 50 µM resulted in no changes compared to the mean LD area of the solvent control. Only the treatment with 100 µM chloroquine significantly reduced the mean LD area, which implies that the mean LD area reduction cause by chloroquine reaches the minimum LD size detectable under these conditions. Consequently, this conceals all but the most extreme changes to mean LD area.

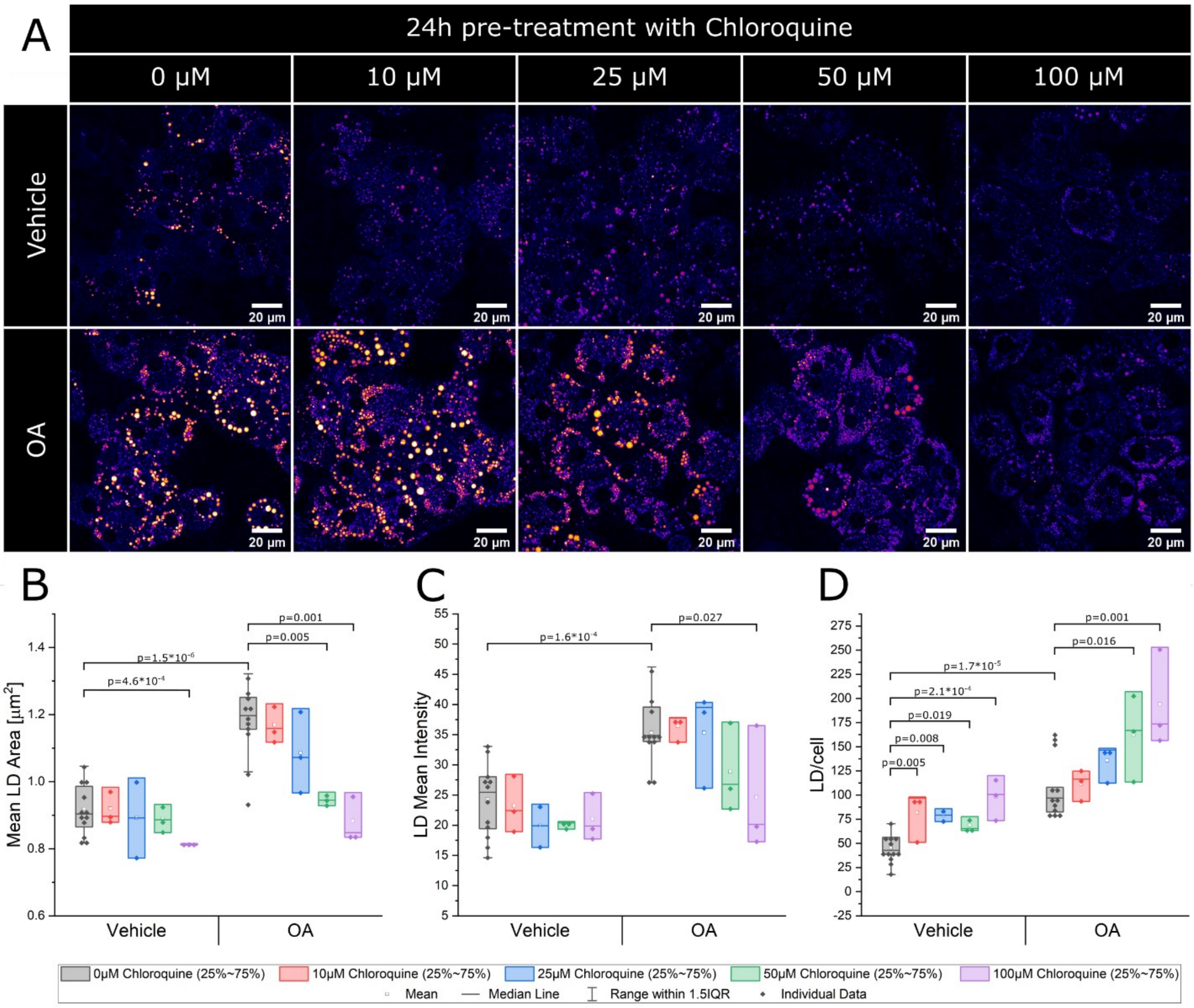

Figure 26 | Inhibition of autophagy reduces LD size in PHH

Representative images depict the FCARS lipid signal at 2847cm⁻¹ of primary human hepatocytes (PHH) in sandwich culture. PHH were pre-treated for 24h with different Chloroquine concentrations pre-LD-accumulation (**A**). LDs were segmented with the *StarDist* algorithm and mean LD area (**B**), mean intensity (**C**) and mean number per cell (**C**) was quantified for each experiment. N≥2. Statistics were calculated using two-sample t-test. P-values below 0.05 were indicated above the boxplots.

In PHHs supplemented with OA the mean LD area decreased inversely proportional to the chloroquine concentration used during treatment. Inhibition of autophagy with 50 µM and 100 µM chloroquine resulted in a statistically significant decrease of mean LD area. Both concentrations reversed the mean LD area to the area detected in PHHs not supplemented with OA, which indicates that autophagy is essential for the formation of large LDs after OA supplementation of PHHs (Figure 26B).

CARS signal intensity provided a relative measure for lipid concentration. OA supplementation significantly increased mean lipid concentration of LDs compared to LDs in uncomplemented PHHs. Treating PHHs without OA supplementation with chloroquine led to no change in the LDs' mean lipid concentration. Analogous to the mean LD area lipid concentration in the LDs also decreased inversely proportional to the chloroquine concentration in PHHs supplemented with OA (Figure 26C).

Finally, the number of LD per cell was evaluated to show that the observed decrease of mean LD area and lipid concentration are inversely correlated to the number of LDs. After OA supplementation, LD number per cell was found significantly increased when compared to PHHs without OA supplementation. However, in PHHs with and without OA supplementation, chloroquine treatment caused an increase of LDs per cell, which was directly proportional to the concentration used for treatment. It is thus assumed that inhibition of autophagy with chloroquine blocks the lipophagy of newly formed LDs, which increases the number of LDs in the cell independent from lipid uptake (Figure 26D).

Taken together these results suggest that in PHHs LD number is inversely proportional to mean area and lipid concentration in PHH, which corroborates the working hypothesis on LD size and number regulation introduced in 4.4.1. Since chloroquine is an autophagy inhibitor, it is thus postulated that the key regulatory mechanism behind the LD number and size regulation in PHH is autophagy.

4.4.4. Autophagy inhibition via chloroquine inhibits the formation of large LDs in mice fed with high fat diet

In the previous section, it could be shown that inhibition of autophagy with chloroquine reduced LD size in PHHs *in vitro*. Besides its use as an autophagy inhibitor in cell culture, chloroquine has been approved for therapeutic use in rheumatic arthritis and malaria, which makes chloroquine a strong candidate for direct clinic application to reduce LD size in NAFLD. Therefore, the effect of chloroquine treatment on early NAFLD progression was studied in a mouse model to prove that chloroquine treatment also reduced the size of hepatic LDs *in vivo*.

In this animal study, male mice were divided in two groups. To inhibit autophagy, group one was injected daily with 60 mg chloroquine per kg body weight, whereas group two was injected daily with PBS as a vehicle control. After one week of injection, half of the mice in each group were set on a steatogenic diet to simulate disease progression, whilst the rest were kept on the regular diet as control. Mice were kept on their respective diet with daily injections for 4 weeks.

At the first day of each week, the live liver tissue of one representative mouse of each group fed with the steatogenic diet was imaged with CARS *in vivo* at 2847 cm^{-1}. This way the LD development and NAFLD progression in the murine liver could be followed over the course of the experiment. After four weeks of feeding, the liver tissue of all mice was imaged with CARS at 2847 cm^{-1}, blood samples were taken and the animals were euthanized (Figure 27).

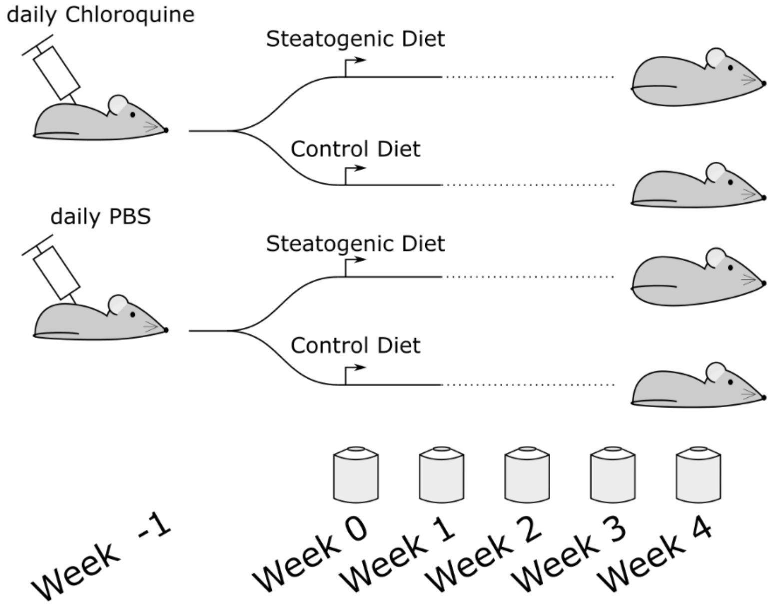

Figure 27 | Mouse study layout

Two populations of mice were injected daily with either 60mg/kg bodyweight Chloroquine phosphate or PBS as vehicle control. After one week of injection, half of both groups were additionally put on a steatogenic diet. LD development in the liver of these mice on the fat heavy diet was imaged on the first day if each week using CARS. This was maintained until week 4 in which all mice livers were imaged, blood samples were taken.

Starting from week 1, mice set on the steatogenic diet developed large LDs in the liver. These droplets increased in size and number until the end of the experiment after week 4. Mice set on the same diet, but injected daily with chloroquine, did also develop LDs during the first week, but these LD were smaller and less numerous than in mice without Chloroquine injection. Over the course of the experiment, these LDs also accumulated but were overall smaller than the LDs detected in mice treated with the vehicle control and fed with steatogenic diet (Figure 28A).

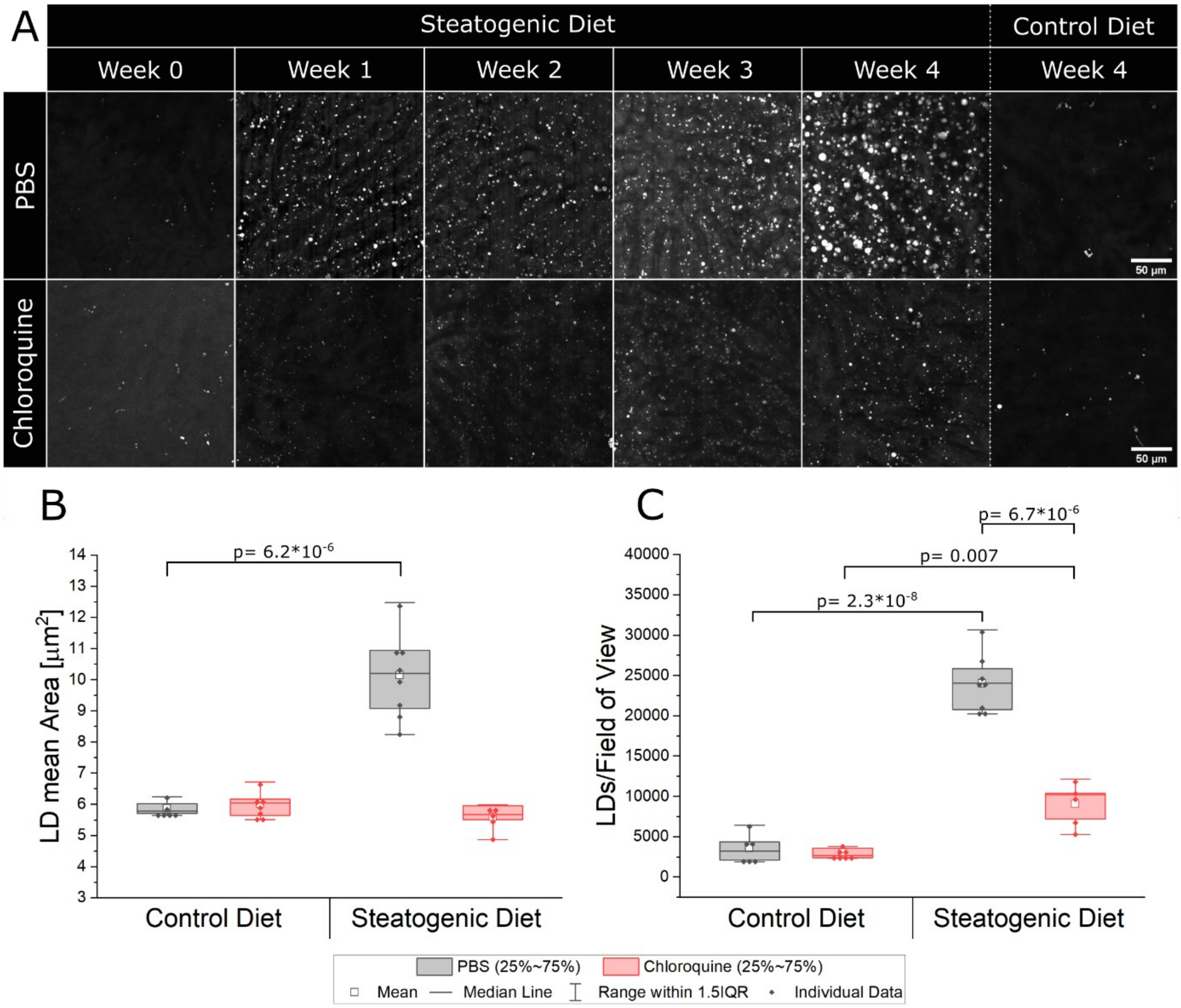

Figure 28 | Daily Chloroquine treatment reduces LD size in mice fed with a steatogenic diet

Representative intravital confocal ECARS images of mice livers at 2847cm^{-1} depict the LD development during 4 weeks of feeding with a steatogenic diet. Mice injected daily with Chloroquine develop smaller and fewer LDs over the same timespan (**A**). LDs were automatically detected using the *StarDist* algorithm and the mean area (**B**) and LD number per field of view (**C**) were measured. LDs below 3 µm² were excluded. Statistical significance was tested with the two sample ttest. P-values below 0.05 were indicated above the boxplots. N≥5

After 4 weeks on the corresponding diet, LDs in the liver tissue of all mice were imaged using CARS. The LDs were then automatically detected and mean area and number of LD per field of view were quantified. Compared to mice fed with control diet, the mean LD area of mice fed with the steatogenic diet had nearly doubled, indicating the onset of steatosis. Chloroquine treatment did not change the mean area of LD detected in mice fed with the control diet. However, chloroquine treatment significantly reduced the mean area of LDs detected in mice fed with the steatogenic diet. Since the mean LD area in chloroquine treated mice fed with steatogenic diet was comparable to the ones fed with control diet, this clearly shows that chloroquine inhibits the formation of large LDs in the liver (Figure 28B).

In mice fed with the control diet daily chloroquine injections did not change the number of LDs. Compared to mice fed with the control diet, feeding with the steatogenic diet resulted in a significant increase in the number of LDs per field of view. However, daily Chloroquine injections resulted in significantly less LDs per field of view in mice set on a steatogenic diet, when compared to daily injections with the vehicle (PBS). Thus, daily chloroquine injections did not only reduce LD size, but also LD number in mice set on a steatogenic diet (Figure 28C).

Since the discrepancy in the lipid accumulation between chloroquine treated and untreated mice fed with the steatogenic diet was so large, it was hypothesized that LD size reduction in the liver by chloroquine treatment could lead to increased export of lipids and lipoproteins into the bloodstream. To test this hypothesis blood samples of all mice were taken and analysed at the end of the experiment. In mice fed with steatogenic diet higher Low Density Lipoprotein (LDL), High Density Lipoprotein (HDL) and cholesterol blood concentrations than in mice on control diet were detected. No difference in these blood concentrations were detected between mice with and without chloroquine treatment (Figure 29A-C). In mice fed with the steatogenic diet, glucose blood levels did not differ from mice fed with the control diet. Daily chloroquine injection, did result in a slight but not a statistically significant decrease of glucose blood levels (Figure 29D). Triglyceride and free fatty acid (FFA) blood levels were slightly reduced in mice fed with the steatogenic diet when compared to mice fed with control diet. Chloroquine treatment slightly but not statistically significantly raised these levels in mice on the steatogenic diet. Taken together, these finding suggest that the reduction of LD size in the liver caused by chloroquine did not change the blood concentration of glucose, lipids and lipoprotein (Figure 29E&F).

It is thus concluded that daily chloroquine injection reduces the size of newly formed LDs in the liver. However, since the blood levels of LDL, HDL, cholesterol and triglycerides were not significantly increased, the location of the surplus lipid, otherwise stored in the larger LDs, remains unknown.

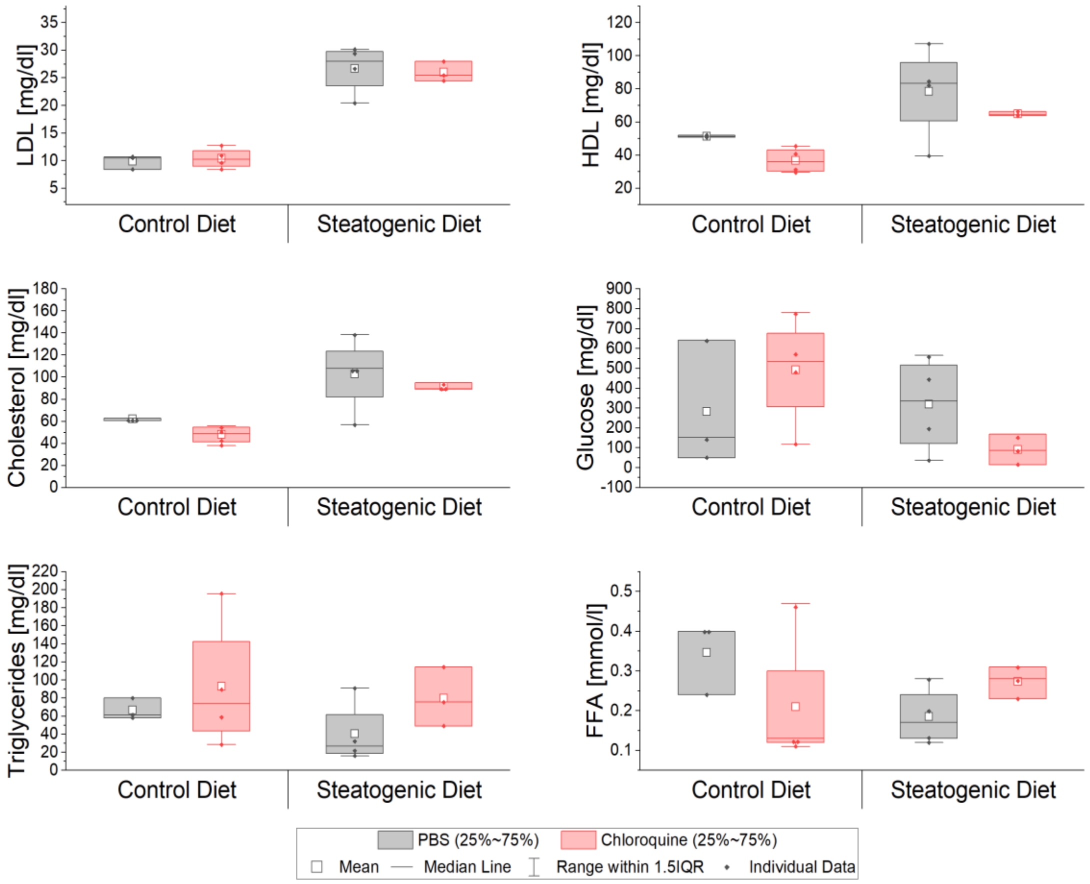

Figure 29 | Blood levels of lipoproteins, cholesterol, glucose and lipids after 4 weeks of steatogenic diet

Blood concentrations of low-density lipoprotein (LDL), high density lipoprotein (HDL), cholesterol, glucose, triglycerides and free fatty acids were quantified and displayed as a boxplot. Blood was taken after four weeks of feeding with control and steatogenic diet as well as five weeks of daily injection with 60mg/kg body weight chloroquine. No significance could be established with Kolmogorov-Smirnov testing. N≥3

5. Discussion

The overarching phenotype of NAFLD is the creation of large LDs in the hepatocytes. Although LDs have been extensively studied over the last two decades, the molecular mechanisms behind LD size and number regulation are still not fully understood. Specifically, the enigmatic role of RAB18 is a topic of the scientific debate.

This thesis aimed to elucidate the mechanism behind the localization of RAB18 to the LD-membrane as well as the function of RAB18 on the LD membrane in HepG2 cells as a model for its role in the liver. Furthermore, it aimed to identify possible interventions to prevent or reverse steatosis. In the next sections the presented findings will be discussed and set into the context of ongoing research, but first a short outlook on the novel tools applied in this thesis shall be given.

5.1. Application of new tools for LD imaging and evaluation

5.1.1. *StarDist* and LD segmentation

Recently, machine learning has made a large impact on science in general and image processing in particular. Its striking advantage is that once a neural network has been trained, it can be applied to extensive sets of varying images, allowing for quick high throughput image analysis. In this thesis, the novel *StarDist* algorithm developed by Schmidt et al. (Schmidt et al., 2018) was successfully adapted and applied to detect LDs.

In this work, two models trained to detect LDs detected by CARS imaging and BODIPY staining were created. Given the time-consuming task of creating the manually annotated data, only few trainings sets were created. For the training of a model, used for LD detection after BODIPY staining 34 manually annotated images were used. The model used for LD detection in CARS images was trained with only 10 images. This is a small training set, when compared to other applications of machine learning in pathology, in which trainings is conducted with over 600 images (Arjmand et al., 2020). Therefore, it is reasonable to question the general use of these models.

However, both models only differed by 5% (±1%) when compared to manually annotated data not used in training the model. This accuracy of 95% was deemed sufficient for the automatic detection of LDs. Nonetheless, there is room for optimization and generalization of the models, especially in the case of the model used for detecting BODIPY stained LDs. This can be achieved by the training with more numerous and more variant training sets.

With an accuracy of 95% established, several pro-active measures were taken to minimize error. First, the quantity of segmented LDs was increased by imaging large numbers of cells. Second, the imaging parameters' variation, particularly resolution changes, was kept to a minimum. Last, the segmentation was regularly verified against the original images to ensure correct LD detection. However, before applying models of this study to other data-sets, it has to be stressed that the application should be first re-evaluated against known test sets.

5.1.2. CARS imaging of LDs

Although it is a comparably novel method in the field of cell biology, CARS microscopy has been previously applied to answer questions regarding lipid accumulation in the LD (Bradley et al., 2016; X. Li et al., 2019; Paul et al., 2019). Tissue of rodents with NAFLD has also been successfully imaged using CARS (Lin et al., 2011).

The advantages of imaging LDs with label free native imaging in contrast to traditional staining methods are numerous. CARS imaging is considerably faster, because of the lack of label incubation and washing steps. CARS detection is found to be more specific than BODIPY labelling and allows for quantification of the LD content. By its nature photobleaching of the label is not an issue, because CARS detects the target substance directly via its molecular properties.

Some attempts have also been made to image vertebrate brain cells *in vivo* using CARS (Evans et al., 2005; Fu et al., 2008). However, the results presented in this thesis are to date the first demonstrations of label free *in vivo* imaging of mice liver tissue. The *in vivo* application of CARS had several additional advantages for LD imaging. Without a label, the uptake, metabolization and export of said label in living tissue is not an issue. Without labels the complexity and duration of the procedure could also be drastically reduced, which reduces the animal's stress during the experiments.

However, the high excitation intensities needed for CARS imaging have been found to induce photo damage in cultured cells and tissue (Fu et al., 2006). In mice, high excitation intensity could induce liver damage in the form of a light-induced 'burn' and compromise liver function. Thus, imaging settings for *in vivo* CARS are chosen judiciously to avoid damaging the tissue. In this work, the total light irradiation per field of view (FOV) was limited by choosing different regions of the liver for each image, by utilizing sensitive detectors rather than strong excitation and finally acquiring only 1 image per FOV. Large regions were acquired using tile scanning and stitching of the liver tissue in vivo.

5.2. RAB18's LD membrane localization depends on a C-terminal acylation cycle

5.2.1. Localization of different RAB18 mutants and variants

Due to the sequence homology between RAB18 and other Ras-superfamily proteins, it was hypothesized that RAB18's localization is determined by an acylation cycle similar to the one described for HRAS localization (Rocks et al., 2005; Dekker et al., 2010). Testing this hypothesis, the effect of the palmitoylation on the localization additional to RAB18 activity was investigated by overexpressing of fluorescently tagged RAB18.

RAB18's localization to the LD has been shown in HepG2 cells before (Ozeki et al., 2005). The published localization of RAB18 to the LD membrane in HepG2 cells was replicated in this thesis. In HepG2 cells, the constitutive active mutant RAB18-Q67L has been reported to also localizes to the LD whilst the inactive mutant S22N was reported to mis-localize to the cytoplasm (Ozeki et al., 2005). Both localizations were also replicated.

The C-terminus of RAB18 has been shown to share the C-terminal CAAX-box motive reported for other Ras-superfamily proteins. This CAAX-box is essential for irreversible geranylgeranylation and subsequent proteolytic removal of the terminal AAX amino acids from the C-terminus (Leung et al., 2007). Elongation of the RAB18 C-terminus, which results in loss of the C-terminal CAAX-box, has been shown to induce the Warburg-Micro-Syndrome. This indicates that C-terminal geranylgeranylation is context dependent and essential for RAB18's function (Bem et al., 2011). The results presented in this thesis confirm these findings. The modification of the C-terminus, which is essential for membrane localization, was localized to the geranylgeranylation site at C203. This also underlines the homology of Ras-superfamily proteins, as the failure of prenylation of the last C-terminal cysteine has been linked to loss of membrane affinity and function in other Ras-superfamily proteins (Hancock et al., 1989).

In the vicinity of the geranylation site at C203 a second cysteine has been reported in the RAB18 C-terminus (C199), which is surmised to be post-translationally palmitoylated by sequence similarities to other Ras/Rab-proteins (UniProt Consortium, 2021). This thesis demonstrates that C199 confers the LD-membrane localization of RAB18, showing that mutation of this cysteine (C199S) resulted in mis-localization of the mutant RAB18 to the cytoplasm. This is in line with similar findings, which show that the reversible palmitoylation of C-terminal cysteine residue confer targeted membrane localization for other members of the Ras-superfamily introduced in 1.3.2 (Rocks et al., 2010). It is thus concluded that the post-translational palmitoylation at C199 is the essential factor for RAB18's localization to the LD-membrane.

Over-expression of RAB18 tethered to the ER by SEC61b displayed a distribution similar to C199S and S22N, showing that inactive as well as non-palmitoylated RAB18 mis-localizes to the ER. With over 50% of intracellular surface the ER is the largest membrane structure of the cell (Alberts et al., 2008). It is thus surmised that C199S and S22N localization is the consequence of a stochastic distribution of non-palmitoylated, but membrane bound RAB18, rather than a distinct ER localization.

The localization of S22N to the ER indicates that only active RAB18 localizes to the LD. It could be argued that this localization to the LD is solely based on activity and the palmitoylation is only stabilizing factor, which could be compensated for by increased activity. However, the mis-localization of the constitutively active Q67L-C199S double mutant to the ER clearly shows that the opposite is the case. Stable localization of RAB18 to the LD is not possible without C-terminal palmitoylation disregarding the protein activity.

Taken together, these findings indicate a localization hierarchy based on RAB18's post-translational modifications and activity. The prenylation confers the basic membrane affinity. The reversible palmitoylation confers higher membrane affinity, which allows for specific targeted recruitment to the LD-membrane. Finally, activity determines the timing of the palmitoylation and translocation. Only when all three factors are present RAB18 localizes to the LD-membrane.

Table 19 | Overview of the effects of activity, palmitoylation and geranylation on RAB18 localization

RAB18 mutation	Activity	Palmitoylation	Geranylgeranylation	LD-Localization
Q67L	+	+	+	+
S22N	-	+	+	-
Q67L-C199S	+	-	+	-
S22N-C199S	-	-	+	-
C203S	+/-	+/-	-	-

5.2.2. RAB18 localization is dynamic

Although the overexpression of mutants showed the importance of palmitoylation for LD-membrane localization, the dynamic nature could not be shown with this approach. To investigate the dynamic acylation cycle of RAB18, fluorescent recovery after photobleaching (FRAP) experiments were conducted on fluorescently labelled RAB18 mutants.

After photobleaching a recovery of fluorescent protein to the LD-membrane was detected within a minute. This is faster than the translation rate detected in eukaryotes, therefore it was concluded that RAB18 localizes dynamically to the LD (Ingolia et al., 2011). A recovery could also be detected by the non-localizing mutants S22N, C199S and C203S. However, as discussed in 5.2.1, these mutants were not enriched on the LD membrane. In case of C203S the measured recovery is most likely based on the FRAP of the cytoplasmic protein in close vicinity of the LD-membrane. For S22N and C199S the recovery is likely caused by the random insertion of both mutants into the LD-membrane.

The mobile fraction of RAB18, S22N, C199S and C203S was detected around 80% showing a high-turnover of the protein on the LD. In contrast, the PolyC and Q67L mutant showed a reduced mobile fraction, with only PolyC's mobile fraction found significantly decreased. The decrease in mobile fraction implies that the solubility of PolyC had decreased, which is an indicator that PolyC is indeed additionally palmitoylated and displays a higher membrane affinity. The reduced solubility of Q67L is likely based on the binding of downstream effectors, which results in lower protein turnover.

The mean half-life of RAB18 recovery under basal conditions was determined to be 19 seconds. This was reduced by the S22N and C199S mutations by half and by the mutation of C203S to a quarter of the WT. The shorter half-life of S22N and C199S indicates the loss of membrane affinity corroborating the theory of random insertion of non-palmitoylated RAB18 in the LD-membrane. C203S shows the fastest mutant in recovery, which reflects its failure to bind the LD membrane at all, so that the measured half-life might reflect the diffusion speed of RAB18 in the cytoplasm. PolyC and Q67L did not display an altered half-life when compared to RAB18 under basal condition.

Treatment with BSA, the vehicle control for BSA complexed OA, resulted in no changes in the mobile fraction. However, BSA induction overall increased the contrast between the half-life of the WT, the non-localizing C199S and C203S as well as the hyper-palmitoylated PolyC and constitutive active Q67L. RAB18 half-life was slight, but not significantly, faster at an average of 10 seconds. The recovery half-life of C199S showed a significant decrease to around 4 seconds, which was comparable to C203S. In contrast, the half-life of Q67L and PolyC was slower than the WT. These changes indicate that BSA might induce RAB18 transport to the LD, but the increased membrane affinity introduced by the additional palmitoylations in PolyC reduces the transport rate of PolyC and therefore increased its recovery half-life.

After supplementation of OA to induce formation of LDs, the mobile fraction of the constitutively active RAB18-Q67L was found to significantly decreased, whilst the mobile fraction of other RAB18 mutants remained unaltered. This demonstrates that the interaction of the GEF and effectors with the constitutively active Q67L increases after OA supplementation. Conversely, the half-lives between all mutants did not change for all but S22N, implying that the activity of RAB18 is the most impactful factor after OA supplementation.

5.2.3. RAB18 acylation cycle can be modulated with small molecule inhibitors

After demonstrating that RAB18 localizes dynamically via its C-terminal modifications, it was hypothesized that RAB18 localization can be affected by small molecule compounds. This was investigated by using the two small molecule inhibitors 2-bromopalmitate (2-BP) and palmostatin B. The palmitoylation inhibitor 2-BP was shown to increase the solubility of HRAS and decreasing its localization half-life (Rocks et al., 2005). palmostatin B was shown to decrease solubility and increase the half-life of localization of Ras (Dekker et al., 2010). Based on these published results and the results of the RAB18 mutant study discussed in 5.2.1 and 5.2.2, following predictions can be made for RAB18 solubility after inhibition of its acylation cycle.

Inactive untreated and non-palmitoylated (2-BP) RAB18 should have a high solubility, because the protein is not bound to any effectors and not modified by palmitoylation, which would increase its membrane affinity. In contrast, when de-palmitoylation is inhibited with palmostatin B, even inactive RAB18 remains palmitoylated preventing solubility. Thus, solubility should be less in comparison with 2BP and untreated cells. Active RAB18 is surmised to bind its downstream effector which should reduce its solubility independently from its palmitoylation. Therefore, it should not be susceptible to inhibitor treatment (***Table 20***).

Table 20 | Model of RAB18 solubility

	RAB18 is inactive			**RAB18 is active**		
	Activity	Palmitoylation	Solubility	Activity	Palmitoylation	Solubility
Untreated	-	-	+	+	+	-
palmostatin B	-	+	-	+	+	-
2-BP	-	-	+	+	-	-

In the experiments RAB18 half-life was expected to rise after OA supplementation as more protein was bound by the GEF and effectors. This was not detected when compared to the vehicle control. Conversely, the solvent control DMSO was shown to decrease mobile fraction under basal conditions and significantly increased localization half-life after OA supplementation.

High dosage of DMSO has been linked with increased membrane permeability (Ménorval et al., 2012), but the concentrations used in the experiments discussed here were considerably lower than the ones used in the study (0.1% vs 10%). On the other hand, even minor changes to LD membrane composition have been shown to change the distribution of LD-membrane proteins *in vitro* (Caillon et al., 2020). It is thus postulated that RAB18, which is bound to LD membranes by two acyl-anchors, is more susceptible to the effects of DMSO than the membrane itself, leading to the observed changes in mobile fraction and half-life.

Palmostatin B treatment under basal conditions resulted in an increase in half-life, which signifies a decrease in solubility. This matches the prediction for inactive RAB18 under palmostatin B treatment (***Table 20***). Counterintuitively, the mobile fraction was also found to increase under basal conditions. A plausible explanation for this could be the accumulation of RAB18 on the LD-membrane. In similar experiments, accumulation of the protein at the site of de-palmitoylation has been described after inhibition of de-palmitoylation with palmostatin B (Dekker et al., 2010; Vartak et al., 2014). Applying this to RAB18, the fraction of protein located on the ER would deplete while the fraction on the LD increases. As a result, an "increased" mobile fraction on the LD is observed as more protein localizes to the LD after the bleach.

After supplementation of OA, the half-life and mobile fraction of RAB18 did not change after inhibition of de-palmitoylation. However, the half-life and mobile fraction in cells only treated with the solvent increased, reducing the differences between cells with and without de-palmitoylation inhibition. Taken together this data indicates that RAB18 might be mostly inactive and de-palmitoylated at basal conditions, whereas it is mostly palmitoylated and active after OA supplementation. In contrast to inhibition of de-palmitoylation, inhibiting palmitoylation with 2-BP was observed to cause no changes in mobile fraction or half-life, under basal conditions, which confirmed the predictions of the model for inactive RAB18. Treatment with the vehicle control BSA resulted in an increase in mobile fraction, but no significant changes of the half-live. This might be due to the increased transport of RAB18 after BSA induction discussed in section 5.2.2, but without palmitoylation RAB18 localization cannot be maintained on the LD resulting in a high mobile fraction.

After OA supplementation, the mobile fraction and half-life were found to decrease in cells treated with 2-BP, which appears to contradict the model for active RAB18. One explanation for this is that inhibiting RAB18 palmitoylation results in the loss of specific membrane localization similar to the situation described for mono-lipidated HRAS (Rocks et al., 2010). Without a second membrane anchor in the form of palmitoylation, RAB18's membrane affinity is reduced. Therefore, the protein is more soluble, which increases the distribution of RAB18 in the cytoplasm. This results in a faster localization half-life. However, due to the loss of membrane affinity less RAB18 is accumulating specifically on the LD. Therefore, less protein binds its effectors, resulting in the observed decrease in mobile fraction.

In summary, it is concluded that RAB18 is mostly de-palmitoylated under basal conditions, but is activated and palmitoylated after the induction of LD formation with OA. By manipulating the palmitoylation status with the small molecule inhibitors palmostatin B and 2BP, the palmitoylation status of RAB18 and therefore its localization can be modulated.

5.2.4. Modulation of the acylation cycle alters LD size

The question remained whether changing the palmitoylation status of RAB18 affected the LD size. In the experiments, it was demonstrated that inhibition of palmitoylation with 2BP resulted in the loss of large LDs. However, the treatment of cells with 2-BP has been reported to inhibit the creation of TAGs in adipocytes. The reason for the inhibition of TAG synthesis is hypothesized to lie within the metabolic inhibition of DGAT1/2. 2-BP is metabolized in the cell to 2-BP-CoA, which cannot be metabolized by the downstream enzyme DGAT1/2. This results in reduced DGAT activity and less TAG synthesis (Haas, 2013). The observed phenotype is thus most likely due to this off-target inhibition of TAG synthesis and not the recruitment of RAB18.

Effects of palmostatin B treatment on LD size have not been described until now. In HepG2 cells induction of LD accumulation with OA and simultaneous inhibition with palmostatin B increased mean LD area of the formed LD. Fittingly, enlarged LDs have been established as RAB18 knock out phenotype in Hela and adipocytes, whilst overexpression was shown to reduce LD size in adipocytes (Bekbulat et al., 2020; Xu et al., 2018). Palmostatin B treatment was shown to slow down RAB18 localization, which could result in the depletion of active RAB18 on the LD. This depletion on the LD mimics a local knockdown, which might lead to the increased LD size.

Though it would be tempting to see the LD area increase as a result of palmostatin B dependent inhibition of RAB18 de-palmitoylation, the described phenomena might also be caused by an off-target effect. Palmostatin B inhibits the APT1 thioesterase, which has targets aside from RAB18, and was first developed to inhibit de-palmitoylation of Ras proteins (Dekker et al., 2010). It is therefore possible that cell signalling might be a cause for LD area increase after palmostatin B treatment.

Nonetheless, although the effects might not be due to RAB18 localization changes alone, these results show that LD size can be regulated by targeting the palmitoylation machinery. Therefore, the cellular palmitoylation machinery poses a plausible target for interventions aimed at regulating LD size.

5.3. RAB18 activity on the droplet prevents LD enlargement by inhibiting autophagy

5.3.1. The localization of RAB18 to the LD reduces LD size

The absence of RAB18 has been reported to cause a drastic increase of LD area in various cell types (O'Mahony et al., 2015; Xu et al., 2018; Bekbulat et al., 2020; Deng et al., 2021). Additionally, the RAB18 knock out phenotype in adipocytes is reported to cause the accumulation of small LDs in close proximity to the large ones after LD formation, but fusion events were not observed (Xu et al., 2018). In this work, this established phenotype could be reproduced via siRNA mediated knockdown in HepG2 cells. After 20h OA supplementation, the LDs detected in HepG2 cells with RAB18 KD were larger than the ones observed in cells without RAB18 KD. Additionally, fusion events of LDs were observed in HepG2 o.n. imaging. Since depletion of RAB18 in HepG2 increased LD size, it is concluded that RAB18's function in HepG2 cells is the reduction of LD-size.

The question remained, whether this function was coupled to the localization of RAB18 to the LD. This work has shown in section 5.2 that RAB18 is dynamically localizing from the ER to the LD. However, which of the two cellular compartments might be site of RAB18 activity remains a topic of debate. Previous experiments suggest the LD to be the site of RAB18 activity (Xu et al., 2018), whereas other studies suggest that RAB18 has a role on the ER (Gerondopoulos et al., 2014). To answer this question, HepG2s cells with RAB18 KD were transfected with the RAB18 localization mutants established in the presented thesis.

In HepG2 cells without RAB18 KD, overexpression of RAB18 or Q67L did not increase the percentage of LDs with an area of 1-2µm^2. This differs from what has been observed in adipocytes, in which overexpression reduced RAB18 size (Xu et al., 2018). The differences could be due to the detection threshold applied in this thesis excluding LD smaller than 1 µm^2, but cell type specific LD phenotypes cannot be ruled out. Overexpression of S22N, which has been described as a dominant negative mutant (Wu et al., 2016; Dejgaard and Presley, 2019b; Deng et al., 2021), was not detected to influence LD size in HepG2 cells. It is thus concluded, that the "dominant-negative" effect of S22N is not a general feature of this mutation. RAB18-S22N is thought to competitively inhibit the function of endogenous RAB18 by binding the RAB18 GEF. Therefore, cell type specific excess of GEF in HepG2 may overrule the effect of the GEF binding "dominant negative" mutant RAB18, thus suppressing its inhibiting effect on endogenous RAB18.

Overexpression of any mis-localization mutants had no effect on the LD area, when transfected in cells without RAB18 downregulation. This shows that the endogenous RAB18 function in HepG2 is not disturbed by overexpression of any RAB18 mutant, additionally highlighting the robustness of the endogenous RAB18 mechanism in HepG2 cells.

Transfection of RAB18 mutants, which localized to the LD membrane, into HepG2 cells with RAB18 KD rescued the LD size distribution of HepG2 in cells without RAB18 KD preventing the overall increase LD size. Mis-localizing RAB18 mutants failed to prevent the increase of LD size in HepG2 cells with RAB18 KD. When comparing the effects of different non-localizing mutant, it could be detected that the transfection C199S and S22N had a slight LD area reducing effect, while C203S LD size distribution is identical to the size distribution detected in cells transfected with unfused fluorescent protein. An explanation for this is that C199S partially localizes to the LD via its geranylgeranylation at C203. This is supported by a small recovery of C199S in cells with OA supplementation in the FRAP experiments discussed in 5.2.2. In combination with overexpression, this effect could be due to a random localization of C199S to the LD partially restoring RAB18 function. However, RAB18-SEC61b, which is bound to the ER-membrane, shows a LD-size distribution similar to RAB18-C199S. It is thus reasoned, that there might be a minor LD related function of ER bound RAB18. This could be indirect via the recruiting of SNARE proteins and the Arf/COPI (Li et al., 2016) or recruitment of the NAG-ZW10 complex (Xu et al., 2018) to tether LDs to the ER. However, in HepG2 cells the main function of RAB18 activity is firmly tied to its localization to the LD-membrane.

5.3.2. Lipophagy and not lipolysis is the mechanism behind reducing LD growth in HepG2

The function of RAB18 on the LD could be established to prevent the enlargement of the LD. This function has been previously ascribed to the two basic LD size reduction mechanism lipolysis and lipophagy. RAB18 has been hypothesized to recruit ATGL to the LD and thus increase lipolysis (Martin et al., 2005; Pulido et al., 2011; Dejgaard and Presley, 2019b). Investigating RAB18's role in lipolysis, HepG2 cells with and without RAB18 KD were incubated with the small molecular inhibitor atglistatin. Atglistatin was developed to inhibit ATGL activity (Mayer et al., 2013) and has been shown to increase LD size in primary hepatocytes (Schott et al., 2019). If the RAB18 KD phenotype was caused by a reduction of ATGL recruitment to the LD, treatment with atglistatin would not change the phenotype of the knockdown but change the phenotype of HepG2 cells without RAB18 KD to look similar to the knockdown. However, treatment with atglistatin did not alter the LD size distribution in HepG2 cells with and without RAB18 after OA supplementation.

These findings are in line with published reports showing that atglistatin did not change FFA or TAG levels in HepG2 (Xie et al., 2020). Conversely, ATGL is expressed in HepG2 and the downregulation was found to reduce TAG excretion, but neither the siRNA mediated knockdown of ATGL nor atglistatin were shown to change LD size (Di Leo et al., 2019; Taxiarchis et al., 2019). These evidence together with the data supplied by the presented thesis demonstrate that ATGL does not play a role in LD size up regulation in HepG2 cells with RAB18 KD.

With lack of ATGL ruled out, lipophagy was tested by inhibiting LAL via the small molecule inhibitor lalistat2. If LAL is inhibited, lipophagy is stopped. Most LD removed by autophagy are thought to be small in hepatocytes (Schott et al., 2019). Therefore, if lipophagy is inhibited in HepG2 cells, the cells will develop numerous small LDs, which would have been removed by autophagy otherwise. If RAB18 controlled the selective lipophagy of LDs to downregulate their size no effect should be seen after RAB18KD. However, upon lalistat2 treatment the small LD population of RAB18 KD was partially restored. This indicated that paradoxically the LD size increase seen in cells with RAB18 KD was due to increased autophagy of LDs.

However, lalistat2 treatment did not fully revert the LD size increase in HepG2 cells with RAB18 KD. A possible explanation for this might lie within the pleiotropic effects established for lalistat2 treatment. In macrophage foam cells it could be shown that lalistat2 reduced cholesteryl-ester degradation and cholesterol efflux. A high concentration of cholesterol in liver cells, on the other hand, has been shown to increase LD size (Ouimet et al., 2011; Makino et al., 2016). In murine hepatocytes lalistat2 did not affect TAG turnover, but lalistat2 did reduce the

FFA oxidation (Sathyanarayan et al., 2017). Combined, these findings show that there are multiple effects linked to lalistat2 inhibition, which could lead to an increase of TAG or cholesterol concentration additional to lipophagy inhibition. This might cause the observed increased LD size, although the smaller LD fraction is rescued. It can also be argued that due to its function in the last step of lipophagy, which is the hydrolysis of lysosomal fatty acids, LAL inhibition might be partially compensated for by the cellular autophagy machinery.

Nonetheless, lipophagy could be established as a decisive contributing factor to the RAB18 KD phenotype indicating that the function of RAB18 on the LD was linked to autophagic removal of the LDs.

5.3.3. RAB18 KD increases autophagosome formation but does not affect autophagic flux

Since lipophagy was determined to be a decisive factor in the RAB18 KD phenotype, autophagy in cells with RAB18 KD was further investigated. Autophagy can be monitored using the autophagosome marker LC3B. Upon autophagosome formation, the protein LC3B is located to the phagophore. Therefore, these focal accumulations of LC3B, called *punctae,* can be measured to quantify autophagy (Schläfli et al., 2015).

Initially, autophagosomes were detected by immunofluorescence staining of LC3B. After OA supplementation, HepG2 cells were fixed and stained for LC3B. An increase of autophagosomes was detected in HepG2 cells with RAB18 KD, but not in HepG2 cells without RAB18 KD. Activation of autophagy with rapamycin did not alter the formation of autophagosomes in HepG2 cells with and without RAB18 KD. The activation of autophagy with torin2 increased the accumulation of LC3B *punctae* in cells with and without RAB18 KD. However, no statistically significant increase could be established. When autophagosome transition to autophagolysosomes was inhibited with chloroquine, an increase of autophagosomes was detected in HepG2 cells with and without RAB18 KD, but no differences could be detected between the cells with and without RAB18 KD. Thus, the inhibition of autophagy overruled the effect of the RAB18 KD. Taken together, these results indicate that RAB18 KD increases autophagy.

To gain further insight into the state of autophagy in cells with RAB18 KD before and after OA supplementation, the amount of LC3B2 protein was quantified by western blotting. Chloroquine, which blocks the maturation of autophagosomes, was used as a positive control for the detection of LC3B. Before and after OA no significant difference in the LC3B2 levels, the ratio of LC3B1 to LC3B2 and the autophagic flux were detected between HepG2 cells with and without RAB18 KD, which contradicts the results of the immunofluorescence staining.

Because the immunofluorescence staining and the western blot showed conflicting outcomes, a fluorescent reporter protein comprising an acid sensitive pHluorin-GFP and a LC3B-mKate2 was expressed in cells with and without RAB18 KD. With this construct autophagosome formation and autophagic flux could be measured simultaneously in live cells. The acid sensitive pHluorin fused to the LC3B could be used to distinguish late stage autophagolysosomes, for easier distinction called lysosomes, from early stage autophagosomes giving insight into the autophagic rate (Tanida et al., 2014).

Quantification of the LC3B *punctae* after OA supplementation revealed a significant rise of autophagosomes per cell after RAB18 KD compared to cells without RAB18 KD. However, the fraction of lysosomes to autophagosomes did not differ between cells with and without RAB18 KD. Treatment with chloroquine to block autophagy resulted in a strong increase of autophagosomes per cell, but no differences between the number of autophagosomes detected in cells with and without RAB18 KD was detected. Cells treated with chloroquine showed a significantly higher fraction of lysosomes than cells treated with the solvent, which would be in conflict with published results of how the sensor reacts to chloroquine. (Tanida et al., 2014). However, in control experiments it could be determined that chloroquine blocked the fusion of autophagosomes for 24h. The rise in lysosomes was thus due to reduced effect of chloroquine after 48h of inhibition and not an effect of siRNA transfection. Corroborating the results from the western blot, no significant difference in the autophagic rate was detected between cells with and without RAB18 KD.

Taken together, the data confirms an increase of autophagosomes in cells with RAB18 KD. On its own ,this would imply an increase of autophagy, which is in line with experiments conducted in stellate cells (BasuRay, 2019). However, neither LC3B2 levels nor autophagic flux was found increased in cells with RAB18 KD, which is in line with findings which do not report that RAB18 KD causes an increase of LD autophagy (Bekbulat et al., 2020). But if there is no change in autophagic flux, the question remains why inhibition of lipophagy partially reverted the RAB18 KD phenotype.

A plausible explanation through which RAB18 could rescue small LDs from autophagy without affecting the autophagic flux could be, paradoxically, by increasing the LD size. It has been reported that RAB18 recruits a ZW10-NAG complex which is thought to establish LD-ER contact sites (Xu et al., 2018). This has been expanded upon by showing that in Huh7 cells DFCP1 cannot create small LDs without RAB18 localization. Through its interaction RAB18 stabilizes the DFCP1 localization to the nascent LD, which results in the increase of the LD size (Li et al., 2019).

Since lipophagy has been reported to be size dependent in hepatocytes (Schott et al., 2019), RAB18 could protect these LDs from autophagy. This would maintain the population of small LDs in hepatocytes. In cells in which RAB18 is absent the small LDs failed to increase in size and are removed by the cellular autophagy machinery. But since autophagy itself is not enhanced, these autophagosomes are processed by the overall basic autophagic turnover, which leads to an increased formation of autophagosomes.

Another explanation, could be that RAB18 does not regulate macro-autophagy of LDs, but their micro-autophagy. It has been recently shown that in hepatocytes, LD size is also controlled by a special form of micro-autophagy (Schulze et al., 2020). One of the proteins associated with micro-autophagy is RAB7, which has been established as a central protein of lipophagy in hepatocytes (Kawamura et al., 2012; Schroeder et al., 2015). Interestingly, RAB18 and RAB7 have been shown to collaborate on autophagy and lipolysis in Warburg Micro Syndrome neurons (Nian et al., 2019) which indicates that RAB18 could be involved in the regulation of micro-autophagy. RAB18 might directly or indirectly via COPI-ARF interact with RAB7 as a regulator for LD microautophagy. This hypothetical mechanism might act similar to the one described for the switch of RAB5 to RAB7 in endocytosis. In this process accumulation of PI3P via the VPS34 kinases is important for the transition from the late endosome marked by RAB7 to the lysosome (Poteryaev et al., 2010; Jaber et al., 2016). Further corroborating a potential link between RAB7, RAB18 and lysosomes, the RAB18 was also found to interact with VSP34 *Drosophila melanogaster*. The knockout of RAB18 in *Drosophila melanogaster* resulted in a phenotype similar to a VPS34 knock out, which also showed a functional connection (Takáts et al., 2021). Combined, these findings show promising prospects for further investigations into the role of RAB18 and Rab7 interaction in LD size regulation by microautophagy.

It is thus concluded that rather than controlling autophagic flux directly, RAB18 protects the LDs in cells from autophagic removal by the two proposed mechanisms. In cells with RAB18 KD LDs are more susceptible to autophagy, leading to their increased incorporation in autophagosomes.

5.3.4. The modulation of autophagy influences LD size by removing newly formed small LDs

If the increased autophagic removal of LDs was the cause behind LD growth in RAB18 KD cells, the activation of autophagy before OA supplementation should replicate the phenotype of RAB18 KD. To test this, HepG2 cells with a and without RAB18 KD were treated with the autophagy activators rapamycin and torin2, before the cells were supplemented with OA to induce formation of LDs.

Rapamycin treatment did not affect the LD size. Together with the results of the LC3B staining discussed in 5.3.3 this indicates that in the presented results rapamycin did not increase the autophagy in HepG2 cells. This was unexpected, since rapamycin has been shown to inhibit phosphorylation of mTOR in HepG2 cells in much lower concentrations than used in this study (Varma and Khandelwal, 2007). This could be because of a reduced cytoplasmic concentration of rapamycin due to reduced uptake of the rapamycin used in this study. Further investigations with different rapamycin analogues would be able to confirm this, but were outside the scope of this thesis. Only autophagy activation with torin2 increased the mean CARS signal intensity and LD area in cells with and without RAB18 KD after OA supplementation. Though this proved that mTOR inhibition by torin2 could increase the LD size, it is important to note that torin2 also has also been shown to inhibit insulin signalling (Yin et al., 2016). Torin2 treatment has also been shown to reduce HepG2 proliferation and survival (Wang et al., 2015). Though the number of imaged cells was comparable in each condition, the reduced proliferation of the HepG2 could have resulted in a higher concentration of OA per cell. Therefore, off-target effects by torin2 cannot be fully excluded. However, since the rise of autophagosomes per cell correlated with the increase of LD size after OA supplementation, it was concluded that LD size after OA supplementation can be increased by mTOR activation before OA supplementation.

In the complementary experiment, autophagy was inhibited with lalistat2 or chloroquine before OA supplementation. This resulted in a decrease in mean LD area and mean CARS intensity, but increased LD number in cells with RAB18 KD after OA supplementation. Thus, the effect of lalistat2 as discussed in 5.3.2 could be replicated. Inhibition of autophagy with chloroquine resulted in complete reversion of the RAB18 KD phenotype. This demonstrated that lysosomal fusion is needed for the generation of large LDs in RAB18 KD cells. This is in line with studies, which employed the inhibitors chloroquine and lalistat2 in hepatocytes. There it was also shown that blocking autophagy reduced LD size, but increased numbers (Sathyanarayan et al., 2017; Schott et al., 2019). The same effect could be observed after inhibiting autophagy in endothelial cells with chloroquine in endothelial cells (Bik et al., 2021)

However, these *in* vitro finding do not match published results *in vivo*, which reported that loss of autophagy creates larger LDs in the liver. After ATG5 and ATG7 downregulation and in ATG7 knockout mice LD size and number were increased (Singh et al., 2009). Yet, another study using the same ATG7 knockout mouse model demonstrated that loss of autophagy results in less and smaller hepatic LDs were detected (Takahashi et al., 2020). It could also be shown that HepG2 mutant for ATG7 showed smaller and less lipid droplets (Takahashi et al., 2020). Further underlining the need of autophagy for the creation of large LDs, ATG5 mutant adipocytes were shown not to differentiate and develop large LDs at all (Baerga et al., 2009)

Thus, it could be concluded that inhibition of autophagy decreases LD size, which would be beneficial for steatosis. However, i*n vivo* experimentation in NAFLD mouse models indicated that chloroquine treatment is actually worsening steatosis in NALFD and alcoholic fatty liver. It has been reported that the number of LD as well as the TAG content in the liver increased significantly in hepatocytes after chloroquine treatment. Rapamycin dependent induction of autophagy was found to be reducing TAG and LD number during steatosis (Ding et al., 2010; Lin et al., 2013). This is in line with findings that show that an increase in autophagy in general is beneficial in the treatment of NAFLD (Czaja, 2016).

This contradicts the results presented in this thesis, which show that inhibition reduces LD size. It could be argued that these experiments were done on already steatotic animals and cells, whilst the experiments discussed in 5.3.4 were done before LD growth was induced. Therefore, the effect of autophagy inhibition after the formation of LDs was tested in HepG2 cells with and without RAB18 KD. It could be shown that autophagy inhibition did not lead to any changes in the phenotypes of HepG2 cells with and without RAB18 KD. This clearly demonstrates that the reduced LD size was due to inhibiting the autophagic removal of small LDs during LD formation.

It is thus concluded that the formation of large LDs in cells with RAB18 KD depends on autophagy, but autophagy is not essential for maintaining large LDs in these cells. This result can be explained by viewing LDs as dynamic lipid storage containers. After RAB18KD fewer of the storage containers are available, since they have been removed by autophagy. However, the same amount of lipid influx needs to be stored in fewer containers, which leads to an increase of the individual container size. Inhibiting autophagy in RAB18KD increases the number of possible containers. In this case the lipid load can be distributed among more, but smaller containers. When there is no lipid influx, increasing the number of the containers does not affect the already established ones, therefore the inhibition of autophagy does not change the size of already existing LDs. If this model is true, increasing the number of LDs outside the context of RAB18 KD, would cause the formation of smaller LDs.

5.4. Autophagy is a driving component in LD size regulation

5.4.1. Inhibition of autophagy increases LD number and decreases LD size.

Chloroquine dependent autophagy inhibition reverted the LD size increase in HepG2 cells with RAB18 KD by increasing the number of LDs, as discussed in 5.3.4. It was thus theorized that inhibiting autophagy in hepatocytes without RAB18 KD. To test this, the effects of inhibiting autophagy with chloroquine on LD size were investigated in primary human hepatocytes. The results show a clear dose dependant effect of chloroquine on the LD size and number after OA supplementation. Thus, it is concluded that the LD size and number in primary hepatocytes depend on the autophagy of the hepatocyte.

An alternative explanation for these results could be cell death after chloroquine treatment. In rat hepatocytes, the cytotoxic concentration (CC50) for chloroquine was established at 100 µM for a treatment of 2 hours (Jamshidzadeh et al., 2007). In this thesis it is reported that treatment with 100 µM chloroquine for 48 h caused extreme LD accumulation disrupting the cell, but otherwise no strong toxic effects were observed. These differences might be due to higher chloroquine tolerance of human hepatocytes compared to rats. This is supported by the established CC50 for chloroquine in Hep3B liver cells, which was determined to be at 130.8µM at 48h (Yang et al., 2020). This concentration is about 30% higher than the highest concentration used in the experiments in this thesis.

5.4.2. Chloroquine treatment reduces hepatic LD growth in mice

Chloroquine is a clinically approved drug, which makes it an attractive target for direct translation to the clinic. Therefore, the inhibition of autophagy with chloroquine to reduce LD size was evaluated in a small-scale mouse study. Previous studies reported that for a sufficient increase of LC3B levels in the liver, 60mg/kg bodyweight chloroquine has to be injected intraperitoneally (Haspel et al., 2011). The same concentration was applied for long-term autophagy inhibition study done for 18 days, which also reported reduced autophagy (Zhao et al., 2015). Therefore, this concentration was used for daily injections in the mouse study presented in this thesis.

Mice were pre-treated with either chloroquine or vehicle control for one week. These two groups were then further subdivided into two groups set on different diets. One was set on a steatogenic diet and one was kept on the normal diet as a control. Surprisingly, enlarged LD were already detected after the first week of feeding with research diet. As predicted by the *in vitro* experiments discussed in 5.4.1 mice treated with chloroquine did not develop large hepatic LD after the first week of feeding the steatogenic diet. After 4 weeks of feeding, LDs detected in the liver of mice fed with the steatogenic diet were twice as large as the LDs detected in the liver of mice set on the control diet. However, daily injection with chloroquine resulted in smaller LDs in mice set on the steatogenic diet reverting the mean LD area to the mean LD area detected in mice on the control diet. Interestingly, mice treated with chloroquine and set on the steatogenic did develop less LDs and not more LDs as predicted by the *in vitro* model.

Previous studies report mild steatosis from week 6 onwards and the effect of feeding has been investigated up to 60 weeks to induce severe steatosis (Crawford et al., 2019; Nakamura and Terauchi, 2013). In this thesis, LD accumulation was already seen after week 1. This was one week earlier than previously described in the literature (Motomura et al., 2006). This can be explained by the higher sensitivity of CARS microscopy, when compared with traditional histology methods, which allows for earlier detection of differences in LD development. The observed difference in LD size between untreated and chloroquine treatment was an ongoing trend up to the end point of the experiments in week 4. Although the duration of the experiment was shorter than previous studies on steatosis, it could be shown that chloroquine treatment in mice was a suitable treatment to stop the development of large LDs during the onset of steatosis in mice.

Although a longer feeding time to further characterize the effect of chloroquine is a viable follow up to this study, toxic secondary effects due to the high chloroquine dosage are to be expected. The dosage used in this thesis is 12 times the dosage considered safe for human long-term treatment (Mackenzie, 1983). In mice, long-term exposure to high concentrated chloroquine injections have been linked to several adverse side effects such as muscles atrophy (Kwon et al., 2015). Efforts have been made to establish long-term inhibition protocol using the less toxic hydroxychloroquine in spaced repetitions, but cannot provide reliable autophagy inhibition yet (Masson et al., 2020).

Analysis of blood samples taken at the end of the study revealed that 4 weeks of research diet feeding increased LDL, HDL and Cholesterol blood concentrations compared to control diet. This was not altered by chloroquine injection. TAG and FFA concentration were lowered after 4 weeks of research diet and slightly, but not significantly elevated by chloroquine treatment. This demonstrates that chloroquine treatment did not alter the uptake to the bloodstream in mice set on the steatogenic diet. However, no strong rise in fatty acids or lipoproteins was detected either. This raises questions concerning the storage location of the excess lipid load which are no longer contained in larger LDs located in the liver after chloroquine treatment.

One possibility could be that the same volume of fatty acids is simply distributed over many smaller LDs. However, the images taken at the end of the experiment also reveal a strong difference in LD number, which implies that the excess in lipids is unlikely to be stored in additional LDs *in vivo*. *In vitro* experimentation indicates that similar accumulation of LDs after chloroquine treatment is observed in endothelial cells, so other cells could act as lipid sink during chloroquine treatment (Bik et al., 2021). In the same study an increase in membrane lipids was also observed after chloroquine treatment, therefore the excess lipid could have been transferred to the membrane of the hepatocyte (Bik et al., 2021). *In* vivo chloroquine treatment is also reported to result in an accumulation of TAG in the lymph fluid and intestine mucosa (Mansbach et al., 1987). This could result from free fatty acid export via the bile canaliculi and intestinal reabsorption. However, given the broad range of effects of chloroquine, further investigations of the lipid content in the liver tissue and bile are needed to determine the exact localization of the excess lipid load.

5.5. Conclusion

The presented thesis provides conclusive evidence that the activity of RAB18 and its localization to the LD membrane is essential to modulate LD size in hepatocytes.

Localization was shown to be regulated by an acylation cycle characterized by reversible C-terminal palmitoylation. Palmitoylated RAB18 has enhanced its membrane affinity allowing it to sequester on lipid droplets, likely through interaction with GEFs and other effectors. If inactivated by GAPs, and subsequently de-palmitoylated, RAB18 is solubilized by GDIs and redistributed to cellular membranes (mainly ER) (Figure 30).

It was further demonstrated that the acylation cycle could be modulated by the small-molecule inhibitors of palmitoylation and de-palmitoylation - 2-bromopalmitate and palmostatin B respectively. The inhibition of palmitoylation resulted in the reduction of LD size whilst the inhibition of de-palmitoylation resulted in the increase of LD size. Thus, modulation of the palmitoylation machinery is a viable and promising new target for steatosis treatment.

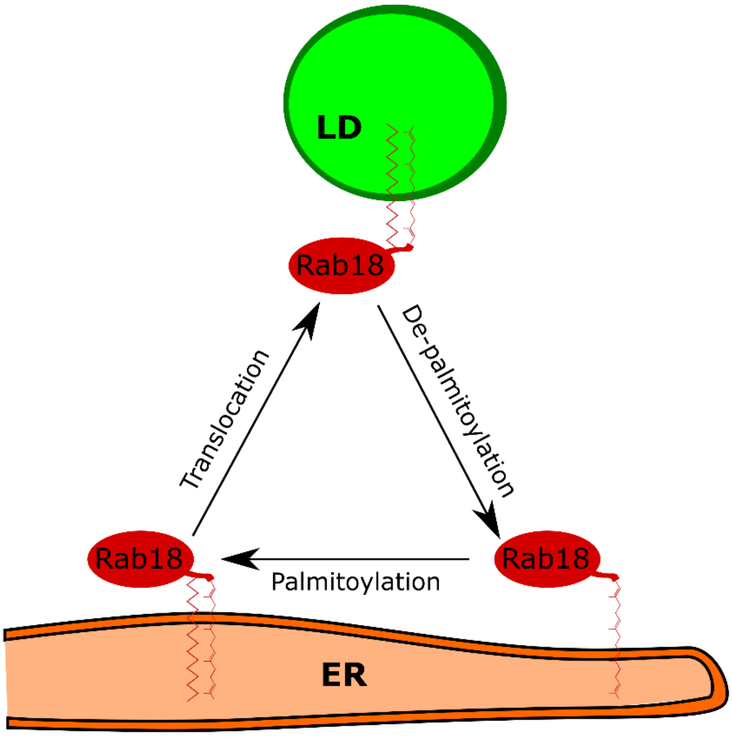

Figure 30 | Model of RAB18 localization

RAB18 is C-terminally geranylgeranylated conferring membrane affinity. This largely localizes to the ER. Upon activation, RAB18 is palmitoylated and translocated to the LD membrane. After its de-palmitoylation RAB18 is solubilized and returned to the ER membrane.

The absence of RAB18 in cells leads to enlarged, but fewer lipid droplets. Only transfection with WT RAB18 and active RAB18 mutants, which localized to the LD, prevented the formation of enlarged LDs in cells without endogenous RAB18. The transfection of mutants that did not localize to the LD – even constitutively active mutants- failed to reduce the LD size proving that the localization of RAB18 to the LD membrane prevented the enlargement. Therefore, RAB18 must have a protective role on the LD.

Testing the two canonical mechanisms of LD size reduction, only the inhibition of lipophagy reversed the enlargement of LDs and restored the LD number in cells with RAB18 downregulation. Thus, the enlargement of LDs after RAB18 KD was due to the increase in lipophagy. However, the autophagic flux in cells with RAB18 KD remained unchanged. Therefore, it is concluded that rather than modulating autophagy, the activity of RAB18 on the LD protects the LD from autophagic removal. Further investigation into the role of autophagy in cells with RAB18 downregulation showed that the activation of autophagy before the addition of OA resulted in the formation of larger LDs, whilst the inhibition of autophagy reverted the LD enlargement.

To explain how autophagy regulates the LD size after OA supplementation, following hypothetical container-based model of LD size regulation is proposed. Under basal unperturbed conditions, hepatocytes metabolize surplus lipotoxic FFAs and store them as TAGs in LDs. These LDs are subject to a steady state of autophagy to keep up an ample supply of phospholipids for the cell. When the LD are too large for autophagy or escape this steady recycling by other means, large LDs are created as seen in steatosis.

Following RAB18 knockdown or generally high autophagy more LDs are removed by autophagy, but the FFA volume which needs to be stored remains the same. To accommodate the same amount of FFA in fewer containers, the remaining LDs need to be enlarged, which results in the creation of large LDs. In the opposite case, when the steady state autophagy is stopped via inhibition, the cells accumulate LDs. This increases the storing capacity of the cell, so the same amount of FFA can be distributed over more LDs, leading to overall smaller LDs, which explains the smaller LDs after chloroquine and lalistat2 treatment. Thus, the ratio of large LDs to small LDs is controlled by the overall autophagy rate and the susceptibility of LDs to autophagy which is controlled by RAB18 (Figure 31).

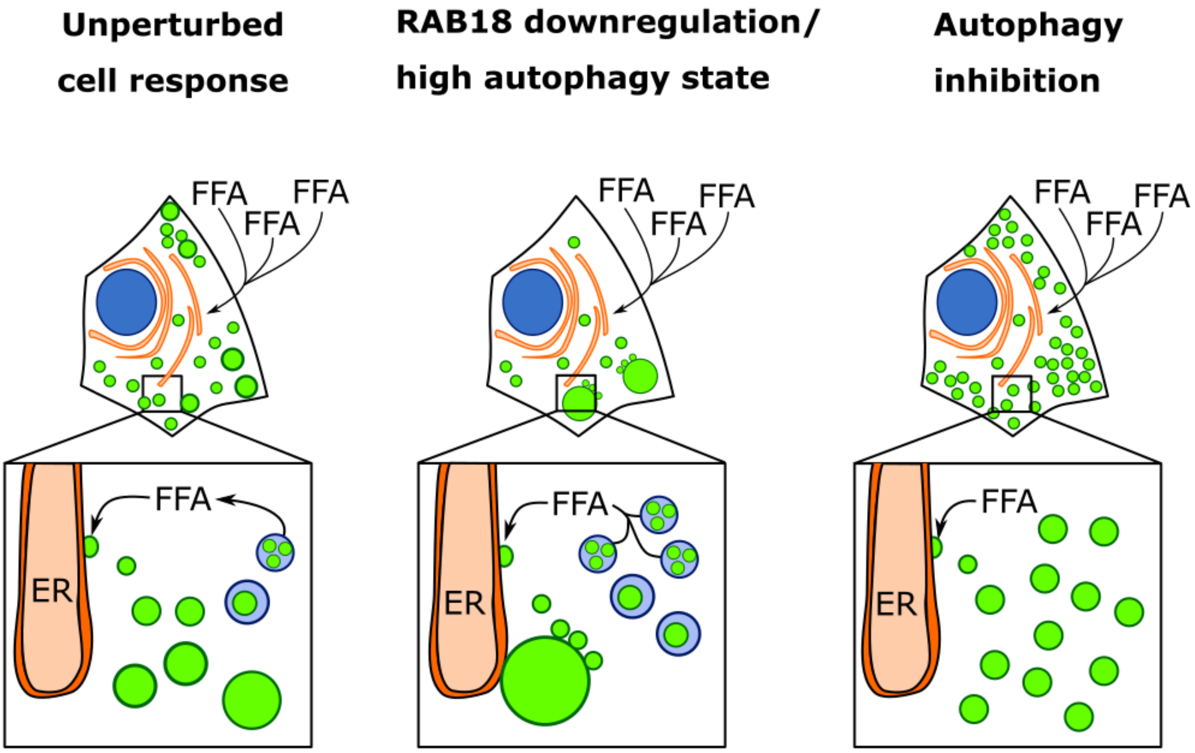

Figure 31 | Model of lipophagy based LD size control

Under physiologic conditions LDs are subjected to a steady state of autophagy. After induction of autophagy or RAB18 downregulation, the small LD are removed by enhanced autophagy. Only few large LDs remain that must store the same amount of FFA. Consequentially, they are further enlarged. Inhibition of the steady state autophagy leads to accumulation of the LDs. The same amount of FFA is now distributed among more LDs which lead to smaller, but more LDs.

Based on this model, it was predicted that blocking autophagy would result in numerous, but small LDs in hepatocytes. This hypothesis was tested *in vitro* in PHH and *in vivo* in mice. As predicted by the model, no large LDs were detected in primary hepatocytes and mice fed with a steatogenic diet after the inhibition of autophagy with chloroquine. Since chloroquine is a clinical approved drug, the inhibition of autophagy with chloroquine is considered a strong candidate for preventing LD accumulation in steatosis. Thus, a more promising candidate for the development of a treatment for NAFLD was identified by investigating the function of RAB18 on the LD.

5.6. Relevance to NAFLD

In this thesis inhibition of autophagy was found to reduce LD size when they are created, but not when they already persist in the cells. It could be argued that this limits the relevance to treating NAFLD. In most cases in which NAFLD is diagnosed, LDs are already present in the tissue. In this case autophagy was found to be beneficial and inhibition of autophagy harmful (Wang et al., 2017).

However, there are applications of this new concept in cases in which steatosis can be expected. Several drugs have been found to create steatosis via different pathways (Szalowska et al., 2014). Autophagy inhibition might prove to be a suitable treatment for these cases or even the cause for drug induced steatosis.

An interesting case for application can be found in combination with liver transplantation. 30.3% of all liver transplantation patients develop steatosis within the first year. 47.6% have developed it after 10 years (Hejlova et al., 2016). Among the prevalent risk factors currently considered are obesity, alcohol consumption and insulin resistance (Argo and Caldwell, 2009; Hejlova et al., 2016). The data presented in this thesis highly suggest that the state of autophagy could be a risk factor in these patients as well.

The inhibition of autophagy could also be part of a combination therapy. LD size reduction could induce via dietary changes or medication and the formation of large LDs temporarily suppressed by autophagy inhibition.

Finally, the causes and progression of NAFLD have not been fully understood yet. Theoretically, autophagy or the lack of it could also deregulate the LD size regulation, which could lead to one "hit" leading to NAFLD. It is therefore assumed that the autophagy in the liver needs to be carefully adjusted depending on the precise disease phenotype and underlying pathology.

5.7. Outlook

This work discussed the localization mechanics of RAB18 and its modulation as a pharmaceutical target for LD size regulation. However, this is only the first step towards a pharmaceutical use of acylation cycle inhibitors. Much is still unknown about the components of the RAB18 acylation machinery and its specificity, which is why caution must be applied when targeting it for therapeutic purposes. Future insights into the specific proteins and processes involved in RAB18 palmitoylation together with the development of more specific compounds to inhibit RAB18 acylation could be a viable route for future steatosis drug development.

A much more potent therapeutic tool was discovered in the modulation of autophagy in steatosis, which could also be easily translated to the clinic. As an approved drug chloroquine could be used for LD size reduction in steatosis, but chloroquine is a rather toxic reagent. The straightforward approach would be a follow-up study using hydroxychloroquine, which is less toxic and also an approved drug used as an anti-rheumatic drug (Fox, 1993). Data on the state of the liver tissue in rheumatic patients could further elucidate the effect of long-term autophagy inhibition on the LD size in the liver.

As another task during this thesis, CARS microscopy was applied for LD detection *in vivo*. However, this is only a small range of the many CARS application. With the right settings, theoretically, any chemical pattern can be imaged by this system. This makes *in vivo* CARS imaging a powerful tool in future mouse experimentation and, in the long run, human diagnostic.

Little is known about lipophagy, which is why the tentative link of RAB18 with autophagy is a promising lead in lipophagy research. The hypothesis that RAB18 interacts with RAB7 to regulate LD (micro-) autophagy can be further investigated using the RAB18 knockdown experiments established in this work.

Finally, this thesis provides a working model for LD size regulation and RAB18's role in it, which explains the data of this thesis, as well as other publications. However, this model of RAB18's function is neither exclusive nor complete and can be further expanded upon by testing it with different autophagy inhibitors and activators. Nonetheless, the findings concerning autophagy in the liver are promising, and show how we only have begun to understand the role of RAB18 and lipophagy in the liver.

6. References

Abarca-Gómez, L., Abdeen, Z.A., Hamid, Z.A., Abu-Rmeileh, N.M., Acosta-Cazares, B., Acuin, C., Adams, R.J., Aekplakorn, W., Afsana, K., Aguilar-Salinas, C.A., Agyemang, C., Ahmadvand, A., Ahrens, W., Ajlouni, K., Akhtaeva, N., Al-Hazzaa, H.M., Al-Othman, A.R., Al-Raddadi, R., Buhairan, F.A., Dhukair, S.A., Ali, M.M., Ali, O., Alkerwi, A., Alvarez-Pedrerol, M., Aly, E., Amarapurkar, D.N., Amouyel, P., Amuzu, A., Andersen, L.B., Anderssen, S.A., Andrade, D.S., Ängquist, L.H., Anjana, R.M., Aounallah-Skhiri, H., Araújo, J., Ariansen, I., Aris, T., Arlappa, N., Arveiler, D., Aryal, K.K., Aspelund, T., Assah, F.K., Assunção, M.C.F., Aung, M.S., Avdicová, M., Azevedo, A., Azizi, F., Babu, B.V., Bahijri, S., Baker, J.L., Balakrishna, N., Bamoshmoosh, M., Banach, M., Bandosz, P., Banegas, J.R., Barbagallo, C.M., Barceló, A., Barkat, A., Barros, A.J., Barros, M.V., Bata, I., Batieha, A.M., Batista, R.L., Batyrbek, A., Baur, L.A., Beaglehole, R., Romdhane, H.B., Benedics, J., Benet, M., Bennett, J.E., Bernabe-Ortiz, A., Bernotiene, G., Bettiol, H., Bhagyalaxmi, A., Bharadwaj, S., Bhargava, S.K., Bhatti, Z., Bhutta, Z.A., Bi, H., Bi, Y., Biehl, A., Bikbov, M., Bista, B., Bjelica, D.J., Bjerregaard, P., Bjertness, E., Bjertness, M.B., Björkelund, C., Blokstra, A., Bo, S., Bobak, M., Boddy, L.M., Boehm, B.O., Boeing, H., Boggia, J.G., Boissonnet, C.P., Bonaccio, M., Bongard, V., Bovet, P., Braeckevelt, L., Braeckman, L., Bragt, M.C., Brajkovich, I., Branca, F., Breckenkamp, J., Breda, J., Brenner, H., Brewster, L.M., Brian, G.R., Brinduse, L., Bruno, G., Bueno-de-Mesquita, H.B., Bugge, A., Buoncristiano, M., Burazeri, G., Burns, C., León, A.C. de, Cacciottolo, J., Cai, H., Cama, T., Cameron, C., Camolas, J., Can, G., Cândido, A.P.C., Capanzana, M., Capuano, V., Cardoso, V.C., Carlsson, A.C., Carvalho, M.J., Casanueva, F.F., Casas, J.-P., Caserta, C.A., Chamukuttan, S., Chan, A.W., Chan, Q., Chaturvedi, H.K., Chaturvedi, N., Chen, C.-J., Chen, F., Chen, H., Chen, S., Chen, Z., Cheng, C.-Y., Chetrit, A., Chikova-Iscener, E., Chiolero, A., Chiou, S.-T., Chirita-Emandi, A., Chirlaque, M.-D., Cho, B., Cho, Y., Christensen, K., Christofaro, D.G., Chudek, J., Cifkova, R., Cinteza, E., Claessens, F., Clays, E., Concin, H., Confortin, S.C., Cooper, C., Cooper, R., Coppinger, T.C., Costanzo, S., Cottel, D., Cowell, C., Craig, C.L., Crujeiras, A.B., Cucu, A., D'Arrigo, G., d'Orsi, E., Dallongeville, J., Damasceno, A., Damsgaard, C.T., Danaei, G., Dankner, R., Dantoft, T.M., Dastgiri, S., Dauchet, L., Davletov, K., Backer, G.D., Bacquer, D.D., Curtis, A.D., Gaetano, G. de, Henauw, S.D., Oliveira, P.D. de, Ridder, K.D., Smedt, D.D., Deepa, M., Deev, A.D., Dehghan, A., Delisle, H., Delpeuch, F., Deschamps, V., Dhana, K., Castelnuovo, A.F.D., Dias-da-Costa, J.S., Diaz, A., Dika, Z., Djalalinia, S., Do, H.T., Dobson, A.J., Donati, M.B., Donfrancesco, C., Donoso, S.P., Döring, A., Dorobantu, M., Dorosty, A.R., Doua, K., Drygas, W., Duan, J.L., Duante, C., Duleva, V., Dulskiene, V., Dzerve, V., Dziankowska-Zaborszczyk, E., Egbagbe, E.E., Eggertsen, R., Eiben, G., Ekelund, U., Ati, J.E., Elliott, P., Engle-Stone, R., Erasmus, R.T., Erem, C., Eriksen, L., Eriksson, J.G., Peña, J.E. la, Evans, A., Faeh, D., Fall, C.H., Sant'Angelo, V.F., Farzadfar, F., Felix-Redondo, F.J., Ferguson, T.S., Fernandes, R.A., Fernández-Bergés, D., Ferrante, D., Ferrari, M., Ferreccio, C., Ferrieres, J., Finn, J.D., Fischer, K., Flores, E.M., Föger, B., Foo, L.H., Forslund, A.-S., Forsner, M., Fouad, H.M., Francis, D.K., Franco, M. do C., Franco, O.H., Frontera, G., Fuchs, F.D., Fuchs, S.C., Fujita, Y., Furusawa, T., Gaciong, Z., Gafencu, M., Galeone, D., Galvano, F., Garcia-de-la-Hera, M., Gareta, D., Garnett, S.P., Gaspoz, J.-M., Gasull, M., Gates, L., Geiger, H., Geleijnse, J.M., Ghasemian, A., Giampaoli, S., Gianfagna, F., Gill, T.K., Giovannelli, J., Giwercman, A., Godos, J., Gogen, S., Goldsmith, R.A., Goltzman, D., Gonçalves, H., González-Leon, M., González-Rivas, J.P., Gonzalez-Gross, M., Gottrand, F., Graça, A.P., Graff-Iversen, S., Grafnetter, D., Grajda, A., Grammatikopoulou, M.G., Gregor, R.D., Grodzicki, T., Grøntved, A., Grosso, G., Gruden, G., Grujic, V., Gu, D., Gualdi-Russo, E., Guallar-Castillón, P., Guan, O.P., Gudmundsson, E.F., Gudnason, V., Guerrero, R., Guessous, I., Guimaraes, A.L., Gulliford, M.C., Gunnlaugsdottir, J., Gunter, M., Guo, X., Guo, Y., Gupta, P.C., Gupta, R., Gureje, O., Gurzkowska, B., Gutierrez, L., Gutzwiller, F., Hadaegh, F., Hadjigeorgiou, C.A., Si-Ramlee, K., Halkjær, J., Hambleton, I.R., Hardy, R., Kumar, R.H., Hassapidou, M., Hata, J., Hayes, A.J., He, J., Heidinger-Felso, R., Heinen, M., Hendriks, M.E., Henriques, A., Cadena, L.H., Herrala, S., Herrera, V.M., Herter-Aeberli, I., Heshmat, R., Hihtaniemi, I.T., Ho, S.Y., Ho, S.C., Hobbs, M., Hofman, A., Hopman, W.M., Horimoto, A.R., Hormiga, C.M., Horta, B.L., Houti, L., Howitt, C., Htay, T.T., Htet, A.S., Htike, M.M.T., Hu, Y., Huerta, J.M., Petrescu, C.H., Huisman, M., Husseini, A., Huu, C.N., Huybrechts, I., Hwalla, N., Hyska, J., Iacoviello, L., Iannone, A.G., Ibarluzea, J.M., Ibrahim, M.M., Ikeda, N., Ikram, M.A., Irazola, V.E., Islam, M., Ismail, A. al-Safi, Ivkovic, V., Iwasaki, M., Jackson, R.T., Jacobs, J.M., Jaddou, H., Jafar, T., Jamil, K.M., Jamrozik, K., Janszky, I., Jarani, J., Jasienska, G., Jelakovic, A., Jelakovic, B., Jennings, G., Jeong, S.-L., Jiang, C.Q., Jiménez-Acosta, S.M., Joffres, M., Johansson, M., Jonas, J.B., Jørgensen, T., Joshi, P., Jovic, D.P., Józwiak, J., Juolevi, A., Jurak, G., Jureša, V., Kaaks, R., Kafatos, A., Kajantie, E.O., Kalter-Leibovici, O., Kamaruddin, N.A., Kapantais, E., Karki, K.B., Kasaeian, A., Katz, J., Kauhanen, J., Kaur, P., Kavousi, M., Kazakbaeva, G., Keil, U., Boker, L.K., Keinänen-Kiukaanniemi, S., Kelishadi, R., Kelleher, C., Kemper, H.C., Kengne, Andre P., Kerimkulova, A., Kersting, M., Key, T., Khader, Y.S., Khalili, D., Khang, Y.-H., Khateeb, M., Khaw, K.-T., Khouw, I.M., Kiechl-Kohlendorfer, U., Kiechl, S., Killewo, J., Kim, J., Kim, Y.-Y., Klimont, J., Klumbiene, J., Knoflach, M., Koirala, B., Kolle, E., Kolsteren, P., Korrovits, P., Kos, J., Koskinen, S., Kouda, K., Kovacs, V.A., Kowlessur, S., Koziel, S., Kratzer, W., Kriemler, S., Kristensen, P.L., Krokstad, S., Kromhout, D., Kruger, H.S., Kubinova, R., Kuciene, R., Kuh, D., Kujala, U.M., Kulaga, Z., Kumar, R.K., Kunešová, M., Kurjata, P., Kusuma, Y.S., Kuulasmaa, K., Kyobutungi, C., La, Q.N., Laamiri, F.Z., Laatikainen, T., Lachat, C., Laid, Y., Lam, T.H., Landrove, O., Lanska, V., Lappas, G., Larijani, B., Laugsand, L.E., Lauria, L., Laxmaiah, A., Bao, K.L.N., Le, T.D., Lebanan, M.A.O., Leclercq, C., Lee, Jeannette, Lee, Jeonghee, Lehtimäki, T., León-Muñoz, L.M., Levitt, N.S., Li, Y., Lilly, C.L., Lim, W.-Y., Lima-Costa, M.F., Lin, H.-H., Lin, X., Lind, L., Linneberg, A., Lissner, L., Litwin, M., Liu, J., Loit, H.-M., Lopes, L., Lorbeer, R., Lotufo, P.A., Lozano, J.E., Luksiene, D., Lundqvist, A., Lunet, N., Lytsy, P., Ma, G., Ma, J., Machado-Coelho, G.L., Machado-Rodrigues, A.M., Machi, S., Maggi, S., Magliano, D.J., Magriplis, E., Mahaletchumy, A., Maire, B., Majer, M., Makdisse, M., Malekzadeh, R., Malhotra, R., Rao, K.M., Malyutina, S., Manios, Y., Mann, J.I., Manzato, E., Margozzini, P., Markaki, A., Markey, O., Marques, L.P., Marques-Vidal, P., Marrugat, J., Martin-Prevel, Y., Martin, R., Martorell, R., Martos, E., Marventano, S., Masoodi, S.R., Mathiesen, E.B., Matijasevich, A., Matsha, T.E., Mazur, A., Mbanya, J.C.N., McFarlane, S.R., McGarvey, S.T., McKee, M., McLachlan, S., McLean, R.M., McLean, S.B., McNulty, B.A., Yusof, S.M., Mediene-Benchekor, S., Medzioniene, J., Meirhaeghe, A., Meisfjord, J., Meisinger, C., Menezes, A.M.B., Menon, G.R., Mensink, G.B., Meshram, I.I., Metspalu, A., Meyer, H.E., Mi, J., Michaelsen, K.F., Michels, N., Mikkel, K., Miller, J.C., Minderico, C.S., Miquel, J.F., Miranda, J.J., Mirkopoulou, D., Mirrakhimov, E., Mišigoj-Durakovic, M., Mistretta, A., Mocanu, V., Modesti, P.A., Mohamed, M.K., Mohammad, K., Mohammadifard, N., Mohan, V., Mohanna, S., Yusoff, Muhammad Fadhli Mohd, Molbo, D., Møllehave, L.T., Møller, N.C., Molnár, D., Momenan, A., Mondo, C.K., Monterrubio, E.A., Monyeki, K.D.K., Moon, J.S., Moreira, L.B., Morejon, A., Moreno, L.A., Morgan, K., Mortensen, E.L., Moschonis, G., Mossakowska, M., Mostafa, A., Mota, J., Mota-Pinto, A., Motlagh, M.E., Motta, J., Mu, T.T., Muc, M., Muiesan, M.L., Müller-Nurasyid, M., Murphy, N., Mursu, J., Murtagh, E.M., Musil, V., Nabipour, I., Nagel, G., Naidu, B.M., Nakamura, H., Námešná, J., Nang, E.E.K., Nangia, V.B., Nankap, M., Narake, S., Nardone, P., Navarrete-Muñoz, E.M., Neal, W.A., Nenko, I., Neovius, M., Nervi, F., Nguyen, C.T., Nguyen, N.D., Nguyen, Q.N., Nieto-Martínez, R.E., Ning, G., Ninomiya, T., Nishtar, S., Noale, M., Noboa, O.A., Norat, T., Norie, S., Noto, D., Nsour, M.A., O'Reilly, D., Obreja, G., Oda, E., Oehlers, G., Oh, K., Ohara, K., Olafsson, Ö., Olinto, M.T.A., Oliveira, I.O., Oltarzewski, M., Omar, M.A., Onat, A., Ong, S.K., Ono, L.M., Ordunez, P., Ornelas, R., Ortiz, A.P., Osler, M., Osmond, C., Ostojic, S.M., Ostovar, A., Otero, J.A., Overvad, K., Owusu-Dabo, E., Paccaud, F.M., Padez, C., Pahomova, E., Pajak, A., Palli, D., Palloni, A., Palmieri, L., Pan, W.-H., Panda-Jonas, S., Pandey, A., Panza, F., Papandreou, D., Park, S.-W., Parnell, W.R., Parsaeian, M., Pascanu, I.M., Patel, N.D., Pecin, I., Pednekar, M.S., Peer, N., Peeters, P.H., Peixoto, S.V., Peltonen, M., Pereira, A.C., Perez-Farinos, N., Pérez, C.M., Peters, A., Petkeviciene, J., Petrauskiene, A., Peykari, N., Pham, S.T., Pierannunzio, D., Pigeot, I., Pikhart, H., Pilav, A., Pilotto, L., Pistelli, F., Pitakaka, F., Piwonska, A., Plans-Rubió, P., Poh, B.K., Pohlabeln, H., Pop, R.M., Popovic, S.R., Porta, M., Portegies, M.L., Posch, G., Poulimeneas, D., Pouraram, H., Pourshams, A., Poustchi, H., Pradeepa, R., Prashant, M., Price, J.F., Puder, J.J., Pudule, I., Puiu, M., Punab, M., Qasrawi, R.F., Qorbani, M., Bao, T.Q., Radic, I., Radisauskas, R., Rahman, Mahfuzar, Rahman, Mahmudur, Raitakari, O., Raj, M., Rao, S.R., Ramachandran, A., Ramke, J., Ramos, E., Ramos, R., Rampal, L., Rampal, S., Rascon-Pacheco, R.A., Redon, J., Reganit, P.F.M., Ribas-Barba, L., Ribeiro, R., Riboli, E., Rigo, F., Wit, T.F.R. de, Rito, A., Ritti-Dias, R.M., Rivera, J.A., Robinson, S.M., Robitaille, C., Rodrigues, D., Rodríguez-Artalejo, F., Rodriguez-Perez, M. del C., Rodríguez-Villamizar, L.A., Rojas-Martinez, R., Rojroongwasinkul, N., Romaguera, D., Ronkainen, K., Rosengren, A., Rouse, I., Roy, J.G., Rubinstein, A., Rühli, F.J., Ruiz-Betancourt, B.S., Russo, P., Rutkowski, M., Sabanayagam, C., Sachdev, H.S., Saidi, O., Salanave, B., Martinez, E.S., Salmerón, D., Salomaa, V., Salonen, J.T., Salvetti, M., Sánchez-Abanto, J., Sandjaja, Sans, S., Marina, L.S., Santos, D.A., Santos, I.S., Santos, O., Santos, R.N. dos, Santos, R., Saramies, J.L., Sardinha, L.B., Sarrafzadegan, N., Saum, K.-U., Savva, S., Savy, M., Scazufca, M., Rosario, A.S., Schargrodsky, H., Schienkiewitz, A., Schipf, S., Schmidt, C.O., Schmidt, I.M., Schultsz, C., Schutte, A.E., Sein, A.A., Sen, A., Senbanjo, I.O., Sepanlou, S.G., Serra-Majem, L., Shalnova, S.A., Sharma, S.K., Shaw, J.E., Shibuya, K., Shin, D.W., Shin, Y., Shiri, R., Siani, A., Siantar, R., Sibai, A.M., Silva, A.M., Silva, D.A.S., Simon, M., Simons, J., Simons, L.A., Sjöberg, A., Sjöström, M., Skovbjerg, S., Slowikowska-Hilczer, J., Slusarczyk, P., Smeeth, L., Smith, M.C., Snijder, M.B., So, H.-K., Sobngwi, E., Söderberg, S., Soekatri, M.Y., Solfrizzi, V., Sonestedt, E., Song, Y., Sørensen, T.I., Soric, M., Jérome, C.S., Soumare, A., Spinelli, A., Spiroski, I., Staessen, J.A., Stamm, H., Starc, G., Stathopoulou, M.G., Staub, K., Stavreski, B., Steene-Johannessen, J., Stehle, P., Stein, A.D., Stergiou, G.S., Stessman, J., Stieber, J., Stöckl, D., Stocks, T., Stokwiszewski, J., Stratton, G., Stronks, K., Strufaldi, M.W., Suárez-Medina, R., Sun, C.-A., Sundström, J., Sung, Y.-T., Sunyer, J., Suriyawongpaisal, P., Swinburn, B.A., Sy, R.G., Szponar, L., Tai, E.S., Tammesoo, M.-L., Tamosiunas, A., Tan, E.J., Tang, X., Tanser, F., Tao, Y., Tarawneh, M.R., Tarp, J., Tarqui-Mamani, C.B., Tautu, O.-F., Braunerová, R.T., Taylor, A., Tchibindat, F., Theobald, H., Theodoridis, X., Thijs, L., Thuesen, B.H., Tjonneland, A., Tolonen, H.K., Tolstrup, J.S., Topbas, M., Topór-Madry, R., Tormo, M.J., Tornaritis, M.J., Torrent, M., Toselli, S., Traissac, P., Trichopoulos, D., Trichopoulou, A., Trinh, O.T., Trivedi, A., Tshepo, L., Tsigga, M., Tsugane, S., Tulloch-Reid, M.K., Tullu, F., Tuomainen, T.-P., Tuomilehto, J., Turley, M.L., Tynelius, P., Tzotzas, T., Tzourio, C., Ueda, P., Ugel, E.E., Ukoli, F.A., Ulmer, H., Unal, B., Uusitalo, H.M., Valdivia, G., Vale, S., Valvi, D., Schouw, Y.T. van der, Herck, K.V., Minh, H.V., Rossem, L. van, Schoor, N.M.V., Valkengoed, I.G. van, Vanderschueren, D., Vanuzzo, D., Vatten, L., Vega, T., Veidebaum, T., Velasquez-Melendez, G., Velika, B., Veronesi, G., Verschuren, W.M., Victora, C.G., Viegi, G., Viet, L., Viikari-Juntura, E., Vineis, P., Vioque, J., Virtanen, J.K., Visvikis-Siest, S., Viswanathan, B., Vlasoff, T., Vollenweider, P., Völzke, H., Voutilainen, S., Vrijheid, M., Wade, A.N., Wagner, A., Waldhör, T., Walton, J., Bebakar, W.M.W., Mohamud, W.N.W., Wanderley, R.S., Wang, M.-D., Wang, Q., Wang, Y.X., Wang, Y.-W., Wannamethee, S.G., Wareham, N., Weber, A., Wedderkopp, N., Weerasekera, D., Whincup, P.H., Widhalm, K., Widyahening, I.S., Wiecek, A., Wijga, A.H., Wilks, R.J., Willeit, J., Willeit, P., Wilsgaard, T., Wojtyniak, B., Wong-McClure, R.A., Wong, J.Y., Wong, J.E., Wong, T.Y., Woo, J., Woodward, M., Wu, F.C., Wu, J., Wu, S., Xu, H., Xu, L., Yamborisut, U., Yan, W., Yang, X., Yardim, N., Ye, X., Yiallouros, P.K., Yngve, A., Yoshihara, A., You, Q.S., Younger-Coleman, N.O., Yusoff, F., Yusoff, Muhammad Fadhli M., Zaccagni, L., Zafiropulos, V., Zainuddin, A.A., Zambon, S., Zampelas, A., Zamrazilová, H., Zdrojewski, T., Zeng, Y., Zhao, D., Zhao, W., Zheng, W., Zheng, Y., Zholdin, B., Zhou, M., Zhu, D., Zhussupov, B., Zimmermann, E., Cisneros, J.Z., Bentham, J., Cesare, M.D., Bilano, V., Bixby, H., Zhou, B., Stevens, G.A., Riley, L.M., Taddei, C., Hajifathalian, K., Lu, Y., Savin, S., Cowan, M.J., Paciorek, C.J., Chirita-Emandi, A., Hayes, A.J., Katz, J., Kelishadi, R., Kengne, Andre Pascal, Khang, Y.-H., Laxmaiah, A., Li, Y., Ma, J., Miranda, J.J., Mostafa, A., Neovius, M., Padez, C., Rampal, L., Zhu, A., Bennett, J.E., Danaei, G., Bhutta, Z.A., Ezzati, M., 2017. Worldwide trends in body-mass index, underweight, overweight, and obesity from 1975 to 2016: a pooled analysis of 2416 population-based measurement studies in 128·9 million children, adolescents, and adults. The Lancet 390, 2627–2642. https://doi.org/10.1016/S0140-6736(17)32129-3

Alberts, B., Johnson, A., Lewis, J., Raff, M., Roberts, K., Walter, P., 2008. Intracellular Compartments and Protein Sorting, in: Molecular Biology of the Cell. Garland Science Taylor & Francis, p. 697.

Argo, C.K., Caldwell, S.H., 2009. Epidemiology and Natural History of Non-Alcoholic Steatohepatitis. Clinics in Liver Disease 13, 511–531. https://doi.org/10.1016/j.cld.2009.07.005

Arjmand, A., Angelis, C.T., Christou, V., Tzallas, A.T., Tsipouras, M.G., Glavas, E., Forlano, R., Manousou, P., Giannakeas, N., 2020. Training of Deep Convolutional Neural Networks to Identify Critical Liver Alterations in Histopathology Image Samples. Applied Sciences 10, 42. https://doi.org/10.3390/app10010042

Ascha, M.S., Hanouneh, I.A., Lopez, R., Tamimi, T.A.-R., Feldstein, A.F., Zein, N.N., 2010. The incidence and risk factors of hepatocellular carcinoma in patients with nonalcoholic steatohepatitis. Hepatology 51, 1972–1978. https://doi.org/10.1002/hep.23527

Baerga, R., Zhang, Y., Chen, P.-H., Goldman, S., Jin, S.V., 2009. Targeted deletion of autophagy-related 5 (atg5) impairs adipogenesis in a cellular model and in mice. Autophagy 5, 1118–1130. https://doi.org/10.4161/auto.5.8.9991

Bartlett, K., Eaton, S., 2004. Mitochondrial β-oxidation. European Journal of Biochemistry 271, 462–469. https://doi.org/10.1046/j.1432-1033.2003.03947.x

BasuRay, S., 2019. RAB18 modulates autophagy in human stellate cells. Journal of Clinical Lipidology 13, 832–838. https://doi.org/10.1016/j.jacl.2019.07.006

Bechmann, L.P., Hannivoort, R.A., Gerken, G., Hotamisligil, G.S., Trauner, M., Canbay, A., 2012. The interaction of hepatic lipid and glucose metabolism in liver diseases. Journal of Hepatology 56, 952–964. https://doi.org/10.1016/j.jhep.2011.08.025

Bekbulat, F., Schmitt, D., Feldmann, A., Huesmann, H., Eimer, S., Juretschke, T., Beli, P., Behl, C., Kern, A., 2020. RAB18 Loss Interferes With Lipid Droplet Catabolism and Provokes Autophagy Network Adaptations. Journal of Molecular Biology 432, 1216–1234. https://doi.org/10.1016/j.jmb.2019.12.031

Bem, D., Yoshimura, S.-I., Nunes-Bastos, R., Bond, F.F., Kurian, M.A., Rahman, F., Handley, M.T., Hadzhiev, Y., Masood, I., Straatman-Iwanowska, A.A., Cullinane, A.R., McNeill, A., Pasha, S.S., Kirby, G.A., Foster, K., Ahmed, Z., Morton, J.E., Williams, D., Graham, J.M., Dobyns, W.B., Burglen, L., Ainsworth, J.R., Gissen, P., MÃ¼ller, F., Maher, E.R., Barr, F.A., Aligianis, I.A., 2011. Loss-of-Function Mutations in RAB18 Cause Warburg Micro Syndrome. American Journal of Human Genetics 88, 499–507.

Bence, K.K., Birnbaum, M.J., 2020. Metabolic drivers of non-alcoholic fatty liver disease. Mol Metab 101143. https://doi.org/10.1016/j.molmet.2020.101143

Bessone, F., Razori, M., Roma, M., 2019. Molecular pathways of nonalcoholic fatty liver disease development and progression. Cellular and Molecular Life Sciences 76. https://doi.org/10.1007/s00018-018-2947-0

Bik, E., Mateuszuk, L., Orleanska, J., Baranska, M., Chlopicki, S., Majzner, K., 2021. Chloroquine-Induced Accumulation of Autophagosomes and Lipids in the Endothelium. International Journal of Molecular Sciences 22, 2401. https://doi.org/10.3390/ijms22052401

Bos, J.L., 1989. ras Oncogenes in Human Cancer: A Review. Cancer Res 49, 4682–4689.

Bradley, J., Pope, I., Masia, F., Sanusi, R., Langbein, W., Swann, K., Borri, P., 2016. Quantitative imaging of lipids in live mouse oocytes and early embryos using CARS microscopy. Development 143, 2238–2247. https://doi.org/10.1242/dev.129908

Brunt, E.M., Neuschwander-Tetri, B.A., Oliver, D., Wehmeier, K.R., Bacon, B.R., 2004. Nonalcoholic steatohepatitis: Histologic features and clinical correlations with 30 blinded biopsy specimens. Human Pathology 35, 1070–1082. https://doi.org/10.1016/j.humpath.2004.04.017

Buzzetti, E., Pinzani, M., Tsochatzis, E.A., 2016. The multiple-hit pathogenesis of non-alcoholic fatty liver disease (NAFLD). Metabolism 65, 1038–1048. https://doi.org/10.1016/j.metabol.2015.12.012

Caillon, L., Nieto, V., Gehan, P., Omrane, M., Rodriguez, N., Monticelli, L., Thiam, A.R., 2020. Triacylglycerols sequester monotopic membrane proteins to lipid droplets. Nature Communications 11, 3944. https://doi.org/10.1038/s41467-020-17585-8

Caldwell, S., Ikura, Y., Dias, D., Isomoto, K., Yabu, A., Moskaluk, C., Pramoonjago, P., Simmons, W., Scruggs, H., Rosenbaum, N., Wilkinson, T., Toms, P., Argo, C.K., Al-Osaimi, A.M.S., Redick, J.A., 2010. Hepatocellular ballooning in NASH. Journal of Hepatology 53, 719–723. https://doi.org/10.1016/j.jhep.2010.04.031

Carpanini, S.M., McKie, L., Thomson, D., Wright, A.K., Gordon, S.L., Roche, S.L., Handley, M.T., Morrison, H., Brownstein, D., Wishart, T.M., Cousin, M.A., Gillingwater, T.H., Aligianis, I.A., Jackson, I.J., 2014. A novel mouse model of Warburg Micro syndrome reveals roles for RAB18 in eye development and organisation of the neuronal cytoskeleton. Disease Models & Mechanisms 7, 711–722. https://doi.org/10.1242/dmm.015222

Cases, S., Smith, S.J., Zheng, Y.-W., Myers, H.M., Lear, S.R., Sande, E., Novak, S., Collins, C., Welch, C.B., Lusis, A.J., Erickson, S.K., Farese, R.V., 1998. Identification of a gene encoding an acyl CoA:diacylglycerol acyltransferase, a key enzyme in triacylglycerol synthesis. Proc Natl Acad Sci U S A 95, 13018–13023.

CDC, 2020. Defining Adult Overweight and Obesity [WWW Document]. URL https://www.cdc.gov/obesity/adult/defining.html (accessed 9.30.20).

Chakrabarti, P., English, T., Shi, J., Smas, C.M., Kandror, K.V., 2010. Mammalian Target of Rapamycin Complex 1 Suppresses Lipolysis, Stimulates Lipogenesis, and Promotes Fat Storage. Diabetes 59, 775–781. https://doi.org/10.2337/db09-1602

Chalasani, N., Younossi, Z., Lavine, J.E., Charlton, M., Cusi, K., Rinella, M., Harrison, S.A., Brunt, E.M., Sanyal, A.J., 2018. The diagnosis and management of nonalcoholic fatty liver disease: Practice guidance from the American Association for the Study of Liver Diseases. Hepatology 67, 328–357. https://doi.org/10.1002/hep.29367

Chavrier, P., Goud, B., 1999. The role of ARF and Rab GTPases in membrane transport. Current Opinion in Cell Biology 11, 466–475. https://doi.org/10.1016/S0955-0674(99)80067-2

Choi, J.Y., Qiao, Q., Hong, S.-H., Kim, C.M., Jeong, J.-H., Kim, Y.-G., Jung, Y.-K., Wu, H., Park, H.H., 2017. CIDE domains form functionally important higher-order assemblies for DNA fragmentation. PNAS 114, 7361–7366. https://doi.org/10.1073/pnas.1705949114

Choudhary, V., Golani, G., Joshi, A.S., Cottier, S., Schneiter, R., Prinz, W.A., Kozlov, M.M., 2018. Architecture of lipid droplets in endoplasmic reticulum is determined by phospholipid intrinsic curvature. Curr Biol 28, 915-926.e9. https://doi.org/10.1016/j.cub.2018.02.020

Chung, J., Wu, X., Lambert, T.J., Lai, Z.W., Walther, T.C., Farese, R.V., 2019. LDAF1 and Seipin Form a Lipid Droplet Assembly Complex. Developmental Cell 51, 551-563.e7. https://doi.org/10.1016/j.devcel.2019.10.006

Coleman, R.A., 2020. The “discovery” of lipid droplets: A brief history of organelles hidden in plain sight. Biochimica et Biophysica Acta (BBA) - Molecular and Cell Biology of Lipids 1865, 158762. https://doi.org/10.1016/j.bbalip.2020.158762

Crawford, M., Whisner, C., Al-Nakkash, L., Sweazea, K.L., 2019. Six-Week High-Fat Diet Alters the Gut Microbiome and Promotes Cecal Inflammation, Endotoxin Production, and Simple Steatosis without Obesity in Male Rats. Lipids 54, 119–131. https://doi.org/10.1002/lipd.12131

Czaja, M.J., 2016. Function of Autophagy in Nonalcoholic Fatty Liver Disease. Dig Dis Sci 61, 1304–1313. https://doi.org/10.1007/s10620-015-4025-x

de Jong, M., 2015. Frank Rösch: Nuclear and Radiochemistry, Volume 1: Introduction. Eur J Nucl Med Mol Imaging 42, 1624–1624. https://doi.org/10.1007/s00259-015-3031-8

Dejgaard, S.Y., Murshid, A., Erman, A., Kızılay, Ö., Verbich, D., Lodge, R., Dejgaard, K., Ly-Hartig, T.B.N., Pepperkok, R., Simpson, J.C., Presley, J.F., 2008. Rab18 and Rab43 have key roles in ER-Golgi trafficking. Journal of Cell Science 121, 2768–2781. https://doi.org/10.1242/jcs.021808

Dejgaard, S.Y., Presley, J.F., 2019a. Rab18: new insights into the function of an essential protein. Cell. Mol. Life Sci. 76, 1935–1945. https://doi.org/10.1007/s00018-019-03050-3

Dejgaard, S.Y., Presley, J.F., 2019b. Rab18 regulates lipolysis via Arf/GBF1 and adipose triglyceride lipase. Biochemical and Biophysical Research Communications 520, 526–531. https://doi.org/10.1016/j.bbrc.2019.10.069

Dekker, F.J., Rocks, O., Vartak, N., Menninger, S., Hedberg, C., Balamurugan, R., Wetzel, S., Renner, S., Gerauer, M., Schölermann, B., Rusch, M., Kramer, J.W., Rauh, D., Coates, G.W., Brunsveld, L., Bastiaens, P.I.H., Waldmann, H., 2010. Small-molecule inhibition of APT1 affects Ras localization and signaling. Nature Chemical Biology 6, 449–456. https://doi.org/10.1038/nchembio.362

Deng, Y., Zhou, C., Mirza, A.H., Bamigbade, A.T., Zhang, S., Xu, S., Liu, P., 2021. Rab18 binds PLIN2 and ACSL3 to mediate lipid droplet dynamics. Biochimica et Biophysica Acta (BBA) - Molecular and Cell Biology of Lipids 1866, 158923. https://doi.org/10.1016/j.bbalip.2021.158923

Di Leo, L., Vegliante, R., Ciccarone, F., Salvatori, I., Scimeca, M., Bonanno, E., Sagnotta, A., Grazi, G.L., Aquilano, K., Ciriolo, M.R., 2019. Forcing ATGL expression in hepatocarcinoma cells imposes glycolytic rewiring through PPAR-α/p300-mediated acetylation of p53. Oncogene 38, 1860–1875. https://doi.org/10.1038/s41388-018-0545-0

Ding, W.-X., Li, M., Chen, X., Ni, H.-M., Lin, C.-W., Gao, W., Lu, B., Stolz, D.B., Clemens, D.L., Yin, X.-M., 2010. Autophagy Reduces Acute Ethanol-Induced Hepatotoxicity and Steatosis in Mice. Gastroenterology 139, 1740–1752. https://doi.org/10.1053/j.gastro.2010.07.041

Donnelly, K.L., Smith, C.I., Schwarzenberg, S.J., Jessurun, J., Boldt, M.D., Parks, E.J., 2005. Sources of fatty acids stored in liver and secreted via lipoproteins in patients with nonalcoholic fatty liver disease. J Clin Invest 115, 1343–1351. https://doi.org/10.1172/JCI23621

Dossou, A.S., Basu, A., 2019. The Emerging Roles of mTORC1 in Macromanaging Autophagy. Cancers 11, 1422. https://doi.org/10.3390/cancers11101422

Duncan, J.A., Gilman, A.G., 1998. A Cytoplasmic Acyl-Protein Thioesterase That Removes Palmitate from G Protein α Subunits and p21RAS*. Journal of Biological Chemistry 273, 15830–15837. https://doi.org/10.1074/jbc.273.25.15830

Estes, C., Razavi, H., Loomba, R., Younossi, Z., Sanyal, A.J., 2018. Modeling the epidemic of nonalcoholic fatty liver disease demonstrates an exponential increase in burden of disease. Hepatology 67, 123–133. https://doi.org/10.1002/hep.29466

Evans, C.L., Potma, E.O., Puoris’haag, M., Cote, D., Lin, C.P., Xie, X.S., 2005. Chemical imaging of tissue in vivo with video-rate coherent anti-Stokes Raman scattering microscopy. Proceedings of the National Academy of Sciences 102, 16807–16812. https://doi.org/10.1073/pnas.0508282102

Feldmann, A., Bekbulat, F., Huesmann, H., Ulbrich, S., Tatzelt, J., Behl, C., Kern, A., 2017. The RAB GTPase RAB18 modulates macroautophagy and proteostasis. Biochemical and Biophysical Research Communications 486, 738–743. https://doi.org/10.1016/j.bbrc.2017.03.112

Folkerts, H., Hilgendorf, S., Vellenga, E., Bremer, E., Wiersma, V.R., 2019. The multifaceted role of autophagy in cancer and the microenvironment. Medicinal Research Reviews 39, 517–560. https://doi.org/10.1002/med.21531

Fox, R.I., 1993. Mechanism of action of hydroxychloroquine as an antirheumatic drug. Seminars in Arthritis and Rheumatism 23, 82–91. https://doi.org/10.1016/S0049-0172(10)80012-5

Friedman, S.L., 2008. Mechanisms of Hepatic Fibrogenesis. Gastroenterology 134, 1655–1669. https://doi.org/10.1053/j.gastro.2008.03.003

Fu, Y., Huff, T.B., Wang, H.-W., Wang, H., Cheng, J.-X., 2008. Ex vivo and in vivo imaging of myelin fibers in mouse brain by coherent anti-Stokes Raman scattering microscopy. Opt. Express, OE 16, 19396–19409. https://doi.org/10.1364/OE.16.019396

Fu, Y., Wang, H., Shi, R., Cheng, J.-X., 2006. Characterization of photodamage in coherent anti-Stokes Raman scattering microscopy. Opt. Express, OE 14, 3942–3951. https://doi.org/10.1364/OE.14.003942

Fukata, Y., Murakami, T., Yokoi, N., Fukata, M., 2016. Chapter Four - Local Palmitoylation Cycles and Specialized Membrane Domain Organization, in: Bennett, V. (Ed.), Current Topics in Membranes, Dynamic Plasma Membranes. Academic Press, pp. 97–141. https://doi.org/10.1016/bs.ctm.2015.10.003

Gallus, S., Lugo, A., Murisic, B., Bosetti, C., Boffetta, P., La Vecchia, C., 2015. Overweight and obesity in 16 European countries. Eur J Nutr 54, 679–689. https://doi.org/10.1007/s00394-014-0746-4

Gerondopoulos, A., Bastos, R.N., Yoshimura, S., Anderson, R., Carpanini, S., Aligianis, I., Handley, M.T., Barr, F.A., 2014. Rab18 and a Rab18 GEF complex are required for normal ER structure. Journal of Cell Biology 205, 707–720. https://doi.org/10.1083/jcb.201403026

Gong, J., Sun, Z., Wu, L., Xu, W., Schieber, N., Xu, D., Shui, G., Yang, H., Parton, R.G., Li, P., 2011. Fsp27 promotes lipid droplet growth by lipid exchange and transfer at lipid droplet contact sites. Journal of Cell Biology 195, 953–963. https://doi.org/10.1083/jcb.201104142

Govender, T., Ramanna, L., Rawat, I., Bux, F., 2012. BODIPY staining, an alternative to the Nile Red fluorescence method for the evaluation of intracellular lipids in microalgae. Bioresource Technology 114, 507–511. https://doi.org/10.1016/j.biortech.2012.03.024

Greenspan, P., Mayer, E.P., Fowler, S.D., 1985. Nile red: a selective fluorescent stain for intracellular lipid droplets. The Journal of Cell Biology 100, 965–973. https://doi.org/10.1083/jcb.100.3.965

Haas, J., 2013. The Role of DGAT1 in Triglyceride Uptake, Synthesis and Storage. UCSF.

Hales, C.M., 2017. Prevalence of Obesity Among Adults and Youth: United States, 2015–2016 8.

Hancock, J.F., Magee, A.I., Childs, J.E., Marshall, C.J., 1989. All ras proteins are polyisoprenylated but only some are palmitoylated. Cell 57, 1167–1177. https://doi.org/10.1016/0092-8674(89)90054-8

Hashimoto, E., Tokushige, K., 2011. Prevalence, gender, ethnic variations, and prognosis of NASH. Journal of gastroenterology 46 Suppl 1, 63–9. https://doi.org/10.1007/s00535-010-0311-8

Haspel, J., Shaik, R.S., Ifedigbo, E., Nakahira, K., Dolinay, T., Englert, J.A., Choi, A.M.K., 2011. Characterization of macroautophagic flux in vivo using a leupeptin-based assay. Autophagy 7, 629–642. https://doi.org/10.4161/auto.7.6.15100

Hejlova, I., Honsova, E., Sticova, E., Lanska, V., Hucl, T., Spicak, J., Jirsa, M., Trunecka, P., 2016. Prevalence and risk factors of steatosis after liver transplantation and patient outcomes. Liver Transplantation 22, 644–655. https://doi.org/10.1002/lt.24393

Helen, Y., Leaf, D.S., Moore, H.-P.H., 1993. Gene cloning and characterization of a GTP-binding Rab protein from mouse pituitary AtT-20 cells. Gene 132, 273–278. https://doi.org/10.1016/0378-1119(93)90207-J

Hennig, A., Markwart, R., Esparza-Franco, M.A., Ladds, G., Rubio, I., 2015. Ras activation revisited: role of GEF and GAP systems. Biological Chemistry 396, 831–848. https://doi.org/10.1515/hsz-2014-0257

Horn, P.J., Ledbetter, N.R., James, C.N., Hoffman, W.D., Case, C.R., Verbeck, G.F., Chapman, K.D., 2011. Visualization of Lipid Droplet Composition by Direct Organelle Mass Spectrometry*. Journal of Biological Chemistry 286, 3298–3306. https://doi.org/10.1074/jbc.M110.186353

Ingolia, N.T., Lareau, L.F., Weissman, J.S., 2011. Ribosome Profiling of Mouse Embryonic Stem Cells Reveals the Complexity and Dynamics of Mammalian Proteomes. Cell 147, 789–802. https://doi.org/10.1016/j.cell.2011.10.002

Inohara, N., Koseki, T., Chen, S., Wu, X., Núñez, G., 1998. CIDE, a novel family of cell death activators with homology to the 45 kDa subunit of the DNA fragmentation factor. EMBO J 17, 2526–2533. https://doi.org/10.1093/emboj/17.9.2526

Jaber, N., Mohd-Naim, N., Wang, Z., DeLeon, J.L., Kim, S., Zhong, H., Sheshadri, N., Dou, Z., Edinger, A.L., Du, G., Braga, V.M.M., Zong, W.-X., 2016. Vps34 regulates Rab7 and late endocytic trafficking through recruitment of the GTPase-activating protein Armus. J Cell Sci 129, 4424–4435. https://doi.org/10.1242/jcs.192260

Jamshidzadeh, A., Niknahad, H., Kashafi, H., 2007. Cytotoxicity of chloroquine in isolated rat hepatocytes. Journal of Applied Toxicology 27, 322–326. https://doi.org/10.1002/jat.1194

Jayson, C.B.K., Arlt, H., Fischer, A.W., Lai, Z.W., Farese, R.V., Walther, T.C., 2018. Rab18 is not necessary for lipid droplet biogenesis or turnover in human mammary carcinoma cells. MBoC 29, 2045–2054. https://doi.org/10.1091/mbc.E18-05-0282

Jones, R.R., Hooper, D.C., Zhang, L., Wolverson, D., Valev, V.K., 2019. Raman Techniques: Fundamentals and Frontiers. Nanoscale Research Letters 14, 231. https://doi.org/10.1186/s11671-019-3039-2

Jung, C.H., Ro, S.-H., Cao, J., Otto, N.M., Kim, D.-H., 2010. mTOR regulation of autophagy. FEBS Letters, Autophagy 584, 1287–1295. https://doi.org/10.1016/j.febslet.2010.01.017

Jüngst, C., Klein, M., Zumbusch, A., 2013. Long-term live cell microscopy studies of lipid droplet fusion dynamics in adipocytes[S]. Journal of Lipid Research 54, 3419–3429. https://doi.org/10.1194/jlr.M042515

Jüngst, C., Winterhalder, M.J., Zumbusch, A., 2011. Fast and long term lipid droplet tracking with CARS microscopy. Journal of Biophotonics 4, 435–441. https://doi.org/10.1002/jbio.201000120

Kanda, T., Matsuoka, S., Yamazaki, M., Shibata, T., Nirei, K., Takahashi, H., Kaneko, T., Fujisawa, M., Higuchi, T., Nakamura, H., Matsumoto, N., Yamagami, H., Ogawa, M., Imazu, H., Kuroda, K., Moriyama, M., 2018. Apoptosis and non-alcoholic fatty liver diseases. World J Gastroenterol 24, 2661–2672. https://doi.org/10.3748/wjg.v24.i25.2661

Kato, K., Cox, A.D., Hisaka, M.M., Graham, S.M., Buss, J.E., Der, C.J., 1992. Isoprenoid addition to Ras protein is the critical modification for its membrane association and transforming activity. PNAS 89, 6403–6407. https://doi.org/10.1073/pnas.89.14.6403

Kaushik, S., Cuervo, A.M., 2018. The coming of age of chaperone-mediated autophagy. Nature Reviews Molecular Cell Biology 19, 365–381. https://doi.org/10.1038/s41580-018-0001-6

Kaushik, S., Cuervo, A.M., 2015. Degradation of lipid droplet-associated proteins by chaperone-mediated autophagy facilitates lipolysis. Nature Cell Biology 17, 759–770. https://doi.org/10.1038/ncb3166

Kawamura, N., Sun-Wada, G.-H., Aoyama, M., Harada, A., Takasuga, S., Sasaki, T., Wada, Y., 2012. Delivery of endosomes to lysosomes via microautophagy in the visceral endoderm of mouse embryos. Nature Communications 3, 1071. https://doi.org/10.1038/ncomms2069

Kim, J., Kundu, M., Viollet, B., Guan, K.-L., 2011. AMPK and mTOR regulate autophagy through direct phosphorylation of Ulk1. Nat Cell Biol 13, 132–141. https://doi.org/10.1038/ncb2152

Kim, S.Y., 2016. The Definition of Obesity. Korean J Fam Med 37, 309–309. https://doi.org/10.4082/kjfm.2016.37.6.309

Kory, N., Farese, R.V., Walther, T.C., 2016. Targeting Fat: Mechanisms of Protein Localization to Lipid Droplets. Trends Cell Biol 26, 535–546. https://doi.org/10.1016/j.tcb.2016.02.007

Kuerschner, L., Moessinger, C., Thiele, C., 2008. Imaging of Lipid Biosynthesis: How a Neutral Lipid Enters Lipid Droplets. Traffic 9, 338–352. https://doi.org/10.1111/j.1600-0854.2007.00689.x

Kumari, R., Sahu, M.K., Tripathy, A., Uthansingh, K., Behera, M., 2018. Hepatocellular carcinoma treatment: hurdles, advances and prospects. Hepatic Oncology 5, HEP08. https://doi.org/10.2217/hep-2018-0002

Kwok, S., Adam, S., Ho, J.H., Iqbal, Z., Turkington, P., Razvi, S., Le Roux, C.W., Soran, H., Syed, A.A., 2020. Obesity: A critical risk factor in the COVID-19 pandemic. Clin Obes. https://doi.org/10.1111/cob.12403

Kwon, I., Lee, Y., Cosio-Lima, L.M., Cho, J.-Y., Yeom, D.-C., 2015. Effects of long-term resistance exercise training on autophagy in rat skeletal muscle of chloroquine-induced sporadic inclusion body myositis. J Exerc Nutrition Biochem 19, 225–234. https://doi.org/10.5717/jenb.2015.15090710

Lagrutta, L.C., Montero-Villegas, S., Layerenza, J.P., Sisti, M.S., García de Bravo, M.M., Ves-Losada, A., 2017. Reversible Nuclear-Lipid-Droplet Morphology Induced by Oleic Acid: A Link to Cellular-Lipid Metabolism. PLoS ONE 12, e0170608. https://doi.org/10.1371/journal.pone.0170608

Lampidonis, A.D., Rogdakis, E., Voutsinas, G.E., Stravopodis, D.J., 2011. The resurgence of Hormone-Sensitive Lipase (HSL) in mammalian lipolysis. Gene 477, 1–11. https://doi.org/10.1016/j.gene.2011.01.007

Langhi, C., Marquart, T.J., Allen, R.M., Baldán, Á., 2014. Perilipin-5 is regulated by statins and controls triglyceride contents in the hepatocyte. J Hepatol 61, 358–365. https://doi.org/10.1016/j.jhep.2014.04.009

Lazarow, P.B., De Duve, C., 1976. A fatty acyl-CoA oxidizing system in rat liver peroxisomes; enhancement by clofibrate, a hypolipidemic drug. Proc Natl Acad Sci U S A 73, 2043–2046.

Leung, K.F., Baron, R., Ali, B.R., Magee, A.I., Seabra, M.C., 2007. Rab GTPases Containing a CAAX Motif Are Processed Post-geranylgeranylation by Proteolysis and Methylation. J. Biol. Chem. 282, 1487–1497. https://doi.org/10.1074/jbc.M605557200

Lewis, G.F., Carpentier, A., Adeli, K., Giacca, A., 2002. Disordered Fat Storage and Mobilization in the Pathogenesis of Insulin Resistance and Type 2 Diabetes. Endocrine Reviews 23, 201–229. https://doi.org/10.1210/edrv.23.2.0461

Li, C., Luo, X., Zhao, S., Siu, G.K., Liang, Y., Chan, H.C., Satoh, A., Yu, S.S., 2016. COPI–TRAPPII activates Rab18 and regulates its lipid droplet association. The EMBO Journal 36, 441–457. https://doi.org/10.15252/embj.201694866

Li, C.H., Tam, P.K.S., 1998. An iterative algorithm for minimum cross entropy thresholding. Pattern Recognition Letters 19, 771–776. https://doi.org/10.1016/S0167-8655(98)00057-9

Li, D., Zhao, Y.G., Li, Di, Zhao, H., Huang, J., Miao, G., Feng, D., Liu, P., Li, Dong, Zhang, H., 2019. The ER-Localized Protein DFCP1 Modulates ER-Lipid Droplet Contact Formation. Cell Reports 27, 343-358.e5. https://doi.org/10.1016/j.celrep.2019.03.025

Li Fang, Zhang Hanrui, 2019. Lysosomal Acid Lipase in Lipid Metabolism and Beyond. Arteriosclerosis, Thrombosis, and Vascular Biology 39, 850–856. https://doi.org/10.1161/ATVBAHA.119.312136

Li, W., Li, J., Bao, J., 2012. Microautophagy: lesser-known self-eating. Cell. Mol. Life Sci. 69, 1125–1136. https://doi.org/10.1007/s00018-011-0865-5

Li, X., Li, Y., Jiang, M., Wu, W., He, S., Chen, C., Qin, Z., Tang, B.Z., Mak, H.Y., Qu, J.Y., 2019. Quantitative Imaging of Lipid Synthesis and Lipolysis Dynamics in *Caenorhabditis elegans* by Stimulated Raman Scattering Microscopy. Anal. Chem. 91, 2279–2287. https://doi.org/10.1021/acs.analchem.8b04875

Li, Z., Thiel, K., Thul, P.J., Beller, M., Kühnlein, R.P., Welte, M.A., 2012. Lipid Droplets Control the Maternal Histone Supply of Drosophila Embryos. Current Biology 22, 2104–2113. https://doi.org/10.1016/j.cub.2012.09.018

Liegel, R.P., Handley, M.T., Ronchetti, A., Brown, S., Langemeyer, L., Linford, A., Chang, B., Morris-Rosendahl, D.J., Carpanini, S., Posmyk, R., Harthill, V., Sheridan, E., Abdel-Salam, G.M.H., Terhal, P.A., Faravelli, F., Accorsi, P., Giordano, L., Pinelli, L., Hartmann, B., Ebert, A.D., Barr, F.A., Aligianis, I.A., Sidjanin, D.J., 2013. Loss-of-Function Mutations in TBC1D20 Cause Cataracts and Male Infertility in blind sterile Mice and Warburg Micro Syndrome in Humans. Am J Hum Genet 93, 1001–1014. https://doi.org/10.1016/j.ajhg.2013.10.011

Lin, C.-W., Zhang, H., Li, M., Xiong, X., Chen, Xi, Chen, Xiaoyun, Dong, X.C., Yin, X.-M., 2013. Pharmacological promotion of autophagy alleviates steatosis and injury in alcoholic and non-alcoholic fatty liver conditions in mice. J Hepatol 58, 993–999. https://doi.org/10.1016/j.jhep.2013.01.011

Lin, J., Lu, F., Zheng, W., Huang, Z., Xu, S., Tai, D.C.S., Yu, H., 2011. Assessment of liver steatosis and fibrosis in rats using integrated coherent anti-Stokes Raman scattering and multiphoton imaging technique. JBO 16, 116024. https://doi.org/10.1117/1.3655353

Loomba, R., Sanyal, A.J., 2013. The global NAFLD epidemic. Nat Rev Gastroenterol Hepatol 10, 686–690. https://doi.org/10.1038/nrgastro.2013.171

Macara, I.G., Lounsbury, K.M., Richards, S.A., McKiernan, C., Bar-Sagi, D., 1996. The Ras superfamily of GTPases1. The FASEB Journal 10, 625–630. https://doi.org/10.1096/fasebj.10.5.8621061

Mackay, D.J.G., Hall, A., 1998. Rho GTPases *. Journal of Biological Chemistry 273, 20685–20688. https://doi.org/10.1074/jbc.273.33.20685

Mackenzie, A.H., 1983. Dose refinements in long-term therapy of rheumatoid arthritis with antimalarials. The American Journal of Medicine, A Reassessment of Plaquenil in the Treatment of Rheumatoid Arthritis 75, 40–45. https://doi.org/10.1016/0002-9343(83)91269-X

Magré, J., Delépine, M., Khallouf, E., Gedde-Dahl, T., Van Maldergem, L., Sobel, E., Papp, J., Meier, M., Mégarbané, A., BSCL Working Group, Lathrop, M., Capeau, J., 2001. Identification of the gene altered in Berardinelli–Seip congenital lipodystrophy on chromosome 11q13. Nature Genetics 28, 365–370. https://doi.org/10.1038/ng585

Makino, A., Hullin-Matsuda, F., Murate, M., Abe, M., Tomishige, N., Fukuda, M., Yamashita, S., Fujimoto, T., Vidal, H., Lagarde, M., Delton, I., Kobayashi, T., 2016. Acute accumulation of free cholesterol induces the degradation of perilipin 2 and Rab18-dependent fusion of ER and lipid droplets in cultured human hepatocytes. MBoC 27, 3293–3304. https://doi.org/10.1091/mbc.E15-10-0730

Mansbach, C.M., Arnold, A., Garrett, M., 1987. Effect of chloroquine on intestinal lipid metabolism. American Journal of Physiology-Gastrointestinal and Liver Physiology 253, G673–G678. https://doi.org/10.1152/ajpgi.1987.253.5.G673

Martin, S., Driessen, K., Nixon, S.J., Zerial, M., Parton, R.G., 2005. Regulated Localization of Rab18 to Lipid Droplets: EFFECTS OF LIPOLYTIC STIMULATION AND INHIBITION OF LIPID DROPLET CATABOLISM. Journal of Biological Chemistry 280, 42325–42335. https://doi.org/10.1074/jbc.M506651200

Martin, S., Parton, R.G., 2008. Characterization of Rab18, a Lipid Droplet–Associated Small GTPase, in: Methods in Enzymology, Small GTPases in Disease, Part A. Academic Press, pp. 109–129. https://doi.org/10.1016/S0076-6879(07)38008-7

Martín, V., González-Casas, R., Mendoza-Jiménez-Ridruejo, J., García-Buey, L., Moreno, R., 2013. Pathogenesis, diagnosis and treatment of non-alcoholic fatty liver disease. Revista espanola de enfermedades digestivas : organo oficial de la Sociedad Espanola de Patologia Digestiva 105, 409–420. https://doi.org/10.4321/S1130-01082013000700006

Masson, J.-D., Blanchet, B., Periou, B., Authier, F.-J., Mograbi, B., Gherardi, R.K., Crépeaux, G., 2020. Long Term Pharmacological Perturbation of Autophagy in Mice: Are HCQ Injections a Relevant Choice? Biomedicines 8, 47. https://doi.org/10.3390/biomedicines8030047

Mauthe, M., Orhon, I., Rocchi, C., Zhou, X., Luhr, M., Hijlkema, K.-J., Coppes, R.P., Engedal, N., Mari, M., Reggiori, F., 2018. Chloroquine inhibits autophagic flux by decreasing autophagosome-lysosome fusion. Autophagy 14, 1435–1455. https://doi.org/10.1080/15548627.2018.1474314

Mayer, N., Schweiger, M., Romauch, M., Grabner, G.F., Eichmann, T.O., Fuchs, E., Ivkovic, J., Heier, C., Mrak, I., Lass, A., Höfler, G., Fledelius, C., Zechner, R., Zimmermann, R., Breinbauer, R., 2013. Development of small-molecule inhibitors targeting adipose triglyceride lipase. Nature Chemical Biology 9, 785–787. https://doi.org/10.1038/nchembio.1359

McMillan, E.A., Longo, S.M., Smith, M.D., Broskin, S., Lin, B., Singh, N.K., Strochlic, T.I., 2018. The protein kinase CK2 substrate Jabba modulates lipid metabolism during Drosophila oogenesis. J. Biol. Chem. 293, 2990–3002. https://doi.org/10.1074/jbc.M117.814657

Ménorval, M.-A. de, Mir, L.M., Fernández, M.L., Reigada, R., 2012. Effects of Dimethyl Sulfoxide in Cholesterol-Containing Lipid Membranes: A Comparative Study of Experiments In Silico and with Cells. PLOS ONE 7, e41733. https://doi.org/10.1371/journal.pone.0041733

Mercer, T.J., Gubas, A., Tooze, S.A., 2018. A molecular perspective of mammalian autophagosome biogenesis. Journal of Biological Chemistry 293, 5386–5395. https://doi.org/10.1074/jbc.R117.810366

Mizushima, N., 2020. The ATG conjugation systems in autophagy. Current Opinion in Cell Biology 63, 1–10. https://doi.org/10.1016/j.ceb.2019.12.001

Mohammed, S., Nicklas, E.H., Thadathil, N., Selvarani, R., Royce, G.H., Kinter, M., Richardson, A., Deepa, S.S., 2021. Role of necroptosis in chronic hepatic inflammation and fibrosis in a mouse model of increased oxidative stress. Free Radical Biology and Medicine 164, 315–328. https://doi.org/10.1016/j.freeradbiomed.2020.12.449

Motomura, W., Inoue, M., Ohtake, T., Takahashi, N., Nagamine, M., Tanno, S., Kohgo, Y., Okumura, T., 2006. Up-regulation of ADRP in fatty liver in human and liver steatosis in mice fed with high fat diet. Biochemical and Biophysical Research Communications 340, 1111–1118. https://doi.org/10.1016/j.bbrc.2005.12.121

Moura, C.C., Tare, R.S., Oreffo, R.O.C., Mahajan, S., 2016. Raman spectroscopy and coherent anti-Stokes Raman scattering imaging: prospective tools for monitoring skeletal cells and skeletal regeneration. Journal of The Royal Society Interface 13, 20160182. https://doi.org/10.1098/rsif.2016.0182

Nakamura, A., Terauchi, Y., 2013. Lessons from Mouse Models of High-Fat Diet-Induced NAFLD. International Journal of Molecular Sciences 14, 21240–21257. https://doi.org/10.3390/ijms141121240

Nian, F.-S., Li, L.-L., Cheng, C.-Y., Wu, P.-C., Lin, Y.-T., Tang, C.-Y., Ren, B.-S., Tai, C.-Y., Fann, M.-J., Kao, L.-S., Hong, C.-J., Tsai, J.-W., 2019. Rab18 Collaborates with Rab7 to Modulate Lysosomal and Autophagy Activities in the Nervous System: an Overlapping Mechanism for Warburg Micro Syndrome and Charcot-Marie-Tooth Neuropathy Type 2B. Mol Neurobiol 56, 6095–6105. https://doi.org/10.1007/s12035-019-1471-z

Novikoff, A.B., Novikoff, P.M., Rosen, O.M., Rubin, C.S., 1980. Organelle relationships in cultured 3T3-L1 preadipocytes. J Cell Biol 87, 180–196. https://doi.org/10.1083/jcb.87.1.180

O'Mahony, F., Wroblewski, K., O'Byrne, S.M., Jiang, H., Clerkin, K., Benhammou, J., Blaner, W.S., Beaven, S.W., 2015. Liver X receptors balance lipid stores in hepatic stellate cells through Rab18, a retinoid responsive lipid droplet protein. Hepatology 62, 615–626. https://doi.org/10.1002/hep.27645

Onal, G., Kutlu, O., Gozuacik, D., Dokmeci Emre, S., 2017. Lipid Droplets in Health and Disease. Lipids in Health and Disease 16, 128. https://doi.org/10.1186/s12944-017-0521-7

Ouimet, M., Franklin, V., Mak, E., Liao, X., Tabas, I., Marcel, Y.L., 2011. Autophagy Regulates Cholesterol Efflux from Macrophage Foam Cells via Lysosomal Acid Lipase. Cell Metab 13, 655–667. https://doi.org/10.1016/j.cmet.2011.03.023

Ozeki, S., Cheng, J., Tauchi-Sato, K., Hatano, N., Taniguchi, H., Fujimoto, T., 2005. Rab18 localizes to lipid droplets and induces their close apposition to the endoplasmic reticulum-derived membrane. Journal of Cell Science 118, 2601–2611. https://doi.org/10.1242/jcs.02401

Paradis, V., Bedossa, P., 2008. Definition and natural history of metabolic steatosis: histology and cellular aspects. Diabetes & Metabolism, Liver and diabetes 34, 638–642. https://doi.org/10.1016/S1262-3636(08)74598-1

Paul, A., Wang, Y., Brännmark, C., Kumar, S., Bonn, M., Parekh, S.H., 2019. Quantitative Mapping of Triacylglycerol Chain Length and Saturation Using Broadband CARS Microscopy. Biophysical Journal 116, 2346–2355. https://doi.org/10.1016/j.bpj.2019.04.036

Pearson, G.L., Mellett, N., Chu, K.Y., Cantley, J., Davenport, A., Bourbon, P., Cosner, C.C., Helquist, P., Meikle, P.J., Biden, T.J., 2014. Lysosomal acid lipase and lipophagy are constitutive negative regulators of glucose-stimulated insulin secretion from pancreatic beta cells. Diabetologia 57, 129–139. https://doi.org/10.1007/s00125-013-3083-x

Pfeffer, S., Aivazian, D., 2004. Targeting Rab GTPases to distinct membrane compartments. Nature Reviews Molecular Cell Biology 5, 886–896. https://doi.org/10.1038/nrm1500

Pfeffer, S.R., Dirac-Svejstrup, A.B., Soldati, T., 1995. Rab GDP Dissociation Inhibitor: Putting Rab GTPases in the Right Place (∗). Journal of Biological Chemistry 270, 17057–17059. https://doi.org/10.1074/jbc.270.29.17057

Phair, R.D., Gorski, S.A., Misteli, T., 2003. Measurement of Dynamic Protein Binding to Chromatin In Vivo, Using Photobleaching Microscopy, in: Methods in Enzymology, Chromatin and Chromatin Remodeling Enzymes, Part A. Academic Press, pp. 393–414. https://doi.org/10.1016/S0076-6879(03)75025-3

Picture Thresholding Using an Iterative Selection Method, 1978. . IEEE Transactions on Systems, Man, and Cybernetics 8, 630–632. https://doi.org/10.1109/TSMC.1978.4310039

Poteryaev, D., Datta, S., Ackema, K., Zerial, M., Spang, A., 2010. Identification of the Switch in Early-to-Late Endosome Transition. Cell 141, 497–508. https://doi.org/10.1016/j.cell.2010.03.011

Proescher, F., 1927. Oil Red O Pyridin, A Rapid Fat Stain. Stain Technology 2, 60–61. https://doi.org/10.3109/10520292709115655

Pulido, M.R., Diaz-Ruiz, A., JimÃ©nez-GÃ³mez, Y., Garcia-Navarro, S., Gracia-Navarro, F., Tinahones, F., LÃ³pez-Miranda, J., FrÃ¼hbeck, G., VÃ¡zquez-MartÃ-nez, R., MalagÃ³n, M.M., 2011. Rab18 Dynamics in Adipocytes in Relation to Lipogenesis, Lipolysis and Obesity. PLOS ONE 6, 1–13. https://doi.org/10.1371/journal.pone.0022931

Raman, C.V., Krishnan, K.S., 1928. A New Type of Secondary Radiation. Nature 121, 501–502. https://doi.org/10.1038/121501c0

Rambold, A.S., Cohen, S., Lippincott-Schwartz, J., 2015. Fatty acid trafficking in starved cells: regulation by lipid droplet lipolysis, autophagy, and mitochondrial fusion dynamics. Dev. Cell 32, 678–692. https://doi.org/10.1016/j.devcel.2015.01.029

Rocks, O., Gerauer, M., Vartak, N., Koch, S., Huang, Z.-P., Pechlivanis, M., Kuhlmann, J., Brunsveld, L., Chandra, A., Ellinger, B., Waldmann, H., Bastiaens, P.I.H., 2010. The Palmitoylation Machinery Is a Spatially Organizing System for Peripheral Membrane Proteins. Cell 141, 458–471. https://doi.org/10.1016/j.cell.2010.04.007

Rocks, O., Peyker, A., Kahms, M., Verveer, P.J., Koerner, C., Lumbierres, M., Kuhlmann, J., Waldmann, H., Wittinghofer, A., Bastiaens, P.I.H., 2005. An Acylation Cycle Regulates Localization and Activity of Palmitoylated Ras Isoforms. Science 307, 1746–1752. https://doi.org/10.1126/science.1105654

Rodriguez, L.G., Lockett, S.J., Holtom, G.R., 2006. Coherent anti-stokes Raman scattering microscopy: A biological review. Cytometry Part A 69A, 779–791. https://doi.org/10.1002/cyto.a.20299

Romanov, J., Walczak, M., Ibiricu, I., Schüchner, S., Ogris, E., Kraft, C., Martens, S., 2012. Mechanism and functions of membrane binding by the Atg5–Atg12/Atg16 complex during autophagosome formation. The EMBO Journal 31, 4304–4317. https://doi.org/10.1038/emboj.2012.278

Rostron, P., Gaber, S., Gaber, D., 2016. Raman Spectroscopy, Review. IJETR 6, 16.

Roy, D., Farabaugh, K.T., Wu, J., Charrier, A., Smas, C., Hatzoglou, M., Thirumurugan, K., Buchner, D.A., 2017. Coordinated transcriptional control of adipocyte triglyceride lipase (Atgl) by transcription factors Sp1 and peroxisome proliferator–activated receptor γ (PPARγ) during adipocyte differentiation. J Biol Chem 292, 14827–14835. https://doi.org/10.1074/jbc.M117.783043

Rubinsztein, D.C., Shpilka, T., Elazar, Z., 2012. Mechanisms of Autophagosome Biogenesis. Current Biology 22, R29–R34. https://doi.org/10.1016/j.cub.2011.11.034

Salo, V.T., Belevich, I., Li, S., Karhinen, L., Vihinen, H., Vigouroux, C., Magré, J., Thiele, C., Hölttä-Vuori, M., Jokitalo, E., Ikonen, E., 2016. Seipin regulates ER–lipid droplet contacts and cargo delivery. The EMBO Journal 35, 2699–2716. https://doi.org/10.15252/embj.201695170

Sathyanarayan, A., Mashek, M.T., Mashek, D.G., 2017. ATGL Promotes Autophagy/Lipophagy via SIRT1 to Control Hepatic Lipid Droplet Catabolism. Cell Reports 19, 1–9. https://doi.org/10.1016/j.celrep.2017.03.026

Schelbert, K.B., 2009. Comorbidities of Obesity. Primary Care: Clinics in Office Practice 36, 271–285. https://doi.org/10.1016/j.pop.2009.01.009

Schienkiewitz, A., Brettschneider, A.-K., Damerow, S., Schaffrath Rosario, A., 2018. Overweight and obesity among children and adolescents in Germany. Results of the cross-sectional KiGGS Wave 2 study and trends. Journal of Health Monitoring 3, 15–22. http://dx.doi.org/10.17886/RKI-GBE-2018-022

Schienkiewitz, A., Mensink, G., Kuhnert, R., Lange, C., 2017. Overweight and obesity among adults in Germany. https://doi.org/10.25646/2588

Schienkiewitz, A., Mensink, G.B.M., Scheidt-Nave, C., 2012. Comorbidity of overweight and obesity in a nationally representative sample of German adults aged 18-79 years. BMC Public Health 12, 658. https://doi.org/10.1186/1471-2458-12-658

Schläfli, A.M., Berezowska, S., Adams, O., Langer, R., Tschan, M.P., 2015. Reliable LC3 and p62 Autophagy Marker Detection in Formalin Fixed Paraffin Embedded Human Tissue by Immunohistochemistry. Eur J Histochem 59. https://doi.org/10.4081/ejh.2015.2481

Schmidt, U., Weigert, M., Broaddus, C., Myers, G., 2018. Cell Detection with Star-convex Polygons. arXiv:1806.03535 [cs] 11071, 265–273. https://doi.org/10.1007/978-3-030-00934-2_30

Schneider, J.L., Suh, Y., Cuervo, A.M., 2014. Deficient Chaperone-Mediated Autophagy in Liver Leads to Metabolic Dysregulation. Cell Metabolism 20, 417–432. https://doi.org/10.1016/j.cmet.2014.06.009

Schott, M.B., Weller, S.G., Schulze, R.J., Krueger, E.W., Drizyte-Miller, K., Casey, C.A., McNiven, M.A., 2019. Lipid droplet size directs lipolysis and lipophagy catabolism in hepatocytes. Journal of Cell Biology 218, 3320–3335. https://doi.org/10.1083/jcb.201803153

Schroeder, B., Schulze, R.J., Weller, S.G., Sletten, A.C., Casey, C.A., McNiven, M.A., 2015. The small GTPase Rab7 as a central regulator of hepatocellular lipophagy. Hepatology 61, 1896–1907. https://doi.org/10.1002/hep.27667

Schuck, S., 2020. Microautophagy – distinct molecular mechanisms handle cargoes of many sizes. J Cell Sci 133. https://doi.org/10.1242/jcs.246322

Schulze, R.J., Krueger, E.W., Weller, S.G., Johnson, K.M., Casey, C.A., Schott, M.B., McNiven, M.A., 2020. Direct lysosome-based autophagy of lipid droplets in hepatocytes. PNAS 117, 32443–32452. https://doi.org/10.1073/pnas.2011442117

Schuppan, D., Afdhal, N.H., 2008. Liver cirrhosis. The Lancet 371, 838–851. https://doi.org/10.1016/S0140-6736(08)60383-9

Schweiger, M., Schreiber, R., Haemmerle, G., Lass, A., Fledelius, C., Jacobsen, P., Tornqvist, H., Zechner, R., Zimmermann, R., 2006. Adipose Triglyceride Lipase and Hormone-sensitive Lipase Are the Major Enzymes in Adipose Tissue Triacylglycerol Catabolism. Journal of Biological Chemistry 281, 40236–40241. https://doi.org/10.1074/jbc.M608048200

Sidjanin, D.J., Park, A.K., Ronchetti, A., Martins, J., Jackson, W.T., 2016. TBC1D20 mediates autophagy as a key regulator of autophagosome maturation. Autophagy 12, 1759–1775. https://doi.org/10.1080/15548627.2016.1199300

Singh, R., Kaushik, S., Wang, Y., Xiang, Y., Novak, I., Komatsu, M., Tanaka, K., Cuervo, A.M., Czaja, M.J., 2009. Autophagy regulates lipid metabolism. Nature 458, 1131–1135. https://doi.org/10.1038/nature07976

Singh, S., Allen, A.M., Wang, Z., Prokop, L.J., Murad, M.H., Loomba, R., 2015. Fibrosis Progression in Nonalcoholic Fatty Liver vs Nonalcoholic Steatohepatitis: A Systematic Review and Meta-analysis of Paired-Biopsy Studies. Clinical Gastroenterology and Hepatology 13, 643-654.e9. https://doi.org/10.1016/j.cgh.2014.04.014

Stone, S.J., Levin, M.C., Zhou, P., Han, J., Walther, T.C., Farese, R.V., 2009. The Endoplasmic Reticulum Enzyme DGAT2 Is Found in Mitochondria-associated Membranes and Has a Mitochondrial

Targeting Signal That Promotes Its Association with Mitochondria*. Journal of Biological Chemistry 284, 5352–5361. https://doi.org/10.1074/jbc.M805768200

Strålfors, P., Olsson, H., Belfrage, P., 1987. 6 Hormone-Sensitive Lipase, in: Boyer, P.D., Krebs, E.G. (Eds.), The Enzymes, Control by Phosphorylation Part B. Academic Press, pp. 147–177. https://doi.org/10.1016/S1874-6047(08)60257-7

Szalowska, E., Burg, B. van der, Man, H.-Y., Hendriksen, P.J.M., Peijnenburg, A.A.C.M., 2014. Model Steatogenic Compounds (Amiodarone, Valproic Acid, and Tetracycline) Alter Lipid Metabolism by Different Mechanisms in Mouse Liver Slices. PLOS ONE 9, e86795. https://doi.org/10.1371/journal.pone.0086795

Takahashi, S., Sou, Y.-S., Saito, T., Kuma, A., Yabe, T., Sugiura, Y., Lee, H.-C., Suematsu, M., Yokomizo, T., Koike, M., Terai, S., Mizushima, N., Waguri, S., Komatsu, M., 2020. Loss of autophagy impairs physiological steatosis by accumulation of NCoR1. Life Sci. Alliance 3, e201900513. https://doi.org/10.26508/lsa.201900513

Takáts, S., Lévay, L., Boda, A., Tóth, S., Simon-Vecsei, Z., Rubics, A., Varga, Á., Lippai, M., Lőrincz, P., Glatz, G., Juhász, G., 2021. The Warburg Micro Syndrome-associated Rab3GAP-Rab18 module promotes autolysosome maturation through the Vps34 Complex I. The FEBS Journal 288, 190–211. https://doi.org/10.1111/febs.15313

Tang, W.-C., Lin, R.-J., Liao, C.-L., Lin, Y.-L., 2014. Rab18 Facilitates Dengue Virus Infection by Targeting Fatty Acid Synthase to Sites of Viral Replication. Journal of Virology 88, 6793–6804. https://doi.org/10.1128/JVI.00045-14

Tanida, I., Ueno, T., Uchiyama, Y., 2014. A Super-Ecliptic, pHluorin-mKate2, Tandem Fluorescent Protein-Tagged Human LC3 for the Monitoring of Mammalian Autophagy. PLOS ONE 9, e110600. https://doi.org/10.1371/journal.pone.0110600

Tauchi-Sato, K., Ozeki, S., Houjou, T., Taguchi, R., Fujimoto, T., 2002. The surface of lipid droplets is a phospholipid monolayer with a unique Fatty Acid composition. J Biol Chem 277, 44507–44512. https://doi.org/10.1074/jbc.M207712200

Taxiarchis, A., Mahdessian, H., Silveira, A., Fisher, R.M., van't Hooft, F.M., 2019. PNPLA2 influences secretion of triglyceride-rich lipoproteins by human hepatoma cells. Journal of Lipid Research 60, 1069–1077. https://doi.org/10.1194/jlr.M090928

Taylor, R.S., Taylor, R.J., Bayliss, S., Hagström, H., Nasr, P., Schattenberg, J.M., Ishigami, M., Toyoda, H., Wai-Sun Wong, V., Peleg, N., Shlomai, A., Sebastiani, G., Seko, Y., Bhala, N., Younossi, Z.M., Anstee, Q.M., McPherson, S., Newsome, P.N., 2020. Association Between Fibrosis Stage and Outcomes of Patients With Nonalcoholic Fatty Liver Disease: A Systematic Review and Meta-Analysis. Gastroenterology 158, 1611-1625.e12. https://doi.org/10.1053/j.gastro.2020.01.043

Thiam, A.R., Antonny, B., Wang, J., Delacotte, J., Wilfling, F., Walther, T.C., Beck, R., Rothman, J.E., Pincet, F., 2013. COPI buds 60-nm lipid droplets from reconstituted water–phospholipid–triacylglyceride interfaces, suggesting a tension clamp function. Proc Natl Acad Sci U S A 110, 13244–13249. https://doi.org/10.1073/pnas.1307685110

Thiam, A.R., Forêt, L., 2016. The physics of lipid droplet nucleation, growth and budding. Biochimica et Biophysica Acta (BBA) - Molecular and Cell Biology of Lipids 1861, 715–722. https://doi.org/10.1016/j.bbalip.2016.04.018

Tornqvist, H., Belfrage, P., 1976. Purification and some properties of a monoacylglycerol-hydrolyzing enzyme of rat adipose tissue. Journal of Biological Chemistry 251, 813–819. https://doi.org/10.1016/S0021-9258(17)33857-7

Ueno, M., Shen, W.-J., Patel, S., Greenberg, A.S., Azhar, S., Kraemer, F.B., 2013. Fat-specific protein 27 modulates nuclear factor of activated T cells 5 and the cellular response to stress. J Lipid Res 54, 734–743. https://doi.org/10.1194/jlr.M033365

UniProt Consortium, 2021. UniProtKB - Q9NP72 (RAB18_HUMAN). UniProt.

Uzbekov, R., Roingeard, P., 2013. Nuclear lipid droplets identified by electron microscopy of serial sections. BMC Res Notes 6, 386. https://doi.org/10.1186/1756-0500-6-386

Uzunbajakava, N., Lenferink, A., Kraan, Y., Volokhina, E., Vrensen, G., Greve, J., Otto, C., 2003. Nonresonant Confocal Raman Imaging of DNA and Protein Distribution in Apoptotic Cells. Biophysical Journal 84, 3968–3981. https://doi.org/10.1016/S0006-3495(03)75124-8

Varma, S., Khandelwal, R.L., 2007. Effects of rapamycin on cell proliferation and phosphorylation of mTOR and p70S6K in HepG2 and HepG2 cells overexpressing constitutively active Akt/PKB. Biochimica et Biophysica Acta (BBA) - General Subjects 1770, 71–78. https://doi.org/10.1016/j.bbagen.2006.07.016

Vartak, N., Papke, B., Grecco, H.E., Rossmannek, L., Waldmann, H., Hedberg, C., Bastiaens, P.I.H., 2014. The Autodepalmitoylating Activity of APT Maintains the Spatial Organization of Palmitoylated Membrane Proteins. Biophysical Journal 106, 93–105. https://doi.org/10.1016/j.bpj.2013.11.024

Vazquez-Martinez, R., Cruz-Garcia, D., Duran-Prado, M., Peinado, J.R., Castaño, J.P., Malagon, M.M., 2007. Rab18 Inhibits Secretory Activity in Neuroendocrine Cells by Interacting with Secretory Granules. Traffic 8, 867–882. https://doi.org/10.1111/j.1600-0854.2007.00570.x

Vazquez-Martinez, R., Martinez-Fuentes, A.J., Pulido, M.R., Jimenez-Reina, L., Quintero, A., Leal-Cerro, A., Soto, A., Webb, S.M., Sucunza, N., Bartumeus, F., Benito-Lopez, P., Galvez-Moreno, M.A., Castaño, J.P., Malagon, M.M., 2008. Rab18 Is Reduced in Pituitary Tumors Causing Acromegaly and Its Overexpression Reverts Growth Hormone Hypersecretion. The Journal of Clinical Endocrinology & Metabolism 93, 2269. https://doi.org/10.1210/jc.2007-1893

Vetter, I.R., Wittinghofer, A., 2001. The Guanine Nucleotide-Binding Switch in Three Dimensions. Science 294, 1299–1304. https://doi.org/10.1126/science.1062023

Walther, T.C., Farese, R.V., 2012. Lipid Droplets And Cellular Lipid Metabolism. Annu Rev Biochem 81, 687–714. https://doi.org/10.1146/annurev-biochem-061009-102430

Wang, B., Yang, H., Fan, Y., Yang, Y., Cao, W., Jia, Y., Cao, Y., Sun, K., Pang, Z., Du, H., 2017. 3-Methyladenine ameliorates liver fibrosis through autophagy regulated by the NF-κB signaling pathways on hepatic stellate cell. Oncotarget 8, 107603–107611. https://doi.org/10.18632/oncotarget.22539

Wang, C., Wang, X., Su, Z., Fei, H., Liu, X., Pan, Q., 2015. The novel mTOR inhibitor Torin-2 induces autophagy and downregulates the expression of UHRF1 to suppress hepatocarcinoma cell growth. Oncology Reports 34, 1708–1716. https://doi.org/10.3892/or.2015.4146

Wang, H., Becuwe, M., Housden, B.E., Chitraju, C., Porras, A.J., Graham, M.M., Liu, X.N., Thiam, A.R., Savage, D.B., Agarwal, A.K., Garg, A., Olarte, M.-J., Lin, Q., Fröhlich, F., Hannibal-Bach, H.K., Upadhyayula, S., Perrimon, N., Kirchhausen, T., Ejsing, C.S., Walther, T.C., Farese, R.V., Jr, 2016. Seipin is required for converting nascent to mature lipid droplets. eLife 5, e16582. https://doi.org/10.7554/eLife.16582

Wang, H., Bell, M., Sreenevasan, U., Hu, H., Liu, J., Dalen, K., Londos, C., Yamaguchi, T., Rizzo, M.A., Coleman, R., Gong, D., Brasaemle, D., Sztalryd, C., 2011. Unique Regulation of Adipose Triglyceride Lipase (ATGL) by Perilipin 5, a Lipid Droplet-associated Protein*. Journal of Biological Chemistry 286, 15707–15715. https://doi.org/10.1074/jbc.M110.207779

Wang, L., Qian, H., Nian, Y., Han, Y., Ren, Z., Zhang, H., Hu, L., Prasad, B.V.V., Laganowsky, A., Yan, N., Zhou, M., 2020. Structure and mechanism of human diacylglycerol O -acyltransferase 1. Nature 581, 329–332. https://doi.org/10.1038/s41586-020-2280-2

Wennerberg, K., Rossman, K.L., Der, C.J., 2005. The Ras superfamily at a glance. J Cell Sci 118, 843–846. https://doi.org/10.1242/jcs.01660

Wilfling, F., Thiam, A.R., Olarte, M.-J., Wang, J., Beck, R., Gould, T.J., Allgeyer, E.S., Pincet, F., Bewersdorf, J., Farese, R.V., Walther, T.C., 2014. Arf1/COPI machinery acts directly on lipid droplets and enables their connection to the ER for protein targeting. eLife 3. https://doi.org/10.7554/eLife.01607

Wilfling, F., Wang, H., Haas, J.T., Krahmer, N., Gould, T.J., Uchida, A., Cheng, J.-X., Graham, M., Christiano, R., Fröhlich, F., Liu, X., Buhman, K.K., Coleman, R.A., Bewersdorf, J., Farese, R.V., Walther, T.C., 2013. Triacylglycerol Synthesis Enzymes Mediate Lipid Droplet Growth by

Relocalizing from the ER to Lipid Droplets. Developmental Cell 24, 384–399. https://doi.org/10.1016/j.devcel.2013.01.013

Wong, R.J., Aguilar, M., Cheung, R., Perumpail, R.B., Harrison, S.A., Younossi, Z.M., Ahmed, A., 2015. Nonalcoholic Steatohepatitis Is the Second Leading Etiology of Liver Disease Among Adults Awaiting Liver Transplantation in the United States. Gastroenterology 148, 547–555. https://doi.org/10.1053/j.gastro.2014.11.039

Wong, V.W.-S., Wong, G.L.-H., Choi, P.C.-L., Chan, A.W.-H., Li, M.K.-P., Chan, H.-Y., Chim, A.M.-L., Yu, J., Sung, J.J.-Y., Chan, H.L.-Y., 2010. Disease progression of non-alcoholic fatty liver disease: a prospective study with paired liver biopsies at 3 years. Gut 59, 969–974. https://doi.org/10.1136/gut.2009.205088

Wu, Q., Sun, X., Yue, W., Lu, T., Ruan, Y., Chen, T., Zhang, D., 2016. RAB18, a protein associated with Warburg Micro syndrome, controls neuronal migration in the developing cerebral cortex. Molecular Brain 9, 19. https://doi.org/10.1186/s13041-016-0198-2

Xie, H., Heier, C., Kien, B., Vesely, P.W., Tang, Z., Sexl, V., Schoiswohl, G., Strießnig-Bina, I., Hoefler, G., Zechner, R., Schweiger, M., 2020. Adipose triglyceride lipase activity regulates cancer cell proliferation via AMP-kinase and mTOR signaling. Biochimica et Biophysica Acta (BBA) - Molecular and Cell Biology of Lipids 1865, 158737. https://doi.org/10.1016/j.bbalip.2020.158737

Xu, D., Li, Yuqi, Wu, L., Li, Ying, Zhao, D., Yu, J., Huang, T., Ferguson, C., Parton, R.G., Yang, H., Li, P., 2018. Rab18 promotes lipid droplet (LD) growth by tethering the ER to LDs through SNARE and NRZ interactions. J Cell Biol 217, 975–995. https://doi.org/10.1083/jcb.201704184

Xu, N., Zhang, S.O., Cole, R.A., McKinney, S.A., Guo, F., Haas, J.T., Bobba, S., Farese, R.V., Mak, H.Y., 2012. The FATP1–DGAT2 complex facilitates lipid droplet expansion at the ER–lipid droplet interface. J Cell Biol 198, 895–911. https://doi.org/10.1083/jcb.201201139

Xu, W., wu, L., Yu, M., Chen, F.-J., Arshad, M., Xia, X., Ren, H., yu, J., Xu, D., Li, J., Li, P., Zhou, L., 2016. Differential Roles of CIDE Proteins in Promoting Lipid Droplet Fusion and Growth in Subpopulations of Hepatocytes. The Journal of biological chemistry 291. https://doi.org/10.1074/jbc.M115.701094

Yang, J., Guo, Z., Liu, X., Liu, Q., Wu, M., Yao, X., Liu, Y., Cui, C., Li, H., Song, C., Liu, D., Xue, L., 2020. Cytotoxicity Evaluation of Chloroquine and Hydroxychloroquine in Multiple Cell Lines and Tissues by Dynamic Imaging System and Physiologically Based Pharmacokinetic Model. Front Pharmacol 11. https://doi.org/10.3389/fphar.2020.574720

Yin, Y., Hua, H., Li, M., Liu, S., Kong, Q., Shao, T., Wang, J., Luo, Y., Wang, Q., Luo, T., Jiang, Y., 2016. mTORC2 promotes type I insulin-like growth factor receptor and insulin receptor activation through the tyrosine kinase activity of mTOR. Cell Research 26, 46–65. https://doi.org/10.1038/cr.2015.133

Zechner, R., Zimmermann, R., Eichmann, T.O., Kohlwein, S.D., Haemmerle, G., Lass, A., Madeo, F., 2012. FAT SIGNALS - Lipases and Lipolysis in Lipid Metabolism and Signaling. Cell Metabolism 15, 279–291. https://doi.org/10.1016/j.cmet.2011.12.018

Zerial, M., McBride, H., 2001. Rab proteins as membrane organizers. Nature Reviews Molecular Cell Biology 2, 107–117. https://doi.org/10.1038/35052055

Zhao, X., Sun, R., Yang, X., Liu, D., Lei, D., Jin, T., Pan, X., 2015. Chloroquine-Enhanced Efficacy of Cisplatin in the Treatment of Hypopharyngeal Carcinoma in Xenograft Mice. PLoS ONE 10, e0126147. https://doi.org/10.1371/journal.pone.0126147

Zimmermann, R., Strauss, J.G., Haemmerle, G., Schoiswohl, G., Birner-Gruenberger, R., Riederer, M., Lass, A., Neuberger, G., Eisenhaber, F., Hermetter, A., Zechner, R., 2004. Fat Mobilization in Adipose Tissue Is Promoted by Adipose Triglyceride Lipase. Science 306, 1383–1386. https://doi.org/10.1126/science.1100747

7. Appendix

7.1. Vector Maps and Sequences

7.1.1. FusionRed RAB18 Vector

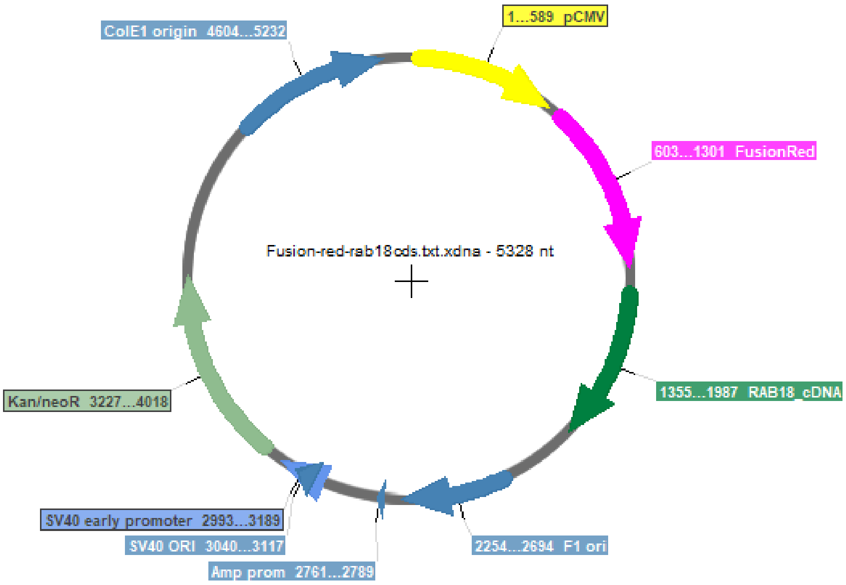

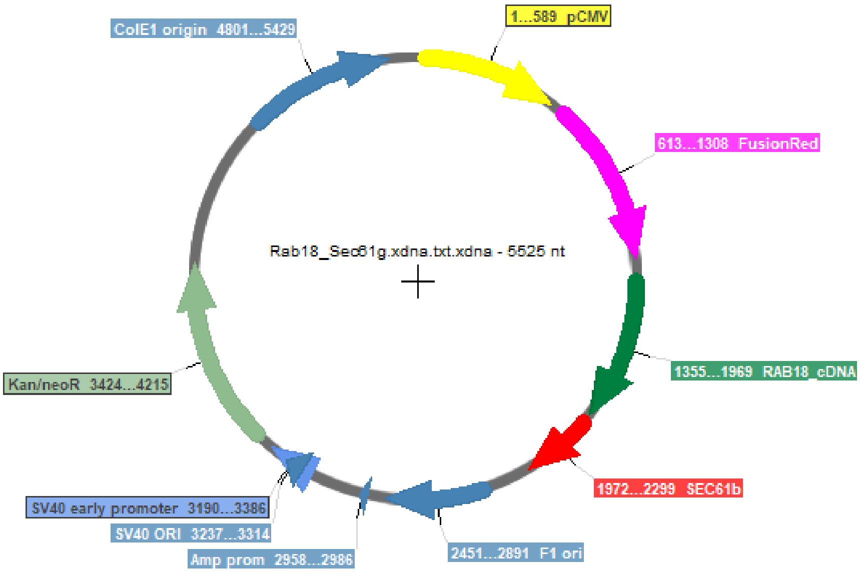

7.1.2. Q67L-Sequence Alignement

```
Seq_1 = WT-RAB18
Seq_2 = RAB18-Q67L
WT-RAB18 Sequence

             S  G  L  R  S  R  A  Q  A  S  N  S  M  D  E  D  V  L  T  T
Seq_1  1321  TCCGGACTCAGATCTCGAGCTCAAGCTTCGaattCGATGGACGAGGACGTGCTAACCACC  1380
             ||||||||||||||||||||||||||||||||||||||||||||||||||||||||||||
Seq_2  143   TCCGGACTCAGATCTCGAGCTCAAGCTTCGAATTCGATGGACGAGGACGTGCTAACCACC  202
             S  G  L  R  S  R  A  Q  A  S  N  S  M  D  E  D  V  L  T  T

             L  K  I  L  I  I  G  E  S  G  V  G  K  S  S  L  L  L  R  F
Seq_1  1381  CTGAAGATCCTCATCATCGGCGAGAGTGGGGTGGGCAAGTCCAGCCTGCTCTTGAGGTTC  1440
             ||||||||||||||||||||||||||||||||||||||||||||||||||||||||||||
Seq_2  203   CTGAAGATCCTCATCATCGGCGAGAGTGGGGTGGGCAAGTCCAGCCTGCTCTTGAGGTTC  262
             L  K  I  L  I  I  G  E  S  G  V  G  K  S  S  L  L  L  R  F

             T  D  D  T  F  D  P  E  L  A  A  T  I  G  V  D  F  K  V  K
Seq_1  1441  ACAGATGATACGTTTGATCCAGAACTTGCAGCAACAATAGGTGTTGACTTTAAGGTGAAA  1500
             ||||||||||||||||||||||||||||||||||||||||||||||||||||||||||||
Seq_2  263   ACAGATGATACGTTTGATCCAGAACTTGCAGCAACAATAGGTGTTGACTTTAAGGTGAAA  322
             T  D  D  T  F  D  P  E  L  A  A  T  I  G  V  D  F  K  V  K

             T  I  S  V  D  G  N  K  A  K  L  A  I  W  D  T  A  G  Q  E
             |||||||||||||||||||||||||||||||||||||||||||||||||||||||#||||
Seq_2  323   ACAATTTCAGTGGATGGAAATAAGGCTAAACTTGCAATATGGGATACTGCTGGTCTAGAG  382
             T  I  S  V  D  G  N  K  A  K  L  A  I  W  D  T  A  G  L  E

             R  F  R  T  L  T  P  S  Y  Y  R  G  A  Q  G  V  I  L  V  Y
Seq_1  1561  AGGTTTAGAACATTAACTCCCAGCTATTATAGAGGTGCACAGGGTGTTATATTAGTTTAT  1620
             ||||||||||||||||||||||||||||||||||||||||||||||||||||||||||||
Seq_2  383   AGGTTTAGAACATTAACTCCCAGCTATTATAGAGGTGCACAGGGTGTTATATTAGTTTAT  442
             R  F  R  T  L  T  P  S  Y  Y  R  G  A  Q  G  V  I  L  V  Y

             D  V  T  R  R  D  T  F  V  K  L  D  N  W  L  N  E  L  E  T
Seq_1  1621  GATGTCACAAGAAGAGATACATTTGTTAAACTGGATAATTGGTTAAATGAATTGGAAACA  1680
             ||||||||||||||||||||||||||||||||||||||||||||||||||||||||||||
Seq_2  443   GATGTCACAAGAAGAGATACATTTGTTAAACTGGATAATTGGTTAAATGAATTGGAAACA  502
             D  V  T  R  R  D  T  F  V  K  L  D  N  W  L  N  E  L  E  T

             Y  C  T  R  N  D  I  V  N  M  L  V  G  N  K  I  D  K  E  N
Seq_1  1681  TACTGTACAAGAAATGACATAGTAAACATGCTAGTTGGAAATAAAATCGATAAGGAAAAT  1740
             ||||||||||||||||||||||||||||||||||||||||||||||||||||||||||||
Seq_2  503   TACTGTACAAGAAATGACATAGTAAACATGCTAGTTGGAAATAAAATCGATAAGGAAAAT  562
             Y  C  T  R  N  D  I  V  N  M  L  V  G  N  K  I  D  K  E  N

             I
Seq_1  1741  CGTGAAGTCGATAGAAATGAAGGCCTGAAATTTGCACGAAAGCATTCCATGTTATTTATA  1800
             ||||||||||||||||||||||||||||||||||||||||||||||||||||||||||||
Seq_2  563   CGTGAAGTCGATAGAAATGAAGGCCTGAAATTTGCACGAAAGCATTCCATGTTATTTATA  622


             E  A  S  A  K  T  C  D  G  V  Q  C  A  F  E  E  L  V  E  K
Seq_1  1801  GAGGCAAGTGCAAAAACCTGTGATGGTGTACAATGTGCCTTTGAAGAACTTGTTGAAAAG  1860
             ||||||||||||||||||||||||||||||||||||||||||||||||||||||||||||
Seq_2  623   GAGGCAAGTGCAAAAACCTGTGATGGTGTACAATGTGCCTTTGAAGAACTTGTTGAAAAG  682
             E  A  S  A  K  T  C  D  G  V  Q  C  A  F  E  E  L  V  E  K

             I  I  Q  T  P  G  L  W  E  S  E  N  Q  N  K  G  V  K  L  S
Seq_1  1861  ATCATTCAGACCCCTGGACTGTGGGAAAGTGAGAACCAGAATAAAGGAGTCAAACTGTCA  1920
             ||||||||||||||||||||||||||||||||||||||||||||||||||||||||||||
Seq_2  683   ATCATTCAGACCCCTGGACTGTGGGAAAGTGAGAACCAGAATAAAGGAGTCAAACTGTCA  742
             I  I  Q  T  P  G  L  W  E  S  E  N  Q  N  K  G  V  K  L  S

             H  R  E  E  G  Q  G  G  G  A  C  G  G  Y  C  S  V  L  *  G
Seq_1  1921  CACAGGGAAGAAGGCCAAGGAGGAGGAGCCTGTGGTGGTTATTGCTCTGTGTTATAAGga  1980
             ||||||||||||||||||||||||||||||||||||||||||||||||||||||||||||
Seq_2  743   CACAGGGAAGAAGGCCAAGGAGGAGGAGCCTGTGGTGGTTATTGCTCTGTGTTATAAGGA  802
             H  R  E  E  G  Q  G  G  G  A  C  G  G  Y  C  S  V  L  *  G
```

7.1.3. S22N-Sequence Alignement

```
Seq_1 = WT-RAB18
Seq_2 = RAB18-S22N
WT-RAB18 Sequence

             S  G  L  R  S  R  A  Q  A  S  N  S  M  D  E  D  V  L  T  T
Seq_1  1321  TCCGGACTCAGATCTCGAGCTCAAGCTTCGaattCGATGGACGAGGACGTGCTAACCACC  1380
             ||||||||||||||||||||||||||||||||||||||||||||||||||||||||||||
Seq_2  144   TCCGGACTCAGATCTCGAGCTCAAGCTTCGAATTCGATGGACGAGGACGTGCTAACCACC  203
             S  G  L  R  S  R  A  Q  A  S  N  S  M  D  E  D  V  L  T  T

             L  K  I  L  I  I  G  E  S  G  V  G  K  S  S  L  L  L  R  F
Seq_1  1381  CTGAAGATCCTCATCATCGGCGAGAGTGGGGTGGGCAAGTCCAGCCTGCTCTTGAGGTTC  1440
             |||||||||||||||||||||||||||||||||||||||##|||||||||||||||||||
Seq_2  204   CTGAAGATCCTCATCATCGGCGAGAGTGGGGTGGGCAAGAACAGCCTGCTCTTGAGGTTC  263
             L  K  I  L  I  I  G  E  S  G  V  G  K  N  S  L  L  L  R  F

             T  D  D  T  F  D  P  E  L  A  A  T  I  G  V  D  F  K  V  K
Seq_1  1441  ACAGATGATACGTTTGATCCAGAACTTGCAGCAACAATAGGTGTTGACTTTAAGGTGAAA  1500
             ||||||||||||||||||||||||||||||||||||||||||||||||||||||||||||
Seq_2  264   ACAGATGATACGTTTGATCCAGAACTTGCAGCAACAATAGGTGTTGACTTTAAGGTGAAA  323
             T  D  D  T  F  D  P  E  L  A  A  T  I  G  V  D  F  K  V  K

             T  I  S  V  D  G  N  K  A  K  L  A  I  W  D  T  A  G  Q  E
Seq_1  1501  ACAATTTCAGTGGATGGAAATAAGGCTAAACTTGCAATATGGGATACTGCTGGTCAAGAG  1560
             ||||||||||||||||||||||||||||||||||||||||||||||||||||||||||||
Seq_2  324   ACAATTTCAGTGGATGGAAATAAGGCTAAACTTGCAATATGGGATACTGCTGGTCAAGAG  383
             T  I  S  V  D  G  N  K  A  K  L  A  I  W  D  T  A  G  Q  E

             R  F  R  T  L  T  P  S  Y  Y  R  G  A  Q  G  V  I  L  V  Y
Seq_1  1561  AGGTTTAGAACATTAACTCCCAGCTATTATAGAGGTGCACAGGGTGTTATATTAGTTTAT  1620
             ||||||||||||||||||||||||||||||||||||||||||||||||||||||||||||
Seq_2  384   AGGTTTAGAACATTAACTCCCAGCTATTATAGAGGTGCACAGGGTGTTATATTAGTTTAT  443
             R  F  R  T  L  T  P  S  Y  Y  R  G  A  Q  G  V  I  L  V  Y

             D  V  T  R  R  D  T  F  V  K  L  D  N  W  L  N  E  L  E  T
Seq_1  1621  GATGTCACAAGAAGAGATACATTTGTTAAACTGGATAATTGGTTAAATGAATTGGAAACA  1680
             ||||||||||||||||||||||||||||||||||||||||||||||||||||||||||||
Seq_2  444   GATGTCACAAGAAGAGATACATTTGTTAAACTGGATAATTGGTTAAATGAATTGGAAACA  503
             D  V  T  R  R  D  T  F  V  K  L  D  N  W  L  N  E  L  E  T

             Y  C  T  R  N  D  I  V  N  M  L  V  G  N  K  I  D  K  E  N
Seq_1  1681  TACTGTACAAGAAATGACATAGTAAACATGCTAGTTGGAAATAAAATCGATAAGGAAAAT  1740
             ||||||||||||||||||||||||||||||||||||||||||||||||||||||||||||
Seq_2  504   TACTGTACAAGAAATGACATAGTAAACATGCTAGTTGGAAATAAAATCGATAAGGAAAAT  563
             Y  C  T  R  N  D  I  V  N  M  L  V  G  N  K  I  D  K  E  N

             R  E  V  D  R  N  E  G  L  K  F  A  R  K  H  S  M  L  F  I
Seq_1  1741  CGTGAAGTCGATAGAAATGAAGGCCTGAAATTTGCACGAAAGCATTCCATGTTATTTATA  1800
             ||||||||||||||||||||||||||||||||||||||||||||||||||||||||||||
Seq_2  564   CGTGAAGTCGATAGAAATGAAGGCCTGAAATTTGCACGAAAGCATTCCATGTTATTTATA  623
             R  E  V  D  R  N  E  G  L  K  F  A  R  K  H  S  M  L  F  I

             E  A  S  A  K  T  C  D  G  V  Q  C  A  F  E  E  L  V  E  K
Seq_1  1801  GAGGCAAGTGCAAAAACCTGTGATGGTGTACAATGTGCCTTTGAAGAACTTGTTGAAAAG  1860
             ||||||||||||||||||||||||||||||||||||||||||||||||||||||||||||
Seq_2  624   GAGGCAAGTGCAAAAACCTGTGATGGTGTACAATGTGCCTTTGAAGAACTTGTTGAAAAG  683
             E  A  S  A  K  T  C  D  G  V  Q  C  A  F  E  E  L  V  E  K

             I  I  Q  T  P  G  L  W  E  S  E  N  Q  N  K  G  V  K  L  S
Seq_1  1861  ATCATTCAGACCCCTGGACTGTGGGAAAGTGAGAACCAGAATAAAGGAGTCAAACTGTCA  1920
             ||||||||||||||||||||||||||||||||||||||||||||||||||||||||||||
Seq_2  684   ATCATTCAGACCCCTGGACTGTGGGAAAGTGAGAACCAGAATAAAGGAGTCAAACTGTCA  743
             I  I  Q  T  P  G  L  W  E  S  E  N  Q  N  K  G  V  K  L  S

             H  R  E  E  G  Q  G  G  G  A  C  G  G  Y  C  S  V  L  *  G
Seq_1  1921  CACAGGGAAGAAGGCCAAGGAGGAGGAGCCTGTGGTGGTTATTGCTCTGTGTTATAAGga  1980
             ||||||||||||||||||||||||||||||||||||||||||||||||||||||||||||
Seq_2  744   CACAGGGAAGAAGGCCAAGGAGGAGGAGCCTGTGGTGGTTATTGCTCTGTGTTATAAGGA  803
             H  R  E  E  G  Q  G  G  G  A  C  G  G  Y  C  S  V  L  *  G
```

7.1.4. C199S-Sequence Alignement

```
Seq_1 = WT-RAB18
Seq_2 = RAB18-C199S
WT-RAB18 Sequence

             S  G  L  R  S  R  A  Q  A  S  N  S  M  D  E  D  V  L  T  T
Seq_1  1321  TCCGGACTCAGATCTCGAGCTCAAGCTTCGaattCGATGGACGAGGACGTGCTAACCACC  1380
             ||||||||||||||||||||||||||||||||||||||||||||||||||||||||||||
Seq_2  145   TCCGGACTCAGATCTCGAGCTCAAGCTTCGAATTCGATGGACGAGGACGTGCTAACCACC  204
             S  G  L  R  S  R  A  Q  A  S  N  S  M  D  E  D  V  L  T  T

             L  K  I  L  I  I  G  E  S  G  V  G  K  S  S  L  L  L  R  F
Seq_1  1381  CTGAAGATCCTCATCATCGGCGAGAGTGGGGTGGGCAAGTCCAGCCTGCTCTTGAGGTTC  1440
             ||||||||||||||||||||||||||||||||||||||||||||||||||||||||||||
Seq_2  205   CTGAAGATCCTCATCATCGGCGAGAGTGGGGTGGGCAAGTCCAGCCTGCTCTTGAGGTTC  264
             L  K  I  L  I  I  G  E  S  G  V  G  K  S  S  L  L  L  R  F

             T  D  D  T  F  D  P  E  L  A  A  T  I  G  V  D  F  K  V  K
Seq_1  1441  ACAGATGATACGTTTGATCCAGAACTTGCAGCAACAATAGGTGTTGACTTTAAGGTGAAA  1500
             ||||||||||||||||||||||||||||||||||||||||||||||||||||||||||||
Seq_2  265   ACAGATGATACGTTTGATCCAGAACTTGCAGCAACAATAGGTGTTGACTTTAAGGTGAAA  324
             T  D  D  T  F  D  P  E  L  A  A  T  I  G  V  D  F  K  V  K

             T  I  S  V  D  G  N  K  A  K  L  A  I  W  D  T  A  G  Q  E
Seq_1  1501  ACAATTTCAGTGGATGGAAATAAGGCTAAACTTGCAATATGGGATACTGCTGGTCAAGAG  1560
             ||||||||||||||||||||||||||||||||||||||||||||||||||||||||||||
Seq_2  325   ACAATTTCAGTGGATGGAAATAAGGCTAAACTTGCAATATGGGATACTGCTGGTCAAGAG  384
             T  I  S  V  D  G  N  K  A  K  L  A  I  W  D  T  A  G  Q  E

             R  F  R  T  L  T  P  S  Y  Y  R  G  A  Q  G  V  I  L  V  Y
Seq_1  1561  AGGTTTAGAACATTAACTCCCAGCTATTATAGAGGTGCACAGGGTGTTATATTAGTTTAT  1620
             ||||||||||||||||||||||||||||||||||||||||||||||||||||||||||||
Seq_2  385   AGGTTTAGAACATTAACTCCCAGCTATTATAGAGGTGCACAGGGTGTTATATTAGTTTAT  444
             R  F  R  T  L  T  P  S  Y  Y  R  G  A  Q  G  V  I  L  V  Y

             D  V  T  R  R  D  T  F  V  K  L  D  N  W  L  N  E  L  E  T
Seq_1  1621  GATGTCACAAGAAGAGATACATTTGTTAAACTGGATAATTGGTTAAATGAATTGGAAACA  1680
             ||||||||||||||||||||||||||||||||||||||||||||||||||||||||||||
Seq_2  445   GATGTCACAAGAAGAGATACATTTGTTAAACTGGATAATTGGTTAAATGAATTGGAAACA  504
             D  V  T  R  R  D  T  F  V  K  L  D  N  W  L  N  E  L  E  T

             Y  C  T  R  N  D  I  V  N  M  L  V  G  N  K  I  D  K  E  N
Seq_1  1681  TACTGTACAAGAAATGACATAGTAAACATGCTAGTTGGAAATAAAATCGATAAGGAAAAT  1740
             ||||||||||||||||||||||||||||||||||||||||||||||||||||||||||||
Seq_2  505   TACTGTACAAGAAATGACATAGTAAACATGCTAGTTGGAAATAAAATCGATAAGGAAAAT  564
             Y  C  T  R  N  D  I  V  N  M  L  V  G  N  K  I  D  K  E  N

             R  E  V  D  R  N  E  G  L  K  F  A  R  K  H  S  M  L  F  I
Seq_1  1741  CGTGAAGTCGATAGAAATGAAGGCCTGAAATTTGCACGAAAGCATTCCATGTTATTTATA  1800
             ||||||||||||||||||||||||||||||||||||||||||||||||||||||||||||
Seq_2  565   CGTGAAGTCGATAGAAATGAAGGCCTGAAATTTGCACGAAAGCATTCCATGTTATTTATA  624
             R  E  V  D  R  N  E  G  L  K  F  A  R  K  H  S  M  L  F  I

             E  A  S  A  K  T  C  D  G  V  Q  C  A  F  E  E  L  V  E  K
Seq_1  1801  GAGGCAAGTGCAAAAACCTGTGATGGTGTACAATGTGCCTTTGAAGAACTTGTTGAAAAG  1860
             ||||||||||||||||||||||||||||||||||||||||||||||||||||||||||||
Seq_2  625   GAGGCAAGTGCAAAAACCTGTGATGGTGTACAATGTGCCTTTGAAGAACTTGTTGAAAAG  684
             E  A  S  A  K  T  C  D  G  V  Q  C  A  F  E  E  L  V  E  K

             I  I  Q  T  P  G  L  W  E  S  E  N  Q  N  K  G  V  K  L  S
Seq_1  1861  ATCATTCAGACCCCTGGACTGTGGGAAAGTGAGAACCAGAATAAAGGAGTCAAACTGTCA  1920
             ||||||||||||||||||||||||||||||||||||||||||||||||||||||||||||
Seq_2  685   ATCATTCAGACCCCTGGACTGTGGGAAAGTGAGAACCAGAATAAAGGAGTCAAACTGTCA  744
             I  I  Q  T  P  G  L  W  E  S  E  N  Q  N  K  G  V  K  L  S

             H  R  E  E  G  Q  G  G  G  A  C  G  G  Y  C  S  V  L  *  G
Seq_1  1921  CACAGGGAAGAAGGCCAAGGAGGAGGAGCCTGTGGTGGTTATTGCTCTGTGTTATAAGga  1980
             ||||||||||||||||||||||||||||||#|||||||||||||||||||||||||||||
Seq_2  745   CACAGGGAAGAAGGCCAAGGAGGAGGAGCCAGTGGTGGTTATTGCTCTGTGTTATAAGGA  804
             H  R  E  E  G  Q  G  G  G  A  S  G  G  Y  C  S  V  L  *  G
```

7.1.5. Q67L-C199S-Sequence Alignement

```
Seq_1 = WT-RAB18
Seq_2 = RAB18-Q67L-C199S
WT-RAB18 Sequence

              S  G  L  R  S  R  A  Q  A  S  N  S  M  D  E  D  V  L  T  T
Seq_1  1321   TCCGGACTCAGATCTCGAGCTCAAGCTTCGaattCGATGGACGAGGACGTGCTAACCACC  1380
              ||||||||||||||||||||||||||||||||||||||||||||||||||||||||||||
Seq_2  142    TCCGGACTCAGATCTCGAGCTCAAGCTTCGAATTCGATGGACGAGGACGTGCTAACCACC  201
              S  G  L  R  S  R  A  Q  A  S  N  S  M  D  E  D  V  L  T  T

              L  K  I  L  I  I  G  E  S  G  V  G  K  S  S  L  L  L  R  F
Seq_1  1381   CTGAAGATCCTCATCATCGGCGAGAGTGGGGTGGGCAAGTCCAGCCTGCTCTTGAGGTTC  1440
              ||||||||||||||||||||||||||||||||||||||||||||||||||||||||||||
Seq_2  202    CTGAAGATCCTCATCATCGGCGAGAGTGGGGTGGGCAAGTCCAGCCTGCTCTTGAGGTTC  261
              L  K  I  L  I  I  G  E  S  G  V  G  K  S  S  L  L  L  R  F

              T  D  D  T  F  D  P  E  L  A  A  T  I  G  V  D  F  K  V  K
Seq_1  1441   ACAGATGATACGTTTGATCCAGAACTTGCAGCAACAATAGGTGTTGACTTTAAGGTGAAA  1500
              ||||||||||||||||||||||||||||||||||||||||||||||||||||||||||||
Seq_2  262    ACAGATGATACGTTTGATCCAGAACTTGCAGCAACAATAGGTGTTGACTTTAAGGTGAAA  321
              T  D  D  T  F  D  P  E  L  A  A  T  I  G  V  D  F  K  V  K

              T  I  S  V  D  G  N  K  A  K  L  A  I  W  D  T  A  G  Q  E
Seq_1  1501   ACAATTTCAGTGGATGGAAATAAGGCTAAACTTGCAATATGGGATACTGCTGGTCAAGAG  1560
              |||||||||||||||||||||||||||||||||||||||||||||||||||||||#||||
Seq_2  322    ACAATTTCAGTGGATGGAAATAAGGCTAAACTTGCAATATGGGATACTGCTGGTCTAGAG  381
              T  I  S  V  D  G  N  K  A  K  L  A  I  W  D  T  A  G  L  E

              R  F  R  T  L  T  P  S  Y  Y  R  G  A  Q  G  V  I  L  V  Y
Seq_1  1561   AGGTTTAGAACATTAACTCCCAGCTATTATAGAGGTGCACAGGGTGTTATATTAGTTTAT  1620
              ||||||||||||||||||||||||||||||||||||||||||||||||||||||||||||
Seq_2  382    AGGTTTAGAACATTAACTCCCAGCTATTATAGAGGTGCACAGGGTGTTATATTAGTTTAT  441
              R  F  R  T  L  T  P  S  Y  Y  R  G  A  Q  G  V  I  L  V  Y

              D  V  T  R  R  D  T  F  V  K  L  D  N  W  L  N  E  L  E  T
Seq_1  1621   GATGTCACAAGAAGAGATACATTTGTTAAACTGGATAATTGGTTAAATGAATTGGAAACA  1680
              ||||||||||||||||||||||||||||||||||||||||||||||||||||||||||||
Seq_2  442    GATGTCACAAGAAGAGATACATTTGTTAAACTGGATAATTGGTTAAATGAATTGGAAACA  501
              D  V  T  R  R  D  T  F  V  K  L  D  N  W  L  N  E  L  E  T

              Y  C  T  R  N  D  I  V  N  M  L  V  G  N  K  I  D  K  E  N
Seq_1  1681   TACTGTACAAGAAATGACATAGTAAACATGCTAGTTGGAAATAAAATCGATAAGGAAAAT  1740
              ||||||||||||||||||||||||||||||||||||||||||||||||||||||||||||
Seq_2  502    TACTGTACAAGAAATGACATAGTAAACATGCTAGTTGGAAATAAAATCGATAAGGAAAAT  561
              Y  C  T  R  N  D  I  V  N  M  L  V  G  N  K  I  D  K  E  N

              R  E  V  D  R  N  E  G  L  K  F  A  R  K  H  S  M  L  F  I
Seq_1  1741   CGTGAAGTCGATAGAAATGAAGGCCTGAAATTTGCACGAAAGCATTCCATGTTATTTATA  1800
              ||||||||||||||||||||||||||||||||||||||||||||||||||||||||||||
Seq_2  562    CGTGAAGTCGATAGAAATGAAGGCCTGAAATTTGCACGAAAGCATTCCATGTTATTTATA  621
              R  E  V  D  R  N  E  G  L  K  F  A  R  K  H  S  M  L  F  I

              E  A  S  A  K  T  C  D  G  V  Q  C  A  F  E  E  L  V  E  K
Seq_1  1801   GAGGCAAGTGCAAAAACCTGTGATGGTGTACAATGTGCCTTTGAAGAACTTGTTGAAAAG  1860
              ||||||||||||||||||||||||||||||||||||||||||||||||||||||||||||
Seq_2  622    GAGGCAAGTGCAAAAACCTGTGATGGTGTACAATGTGCCTTTGAAGAACTTGTTGAAAAG  681
              E  A  S  A  K  T  C  D  G  V  Q  C  A  F  E  E  L  V  E  K

              I  I  Q  T  P  G  L  W  E  S  E  N  Q  N  K  G  V  K  L  S
Seq_1  1861   ATCATTCAGACCCCTGGACTGTGGGAAAGTGAGAACCAGAATAAAGGAGTCAAACTGTCA  1920
              ||||||||||||||||||||||||||||||||||||||||||||||||||||||||||||
Seq_2  682    ATCATTCAGACCCCTGGACTGTGGGAAAGTGAGAACCAGAATAAAGGAGTCAAACTGTCA  741
              I  I  Q  T  P  G  L  W  E  S  E  N  Q  N  K  G  V  K  L  S

              H  R  E  E  G  Q  G  G  G  A  C  G  G  Y  C  S  V  L  *  G
Seq_1  1921   CACAGGGAAGAAGGCCAAGGAGGAGGAGCCTGTGGTGGTTATTGCTCTGTGTTATAAGga  1980
              ||||||||||||||||||||||||||||||#|||||||||||||||||||||||||||||
Seq_2  742    CACAGGGAAGAAGGCCAAGGAGGAGGAGCCAGTGGTGGTTATTGCTCTGTGTTATAAGGA  801
              H  R  E  E  G  Q  G  G  G  A  S  G  G  Y  C  S  V  L  *  G
```

7.1.6. S22N-C199S-Sequence Alignement

```
Seq_1 = WT-RAB18
Seq_2 = RAB18-S22N-C199S
```

WT-RAB18 Sequence

```
             S  G  L  R  S  R  A  Q  A  S  N  S  M  D  E  D  V  L  T  T
Seq_1  1321  TCCGGACTCAGATCTCGAGCTCAAGCTTCGaattCGATGGACGAGGACGTGCTAACCACC  1380
             ||||||||||||||||||||||||||||||||||||||||||||||||||||||||||||
Seq_2  134   TCCGGACTCAGATCTCGAGCTCAAGCTTCGAATTCGATGGACGAGGACGTGCTAACCACC  193
             S  G  L  R  S  R  A  Q  A  S  N  S  M  D  E  D  V  L  T  T

             L  K  I  L  I  I  G  E  S  G  V  G  K  S  S  L  L  L  R  F
Seq_1  1381  CTGAAGATCCTCATCATCGGCGAGAGTGGGGTGGGCAAGTCCAGCCTGCTCTTGAGGTTC  1440
             |||||||||||||||||||||||||||||||||||||||##|||||||||||||||||||
Seq_2  194   CTGAAGATCCTCATCATCGGCGAGAGTGGGGTGGGCAAGAACAGCCTGCTCTTGAGGTTC  253
             L  K  I  L  I  I  G  E  S  G  V  G  K  N  S  L  L  L  R  F

             T  D  D  T  F  D  P  E  L  A  A  T  I  G  V  D  F  K  V  K
Seq_1  1441  ACAGATGATACGTTTGATCCAGAACTTGCAGCAACAATAGGTGTTGACTTTAAGGTGAAA  1500
             ||||||||||||||||||||||||||||||||||||||||||||||||||||||||||||
Seq_2  254   ACAGATGATACGTTTGATCCAGAACTTGCAGCAACAATAGGTGTTGACTTTAAGGTGAAA  313
             T  D  D  T  F  D  P  E  L  A  A  T  I  G  V  D  F  K  V  K

             T  I  S  V  D  G  N  K  A  K  L  A  I  W  D  T  A  G  Q  E
Seq_1  1501  ACAATTTCAGTGGATGGAAATAAGGCTAAACTTGCAATATGGGATACTGCTGGTCAAGAG  1560
             ||||||||||||||||||||||||||||||||||||||||||||||||||||||||||||
Seq_2  314   ACAATTTCAGTGGATGGAAATAAGGCTAAACTTGCAATATGGGATACTGCTGGTCAAGAG  373
             T  I  S  V  D  G  N  K  A  K  L  A  I  W  D  T  A  G  Q  E

             R  F  R  T  L  T  P  S  Y  Y  R  G  A  Q  G  V  I  L  V  Y
Seq_1  1561  AGGTTTAGAACATTAACTCCCAGCTATTATAGAGGTGCACAGGGTGTTATATTAGTTTAT  1620
             ||||||||||||||||||||||||||||||||||||||||||||||||||||||||||||
Seq_2  374   AGGTTTAGAACATTAACTCCCAGCTATTATAGAGGTGCACAGGGTGTTATATTAGTTTAT  433
             R  F  R  T  L  T  P  S  Y  Y  R  G  A  Q  G  V  I  L  V  Y

             D  V  T  R  R  D  T  F  V  K  L  D  N  W  L  N  E  L  E  T
Seq_1  1621  GATGTCACAAGAAGAGATACATTTGTTAAACTGGATAATTGGTTAAATGAATTGGAAACA  1680
             ||||||||||||||||||||||||||||||||||||||||||||||||||||||||||||
Seq_2  434   GATGTCACAAGAAGAGATACATTTGTTAAACTGGATAATTGGTTAAATGAATTGGAAACA  493
             D  V  T  R  R  D  T  F  V  K  L  D  N  W  L  N  E  L  E  T

             Y  C  T  R  N  D  I  V  N  M  L  V  G  N  K  I  D  K  E  N
Seq_1  1681  TACTGTACAAGAAATGACATAGTAAACATGCTAGTTGGAAATAAAATCGATAAGGAAAAT  1740
             ||||||||||||||||||||||||||||||||||||||||||||||||||||||||||||
Seq_2  494   TACTGTACAAGAAATGACATAGTAAACATGCTAGTTGGAAATAAAATCGATAAGGAAAAT  553
             Y  C  T  R  N  D  I  V  N  M  L  V  G  N  K  I  D  K  E  N

             R  E  V  D  R  N  E  G  L  K  F  A  R  K  H  S  M  L  F  I
Seq_1  1741  CGTGAAGTCGATAGAAATGAAGGCCTGAAATTTGCACGAAAGCATTCCATGTTATTTATA  1800
             ||||||||||||||||||||||||||||||||||||||||||||||||||||||||||||
Seq_2  554   CGTGAAGTCGATAGAAATGAAGGCCTGAAATTTGCACGAAAGCATTCCATGTTATTTATA  613
             R  E  V  D  R  N  E  G  L  K  F  A  R  K  H  S  M  L  F  I

             E  A  S  A  K  T  C  D  G  V  Q  C  A  F  E  E  L  V  E  K
Seq_1  1801  GAGGCAAGTGCAAAAACCTGTGATGGTGTACAATGTGCCTTTGAAGAACTTGTTGAAAAG  1860
             ||||||||||||||||||||||||||||||||||||||||||||||||||||||||||||
Seq_2  614   GAGGCAAGTGCAAAAACCTGTGATGGTGTACAATGTGCCTTTGAAGAACTTGTTGAAAAG  673
             E  A  S  A  K  T  C  D  G  V  Q  C  A  F  E  E  L  V  E  K

             I  I  Q  T  P  G  L  W  E  S  E  N  Q  N  K  G  V  K  L  S
Seq_1  1861  ATCATTCAGACCCCTGGACTGTGGGAAAGTGAGAACCAGAATAAAGGAGTCAAACTGTCA  1920
             ||||||||||||||||||||||||||||||||||||||||||||||||||||||||||||
Seq_2  674   ATCATTCAGACCCCTGGACTGTGGGAAAGTGAGAACCAGAATAAAGGAGTCAAACTGTCA  733
             I  I  Q  T  P  G  L  W  E  S  E  N  Q  N  K  G  V  K  L  S

             H  R  E  E  G  Q  G  G  G  A  C  G  G  Y  C  S  V  L  *  G
Seq_1  1921  CACAGGGAAGAAGGCCAAGGAGGAGGAGCCTGTGGTGGTTATTGCTCTGTGTTATAAGga  1980
             ||||||||||||||||||||||||||||||#|||||||||||||||||||||||||||||
Seq_2  734   CACAGGGAAGAAGGCCAAGGAGGAGGAGCCAGTGGTGGTTATTGCTCTGTGTTATAAGGA  793
             H  R  E  E  G  Q  G  G  G  A  S  G  G  Y  C  S  V  L  *  G
```

7.1.7. C203S-Sequence Alignement

```
Seq_1 = WT-RAB18
Seq_2 = RAB18-C203S
```

WT-RAB18 Sequence

```
              S  G  L  R  S  R  A  Q  A  S  N  S  M  D  E  D  V  L  T  T
Seq_1  1321   TCCGGACTCAGATCTCGAGCTCAAGCTTCGaattCGATGGACGAGGACGTGCTAACCACC  1380
              ||||||||||||||||||||||||||||||||||||||||||||||||||||||||||||
Seq_2  144    TCCGGACTCAGATCTCGAGCTCAAGCTTCGAATTCGATGGACGAGGACGTGCTAACCACC  203
              S  G  L  R  S  R  A  Q  A  S  N  S  M  D  E  D  V  L  T  T

              L  K  I  L  I  I  G  E  S  G  V  G  K  S  S  L  L  L  R  F
Seq_1  1381   CTGAAGATCCTCATCATCGGCGAGAGTGGGGTGGGCAAGTCCAGCCTGCTCTTGAGGTTC  1440
              ||||||||||||||||||||||||||||||||||||||||||||||||||||||||||||
Seq_2  204    CTGAAGATCCTCATCATCGGCGAGAGTGGGGTGGGCAAGTCCAGCCTGCTCTTGAGGTTC  263
              L  K  I  L  I  I  G  E  S  G  V  G  K  S  S  L  L  L  R  F

              T  D  D  T  F  D  P  E  L  A  A  T  I  G  V  D  F  K  V  K
Seq_1  1441   ACAGATGATACGTTTGATCCAGAACTTGCAGCAACAATAGGTGTTGACTTTAAGGTGAAA  1500
              ||||||||||||||||||||||||||||||||||||||||||||||||||||||||||||
Seq_2  264    ACAGATGATACGTTTGATCCAGAACTTGCAGCAACAATAGGTGTTGACTTTAAGGTGAAA  323
              T  D  D  T  F  D  P  E  L  A  A  T  I  G  V  D  F  K  V  K

              T  I  S  V  D  G  N  K  A  K  L  A  I  W  D  T  A  G  Q  E
Seq_1  1501   ACAATTTCAGTGGATGGAAATAAGGCTAAACTTGCAATATGGGATACTGCTGGTCAAGAG  1560
              ||||||||||||||||||||||||||||||||||||||||||||||||||||||||||||
Seq_2  324    ACAATTTCAGTGGATGGAAATAAGGCTAAACTTGCAATATGGGATACTGCTGGTCAAGAG  383
              T  I  S  V  D  G  N  K  A  K  L  A  I  W  D  T  A  G  Q  E

              R  F  R  T  L  T  P  S  Y  Y  R  G  A  Q  G  V  I  L  V  Y
Seq_1  1561   AGGTTTAGAACATTAACTCCCAGCTATTATAGAGGTGCACAGGGTGTTATATTAGTTTAT  1620
              ||||||||||||||||||||||||||||||||||||||||||||||||||||||||||||
Seq_2  384    AGGTTTAGAACATTAACTCCCAGCTATTATAGAGGTGCACAGGGTGTTATATTAGTTTAT  443
              R  F  R  T  L  T  P  S  Y  Y  R  G  A  Q  G  V  I  L  V  Y

              D  V  T  R  R  D  T  F  V  K  L  D  N  W  L  N  E  L  E  T
Seq_1  1621   GATGTCACAAGAAGAGATACATTTGTTAAACTGGATAATTGGTTAAATGAATTGGAAACA  1680
              ||||||||||||||||||||||||||||||||||||||||||||||||||||||||||||
Seq_2  444    GATGTCACAAGAAGAGATACATTTGTTAAACTGGATAATTGGTTAAATGAATTGGAAACA  503
              D  V  T  R  R  D  T  F  V  K  L  D  N  W  L  N  E  L  E  T

              Y  C  T  R  N  D  I  V  N  M  L  V  G  N  K  I  D  K  E  N
Seq_1  1681   TACTGTACAAGAAATGACATAGTAAACATGCTAGTTGGAAATAAAATCGATAAGGAAAAT  1740
              ||||||||||||||||||||||||||||||||||||||||||||||||||||||||||||
Seq_2  504    TACTGTACAAGAAATGACATAGTAAACATGCTAGTTGGAAATAAAATCGATAAGGAAAAT  563
              Y  C  T  R  N  D  I  V  N  M  L  V  G  N  K  I  D  K  E  N

              R  E  V  D  R  N  E  G  L  K  F  A  R  K  H  S  M  L  F  I
Seq_1  1741   CGTGAAGTCGATAGAAATGAAGGCCTGAAATTTGCACGAAAGCATTCCATGTTATTTATA  1800
              ||||||||||||||||||||||||||||||||||||||||||||||||||||||||||||
Seq_2  564    CGTGAAGTCGATAGAAATGAAGGCCTGAAATTTGCACGAAAGCATTCCATGTTATTTATA  623
              R  E  V  D  R  N  E  G  L  K  F  A  R  K  H  S  M  L  F  I

              E  A  S  A  K  T  C  D  G  V  Q  C  A  F  E  E  L  V  E  K
Seq_1  1801   GAGGCAAGTGCAAAAACCTGTGATGGTGTACAATGTGCCTTTGAAGAACTTGTTGAAAAG  1860
              ||||||||||||||||||||||||||||||||||||||||||||||||||||||||||||
Seq_2  624    GAGGCAAGTGCAAAAACCTGTGATGGTGTACAATGTGCCTTTGAAGAACTTGTTGAAAAG  683
              E  A  S  A  K  T  C  D  G  V  Q  C  A  F  E  E  L  V  E  K

              I  I  Q  T  P  G  L  W  E  S  E  N  Q  N  K  G  V  K  L  S
Seq_1  1861   ATCATTCAGACCCCTGGACTGTGGGAAAGTGAGAACCAGAATAAAGGAGTCAAACTGTCA  1920
              ||||||||||||||||||||||||||||||||||||||||||||||||||||||||||||
Seq_2  684    ATCATTCAGACCCCTGGACTGTGGGAAAGTGAGAACCAGAATAAAGGAGTCAAACTGTCA  743
              I  I  Q  T  P  G  L  W  E  S  E  N  Q  N  K  G  V  K  L  S

              H  R  E  E  G  Q  G  G  G  A  C  G  G  Y  C  S  V  L  *  G
Seq_1  1921   CACAGGGAAGAAGGCCAAGGAGGAGGAGCCTGTGGTGGTTATTGCTCTGTGTTATAAGga  1980
              |||||||||||||||||||||||||||||||||||||||#||||||||||||||||||||
Seq_2  744    CACAGGGAAGAAGGCCAAGGAGGAGGAGCCTGTGGTGGTTATAGCTCTGTGTTATAAGGA  803
              H  R  E  E  G  Q  G  G  G  A  C  G  G  Y  S  S  V  L  *  G
```

7.1.8. PolyC-Sequence Alignement

```
Seq_1 = WT-RAB18
Seq_2 = RAB18-PolyC
WT-RAB18 Sequence

             S  G  L  R  S  R  A  Q  A  S  N  S  M  D  E  D  V  L  T  T
Seq_1  1321  TCCGGACTCAGATCTCGAGCTCAAGCTTCGaattCGATGGACGAGGACGTGCTAACCACC  1380
             ||||||||||||||||||||||||||||||||||||||||||||||||||||||||||||
Seq_2  146   TCCGGACTCAGATCTCGAGCTCAAGCTTCGAATTCGATGGACGAGGACGTGCTAACCACC  205
             S  G  L  R  S  R  A  Q  A  S  N  S  M  D  E  D  V  L  T  T

             L  K  I  L  I  I  G  E  S  G  V  G  K  S  S  L  L  L  R  F
Seq_1  1381  CTGAAGATCCTCATCATCGGCGAGAGTGGGGTGGGCAAGTCCAGCCTGCTCTTGAGGTTC  1440
             ||||||||||||||||||||||||||||||||||||||||||||||||||||||||||||
Seq_2  206   CTGAAGATCCTCATCATCGGCGAGAGTGGGGTGGGCAAGTCCAGCCTGCTCTTGAGGTTC  265
             L  K  I  L  I  I  G  E  S  G  V  G  K  S  S  L  L  L  R  F

             T  D  D  T  F  D  P  E  L  A  A  T  I  G  V  D  F  K  V  K
Seq_1  1441  ACAGATGATACGTTTGATCCAGAACTTGCAGCAACAATAGGTGTTGACTTTAAGGTGAAA  1500
             ||||||||||||||||||||||||||||||||||||||||||||||||||||||||||||
Seq_2  266   ACAGATGATACGTTTGATCCAGAACTTGCAGCAACAATAGGTGTTGACTTTAAGGTGAAA  325
             T  D  D  T  F  D  P  E  L  A  A  T  I  G  V  D  F  K  V  K

             T  I  S  V  D  G  N  K  A  K  L  A  I  W  D  T  A  G  Q  E
Seq_1  1501  ACAATTTCAGTGGATGGAAATAAGGCTAAACTTGCAATATGGGATACTGCTGGTCAAGAG  1560
             ||||||||||||||||||||||||||||||||||||||||||||||||||||||||||||
Seq_2  326   ACAATTTCAGTGGATGGAAATAAGGCTAAACTTGCAATATGGGATACTGCTGGTCAAGAG  385
             T  I  S  V  D  G  N  K  A  K  L  A  I  W  D  T  A  G  Q  E

             R  F  R  T  L  T  P  S  Y  Y  R  G  A  Q  G  V  I  L  V  Y
Seq_1  1561  AGGTTTAGAACATTAACTCCCAGCTATTATAGAGGTGCACAGGGTGTTATATTAGTTTAT  1620
             ||||||||||||||||||||||||||||||||||||||||||||||||||||||||||||
Seq_2  386   AGGTTTAGAACATTAACTCCCAGCTATTATAGAGGTGCACAGGGTGTTATATTAGTTTAT  445
             R  F  R  T  L  T  P  S  Y  Y  R  G  A  Q  G  V  I  L  V  Y

             D  V  T  R  R  D  T  F  V  K  L  D  N  W  L  N  E  L  E  T
Seq_1  1621  GATGTCACAAGAAGAGATACATTTGTTAAACTGGATAATTGGTTAAATGAATTGGAAACA  1680
             ||||||||||||||||||||||||||||||||||||||||||||||||||||||||||||
Seq_2  446   GATGTCACAAGAAGAGATACATTTGTTAAACTGGATAATTGGTTAAATGAATTGGAAACA  505
             D  V  T  R  R  D  T  F  V  K  L  D  N  W  L  N  E  L  E  T

             Y  C  T  R  N  D  I  V  N  M  L  V  G  N  K  I  D  K  E  N
Seq_1  1681  TACTGTACAAGAAATGACATAGTAAACATGCTAGTTGGAAATAAAATCGATAAGGAAAAT  1740
             ||||||||||||||||||||||||||||||||||||||||||||||||||||||||||||
Seq_2  506   TACTGTACAAGAAATGACATAGTAAACATGCTAGTTGGAAATAAAATCGATAAGGAAAAT  565
             Y  C  T  R  N  D  I  V  N  M  L  V  G  N  K  I  D  K  E  N

             R  E  V  D  R  N  E  G  L  K  F  A  R  K  H  S  M  L  F  I
Seq_1  1741  CGTGAAGTCGATAGAAATGAAGGCCTGAAATTTGCACGAAAGCATTCCATGTTATTTATA  1800
             ||||||||||||||||||||||||||||||||||||||||||||||||||||||||||||
Seq_2  566   CGTGAAGTCGATAGAAATGAAGGCCTGAAATTTGCACGAAAGCATTCCATGTTATTTATA  625
             R  E  V  D  R  N  E  G  L  K  F  A  R  K  H  S  M  L  F  I

             E  A  S  A  K  T  C  D  G  V  Q  C  A  F  E  E  L  V  E  K
Seq_1  1801  GAGGCAAGTGCAAAAACCTGTGATGGTGTACAATGTGCCTTTGAAGAACTTGTTGAAAAG  1860
             ||||||||||||||||||||||||||||||||||||||||||||||||||||||||||||
Seq_2  626   GAGGCAAGTGCAAAAACCTGTGATGGTGTACAATGTGCCTTTGAAGAACTTGTTGAAAAG  685
             E  A  S  A  K  T  C  D  G  V  Q  C  A  F  E  E  L  V  E  K

             I  I  Q  T  P  G  L  W  E  S  E  N  Q  N  K  G  V  K  L  S
Seq_1  1861  ATCATTCAGACCCCTGGACTGTGGGAAAGTGAGAACCAGAATAAAGGAGTCAAACTGTCA  1920
             ||||||||||||||||||||||||||||||||||||||||||||||||||||||||||||
Seq_2  686   ATCATTCAGACCCCTGGACTGTGGGAAAGTGAGAACCAGAATAAAGGAGTCAAACTGTCA  745
             I  I  Q  T  P  G  L  W  E  S  E  N  Q  N  K  G  V  K  L  S

             H  R   E  E  G  Q  G  G  G  A  C  G  G  Y  C  S  V  L  *  G
Seq_1  1921  CACAGG-GAAGAAGGCCAAGGAGGAGGAGCCTGTGGTGGTTATTGCTCTGTGTTATAAGg  1979
             ||||||#|##|||||||||#|#||||||||||||||||||||||||||||||||||||||
Seq_2  746   CACAGGTG-CGAAGGCCAATGCGGAGGAGCCTGTGGTGGTTATTGCTCTGTGTTATAAGG  804
             H  R  C   E  G  Q  C  G  G  A  C  G  G  Y  C  S  V  L  *  G
```

7.2. Abbreviations

°C	Degree Celsius
2-BP	2-bromopalmitate
µg	micro gram
µl	micro litre
µM	Micromolar
ACAT	Acyl-CoA-cholesterol acyltransferase
ACSL3	Long-chain-fattyacid-CoA ligaes3
ADRP	Adipose differentiation-related protein
ATGL	adipose triglyceride lipase
BMI	Body mass index
bp	base pair
BSA	Bovine serum albumin
CARS	Coherent Anti-Stokes Raman Spectroscopy
CC50	Cytotoxic concentration
CDC	Central for Disease Control
cDNA	complementary DNA
cm	centimetre
CMA	Chaperon mediated autophagy
CoA	Coenzyme A
DAG	Diacylglyceride
DGAT 1/2	Diglyceride acyltransferase 1/2
DMEM	Dulbecco's Modified Eagle Medium
DMSO	Dimethyl sulfoxid
DNA	Desoxyribonucleic acid
dNTP	Nucleotide-triphosphate
ECARS	Epi scattered CARS signal
ER	Endoplasmic reticulum

ESCRT	Endosomal sorting complex
EtBr	Ethidium Bromide
FATP1	Fatty acid transport protein 1
FBS	Fetal Bovine Serum
FCARS	Forward scattered CARS signal
FFA	Free fatty acids
FIJI	FIJI is just imagej
FR	FusionRed
FRAP	Fluorescence recovery after photobleaching
FSP27	Fat-specific protein 27
GAP	GTPase activating protein
GDF	GDI displacement factor
GDI	GDP dissociation inhibitor
GDP	Guanosine-diphosphate
GEF	Guanosine exchange factor
GFP	Green Fluorescence Protein
GPAT2	Glycerol-3-phosphate acyltransferase 2
GTP	Guanosine-triphosphate
h	hour
HCC	Hepatocellular carcinoma
HCV	Hepatitis C virus
HDL	High-density lipoprotein
HSC70	Heat shock cognate protein 70
HSL	Hormone sensitive lipase
IPTG	Isopropylthiogalactopyranoside
IR	Infrared
Kg	kilogram
LAL	Lysosomal acid lipase

LAMP	Lysosomal-associated membrane protein
LD	Lipid droplet
LDAF1	Lipid droplet assembly factor1
LDL	Low-density lipoprotein
m	meter
M	Molar ratio mol/L
MAG	Monoacylglyceride
MetOH	Methanol
MGL	Monoacylglycerol lipase
min	minutes
ml	millilitre
mM	Millimolar
NA	Numerical aperture
NAFLD	Non-alcoholic fatty liver disease
NASH	Non-alcoholic liver steatohepatitis
NFAT5	Nuclear factor of activated T cells 5
ng	nanogram
Nm	Nanometre
o.n.	Over night
OA	Oleic acid
ORF	Open reading frame
PBS	Phosphate Buffer System
PCR	Polymerase Chain Reaction
pHCMV	Human Cytomegalovirus promoter
PHH	Primary human hepatocytes
PI3P	Phospho-inositol-triphosphate
PolyC	RAB18 E191C G195C

PPARγ	Peroxisome proliferator-activated receptor gamma
RAB18 KD	RAB18 knock down
RAB18KO	RAB18 knock out
RNA	Ribonucleic acid
RNAi	RNA interference
RT	Room temperature (21°C)
S.O.C.	Super Optimal broth with Catabolite repression
sec	seconds
siRNA	Small interference DNA RNA
TAE	Tris-Acetate-EDTA
TAG	Triacyl glycerides
VPS34	Phospho-inositol-triphosphate
WHO	World health organisation
WT	Wildtype

7.3. Posters

LiSyM Jamboree

15.-17.5.2017, Dresden

Poster: “Influence of RAB18 on steatosis “

LiSyM PhD retreat:

20.-22.11.2017, Hünfeld

Poster: “Small GTPases in Steatosis: the role of RAB18“

Best Poster award

7th Conference on Systems Biology of Mammalian Cells (SBMC)

04.-06.07.2018, Bremen

Poster: "Lipid Droplet regulation in the liver: The role of RAB18"

LiSyM PhD retreat

26.-28.08.2018, Hünfeld

Poster: "Small GTPases in steatosis: The role of RAB18"

LiSyM Jamboree

9.-10.05.2019, Leipzig

Poster: "Small GTPases in steatosis: The role of RAB18"

Seeing is Believing

09-12.10.2019, Heidelberg

Poster: "Small GTPases in steatosis: The role of RAB18"

LiSyM PhD retreat

29-31.01.2020, Hofgeismar

Poster: "Small GTPases in steatosis: The role of RAB18"

7.4. Publication

The findings of this current thesis are in preparation to be published as a peer reviewed manuscript

7.5. Acknowledgement

First, I would like to thank the BMBF for graciously funding this work. It has been a privilege to be part of the LiSyM project working and learning from great minds in the field of liver research.

I also would like to thank my first examiner and supervisor Prof. Dr. Hengstler the opportunity to work at the IfADo and his many suggestions to make it more relevant for the liver. Further, I would like to thank him for his supervisions and guidance during this project.

My deepest thanks go to my second supervisor and Principal Investigator Dr. Nachiket Vartak for supporting me throughout the course of my PhD. His immense knowledge of microscopy and cell biology never failed to amaze me, and meetings with him always left me with new aspects to ponder on. Throughout my thesis working with him inspired me to work harder becoming a better scientist. Even during the more stressful times his door was always open for me and my strange LD hypothesizes. In short, thank you for being such a great supervisor.

I also would like to thank my two colleagues in the Vartak group. Dr. Amruta Damle-Vartak taught me the techniques for primary cell culture and supported me in long overnight experiments. Without the support of Georgia Guenther in primary cell culture and animal husbandry, large parts of this thesis would not have been possible. Asides from the scientific support, I would like to thank both for supporting me through the highs and lows of this project.

Special thanks also go to Martin Schmitz and all members of the Werkstatt for their help during the installing of the SP8 microscope.

I would like to thank my colleague Dr. Gregor Leonhardt for all the commiserating and scientific debates with me during the breaks. At this point, I also want to thank all the amazing members of the Toxicology department as well as the members of the PhD representatives. It has always been a pleasure working with you.

This was by far the most ambitious project in my life, and I came close to quitting at several points. Therefore, it is without doubt that without my fiancé's unrelenting support, none of this would have been possible. Dani, thank you for being there. My deepest apologies for all the times I came home in a mess at 1:00 o'clock in the morning.

Last, I also would like to thank my family who continue to always be there when I needed them. Although we may be far apart and seldom see each other these days, you are always on my mind.